



**HAL**  
open science

# Dosimetric studies for proton minibeam radiation therapy

Ramon Ortiz Catalan

► **To cite this version:**

Ramon Ortiz Catalan. Dosimetric studies for proton minibeam radiation therapy. Medical Physics [physics.med-ph]. Université Paris-Saclay, 2022. English. NNT : 2022UPASP147 . tel-03957981

**HAL Id: tel-03957981**

**<https://theses.hal.science/tel-03957981>**

Submitted on 26 Jan 2023

**HAL** is a multi-disciplinary open access archive for the deposit and dissemination of scientific research documents, whether they are published or not. The documents may come from teaching and research institutions in France or abroad, or from public or private research centers.

L'archive ouverte pluridisciplinaire **HAL**, est destinée au dépôt et à la diffusion de documents scientifiques de niveau recherche, publiés ou non, émanant des établissements d'enseignement et de recherche français ou étrangers, des laboratoires publics ou privés.

# Dosimetric studies for proton minibeam radiation therapy

*Études de dosimétrie par radiothérapie par mini-faisceau de protons*

## Thèse de doctorat de l'université Paris-Saclay

École doctorale n° 576 - Particules, hadrons, énergie et noyau :  
instrumentation, imagerie, cosmos et simulation (PHENIICS)

Spécialité de doctorat: radio et hadron-thérapies

Graduate School : Physique. Référent : Faculté des Sciences d'Orsay

Thèse préparée dans l'unité de recherche **Signalisation radiobiologie et cancer (Université Paris-Saclay, Inserm, CNRS)**, sous la direction de **Yolanda PREZADO**, directrice de recherche, et le co-encadrement de **Ludovic DE MARZI**, physicien médical.

Thèse soutenue à Paris-Saclay, le 12 décembre 2022, par

**Ramon ORTIZ CATALAN**

### Composition du jury

Membres du jury avec voix délibérative

<b>Elias KHAN</b> Professeur, Université Paris-Saclay	Président
<b>Karen KIRKBY</b> Professeure, University of Manchester	Rapporteuse & Examinatrice
<b>Tony LOMAX</b> Professeur, Paul Scherrer Institute	Rapporteur & Examinateur
<b>Diego AZCONA</b> Physicien médical, Clínica Universitaria de Navarra	Examinateur
<b>Immaculada MARTÍNEZ-ROVIRA</b> Maîtresse de conférences, Universitat Autònoma Barcelona	Examinatrice

**Titre:** Études de dosimétrie par radiothérapie par mini-faisceau de protons

**Mots clés:** radiothérapie, protonthérapie, fractionnement spatial de la dose, mini-faisceaux, pMBRT, dosimétrie, simulations de Monte Carlo.

**Résumé :** Au cours des dernières décennies, la radiothérapie a bénéficié de nombreuses avancées permettant de conformer une dose très élevée à la tumeur et de réduire la dose délivrée aux tissus normaux. Cependant, la toxicité radio-induite dans les tissus normaux reste l'un des principaux facteurs limitants de la radiothérapie, compromettant le traitement des tumeurs radiorésistantes (par exemple, les glioblastomes), des cancers pédiatriques ou des tumeurs proches d'organes hautement radiosensibles (par exemple, la moelle épinière). Plusieurs approches ont été proposées ces dernières années pour diminuer les effets secondaires des rayonnements et améliorer l'index thérapeutique pour ces indications cliniques. La radiothérapie à fractionnement spatial (SFRT) en est un exemple. Cette modalité est basée sur la délivrance de faisceaux étroits séparés spatialement par une certaine distance, créant un schéma de fortes doses intercalées par des régions à faible dose.

Cette thèse de doctorat s'inscrit dans le cadre du développement d'une technique de SFRT appelée radiothérapie par mini-faisceaux de protons (pMBRT). La pMBRT a déjà démontré une remarquable préservation des tissus ainsi qu'une grande efficacité en termes de contrôle des tumeurs, par rapport aux techniques conventionnelles. Cependant, certains aspects de cette technique ne sont pas encore complètement caractérisés et doivent être étudiés plus avant (par exemple, les mécanismes biologiques qui sous-tendent la réponse tissulaire favorable).

Le travail de cette thèse contribue au développement de la pMBRT sous trois aspects principaux.

En premier lieu, il optimise la pratique dosimétrique de cette technique en évaluant la performance de différents dosimètres dans des conditions de pMBRT et en effectuant une analyse de robustesse sur la sensibilité des distributions de dose aux incertitudes des paramètres de configuration et d'irradiation. Sur la base de ces résultats, des lignes directives

et des protocoles visant à garantir une dosimétrie reproductible et robuste sont proposés. Les protocoles proposés permettent de réaliser la dosimétrie nécessaire aux études précliniques menées dans notre institution.

Dans la deuxième partie de ce travail, le potentiel de la pMBRT pour le traitement de différentes indications cliniques (c'est-à-dire les métastases cérébrales, hépatiques et pulmonaires) est évalué par une étude de plan de traitement dans le contexte de la préparation des essais cliniques. Les résultats de cette étude montrent que les traitements par pMBRT peuvent assurer une couverture tumorale similaire à celle des techniques stéréotaxiques conventionnelles et réduire la dose intégrale aux organes à risque. De plus, le potentiel accru de préservation des tissus normaux de la pMBRT permet d'administrer le traitement en utilisant un nombre réduit de champs et une seule fraction tout en respectant les tolérances de dose aux tissus normaux. Par conséquent, on peut s'attendre à une augmentation de l'index thérapeutique dans le traitement de ces tumeurs malignes avec la pMBRT.

Enfin, une nouvelle forme de pMBRT appelée thérapie par arcs de mini-faisceaux de protons (pMBAT) est proposée sur la base de l'administration de matrices de mini-faisceaux de protons par des arcs, c'est-à-dire en combinant la pMBRT et les thérapies par arcs. La pMBAT maintient et additionne les avantages individuels de la pMBRT et des techniques d'arcs pour la préservation des tissus normaux en termes de préservation du fractionnement spatial de la dose et de réduction des doses de crête et de vallée, ainsi que de l'escalade du LET. Par conséquent, cette nouvelle approche peut permettre d'utiliser des schémas d'irradiation plus agressifs, ce qui pourrait être avantageux dans la gestion des tumeurs radiorésistantes.

En résumé, cette thèse contribue à l'avancement du pMBRT en optimisant la pratique de la dosimétrie dans sa phase préclinique actuelle et en explorant ses applications cliniques à court et moyen terme.

**Title:** Dosimetric studies for proton minibeam radiation therapy

**Keywords:** radiotherapy, proton therapy, spatial fractionation of the dose, minibeam, pMBRT, dosimetry, Monte Carlo simulations.

**Abstract:** In the last decades, radiotherapy has profited from numerous advances allowing a very high dose conformation to the tumor and a reduction in the dose delivered to normal tissues. However, the radio-induced toxicity in normal tissues remains one of the main limiting factors in radiotherapy, compromising the treatment of radioresistant tumors (e.g., glioblastomas), pediatric cancer, or tumors close to highly radiosensitive organs (e.g. the spinal cord). Several approaches have been proposed in recent years to diminish the side effects of radiation and improve the therapeutic index for those clinical indications. An example is spatially-fractionated radiotherapy (SFRT). This modality is based on delivering narrow beams separated spatially by a certain distance, creating a pattern of high doses intercalated by low-dose regions.

This PhD thesis is framed within the development of an SFRT technique called proton minibeam radiation therapy (pMBRT). pMBRT has already shown remarkable tissue sparing along with high efficacy in terms of tumor control, as compared to conventional techniques. However, there are still some aspects of this technique that are not fully characterized and need further study (e.g., the biological mechanisms that underlie the favorable tissue response). The work of this thesis contributes to the further development of pMBRT in three main aspects.

In the first place, it optimizes the dosimetric practice for this technique by evaluating the performance of different dosimeters in pMBRT conditions and performing a robustness analysis on the sensitivity of dose distributions to uncertainties in setup and irradiation parameters. Based on those results, guidelines and protocols to ensure reproducible and

robust dosimetry are proposed. Following the proposed protocols, the needed dosimetry for the preclinical studies at our institution is performed.

In the second part of this work, the potential of pMBRT for treating different clinical indications (i.e., brain, liver, and lung metastases) is evaluated by a treatment plan study in the context of preparing the clinical trials. The result of this study shows that pMBRT treatments can provide a similar tumor coverage with respect to conventional stereotactic techniques and reduce the integral dose to organs-at-risk. Moreover, the increased normal tissue-sparing potential in pMBRT allows the treatment delivery using a reduced number of fields and a single fraction while meeting normal tissue dose tolerances. Therefore, an increase in the therapeutic index may be expected in the treatment of those malignancies with pMBRT.

Finally, a new form of pMBRT termed proton minibeam arc therapy (pMBAT) is proposed on the basis of delivering proton minibeam arrays through arcs, i.e., combining pMBRT with arc therapies. pMBAT maintains and adds up the individual benefits of pMBRT and arc techniques for normal tissue sparing in terms of the preservation of the spatial fractionation of the dose and reduction in both peak and valley doses, as well as the LET escalation. Therefore, this new approach may allow using more aggressive irradiation schemes, which could be advantageous in the management of radioresistant tumors.

In summary, this thesis assists in the progress of pMBRT by optimizing the dosimetry practice in its current preclinical stage and exploring its short- and intermediate-term applications in clinics.



# Acknowledgements

First and foremost, I would like to express my gratitude to my supervisors **Yolanda Prezado** and **Ludovic De Marzi**. Yolanda, as you told me on the first day of my thesis, you have been my academic advisor but also my advisor on the personal aspects of science and always guided me to which is the best for my career. I really appreciate that and I want to acknowledge you for all the advice and for always finding the time for discussion. Ludovic, thanks for the guidance on the experimental and clinical part of this thesis and the long nights at the hospital doing measurements and experiments; although they were tough sometimes, I enjoyed the learning process during these sessions. In short, you both help me to grow immensely as a scientist. I would like to extend my sincere thanks to my professor **J.M Fernández-Varea** for introducing me to the exciting field of Medical Physics.

Thanks should also go to the members of my team for their support during these three years; I'm grateful for being part of this group and seeing it grow. Special thanks to the postdocs of the group, **Annaïg Bertho**, **Lorea Iturri**, and **Tim Schneider** for your guidance and being a reference. Annaïg and Lorea, it has been a pleasure to work with you on the biological side of the project and, despite the chunks of *drama* on some occasions for the almost failed experiments, I learned a lot thanks to you, and, most importantly, you have conveyed your passion for science to me. Finally, thanks to my co-PhD student, **Thongchai Masilela**, for being my *partner in crime* during this journey and the long *soirées* in the office talking about science and life in general; this is one of the things I will miss the most from the office.

Thanks also to my friends, **Miriam**, **Laura**, **Adrián**, **Iván**, **Elena**, **Carlos**, **Laura**, **Marián** and **Sukaina** for behaving like my family in Paris during the last three years and for the support. Special thanks to **Carlos Heredia** for always motivating me and sharing his love for science.

Last but not least I would like to like to express my deepest appreciation to my family for their unconditional support: *Gracias por siempre haberme inculcado lo importante que es conocer y saber, que el saber se elige, no se impone y por haberme dado la libertad siempre de elegir mi camino apoyanado mis decisiones..*



# Abstract

In the last decades, radiotherapy has profited from numerous technological advances allowing a very high dose conformation to the tumor and a reduction in the dose delivered to normal tissues. However, the radio-induced toxicity in normal tissues still remains one of the main limiting factors in radiotherapy, compromising the efficiency and safety of the treatment of radioresistant tumors (e.g., glioblastomas), pediatric cancers, or tumors close to highly radiosensitive organs (e.g. the spinal cord). The use of innovative dose delivery methods, different from conventional techniques, is being explored nowadays to find new avenues to enhance the therapeutic index for those clinical indications. An example of these approaches is spatially-fractionated radiotherapy (SFRT). This modality is based on delivering narrow beams separated spatially by a certain distance, creating a pattern of high doses intercalated by low-dose regions. This dose pattern appears to trigger a favorable tissue response in terms of tissue sparing. This PhD thesis is framed within the development of an SFRT technique called proton minibeam radiation therapy (pMBRT). This technique combines the improved ballistics of protons with the enhanced tissue sparing of SFRT. pMBRT has already shown a remarkable reduction in radiotoxicity, as compared to conventional techniques, along with high efficacy in terms of tumor control. However, there are still some aspects of this distinct dose delivery method (and SFRT in general) that are not fully characterized and need further study (e.g., the biological mechanisms that underlie the favorable tissue response).

The work in this thesis contributes to the further development of pMBRT in three main aspects. In the first place, it optimizes the dosimetry for this technique in preclinical studies. The performance of different detectors, i.e., RAZOR diode, microdiamond detector, and radiochromic films (EBT-XD and OC-1), is validated for dose measurements in pMBRT conditions. In addition, the good parametrization of our MC codes is shown. This validation allows performing different dosimetric studies. For instance, the sensitivity of dose distributions to uncertainties in setup and irradiation parameters is studied by a robustness analysis. This study reveals the increased sensitivity of pMBRT dose distributions to key irradiation conditions, such as the tilt of the collimator with respect to the beamline. Based on these results, guidelines and protocols to optimize the experimental setup and perform reproducible dosimetry are proposed. Then, following that protocol, the needed dosimetry for the preclinical trials held at our institution during this thesis is computed and evaluated.

In the second part of this work, the potential of pMBRT for treating different clinical indications (i.e., brain, liver, and lung metastases) is evaluated in the context of preparing pMBRT clinical trials. This study shows that pMBRT treatments can provide a similar or superior target coverage than the standard of care for those malignancies (i.e., stereotactic radiotherapy), while reducing the dose to organs-at-

risk and maintaining dose to normal tissues below tolerance dose limits. In addition, more favorable treatment delivery regimes may be expected from this new approach since it uses a reduced number of fields and fractions. Overall, these results suggest that pMBRT may provide an increase in the therapeutic index for the treatment of metastases.

Finally, the combination of pMBRT with complementary radiotherapy techniques (i.e., proton arc therapy) is proposed, and its potential benefits are assessed. Delivering proton minibeam arrays through arcs results in the preservation of the beneficial spatial fractionation of the dose in normal tissues as well as the dose and LET escalation. Therefore, this new approach is expected to further enhance the potential of pMBRT in the treatments of radioresistant tumors.

In summary, this thesis assists in the progress of pMBRT by optimizing the dosimetry practice in its current preclinical stage and exploring its short- and intermediate-term applications in clinics.





# Contents

<b>List of Acronyms</b>	<b>v</b>
<b>1 Introduction</b>	<b>1</b>
1.1 Cancer	2
1.2 Radiotherapy	4
1.2.1 Ionizing radiation	4
1.2.2 Radiotherapy modalities and techniques	16
1.2.3 Dose and LET distributions in EBRT	23
1.2.4 Radiobiology	26
1.2.5 Tumor control probability and normal tissue complication probability	42
1.2.6 Treatment planning in EBRT	43
1.3 Proton therapy	46
1.3.1 Physical aspects	46
1.3.2 Technical aspects	51
1.3.3 Radiobiological aspects	58
1.3.4 Clinical aspects	60
1.4 Spatially-fractionated radiotherapy	63
1.4.1 Fundamentals of spatially-fractionated radiotherapy	63
1.4.2 Spatially-fractionated radiotherapy techniques	65
1.4.3 Biological responses in spatially fractionated radiotherapy	75
1.4.4 Proton minibeam radiotherapy	78
1.5 Work outline	88
<b>2 Materials and methods</b>	<b>89</b>
2.1 Experimental dosimetry	89
2.1.1 Description of ICPO facility	89
2.1.2 Implementation of pMBRT at ICPO	90
2.1.3 pMBRT dosimetry	92
2.1.4 Preclinical dosimetry in pMBRT	100
2.2 Monte Carlo simulations	107
2.2.1 The Monte Carlo method	108
2.2.2 TOPAS simulations toolkit in medical physics	109
2.2.3 Simulation details	111
2.3 Treatment planning studies	116
2.3.1 Software	117
2.3.2 Treatment planning in pMBRT	117
<b>3 Dosimetry for pMBRT preclinical trials</b>	<b>121</b>
3.1 Rationale	121
3.2 Validation of Monte Carlo codes and dosimetric protocols	122

3.3	Robustness analysis . . . . .	130
3.3.1	Collimator tilt . . . . .	132
3.3.2	Collimator translation . . . . .	132
3.3.3	Target volume tilt . . . . .	133
3.3.4	Collimator specifications . . . . .	134
3.3.5	Air gap and collimator-isocenter distance . . . . .	134
3.3.6	Spot shape . . . . .	136
3.4	Optimization of the experimental setup . . . . .	139
3.5	Guidelines for pMBRT dosimetry in preclinical studies . . . . .	141
3.6	Dosimetric protocol for pMBRT preclinical trials . . . . .	143
3.6.1	Determination of absorbed dose under reference conditions . . . . .	143
3.6.2	Determination of absorbed dose under pMBRT conditions . . . . .	144
3.7	Dosimetry for <i>in vivo</i> and <i>in vitro</i> studies . . . . .	146
3.7.1	<i>In vivo</i> experiments . . . . .	146
3.7.2	<i>In vitro</i> experiments . . . . .	153
3.8	Discussion and conclusions . . . . .	155
<b>4</b>	<b>Assessment of the potential of pMBRT for treating metastases</b>	<b>159</b>
4.1	Rationale . . . . .	159
4.2	Clinical cases considered . . . . .	160
4.3	Treatment plans . . . . .	161
4.3.1	Stereotactic radiotherapy treatments . . . . .	162
4.3.2	pMBRT treatment plans . . . . .	162
4.3.3	PT treatment plans . . . . .	165
4.4	Evaluation of dose distributions . . . . .	165
4.4.1	Target coverage . . . . .	167
4.4.2	Mean dose to organs-at-risk . . . . .	173
4.4.3	Assessment of tolerance dose limits . . . . .	174
4.5	Evaluation of technical aspects . . . . .	178
4.6	Influence of plan parameters on dose distributions . . . . .	179
4.6.1	Orientation and position of the slits . . . . .	179
4.6.2	Center-to-center distance . . . . .	180
4.7	Discussion and conclusions . . . . .	181
<b>5</b>	<b>Proton minibeam arc therapy: a proof-of-concept study</b>	<b>185</b>
5.1	Rationale . . . . .	185
5.2	Treatment plans . . . . .	186
5.2.1	pMBRT plan . . . . .	187
5.2.2	PAT and pMBAT plans . . . . .	187
5.3	Evaluation of dose distributions . . . . .	188
5.3.1	Preservation of the spatial modulation of the dose . . . . .	188
5.3.2	Dose reduction to normal tissues . . . . .	190
5.4	Evaluation of LET distributions . . . . .	192
5.5	Influence of plan parameters on dose distributions . . . . .	194

---

5.5.1	Number of minibeam arrays . . . . .	194
5.5.2	Angular separation between arrays . . . . .	195
5.5.3	Center-to-center distance . . . . .	195
5.5.4	Size of the target volume . . . . .	197
5.6	Discussion and conclusions . . . . .	197
<b>6</b>	<b>Final discussion and conclusion</b>	<b>201</b>
	<b>Scientific production</b>	<b>205</b>
	<b>Résumé du travail de thèse en français</b>	<b>207</b>
	<b>List of figures</b>	<b>225</b>
	<b>List of tables</b>	<b>229</b>
	<b>Bibliography</b>	<b>231</b>



# List of Acronyms

<b>3DRT</b>	3D-conformal radiotherapy
<b>4DCT</b>	four-dimensional computed tomography
<b>4DRT</b>	Four-dimensional radiotherapy
<b>AAPM</b>	American Association of Physicists in Medicine
<b>ABNS</b>	accelerator-based neutron sources
<b>ART</b>	adaptative radiotherapy
<b>ASTRO</b>	American Society for Radiation Oncology
<b>BED</b>	biologically effective dose
<b>BEDR</b>	Bragg-peak-to-entrance dose ratio
<b>BER</b>	base excision repair
<b>BEV</b>	beam-eye-view
<b>BM</b>	brain metastases
<b>BNCT</b>	boron-neutron capture therapy
<b>BP</b>	Bragg peak
<b>CBCT</b>	cone beam computed tomography
<b>CID</b>	collimator exit-to-isocenter distance
<b>COP</b>	<i>Code of Practice</i>
<b>CSDA</b>	continuous-slowing-down approximation
<b>CT</b>	computed tomography
<b>c-t-c</b>	center-to-center
<b>CTV</b>	clinical target volume
<b>DCAT</b>	dynamic conformal arc therapy
<b>DNA</b>	deoxyribonucleic acid
<b>DSB</b>	Double-strand breaks
<b>DVH</b>	dose-volume histograms
<b>EBRT</b>	external beam radiotherapy
<b>ED<sub>50</sub></b>	isoeffective dose
<b>EQD</b>	equivalent total dose
<b>ESS</b>	energy selection system
<b>EUD</b>	equivalent uniform dose
<b>FFF</b>	flattening filter-free
<b>FSU</b>	functional subunits
<b>FWHM</b>	full-width at half maximum
<b>GBM</b>	glioblastoma multiforme
<b>GTV</b>	gross tumor volume
<b>Gy</b>	gray
<b>HDR</b>	high-dose-rate
<b>HR</b>	homologous recombination

**IAEA** International Atomic Energy Agency  
**IC** ionization chambers  
**ICPO** Institut-Curie Proton Therapy Center  
**ICRU** International Commission on Radiation Units and Measurements  
**IED** immunologically effective dose  
**IGRT** Image-guided radiotherapy  
**IMRT** Intensity-modulated radiotherapy  
**IORT** intraoperative radiotherapy  
**ITV** internal target volume  
**LCPE** lateral charged particle equilibrium  
**LDR** low-dose-rate  
**LET** linear energy transfer  
**LET<sub>d</sub>** dose-weighted average LET  
**LET<sub>φ</sub>** fluence-weighted average LET  
**LINAC** medical linear accelerators  
**LQ** linear-quadratic  
**LRT** LATTICE radiotherapy  
**MBRT** minibeam radiation therapy  
**MC** Monte Carlo  
**MCS** multiple Coulomb Scattering  
**MDR** medium-dose-rate  
**MLC** multi-leaf collimators  
**MRI** magnetic resonance imaging  
**MRT** microbeam radiation therapy  
**MU** monitor units  
**NHEJ** non-homologous end-joining  
**NTCP** normal tissue complication probability  
**NTD** normalized total dose  
**NTE** non-DNA-targeted effects  
**OAR** organs-at-risk  
**OD** optical density  
**OER** oxygen enhancement ratio  
**OF** output factors  
**PAT** proton arc therapy  
**PBS** pencil beam scanning  
**PDD** percentage depth dose  
**PEDG** post-exposure density growth  
**PET** positron emission tomography  
**pMBAT** proton minibeam arc therapy  
**pMBRT** proton minibeam radiation therapy  
**PRV** planning risk volume

---

**PT** Proton therapy  
**PTCOG** Particle Therapy Co-Operative Group  
**PTV** planning target volume  
**PVDR** peak-to-valley dose ratio  
**QA** quality assurance  
**QCF** Quenching correction factors  
**RBE** relative biological effectiveness  
**RCF** Radiochromic film  
**RF** radiofrequency  
**RN** radiation necrosis  
**ROS** *reactive oxygen species*  
**RS** range shifter  
**RT** Radiotherapy  
**SBRT** stereotactic body radiation therapy  
**SFRT** Spatially fractionated radiotherapy  
**SRS** stereotactic radiosurgery  
**SRT** Stereotactic radiotherapy  
**SOBP** spread-out Bragg peak  
**SPArc** spot-scanning arc therapy  
**SSB** Single-strand breaks  
**SSBR** single-strand break repair  
**TCP** tumor control probability  
**TE** targeted effects  
**TG** Task Groups  
**TI** therapeutic index  
**TME** tumor microenvironment  
**TP** treatment planning  
**TPS** treatment planning systems  
**TR** therapeutic ratio  
**TRS** Technical Report Series  
**TRT** targeted radionuclide therapy  
**VHEE** very-high energy electrons  
**VMAT** volumetric modulated arc therapy



# Introduction

---

## Contents

<b>1.1</b>	<b>Cancer</b> . . . . .	<b>2</b>
<b>1.2</b>	<b>Radiotherapy</b> . . . . .	<b>4</b>
1.2.1	Ionizing radiation . . . . .	4
1.2.2	Radiotherapy modalities and techniques . . . . .	16
1.2.3	Dose and LET distributions in EBRT . . . . .	23
1.2.4	Radiobiology . . . . .	26
1.2.5	Tumor control probability and normal tissue complication probability . . . . .	42
1.2.6	Treatment planning in EBRT . . . . .	43
<b>1.3</b>	<b>Proton therapy</b> . . . . .	<b>46</b>
1.3.1	Physical aspects . . . . .	46
1.3.2	Technical aspects . . . . .	51
1.3.3	Radiobiological aspects . . . . .	58
1.3.4	Clinical aspects . . . . .	60
<b>1.4</b>	<b>Spatially-fractionated radiotherapy</b> . . . . .	<b>63</b>
1.4.1	Fundamentals of spatially-fractionated radiotherapy . . . . .	63
1.4.2	Spatially-fractionated radiotherapy techniques . . . . .	65
1.4.3	Biological responses in spatially fractionated radiotherapy . . . . .	75
1.4.4	Proton minibeam radiotherapy . . . . .	78
<b>1.5</b>	<b>Work outline</b> . . . . .	<b>88</b>

---

Cancer is one of the leading causes of premature death worldwide [Mattiuzzi & Lippi 2019]. Besides chemotherapy and surgical resection, radiotherapy constitutes one of the most important treatment options for this malignancy [Baskar & Itahana 2017]. Radiotherapy has evolved significantly in the last decades regarding the precision in the dose delivery [Gerber & Chan 2008], leading to increased dose conformity to the tumor and reduced normal tissue toxicities. However, many cancer types (e.g., glioblastoma or brain metastases) respond poorly to radiotherapy treatments, mainly due to their inherent radioresistance [Chen & Kuo 2017]. These clinical indications would benefit from more aggressive treatments (i.e., higher prescribed doses), but the increase in the dose received by normal tissues would lead to prohibitive side effects. Besides normal tissue toxicities, another important limiting factor in the efficacy of

radiotherapy is the poor detection of the microscopic spread of cancer cells and the identification of active metabolic areas of a tumor mass employing the current imaging techniques. Several strategies have been proposed to increase the tolerance dose of normal tissues, such as using ultra-high dose rates, as in FLASH therapy [Favaudon *et al.* 2014], or distinct spatial dose distributions, as in spatially fractionated radiotherapy [Prezado 2022]. This PhD thesis is framed within the second one.

Spatially fractionated radiotherapy (SFRT) exploits the increase in the tolerance dose of normal tissues when very small beam sizes are used [Hopewell & Trott 2000]. In SFRT, dose delivery patterns consist of multiple beamlets of reduced size (50  $\mu\text{m}$  to 2 cm) separated by a certain distance (200  $\mu\text{m}$  to 4 cm) [Prezado 2022]. Contrary to dose distributions in conventional radiotherapy, SFRT is characterized by a pattern of alternating high dose (peaks) and low dose (valleys) regions. These dose distributions appear to favor the normal tissue sparing while simultaneously achieving substantial tumor control [Billena & Khan 2019].

This thesis focuses on a novel SFRT technique called proton minibeam radiation therapy (pMBRT) [Prezado & Fois 2013]. This approach combines the spatial fractionation of the dose with the use of submillimeter proton beams. pMBRT has already shown a remarkable increase in normal tissue tolerance dose [Prezado *et al.* 2017b] and tumor control rates [Bertho *et al.* 2021b] as compared to seamless irradiations. The main objective of this work is advancing the knowledge of the dosimetry for this technique and is framed within the work plan of an ERC consolidator grant (Spatial fractionation of the dose in proton therapy: a novel therapeutic approach, ERC COG agreement number 817908., Y.Prezado).

*With the objective of laying the groundwork to describe in detail the research performed in this PhD thesis, this chapter aims to introduce the fundamental concepts of cancer (Section 1.1), radiotherapy (Section 1.2), proton therapy (Section 1.3), and spatial fractionation of the dose (Section 1.4). Finally, Section 1.5 outlines the work performed during this thesis.*

## 1.1 Cancer

Cancer is a group of diseases characterized by the loss of balance between growth-promoting and growth-restraining signals in cells [Macdonald *et al.* 2004]. Cancer cells present mutations that prevent the cell from operating the normal process of programmed cell death when cell division is not required, resulting in continued cell proliferation. This abnormal proliferation may create a mass of tissue called tumors. Tumors can be benign or malignant. Contrary to benign tumors, malignant tumors are able to invade surrounding tissues and distant structures, generating metastases.

The factors that lead to those mutations may be external or internal. The leading external causes of cancer are smoking tobacco, infectious agents, and exposition to ionizing radiation or chemicals. Major non-external factors include

inherited genetic mutations, immunosuppression, or hormones acting as carcinogens. In addition, lifestyle and diet influence the occurrence of this disease [Hesketh 2013].

Cancer is one of the leading causes of morbidity and mortality worldwide. In 2020, around 19 millions of cases were diagnosed. The most common forms of cancer in 2020 were breast (11.7 %), lung (11.4 %), and colorectal (10 %) [WHO 2020]. The number of new cancer cases increases each year. For instance, in the United States of America (USA), the annual number of people diagnosed with cancer grew from 1.3 million of cases in 1999 to 1.8 million in 2019. This trend correlates with the increase in the size and age of the population. In 2020, almost 10 millions of people died from cancer worldwide [WHO 2020]. The most lethal types of cancer were lung (18 %), colorectal (9.4 %), and liver (8.3 %) [WHO 2020]. Epidemiologic trends predict cancer to be the first cause of death, with a 2-fold increase, by 2060 [Mattiuzzi & Lippi 2019].

The diagnosis and treatment of cancer have evolved in the last decades [Arruebo *et al.* 2011]. The increment in the 5-year relative survival rates reflects this improvement. For instance, the survival rate for all cancers in the USA has increased from 27 % in the 1960s to 68 % in 2022 [American Cancer Society 2022]. However, 5-year survival rates for certain types of cancer, such as lung, esophagus, liver, brain, and pancreas cancers, remain below 20 % [Mattiuzzi & Lippi 2019]. Figure 1.1 shows the five-year cancer survival of different types of cancer in England in 2019.

The most common cancer treatment modalities are the surgical resection of localized solid tumors, chemotherapy, and radiotherapy. The selection of the treatment technique or their combination depends on the patient's medical state and the type, location, and stage of the tumor. Radiotherapy is used in the treatment of more than half of cancer cases [Baskar & Itahana 2017]. This modality is based on the capability of ionizing radiation to induce damage in the genetic material of cancer cells, leading to tumor eradication. Examples of indications commonly treated with radiotherapy, alone or combined with other modalities, are prostate, lung, and head and neck cancers [Baskar *et al.* 2012]. Chemotherapy refers to the use of drugs to reduce the proliferation rate of rapidly-growing cells (i.e., cancer cells). It is used as a curative treatment in some types of advanced cancer (e.g., leukemia, lymphomas, or small cell lung cancer) and as adjuvant therapy to reduce the tumor size and prevent micro-metastases [Arruebo *et al.* 2011]. Other innovative approaches, such as gene therapy, targeted therapy, or immunotherapy, have been proposed in the last decades [Debela *et al.* 2021, Pucci *et al.* 2019].

*Since this PhD thesis deals with the development of a radiotherapy technique, the following sections are devoted to describing this therapeutic modality in detail, including its physical and radiobiological aspects, as well as its state of the art.*

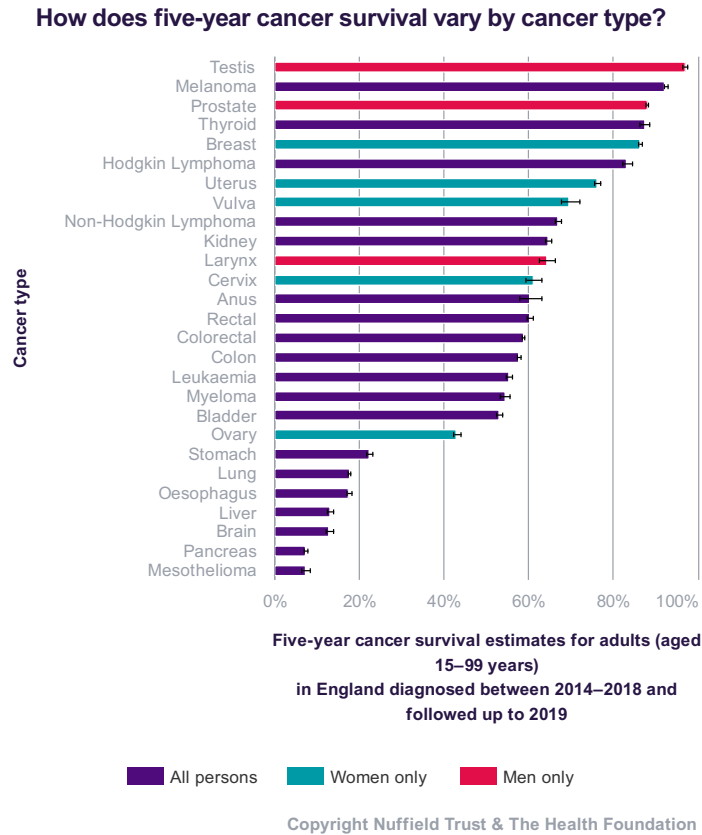


**Figure 1.1:** Five-year survival estimate for adults diagnosed with different cancer types in England as for 2019. Taken from [Nuffield Trust 2022].

## 1.2 Radiotherapy

Radiotherapy (RT) is the medical use of ionizing radiation for treating, typically, malignant tumors with curative or palliative intents [Gerber & Chan 2008]. It is based on the ability of ionizing radiation to damage biological tissues.

*This section aims to provide a basis for how ionizing radiation interacts with matter, how these interactions are quantified and measured, and its effects on living tissues. In addition, the current RT modalities and the process of treatment planning and dose delivery are described.*

### 1.2.1 Ionizing radiation

Ionizing radiation refers to radiation with sufficient energy to ionize matter, i.e., remove electrons from atoms [Pawlicki *et al.* 2016]. The ionization process occurs when the energy transferred to atomic electrons is larger than their binding energy, causing the ejection of the electron and leaving a vacancy behind [Symonds *et al.* 2012]. Ionizing radiation can be divided into two main categories:

directly ionizing radiation (i.e., charged particles), able to ionize the atoms by means of collision-like interactions, and indirectly ionizing radiation (e.g., neutrons and photons), which causes ionization by releasing directly ionizing particles [Pawlicki *et al.* 2016].

### 1.2.1.1 Radiation interactions with matter

The different types of ionizing radiation may undergo distinct interactions with matter. These interactions can be classified into two main categories: elastic or inelastic collisions. Elastic collisions are defined as interactions that do not imply a net loss of kinetic energy. Conversely, inelastic (or non-elastic) collisions involve a change in the kinetic energy of the incident particle in a material. Incident particles that traverse a material without undergoing inelastic interactions are called primary radiation. Contrarily, particles that have undergone any non-elastic interactions are known as secondary radiation [Pawlicki *et al.* 2016]. The specific energy transference patterns of each radiation type (i.e., photons, electrons, neutrons, protons, and heavy ions) are presented hereafter.

#### X- and $\gamma$ -ray photons

Photons have no electrical charge; thus, they are considered indirectly ionizing radiation [Chang *et al.* 2014]. A photon impinging a material leads to three possible scenarios: (i) transmission without interaction, (ii) scattering, or (iii) absorption (i.e., total transference of the photon energy to the medium). In the latter case, the energy of the incident photon beam decreases by the reduction in the number of photons. This process is known as attenuation. Attenuation may be produced by a combination of several interactions. Figure 1.2 illustrates the main interactions of photons with matter, i.e., coherent scattering, photoelectric effect, Compton scattering, and pair production [Pawlicki *et al.* 2016].

In the photoelectric effect, the incident photon transfers all its energy to an inner-shell atomic electron. If the transferred energy is larger than the electron binding energy, the electron is ejected, ionizing the atom as a result. The vacancy created is filled by an atomic electron of an outer layer. In the process of de-excitation, the excess of energy is emitted in the form of a characteristic photon or an electron (Auger electron). The probability of this interaction occurring (i.e., the cross-section) increases with  $Z^3$  ( $Z$  being the atomic number of the material) and decreases with the third power of the energy of the primary photon [Symonds *et al.* 2012]. In water or body tissues, this phenomenon takes place at energies lower than 150 keV [Chang *et al.* 2014]; thus, it is rarely observed at the energies employed in RT.

Coherent scattering refers to the total absorption of the photon energy, which is not large enough to ionize the atom but can produce the excitation of an atomic electron. In the process of de-excitation, the energy is released in the form of a photon with the same energy as the absorbed one. Thus, the final result appears to be the change of direction of the incoming photon with no change in energy. This

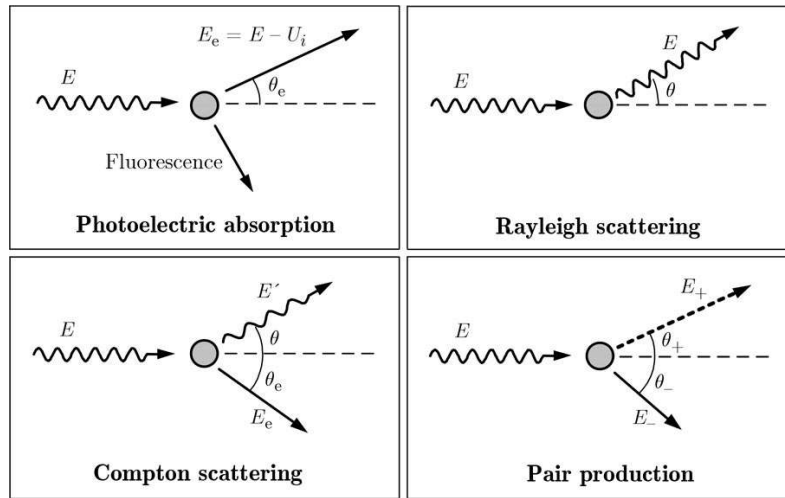


**Figure 1.2:** Main photon interactions with matter. Taken from [Salvat 2015].

interaction is negligible for high-energy photons interacting with low- $Z$  tissues; thus, it is not relevant in conventional RT [Pawlicki *et al.* 2016].

In Compton scattering, the incoming photon interacts with an atomic electron transferring a part of its energy. The energy transferred is equal to or greater than the electron binding energy, causing the ejection of the atomic electron. The incident photon is deflected, carrying the remaining energy. The cross-section of this interaction depends on the density of electrons in the material, which is roughly proportional to the mass density. Compton scattering is the dominant interaction in the energy range of photons used in RT (100 keV to 20 MeV) [Symonds *et al.* 2012].

Pair production is the process where the primary photon vanishes when interacting with the electromagnetic field of a nucleus, producing a positron-electron pair. The positron-electron pair may be annihilated, creating two  $\gamma$ -rays. This interaction only occurs at photon energies greater than 1.02 MeV, i.e., the energy required to create the mass of a positron and electron. Its cross-section increases with  $Z$  and the energy of the incident photon. The contribution of pair production to the total attenuation of photon beam in soft tissues becomes significant above 10 MeV [Symonds *et al.* 2012]. Hence, the amount of absorbed dose due to this process in RT is minor.

Figure 1.3 shows the relative importance of the main photon interactions with matter in terms of photon energy and the material's atomic number.

Other photon interactions are possible but have no significant contribution to the dose absorbed by the patient in RT. An example of these interactions is photodisintegration, which is the emission of neutrons or alpha particles after the interaction of incident photons with atomic nuclei.

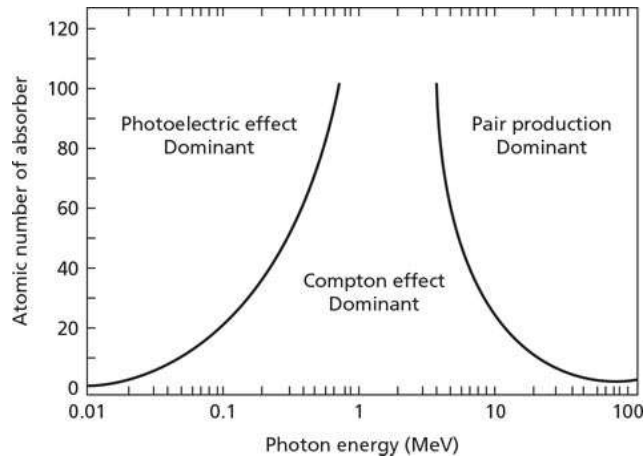


**Figure 1.3:** Relative importance of the main interactions of photons with matter as a function of the photon energy and the atomic number of the absorber material. Taken from [Pawlicki *et al.* 2016].

## Electrons

Electrons are negatively charged particles with a relatively small mass. Like other charged particles, electrons are directly ionizing radiation [Chang *et al.* 2014]. The transport of electrons through matter is characterized by a quasi-continuous transference of energy to the medium in a large number of interactions, which is termed continuous-slowing-down approximation (CSDA) [Symonds *et al.* 2012]. The main interactions that electrons undergo in matter are elastic and inelastic scattering, Bremsstrahlung emission, and positron annihilation. They are illustrated in Figure 1.4 and described hereafter.

Electromagnetic collisions of incident electrons with atomic electrons result in the transference of energy and excitation or ionization of atoms. As a result, incident electrons lose part of their energy and are deflected. When the energy required for excitation or ionization is negligible, the energy of scattered or ejected electrons is equal to the incident electron's energy. This type of interaction is known as elastic scattering. Contrarily, when the kinetic energy of the primary electron is not conserved, the interaction is called inelastic scattering. The energy loss due to this kind of process is directly proportional to  $Z^2$  and inversely proportional to the square of the electron velocity [Pawlicki *et al.* 2016].

The inelastic collision of electrons with nuclei involves the loss of energy and deflection of the incident electron due to its interaction with the nuclear electromagnetic field (Coulomb's force of attraction). The lost energy is radiated as a photon, called Bremsstrahlung radiation ("braking radiation"). The cross-section of this interaction increases with  $Z^2$  of the medium [Pawlicki *et al.* 2016].

Finally, the interaction of a positron-electron pair, i.e., annihilation, results in the production of two  $\gamma$ -rays that are ejected at  $180^\circ$  to one another.

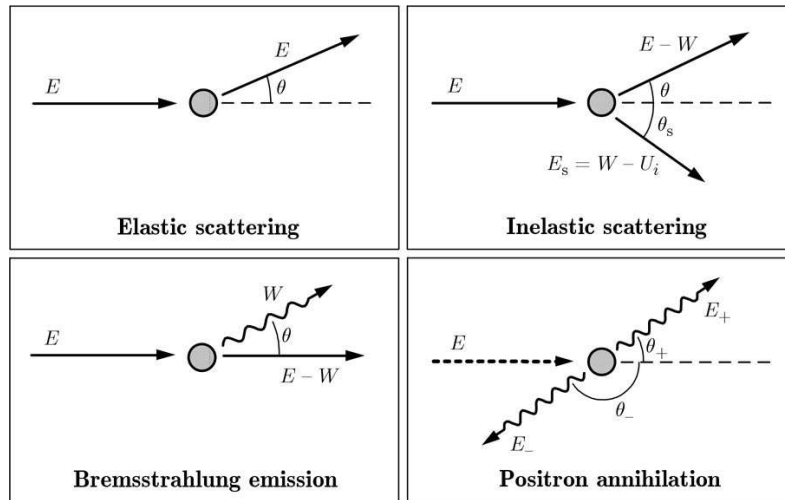


Figure 1.4: Main electron interactions with matter. Taken from [Salvat 2015].

## Protons and heavy ions

Protons and heavy ions are positively charged particles, i.e., directly ionizing radiation. The main interactions of proton and ion beams with the medium are the stopping by collisions with atomic electrons, scattering by collision with nuclei, and nuclear interactions [Paganetti 2018].

Electromagnetic inelastic interactions with atomic electrons slow down protons and ions due to the partial transfer of their kinetic energy. Ultimately, these particles stop when they have lost all their energy.

Electromagnetic interactions of protons and ions with nuclei cause the change of direction of incident particles. The process of repeated deflections is called multiple Coulomb Scattering (MCS).

Incident particles may also interact inelastically with nuclei, creating an excited state or fragmenting the nucleus. As a result, secondary particles (e.g., protons, neutrons,  $\alpha$ -particles, or different isotopes) are emitted and deposit their energy away from the interaction site.

Bremsstrahlung, a relevant interaction for less massive charged particles (i.e., electrons), is not significant for protons and ions since the probability of this interaction occurring is inversely proportional to the square of the mass of the incident particle [Symonds *et al.* 2012].

## Neutrons

Neutrons are indirectly ionizing radiation and have no electrical charge. Thus, they are slowed down predominantly by nuclear interactions. The processes they undergo in matter are highly dependent on their velocity (i.e., energy). So, in the context of RT, they are classified as low (thermal) energy neutrons (around 0.025 eV) and fast neutrons (in the keV - MeV range).

The main interactions of fast neutron beams with atomic nuclei are elastic and inelastic collisions and nuclear spallation. Neutrons can collide elastically with hydrogen nuclei and set a proton in motion (recoil proton), which deposits its energy in the stopping process. This is the dominant interaction of fast neutrons. Neutrons may also collide inelastically with heavy nuclei, emitting  $\gamma$ -rays as they slow down. Incident neutrons at energies above 7 MeV may interact with heavy nuclei producing fission reactions and associated products (i.e., nuclear fragments such as  $\alpha$ -particles), which can cause dense ionization clusters nearby the interaction site. This process is called nuclear spallation [Chang *et al.* 2014].

The primary interaction of thermal neutrons with matter in RT is transmutation. In this process, a neutron is absorbed by a nucleus, creating atomic species that disintegrate releasing protons or  $\alpha$ -particles. These secondary (directly ionizing) particles deposit their energy as they interact with matter. This phenomenon is the basis of boron-neutron capture therapy (BNCT), where neutrons are captured by boron nuclei ( $^{10}\text{B}$ ), previously deposited in the tumor, creating  $^{11}\text{B}$ , which disintegrates in helium and lithium [Symonds *et al.* 2012].

*In the context of RT, the effect of the interactions of ionizing radiation with matter needs to be determined to accurately correlate the physical processes with biological and clinical endpoints. The next section presents the main quantities used to quantify the physical action of radiation.*

### 1.2.1.2 Dosimetric quantities

As described in the previous section, the interaction of radiation with matter leads to the transference of energy to the medium. In the context of RT, three main quantities are used to describe the absorption of energy by the medium: the absorbed dose, the stopping power, and the linear energy transfer (LET).

The absorbed dose (or dose) measures the total energy absorbed by the material. It is defined by the International Commission on Radiation Units and Measurements (ICRU) report 85 [ICRU 2011] as the quantity of energy absorbed per unit mass in a volume element of material:

$$D = \frac{d\bar{\epsilon}}{dm}, \quad (1.1)$$

where  $d\bar{\epsilon}$  is the mean energy imparted by ionizing radiation to a mass  $dm$  of material. The unit of dose is gray (Gy), defined as  $\text{J}\cdot\text{Kg}^{-1}$ .

Conversely, the stopping power and LET describe the dose deposition patterns related to the average energy transferred by individual charged particles. The mass stopping power is defined as the energy lost by a charged particle of a given type and energy when traversing a distance  $dl$  of a medium of density  $\rho$ :

$$S = \frac{1}{\rho} \frac{dE}{dl}. \quad (1.2)$$

It accounts for the losses due to ionization and excitation of atomic electrons (electronic stopping power), nuclear interactions (nuclear stopping power), and

radiative losses (radiative stopping power). The unit to measure the mass stopping power is  $\text{MeV}\cdot\text{cm}^2\cdot\text{g}^{-1}$  [ICRU 2011].

The LET, also called restricted electronic stopping power, is the fraction of energy lost by radiation that remains in the interaction site. Hence, it does not account for the energy transferred to ejected electrons capable of depositing part of their energy away from the primary interaction point ( $\delta$ -rays). LET is defined as the mean energy lost by a charged particle of a given type and energy due to electronic interactions minus the kinetic energy of the electrons released,  $dE_\Delta$ , in traversing a distance  $dl$ :

$$LET_\Delta = \frac{dE_\Delta}{dl}. \quad (1.3)$$

Thus, the value of  $\Delta$  is the maximum released kinetic energy that may contribute to the LET. Particles with energies higher than this value produce  $\delta$ -rays. The unit of LET is  $\text{keV}\cdot\mu\text{m}^{-1}$  or equivalent [ICRU 2011].

The individual particles of an incident clinical beam may have a different LET. Then, for a complete characterization of the beam as a single-value metric, averaged LET values are often calculated. The two main approaches to computing the averaged LET are the dose-weighted average LET ( $LET_d$ ) and fluence-weighted average LET ( $LET_\Phi$ ) [Kalholm *et al.* 2021].  $LET_d$  is defined as:

$$LET_d = \frac{\sum_i d_i LET_i}{\sum_i d_i}, \quad (1.4)$$

where  $d_i$  is the microscopic dose given to an infinitesimally small volume by the track of a single particle  $i$  with a certain stopping power  $LET_i$ . Alternatively,  $LET_\Phi$  can be computed as

$$LET_\Phi = \frac{\sum_i \Phi_i LET_i}{\sum_i \Phi_i}, \quad (1.5)$$

where  $\Phi_i$  is the fluence of the charged particle  $i$  with an associated LET value  $LET_i$ .

$LET_d$  is more commonly used since it better correlates with the biological damage to tissues [Granville & Sawakuchi 2015] since the dose is used to quantify the biological detriment [Kalholm *et al.* 2021].

Averaged LET values may be highly influenced by the calculation method employed [Kalholm *et al.* 2021, Granville & Sawakuchi 2015]. For instance, the study by Granville *et al.* [Granville & Sawakuchi 2015] reported the sensitivity of the average LET calculations, especially for  $LET_d$ , on different scoring techniques. For that reason, Kalholm *et al.* [Kalholm *et al.* 2021] provided recommendations on how to report the averaged LET to compare different studies reliably.

*The process of evaluating the dosimetric quantities in the context of RT is called dosimetry, which is described in detail in the next section.*

### 1.2.1.3 Dosimetry

Radiation dosimetry in RT refers to measuring, calculating, and assessing dosimetric quantities to characterize clinical beams.

Recommendations for the dosimetry of external beams in conventional RT are reported in the *Code of Practice (COP)* Technical Report Series (TRS) 398 [IAEA 2001] by the International Atomic Energy Agency (IAEA). The rationale behind developing this report was to obtain an accuracy level in the delivery of the absorbed dose to a target volume of  $\pm 5\%$ . This accuracy level could also be interpreted as the tolerance of the difference between the prescribed and delivered dose [IAEA 2001]. The precision in the dose delivery is limited by uncertainties in the several steps between the calibration of radiation detectors and the determination of the absorbed dose at hospitals, which involve many conversion factors (examples can be found hereafter). The TRS-398 aimed to reduce such uncertainties by directly calibrating ionization chambers in terms of dose to water, providing a robust system of primary standard detectors, and proposing simple formalisms based on calibration and correction factors for all influence quantities [IAEA 2001].

This COP also provides recommendations for the type of radiation detectors used in each step of the dosimetric process. These instruments can be classified into primary, secondary, and national standards and reference and field instruments [IAEA 2001]. A primary standard refers to an instrument of the highest metrological quality that allows the determination of a quantity according to its definition. Commonly, the detectors used as primary standards are graphite calorimeters, given their high sensitivity and robustness [IAEA 2017]. Secondary standards are detectors calibrated by comparison with the primary standard. Other standards may also be recognized at the national level. Reference instruments are devices of the highest metrological quality available at a given institution from which measurements at that institution are derived. Reference instruments are typically ionization chambers with cylindrical sensitive volumes of around 6.4 mm diameter and 24 mm in length (Farmer-type chambers) since they have been proven to be robust, simple, and suitable for clinical reference dosimetry [IAEA 2001]. Finally, field instruments are detectors employed for daily routine and calibrated against reference instruments.

The TRS-398 also recommends phantoms to determine the absorbed dose in water. Although water is advised to be the reference medium for measurements, water phantoms are sometimes impractical and solid phantoms may be used instead. Plastic, or equivalent material, phantoms with well-defined physical properties (density and composition) are commercialized in different forms and shapes (e.g., slab, cubes, cylinders, or spheres) for accurate positioning of dosimeters in a wide range of conditions [IAEA 2017].

Besides IAEA, other organisms, such as the American Association of Physicists in Medicine (AAPM), develop protocols for the dosimetry of external beam RT in the form of Task Groups (TG) reports (e.g., TG-51 [Almond *et al.* 1999]).

Dosimetric measurements in COPs could be divided into two main categories: absolute and relative dosimetry. Absolute dosimetry refers to measuring a quantity

which allows its determination according to its definition. Absolute dosimetry measurements and protocols must consider the specific physical conditions of the interactions between the radiation and the detector [de Almeida & Salata 2022]. Examples of quantities measured in absolute dosimetry procedures are exposure, air kerma, and absorbed dose in air and water. The absorbed dose in water is the quantity of main interest since it closely relates to the biological effects of radiation [IAEA 2001]. The TRS-398 [IAEA 2001] describes the absorbed dose to water as:

$$D_{w,Q} = M_Q N_{D,w,Q_0} k_{Q,Q_0} \text{ [Gy]}, \quad (1.6)$$

where  $M_Q$  is the reading of the dosimeter at the reference point corrected for the influence of temperature, pressure, polarity, and electrometer calibration,  $N_{D,w,Q_0}$  is the calibration factor for the dosimeter at the reference radiation quality  $Q_0$ , and  $k_{Q,Q_0}$  is the chamber-specific factor that corrects for differences between the reference beam quality  $Q_0$  and the measured beam quality  $Q$ . The beam quality refers to the type and energy of radiation. Absolute dose measurements are typically performed in reference conditions. Reference conditions are a set of values that specify the values of the magnitudes that influence measurements (e.g., measurement depth, field size, phantom material, dosimeter specifications, and the pressure and temperature of the room) for which calibration factors from a calibration laboratory are valid without further correction factors [IAEA 2001]. They are specified in COPs (e.g., TRS-398 [IAEA 2001]) for each radiation quality considered. Dosimeters employed for absolute dosimetry, such as ionization chambers, must be calibrated to be traceable to primary standard instruments [IAEA 2009].

Relative dosimetry refers to measurements performed under non-reference conditions. These measurements are relative to absolute dosimetry measurements [de Almeida & Salata 2022]. Clinical situations may differ from reference conditions and require relative dosimetry in a wide range of radiation fields and beam types. Examples of this type of measurement are lateral and depth dose profiles and output factors. Lateral (or off-axis) profiles measure the dose variation along an axis perpendicular to the beam direction at a given depth. Depth dose profiles (or percentage depth dose (PDD) profiles) measure the dose variation along the central beam axis in depth. Finally, output factors (OF) (or scatter factors) evaluate the variation of absorbed dose at a given point as a function of the beam size.

Dosimeters for absolute and relative dosimetry need to be selected considering the specific measurements, beam properties, and technique since the characteristics of a detector (e.g., size, shape, and materials) may considerably affect its response to ionizing radiation. For that reason, dosimetry protocols involve determining perturbation correction factors necessary to correct the detector response from the calibration and user's conditions [Grimes *et al.* 2017].

Overall, dosimetry measurements are used to ensure the delivery of the prescribed dose to a patient aiming for the least possible uncertainty in the absorbed dose, compare measurements at different institutions adopting different protocols, and correlate clinical outcomes [de Almeida & Salata 2022].

### 1.2.1.4 Dosimeters

The measurement of radiation dose is crucial in RT since it directly relates to the biological effects of radiation. The absorbed dose can be determined by measuring or detecting the different effects of energy deposition in matter, for instance, the temperature increment (calorimetry), chemical changes (chemical dosimetry), ionization produced to charged particles (ion-pair generation dosimetry), or the excited states created by radiation (thermoluminescent dosimetry) [Symonds *et al.* 2012].

*Due to their essential role in this thesis, the basic principles of ionization chambers, radiochromic films, diodes, diamond detectors, and scintillation devices are described hereafter.*

#### Ionization chambers

Free air ionization chambers (IC), along with calorimeters, are the gold standard dosimeters for absolute dosimetry. The principle of this type of detector is measuring the energy used to create ion pairs in a mass of air [Khan & Gibbons 2014]. ICs are gas-filled cavities placed between two electrodes connected to a potential difference (polarizing voltage). Radiation interacts with the air and causes ionization, which results in free electrons. Then, positive and negative ions separate due to the polarizing voltage and are collected by electrodes. The measured current created by the drift of charges correlates to the number of ions produced since the charge of each electron is constant and well-known. The total energy transferred to the gas (i.e., dose to the material) can be calculated by knowing the average energy to create each ion in the material. Correction factors are needed for accurate dose measurements with ICs to account for ion recombination losses, geometrical effects (e.g., stem effect), or the change in the air mass depending on the ambient temperature and pressure [Khan & Gibbons 2014]. A wide range of IC shapes and sizes are used in RT, e.g., plane-parallel and cylindrical chambers. The IAEA TRS-398 [IAEA 2001] provides guidelines on the type of IC that should be used for different reference conditions and beam types.

#### Diode detectors

Diode detectors consist of a semiconductor p-n junction, i.e., a p-type (with holes in the valence band) and n-type (with free electrons) materials [Khan & Gibbons 2014]. A difference of potential exists in the interface region of this junction. The junction region is called the depletion layer. When the depletion layer is irradiated, electrons are released by ionization and drift under the influence of the internal electric field. The charge produced in the depletion region, which is proportional to the dose deposited, is measured by an electrometer. Due to the high-density semiconductor material employed (generally silicon), the sensitivity of diode detectors is over 1000 times higher than free air ICs [Symonds *et al.* 2012].

Therefore, the sensitive region of the diode can be relatively small, so they may be used for small-field dosimetry [Parwaie *et al.* 2018]. For instance, the RAZOR detector (IBA Dosimetry, Germany) has a sensitive volume of  $0.006 \text{ mm}^3$ . However, some diode detectors exhibit an overresponse in some situations, e.g., the determination of OFs for small fields [Garnier *et al.* 2018, Gul *et al.* 2020, Bahreyni & Koshbin 2004], mainly due to the fluence perturbation caused by the high-density material of detectors [Gul *et al.* 2020].

Diodes can operate in passive mode, i.e., an applied voltage is not necessary. However, their sensitivity may depend on their orientation and radiation history (i.e., they exhibit radiation damage), the temperature, beam energy, and dose rate [Eklund & Ahnesjö 2010, Jursinic 2009, Lindström *et al.* 1999, Van Dam *et al.* 1990] and corrections are needed to convert measured doses in such high-atomic number materials to water. Diode detectors are typically used for relative dosimetry.

### Diamond detectors

Most of the diamond detectors employed in RT nowadays are synthetic single-crystal diamonds [IAEA 2017]. These detectors present a similar structure and principle of operation to semiconductor p-diodes. They also operate without applied voltage and are used for small-field dosimetry due to their small volumes (i.e., high spatial resolution) [Pappas *et al.* 2008]. For instance, the sensitive volume of the PTW-60019 Microdiamond detector (PTW, Freiburg) is  $0.004 \text{ mm}^3$ .

Contrarily to diode detectors, diamond detectors are tissue-equivalent and, generally, exhibit lower dependence on radiation history, temperature, energy, dose rate, and LET [Brace *et al.* 2020, Damodar *et al.* 2018, Gomà *et al.* 2016, Reggiori *et al.* 2017, Rossomme *et al.* 2016]. However, some detector series do exhibit LET and dose rate dependence [Marsolat *et al.* 2016]. Optimal performance for relative dosimetry (e.g., accurate OF measurements in a wide range of field sizes) has been reported for diamond detectors [Reggiori *et al.* 2017].

### Radiochromic films

Radiochromic film (RCF) measurements are based on the change of colorization of a polymer by energy absorption [Khan & Gibbons 2014]. The process of colorization involves the polymerization of molecules of the film emulsion (chromophores) due to the energy absorbed from radiation. The polymers created are colored (blue color), and the degree of color formation, i.e., the quantity of polymers produced, is proportional to the absorbed dose in the emulsion.

The reading of films is performed using flatbed scanners and the film colorization is quantified in terms of change in optical density (OD), i.e., the fraction of incident light transmitted by the film. The change in OD is converted to dose by using a calibration curve. The process of film calibration is described in more detail in Chapter 2 of this thesis. The exact geometry of films depends on the manufacturer,

but, generally, they consist of a 10 to 90  $\mu\text{m}$ -width active layer (emulsion) wrapped in transparent protective layers (base). The material of these films is tissue-like, with physical densities of 1 to 1.2  $\text{g}/\text{cm}^3$  and effective atomic numbers of 6 to 9 [Pawlicki *et al.* 2016, Symonds *et al.* 2012].

RCFs are very useful for relative dosimetry since they allow high-spatial resolution dosimetry in two dimensions [Carnicer *et al.* 2013]. The dynamic measurement range of commercially available films is 0.1 to 100 Gy (see Table 1.1). In addition, they have a minimal dose rate and energy dependence at clinical RT energies. However, their response may vary depending on the type of radiation due to each particle type's specific dose deposition patterns. Although radiochromic films have very little or no sensitivity to visible light, they may be sensitive to temperature changes and post-irradiation time-to-readout. Dose measurement with films may also be dependent on the dosimetric protocol, film batch, or equipment used for the read-out (i.e., scanners) [Cavallone 2020, Wołowicz & Kukołowicz 2016]. Specific guidelines for performing film dosimetry can be found elsewhere in the literature [Devic *et al.* 2016, Niroomand-Rad *et al.* 2020]. The specific protocol adopted in this work is described in Chapter 2.

Film	EBT-3 [Gafchromic 2022]	EBT-XD [Gafchromic 2022]	MD-V3 [Gafchromic 2022]	OC-1 [OrthoChrome 2022]
Dose range (Gy)	0.1 - 20	0.1 - 40	0.1 - 100	0.1 - 100

**Table 1.1:** Dynamic dose range of EBT-3, EBT-XD, MD-V3 GAFchromic films (Ashland, USA), and OC-1 OrthoChrome films (OrthoChrome, USA), as reported by manufacturers.

RCF response also exhibits a dependence on the LET. An under-response, known as the quenching effect, is observed in high-LET regions, [Khachonkham *et al.* 2018]. This effect is associated with the saturation of the sensitive site due to the clustered energy depositions events of high-LET particles. This effect is especially relevant for proton and heavy-ion dosimetry since LET values may vary within their dose distributions. For instance, an under-response of up to 20 % has been observed for proton beams at clinical energies (50 to 250 MeV). For accurate dosimetry, the RCF response as a function of LET needs to be quantified, and correction factors should be applied to dose measurements [Anderson *et al.* 2019]. Quenching correction factors (QCF) are often calculated as the ratio of dose measured by RCFs and dose values not affected by the quenching effect, i.e., computed dose or dose measured with detectors that do not show RCF-dependence (e.g., ionization chambers). Figure 1.5 illustrates the RCF under-response and corrected dose distribution applying that methodology.

### Scintillation detectors

In scintillation detectors, the impinging radiation excites atoms or molecules of the scintillating medium, which emit photons in the visible spectrum in the

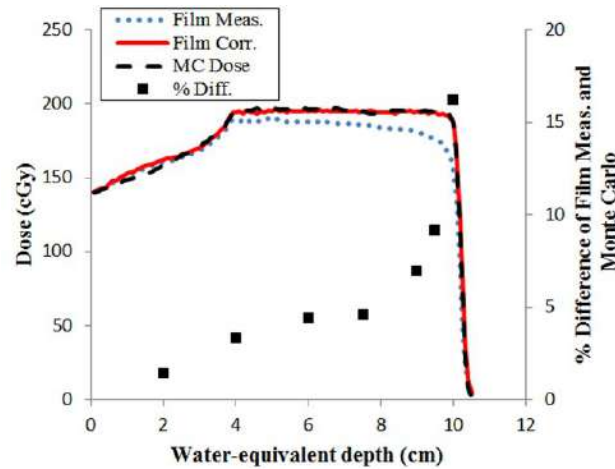


**Figure 1.5:** Depth dose profile of a proton beam measured with RCF (dotted blue line), calculated by Monte Carlo (dashed black line), the difference between measured and simulated doses (black squares), and corrected measured dose by using QCF (solid red line). Taken from [Anderson *et al.* 2019].

process of deexcitation [Beddar 2006]. The amount of light emitted is proportional to the energy deposited in the crystal [Symonds *et al.* 2012]. In modern scintillation devices, the light is detected by charged-coupled devices (CCD) cameras or photomultipliers (PM) outside the irradiation field. Plastic scintillation detectors, e.g., the Lynx detector (IBA Dosimetry, Germany), has been proven suitable for small-field conditions (i.e., proton GRID therapy) [Gao *et al.* 2018] due to their relatively small sensitive volume which provides a high spatial resolution [Burke *et al.* 2017]. Another advantage of scintillation detectors is that they provide two-dimensional real-time information on dose distributions. However, they exhibit a significant LET dependence [Beddar 2006].

## 1.2.2 Radiotherapy modalities and techniques

RT is classified into four categories depending on the dose delivery method and radiation source: brachytherapy, intraoperative radiotherapy (IORT), targeted radionuclide therapy (TRT), and external beam radiotherapy (EBRT). These modalities are described in the following sections.

### 1.2.2.1 Brachytherapy

Brachytherapy is a RT modality that consists of precisely placing radioactive sources into or near the volume to be treated [Chargari *et al.* 2019]. These sources can be implanted or loaded directly into the tumor (interstitial brachytherapy), adjacent cavities (intracavitary), or blood vessels (intravascular). The implantation is performed by endoscopic guidance or perioperative placement of the sources. Imaging after the placement of sources is also required to guide the dosimetric process, i.e., calculating the irradiation time to achieve the prescribed dose to the

target depending on the position of the sources. The treatment time varies from a few minutes, followed by the removal of the radioactive seed (afterloading), or more extended periods over the effective lifetime of the radionuclide, where the source remains permanently in the patient (seed implantation).

Most radionuclides used in brachytherapy are photon emitters, but beta- and neutron-emitting sources may also be used [Symonds *et al.* 2012]. The most common radionuclides used nowadays are iridium-192, cobalt-60, iodine-125, and palladium-103 [Chargari *et al.* 2019]. The selection of the source depends on its properties (half-life and energy) and specific treatment. The main advantage of brachytherapy is the highly-localized dose delivery to a small target volume, which benefits local control and reduces the dose delivered to surrounding normal tissue. Thus, large tumors are not suitable for this modality. Suitable candidates for brachytherapy are small localized tumors in the prostate, breast, cervix, or esophagus. Three modalities of brachytherapy may be used: low-dose-rate (LDR) irradiation (0.4 to 1 Gy/h) delivered continuously or in short pulses, medium-dose-rate (MDR) (1 to 12 Gy/h) or high-dose-rate (HDR) (>12 Gy/h) brachytherapy. The modality used depends on the characteristics of each tumor and the patient condition.

The main limitations of brachytherapy are its invasiveness, the lack of proper treatment monitoring, and the high susceptibility to operational mistakes due to the several manual steps involved in the treatment process [Chargari *et al.* 2019, Fonseca *et al.* 2020]. Fonseca *et al.* [Fonseca *et al.* 2020] reported that the main causes of deviation between the treatment delivery and treatment plan are the inappropriate positioning of the sources, the deviation in the source dwell time, and incorrect source-specific parameters. In addition, treatment plans are not personalized, i.e., dose distributions are commonly calculated using simplified formalisms without considering the specific patient's anatomy [Akhavanallaf *et al.* 2021]. Overall, these potential errors may lead to tumor underdosing and excessive irradiation of critical organs [Chargari *et al.* 2019].

### 1.2.2.2 Intraoperative radiotherapy

Intraoperative radiotherapy (IORT) refers to the delivery of ionizing radiation to the target volume, or tumor bed, during a surgical process [Pilar *et al.* 2017]. So it consists of single-fraction treatments. The rationale for using RT during surgery is to prevent the remaining tumor from repopulating after its surgical resection and the direct visualization of the tumor bed, which allows precise dose delivery. The efficacy of IORT has been proven for treating early breast [Veronesi *et al.* 2013], gastric [Fu *et al.* 2008], retroperitoneal [Gieschen *et al.* 2001], pancreatic [Alferi *et al.* 2001], and colorectal cancers [Valentini *et al.* 2009]. HDR brachytherapy and electron and X-rays beams are the most common forms of IORT delivery [Calvo *et al.* 2006, Pilar *et al.* 2017]. Dedicated intraoperative machines (i.e., accelerators) and applicators are often required for this type of treatment [Symonds *et al.* 2012].

### 1.2.2.3 Targeted radionuclide therapy

Targeted radionuclide therapy (TRT) is a RT approach based on attaching a radioactive source (radionuclide) to a vector (e.g., monoclonal antibodies or peptides) [Gudkov *et al.* 2015]. Contrary to chemotherapy, such vectors are exclusively directed to cancer cells. Thus, the dose is delivered selectively to the target minimizing the toxicity to normal tissues. Vectors (radiopharmaceuticals) are high-affinity molecules to cancer cells. These pharmaceuticals usually are injected intravenously or intracavitary. The selection of radionuclides attached to vectors depends on their affinity to vectors, type and energy of the emitted particle, half-life, and cost of production. In clinics,  $^{124}\text{I}$  and  $^{90}\text{Y}$  (beta-emitters of less than 2.2 MeV) are commonly employed. TRT is used mainly to treat radiosensitive tumors, particularly leukemias, lymphomas, or thyroid cancer. The efficacy of TRT for treating solid tumors is low since the doses of ionizing radiation required to achieve tumor control are not achievable by those radionuclides [Gudkov *et al.* 2015].

### 1.2.2.4 External beam radiotherapy

External beam radiotherapy (EBRT) involves delivering ionizing radiation from a source external to the patient. EBRT is the most common form of RT, accounting for nine-tenths of the total treatments and being a palliative and curative option for most solid tumors [Gerber & Chan 2008].

In EBRT, megavoltage X-ray and electron beams are mainly generated by medical linear accelerators (LINAC). LINACs accelerate electrons to energies in the MeV range using radiofrequency electromagnetic waves. Collimators, scatterers, and applicators may be used to modify these accelerated electron beams to obtain clinical beams (up to 25 MeV).

In a similar mode of operation, LINACs can also produce megavoltage X-ray beams. Photons are created by Bremsstrahlung by placing a tungsten target in the path of the primary electron beam. The X-ray beam produced is shaped and flattened by collimators and filters to create clinical photon beams [Symonds *et al.* 2012]. X-ray beams produced by Bremsstrahlung are not monoenergetic but show an energy spectrum; then, they are defined by the voltage utilized to accelerate the primary electron beam (up to 18 MV). Figure 1.6 illustrates a schematic view of a LINAC operating in electron and X-ray modes. Other applications of photon-EBRT, such as stereotactic radiotherapy, may also use multiple radioactive sources of  $^{60}\text{Co}$  pointing to a common location in the patient [Chung & Lee 2020].

Proton and ion beams are produced by larger and more complex accelerators, e.g., cyclotrons or synchrotrons (see Section 1.3.2.1). Neutron beams can be produced nowadays in clinical facilities using accelerator-based neutron sources (ABNS), where a proton beam hits a beryllium or lithium target, producing neutrons.

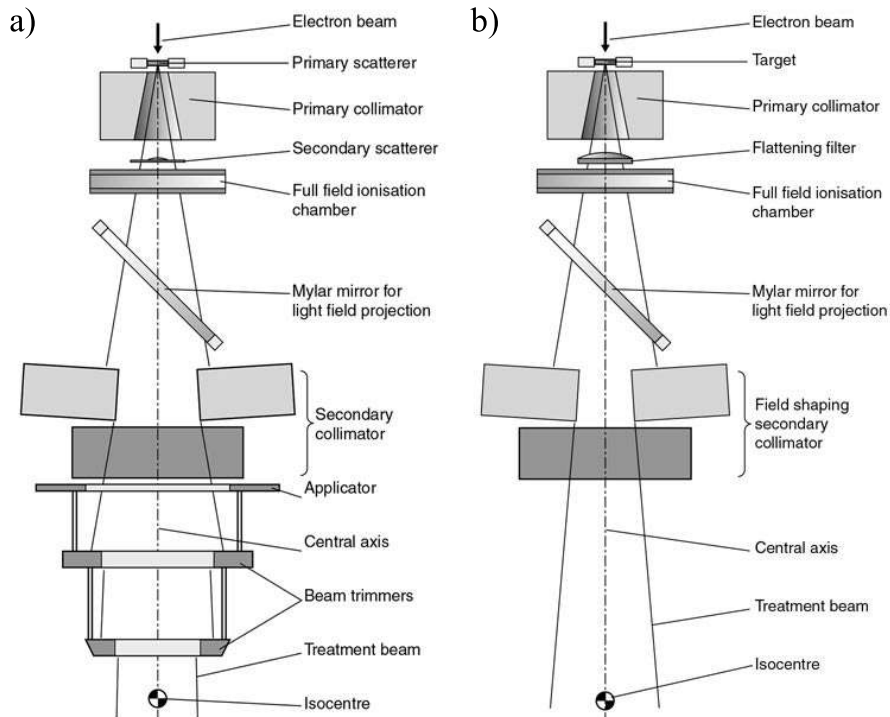


**Figure 1.6:** LINAC operating in (a) electron and (b) X-ray mode. Taken from [Symonds *et al.* 2012].

EBRT techniques have evolved significantly in the last decades due to the improvement and increased availability of imaging techniques, e.g., computed tomography (CT), magnetic resonance imaging (MRI), cone beam computed tomography (CBCT), and positron emission tomography (PET), allowing the precise localization of target volumes [Gerber & Chan 2008]. The improvement of irradiation devices and dose calculation algorithms has also contributed to the increased precision of EBRT in terms of dose conformity to the tumor and the sparing of normal tissues. A brief review of the most common techniques and recent advancements in EBRT is presented hereafter.

### 3D-conformal radiotherapy

3D-conformal radiotherapy (3DRT) shapes dose distributions to obtain homogeneous high-dose regions in the target volume while minimizing the dose to adjacent normal tissues. To achieve such dose distributions, 3DRT uses more than one field, and the aperture of each beam is shaped to the contour of the target volume in its beam-eye-view (BEV) [Schlegel 2006].

### Intensity-modulated radiotherapy

Intensity-modulated radiotherapy (IMRT) refers to the delivery of radiation beams of non-uniform fluence [Elith *et al.* 2011]. It represents the most advanced

form of conformal EBRT and is a mainstream technique available at most major RT centers worldwide [Podgoršak *et al.* 2006]. IMRT treatments consist of several fields (three to seven typically). These fields can be considered as a combination of multiple individual beamlets. Each beamlet is meant to treat only a small volume of the target, so the intensity of each one is modulated to optimize the dose deposition in that volume while minimizing the dose to the surrounding normal tissues. The fluence of each beam is modified using multi-leaf collimators (MLC) (see Figure 1.7). MLCs consist of 40 to 120 leaves arranged in pairs that can move independently in one direction to generate any field shape and modify the beam intensity by blocking fractions of the radiation field [Jeraj & Robar 2004]. As a result, dose distributions are sculpted to shape complex-shaped targets, the dose homogeneity within the target is increased, and a rapid dose fall-off outside the target is achieved. This approach allows for delivering more complex non-uniform dose distributions and, thus, achieving a higher degree of conformity to the target volume. The main drawbacks of IMRT are the increased integral dose to the whole body, the precision required when delineating the target volume [Elith *et al.* 2011], and the increased treatment duration [Raina *et al.* 2020].

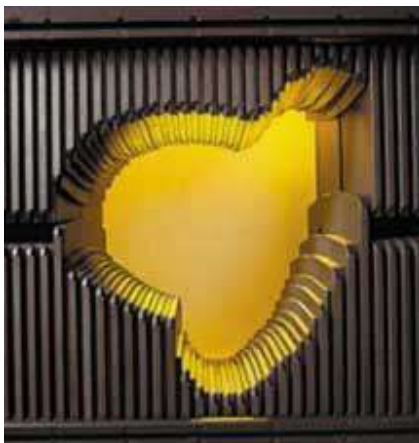


**Figure 1.7:** Representation of a multi-leaf collimator. Taken from [Jeraj & Robar 2004].

Rotational forms of IMRT, such as volumetric modulated arc therapy (VMAT) and dynamic conformal arc therapy (DCAT), have also been implemented. VMAT delivers dose distributions by continuously modulating the intensity and aperture of fields while the gantry rotates around the patient [Elith *et al.* 2011]. Several studies reported an excellent sparing of critical structures with VMAT, compared to conventional IMRT, in six major clinical indications, i.e., head and neck, genitourinary and anorectal tumors, thoracic neoplasm, brain metastases, and oligometastases [Macchia *et al.* 2017]. For instance, in the comparative study by Shaffer *et al.* [Shaffer *et al.* 2010] for treating temporal high-grade gliomas, VMAT significantly reduced the maximum and mean dose to the retina, lens, and optic nerve, in comparison with IMRT, while achieving an equivalent target coverage and conformity. Similar to VMAT, in DCAT, the gantry rotates while shaping the

MLC around the tumor to deliver dose distributions [Morales-Paliza *et al.* 2011]. However, the intensity of fields is not modulated. Its main advantage over VMAT is that the entire target remains inside the open field for the whole treatment [Moon *et al.* 2020]. Thus, DCAT may be beneficial for treating moving targets such as lung or liver tumors. In addition, DCAT offers shorter delivery times, reduced complexity of treatment plans, and fewer monitor units are required to deliver the same dose. Nevertheless, the tumor coverage is inferior as compared to VMAT.

### Image-guided radiotherapy

Image-guided radiotherapy (IGRT) aims to reduce the contribution of uncertainties related to variations in the daily patient setup to the dose delivery. It integrates imaging technology into treatment devices, allowing the verification of the patient's position prior to the treatment delivery and consequent repositioning to correct possible misalignments with treatment fields. It may also reveal unexpected organ motion and tumor changes. The reduction of these uncertainties allows diminishing error margins around the target volume. This leads to a more precise dose delivery, which may prevent the underdosing of the target and excessive irradiation of normal tissues. Standard imaging devices integrated into treatment devices (e.g., LINACs) are CT or MRI scanners. Other imaging modalities such as ultrasounds or optical imaging techniques may also be used but are less common in the clinical practice [Dawson & Sharpe 2006].

### Adaptative radiotherapy

In adaptative radiotherapy (ART), images are acquired prior to each treatment session to identify anatomical changes in the patients (e.g., internal motion, weight loss, or tumor shrinkage) and modify treatment plans accordingly. The adaptation of treatment considering such changes increases the accuracy and precision of dose delivery [Sonke *et al.* 2019].

### Four-dimensional radiotherapy

Four-dimensional radiotherapy (4DRT) refers to the treatment delivery considering some degree of temporal information. The main aim of this technique is to keep the target volume stationary during the dose delivery. The most relevant example of target and organ motion in RT treatments is the thoracic movement through the respiratory cycle. Different strategies have been implemented in the last decades to manage this motion, such as holding the breath naturally or using mechanical devices at some point of the breathing cycle, breath gating, where the patient breathes normally and the beam operates only at a specific phase of the breathing cycle, or tracking deliveries, where the movement of the target volume is tracked continuously and the treatment plan is modified according to that motion. The implementation and efficacy of 4DRT techniques rely on acquiring a set of

patient images that contain temporal information, i.e., four-dimensional computed tomography (4DCT) images [Moorrees & Bezak 2012].

### Stereotactic radiotherapy

Stereotactic radiotherapy (SRT) concentrates the radiation within the target volume with millimetric precision by using several narrow beams delivered through noncoplanar arcs around a specific point (isocenter) [Khan & Gibbons 2014]. Thus, high conformity to the tumor is achieved while sparing normal tissue due to the rapid dose fall-off outside the target volume. SRT is used to treat relatively small tumors (up to 4 cm diameter), such as metastatic tumors in the brain [Soliman *et al.* 2016], liver [Aitken & Hawkins 2015] or lung [Okunieff *et al.* 2006]. SRT for extracranial lesions can also be called stereotactic body radiation therapy (SBRT).

Prescribed doses in SRT treatments are of the order of 10 to 60 Gy delivered in 1 to 5 fractions. Treatments delivered in a single fraction are called stereotactic radiosurgery (SRS). Such high doses per fraction require high precision in the dose delivery ( $\pm 5\%$ ) and patient positioning ( $\pm 1$  mm). Immobilization devices (e.g., thermoplastic masks or vacuum cushions) or four-dimensional techniques are typically used. SRT treatments can be delivered using conventional LINACs (i.e., VMAT and DCAT techniques) or dedicated systems such as Gamma Knife or Cyberknife. Gamma Knife consists of several  $^{60}\text{Co}$  sources around the patient pointing to the isocenter, while Cyberknife uses a miniature LINAC on a robotic arm [Khan & Gibbons 2014, Podgorsak *et al.* 2005]. SRT using protons (proton SRS) has also been successfully used for treating brain metastases [Atkins *et al.* 2018].

### Proton and heavy-ion therapy

Proton therapy (PT) and heavy-ion therapy use protons or heavy ions, respectively, instead of X-rays. The distinct energy deposition of these particles leads to more favorable dose distributions, i.e., inverse depth dose profiles and negligible/reduced dose deposition behind the target (see Section 1.2.3). As a result, a more targeted dose deposition to the tumor is achieved while sparing normal tissues. However, heavy ion beams exhibit a fragmentation tail, which may lead to the irradiation of tissues distal to the target.

Besides their dosimetric benefits, protons and heavy ions exhibit increased biological effectiveness, compared to photons, due to their higher LET and more condensed ionization patterns [Durante & Flanz 2019a]. Clinical proton and ion beams are produced by particle accelerators (i.e., cyclotrons and synchrotrons) and dedicated beam delivery systems (see Section 1.3.2).

A more detailed description of PT, including physical, technical, radiobiological, and clinical aspects, is given in Section 1.3 due to its relevance in this thesis.

Regarding heavy ions, their clinical use nowadays is restricted to carbon [PTCOG 2022b] and helium [RaySearch Laboratories 2021] ion beams. Several clinical trials have shown the favorable toxicity profile and superior local control

of carbon ion therapy (alone or as a boost) in various clinical indications (e.g., meningioma, glioma, tumor in the base of the skull, head and neck cancers, lung tumors and sarcomas) [Malouff *et al.* 2020]. For instance, in the study by Mizoe *et al.* [Mizoe *et al.* 2007], carbon ion therapy used as a boost increased the survival of high-grade glioma patients up to 26 months, avoiding grade 3 late toxicities. Carbon ion beams may also benefit the treatment of radioresistant tumors due to their increased biological effectiveness [Durante & Flanz 2019a]. The review article by Malouff *et al.* [Malouff *et al.* 2020] provides a summary of the current clinical trials using carbon ion therapy. The main drawbacks of carbon ion therapy are its cost and the uncertainty in their dose distributions [Malouff *et al.* 2020]. Carbon dose distributions are more sensitive than photons and protons to uncertainties in the target position. These uncertainties may be caused by incorrect patient setup and intra- and inter-fraction organ motion. Changes in the density of tissues in the beam path may also degrade significantly dose distributions, which may lead to less robust treatments and severe toxicities in treatments involving tissue inhomogeneities. In addition, the accuracy in the calculation of the biological dose in treatments is limited by uncertainties in the relative biological effectiveness of carbon ion beams [Karger *et al.* 2021].

Other heavy ions, e.g., silicon and argon ions, were used in the past (1979 - 1982) for treating hypoxic tumors [Castro *et al.* 1994]. However, its use was abandoned due to the excessive late adverse effects observed. Nowadays, the renewed use of very heavy ions (e.g., neon, oxygen, and lithium) is being considered due to the reduced oxygen enhancement effect provided [Mein *et al.* 2022].

*Due to the importance in this thesis of RT techniques based on the delivery of radiation through external beams, a detailed description of dose and LET metrics in EBRT is given in the following section.*

### 1.2.3 Dose and LET distributions in EBRT

Photons, neutrons, and charged particles (electrons, protons, and heavy ions) exhibit different dose and LET distributions due to their distinct mechanism of interaction with matter. These distributions play a relevant role in the selection of the treatment modality for each specific clinical case. The main characteristics of dose and LET distributions in EBRT modalities are described hereafter.

#### Photons

Figure 1.8a shows the characteristic depth dose profile of MV photon beams at clinical energies. The dose deposited by photons increases up to a maximum at a few millimeters in-depth as they penetrate matter. This phenomenon is called the dose-built-up effect [Symonds *et al.* 2012]. It is produced because electrons liberated by ionization do not deposit their energy at the interaction site, but they do it over a finite range. At a shallow depth, the energy that propagates

downstream from the interaction site is not compensated by the contribution of electrons created upstream. The maximum dose point,  $d_{\max}$ , is located at the depth where the number of electrons crossing upstream and downstream is equal (i.e., charged-particle equilibrium). The position of this point depends on the initial energy of the beam; the higher the energy, the deeper  $d_{\max}$ . For megavoltage beams, it amounts to 1 to 2 cm. Behind this point, the dose decreases exponentially as the transmission of photons and the ionization events do it so since primary photons are absorbed. Although this dose distribution shape is beneficial in terms of skin-sparing thanks to the buildup effect, the exponential tail results in the irradiation of normal tissues behind the tumor. In addition, several beams are required to create a homogeneous dose distribution within the target, which is typically required in RT treatments [Khan & Gibbons 2014].

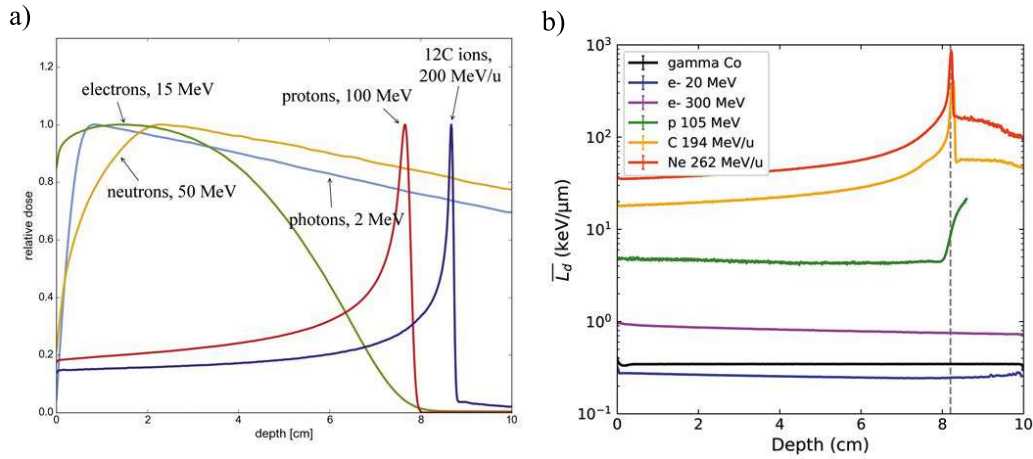


**Figure 1.8:** Depth (a) dose and (b) LET distributions of different radiation beams at clinical energies in water. Taken from [Schneider 2020] and [Delorme *et al.* 2021], respectively.

Regarding LET, clinical photon beams are considered low-LET radiation ( $< 1 \text{ keV}/\mu\text{m}$ ), and their LET distributions are constant in depth (see Figure 1.8b). The LET of photon beams refers to the LET of free electrons released by ionization in the process of Compton scattering of photons with atomic electrons.

## Electrons

The constant rate of energy loss of electrons implies that the electron beam has a finite depth of penetration (also called the range) at which electrons stop. The range is dependent on the initial beam energy. The practical range at clinically relevant energies (up to 20 MeV) is relatively short ( $< 10 \text{ cm}$  in water), which restricts the use of electrons to the treatment of superficial tumors. This is caused by the large deflections suffered by electrons in a medium due to their relatively small mass. Electron beams show a relatively high entrance dose and a slow dose fall-off after the maximum dose point (see Figure 1.8a). The low gradient of the dose

fall-off is caused because electrons that compose the beam do not undergo the same number of interactions in matter due to their different paths and stop at slightly different depths. This effect is called range straggling. The production of photons by bremsstrahlung that deposits their energy at some distance away from the electron interaction point also causes the slow dose fall-off [Symonds *et al.* 2012].

The use of very-high energy electrons (VHEE) of energies above 50 MeV has also been proposed for RT applications [DesRosiers *et al.* 2000], but it is not clinically available yet. These high energies, i.e., increased range, allow the treatment of deep-seated tumors and present dosimetric advantages over megavoltage photon beams in terms of improved penumbra and ballistics [Ronga *et al.* 2021].

Electron beams used in RT are considered low-LET radiation. The LET of electron beams is around 0.25 keV/ $\mu\text{m}$  for conventional 20 MeV beams and up to 0.8 keV/ $\mu\text{m}$  for VHEE. The LET of clinical electron beams do not vary as a function of depth (see Figure 1.8b) [Delorme *et al.* 2021, Ronga *et al.* 2021].

### Protons and heavy ions

Like other charged particles, protons and heavy ion beams have a finite penetration depth. The range increases with the beam energy. The range in water for typical proton (70 to 250 MeV) and ion beams, such as carbon (200 to 350 MeV/u<sup>1</sup>), is 4 to 38cm and 8 to 22 cm, respectively, which allows the treatment of deep-seated tumors. Their depth dose curves exhibit a low entrance dose and a pronounced maximum at the end of the range (Bragg peak) due to the increased stopping power as these particles slow down. Heavy ions exhibit a sharper Bragg peak than protons because the range straggling decreases as the mass of the particle increases. After this point, the dose falls off rapidly. In the case of heavy ions, depth dose curves exhibit a dose tail resulting from nuclear fragments produced at the Bragg peak position (fragmentation tail) [Rackwitz & Debus 2019]. Figure 1.8a shows proton and heavy-ion dose distributions. Thus, proton and heavy-ion dose distributions are more favorable as compared to photons or electrons since the high dose region (Bragg peak) is concentrated at the tumor depth, and normal tissue behind the tumor is spared thanks to the rapid dose fall-off.

Proton and heavy ions are considered high-LET radiation since the rate of energy deposition increases considerably at the Bragg peak (up to 12 and 100 keV/ $\mu\text{m}$ , respectively) due to the slowing down of the incident particles (see Figure 1.8b) [Kantemiris *et al.* 2011].

Regarding lateral dose distributions, the lateral fall-off (or penumbra) of protons is sharper than photons beams up to 17 cm in depth [ICRU 2007]. Heavy ions exhibit a narrower penumbra than protons (see Figure 1.9). The lateral penumbra is typically defined as the distance between the points at 80 % and 20 % of the maximum dose in the lateral direction of the beam [ICRU 2007]. Sharper penumbras are typically beneficial in RT since the dose conformity to the tumor increases.

<sup>1</sup>The energy of a heavy ion beam is defined as the energy per nucleon (protons and neutrons).

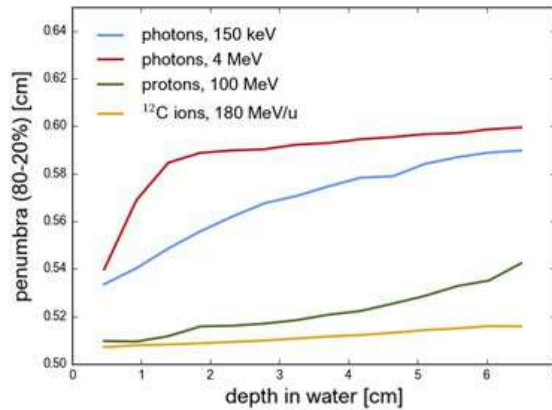


**Figure 1.9:** Evolution of the penumbra of photon, proton, and carbon beams in depth. Taken from [Schneider 2020].

A detailed description of the characteristic of dose and LET distribution of proton beams can be found in Section 1.3 due to the key role of proton beams in this thesis.

## Neutrons

Depth dose distributions of fast neutrons are very similar to MV photons since they are both uncharged particles (see Figure 1.8a). The neutron dose curve also exhibits a buildup region due to the lack of charged particle equilibrium (of secondary protons in this case) and an exponential decay after the maximum dose point due to the absorption of neutrons.

Contrary to X-rays, neutrons are considered high-LET radiation. The LET of neutron beams is associated with the recoil protons produced by incident neutrons. The LET varies with the neutron energy and within their dose distribution due to the different mechanisms of interaction and the many types of charged particles set in motion [Söderberg & Carlsson 2000].

*Previous sections describe the physical characteristics of radiation and its interactions with matter. Those interactions cause a biological response in living tissues that determines the outcome of radiotherapy treatments. In the following section, the effects of radiation on living tissues are addressed by introducing the fundamentals of radiobiology.*

### 1.2.4 Radiobiology

Radiobiology, or radiation biology, studies the biological effects of ionizing radiation on living tissues. It influences RT treatments in three main aspects: (i) it provides an insight into the mechanisms that underly the response of tissues to radiation, (ii) it is the rational basis for the creation of treatment protocols (e.g., treatment regimens), and (iii) it guides the development of new treatment modalities (e.g., multimodality therapies) [Joiner & van der Kogel 2018].

*Due to the relevance of radiobiology in the development of new RT techniques, which is the focus of this thesis, this section presents the basis of the effects of ionizing radiation on tissues and their quantification.*

#### 1.2.4.1 Fundamentals of cell and tissue biology

*This subsection aims to introduce the concept of the cell, DNA, cell cycle, tissue, and organ since they are relevant to describe the biological effects of radiation.*

The cell is the most basic unit that can perform life functions, being essential for every organism's structure and function [Lodish *et al.* 2006]. Human cells consist of a cytoplasm enclosed by an external membrane and a nucleus (see Figure 1.10a). The cytoplasm contains organelles, which are subcellular structures with specific functions. The nucleus contains the deoxyribonucleic acid (DNA). The DNA stores the genetic information, i.e., it contains the instructions for the cell to perform life functions such as developing, surviving, or reproducing. Damage to the DNA may cause malfunctioning or even the cell's death. The DNA molecule consists of two helical strands forming a double helix (see Figure 1.10b). Strands are composed of a sequence of monomers called nucleotides. These nucleotides contain nitrogen bases, which bind to each other to hold together the DNA strands. The DNA is folded to form organized structures called chromosomes. The chromosome consists of two sister arms called chromatids.

Cells undergo a series of events to grow and divide (cell proliferation). This cycle consists of different stages (see Figure 1.10c) where damages and the viability of the cell are evaluated to proceed or not with the cell reproduction process [Lodish *et al.* 2006].

At a larger scale, cells lump together to form tissues, which compose the organs [Joiner & van der Kogel 2018]. Organs can be thought of as a cluster of tissue portions called functional subunits (FSU). In parallel organs (e.g., kidney, liver, or lung), FSUs perform independently, i.e., the organ failure occurs after the damage of a critical number of FSUs. Contrarily, in serial organs (e.g., spinal cord), FSUs have a tubular architecture and the failure of one of them causes the loss of function in the entire organ. The tissue behavior is also influenced by the tissue microenvironment [Anderson & Simon 2020]. The tissue microenvironment is a collection of infiltrating and resident host cells (e.g., immune and stromal cells), secreted factors, blood vessels, and the extracellular matrix that surrounds a specific tissue. In particular, the tumor microenvironment (TME) plays an important role in the progression and treatment of cancer since it regulates cancer cell motility and invasion [Brábek *et al.* 2010].

#### 1.2.4.2 Fundamentals of radiobiology

The biological effects of radiation are derived from a concatenation of processes at a timescale of  $10^{-18}$  to  $10^9$  seconds. Such processes can be classified into the

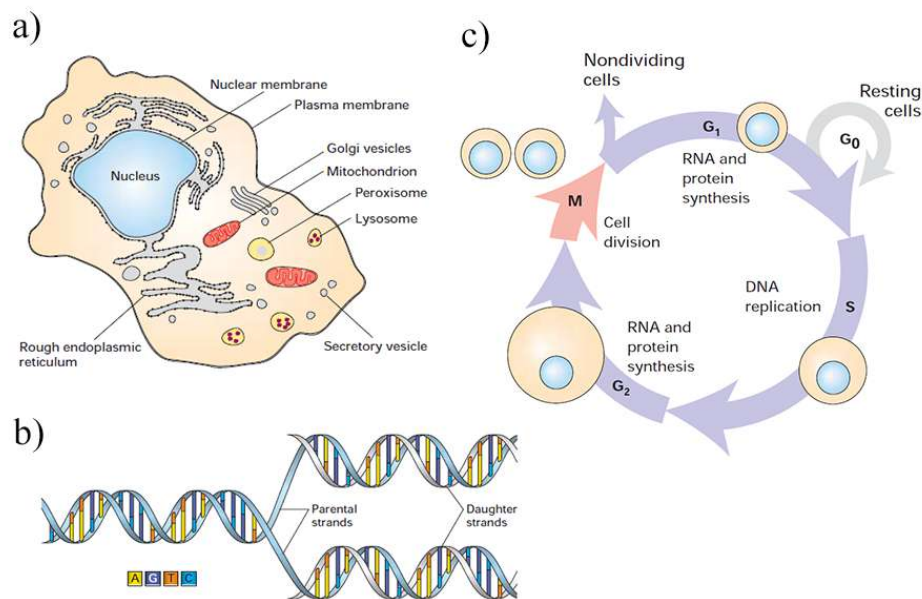


**Figure 1.10:** (a) Schematic representation of a human cell, (b) DNA, and (c) the cell cycle. Taken from [Lodish *et al.* 2006].

physical, chemical, and biological stages. Figure 1.11 illustrates these three stages and their timescale.

The physical stage involves the interaction of ionizing radiation with matter, described in Section 1.2.1.1. These interactions result in the deposition of energy and consequent excitation and ionization of atoms. Physical processes take around  $10^{-18}$  to  $10^{-6}$  seconds. In the chemical stage, the products of the physical phase (ionized atoms and released particles) interact with molecules of the cell medium by chemical reactions. The result of these interactions is the ionization of these molecules and the production of free radicals. The most relevant free radicals in the context of RT are the *reactive oxygen species* (ROS) (e.g., hydroxyl or hydrogen peroxide). They are created by the radiolysis of water. ROS are highly reactive molecules that can diffuse within the cell and interact with other molecules breaking up their chemical bonds. These chemical reactions occur within one millisecond after the radiation exposure. Interactions of ROS with other molecules of the cell are included in the biological stage. In this stage, molecules that form cell components can be modified and damaged. The most critical damage to the cell is caused to DNA molecules. The processes of damage involving ROS are so-called indirect effects. Charged particles, such as electrons, protons, or ions, may also interact and damage the DNA directly (direct effects). The biological phase may last up to the human lifespan [Joiner & van der Kogel 2018].

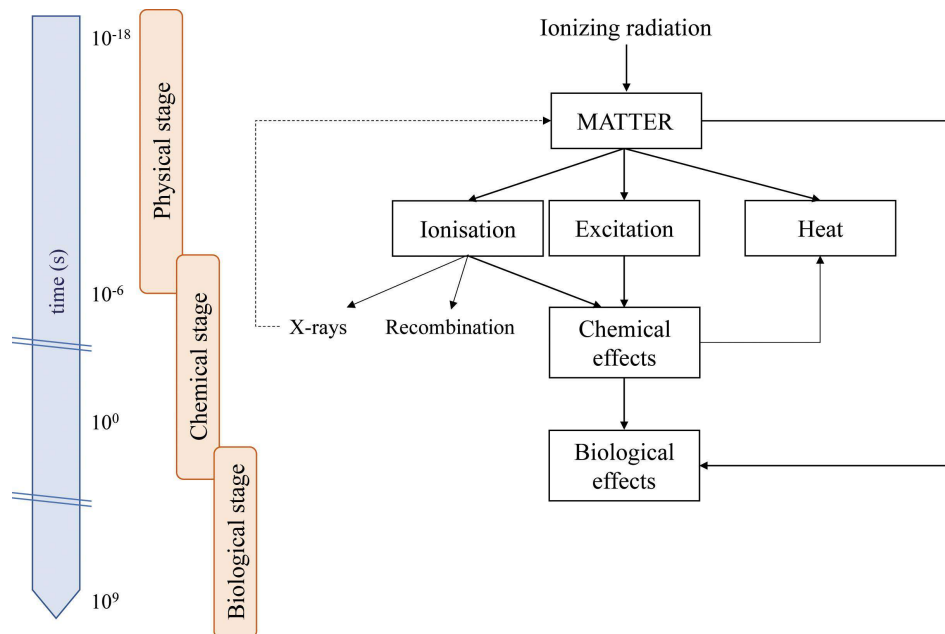


**Figure 1.11:** Representation of the processes involved in the physical, chemical, and biological stages and their timescale.

#### 1.2.4.3 The 6 Rs of radiobiology

In RT, the efficacy of treatments in terms of radiobiological effects is hypothesized to depend upon five main hallmarks (the 5 *Rs*): the repair of the DNA damage, radiosensitivity of cells, repopulation of the tumor cells, reoxygenation of tumors, and redistribution of cells in the cell cycle [Withers 1975, Steel *et al.* 1989]. In 2019, Boustani *et al.* [Boustani *et al.* 2019] proposed the reactivation of the anti-tumor immune response as the sixth *R* of radiobiology. The 6 *Rs* describe how tumors and normal tissues respond to radiation and are described in more detail in the following subsections.

#### DNA damage and repair

As described in Section 1.2.4.2, ionizing radiation can damage DNA molecules by direct or indirect effects. Among other types of DNA damage, such as alteration of the bases or DNA-crosslink, the most relevant damage produced by radiation are the single- and double-strand breaks. Single-strand breaks (SSB) are ruptures of the bonds that form one strand of the double helix. These breakages are produced due to the interaction of free radicals produced by radiation or radiation itself with the molecules that constitute the DNA backbone. Double-strand breaks (DSB) are defined as two SSBs occurring on opposite strands within ten base pairs. As a result, the bonds between the two strands break. DSBs are the most lethal type of radiation-induced lesion since they cause difficulties in the replication process, leading to cell death [Joiner & van der Kogel 2018]. Figure 1.12 illustrates examples

of the process of radiation-induced SSBs and DSBs.

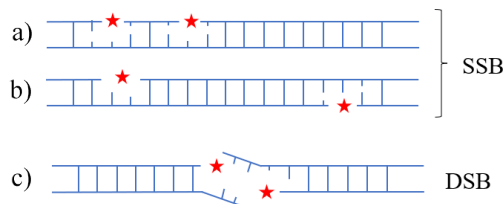


**Figure 1.12:** Representation of how two interactions (represented by red stars) can lead to SSBs and DSBs. The DNA double helix is represented in blue. In (a), interaction points are close together but in the same strand. In (b), they are in different strands but far away from each other. Both scenarios only cause the breakage of individual strands (SSBs). Contrarily, in (c), the interaction occurs in the two strands within 10 base pairs, causing the break of the bond between the two strands (DSB).

Types of radiation with different track structures promote distinct types of DNA damage [Goodhead *et al.* 1993]. Low-LET radiation (e.g., photons and electrons) creates randomly distributed ionization events, being unlikely to produce clustered interactions with the DNA. Thus, SSBs are more probable than DSBs. Contrarily, high-LET radiation (e.g., protons or heavy ions) produces more ionizations per unit length following the primary particle path. Therefore, clustered damage (i.e., DSBs) is more likely to occur [Symonds *et al.* 2012]. Figure 1.13a illustrates these distinct dose deposition patterns at the sub-cellular level. Clustered damage is more difficult to repair and produces higher rates of cell death (see Figure 1.13b) [Girdhani *et al.* 2013]. Independently of the LET, higher doses imply a more significant number of ionization events, i.e., more potential damage to the DNA, in a linear relationship.

Cells have different mechanisms to identify and repair DNA damage. The attempt to repair these lesions may lead to three main outcomes: (i) the damage cannot be repaired and the cell dies by mitotic catastrophe (i.e., the cell dies after several unsuccessful attempts to replicate), (ii) the DNA is correctly repaired and cell performs its functions normally, or (iii) the lesion is incorrectly repaired. The latter may lead to cell death, cell survival but in a senescence state (the cell does not divide), or the continuation of the cell performance but with mutations, called chromosome aberrations (see Figure 1.14).

The leading pathways to repair DNA lesions are base excision repair (BER), single-strand break repair (SSBR), homologous recombination (HR), and non-homologous end-joining (NHEJ). Base alterations and SSBs can be repaired by similar processes: BER and SSBR, respectively. These pathways consist of the recognition and removal of the damaged base and the repolymerization of the DNA to reconstruct damaged bonds by using the undamaged strand as a template [Joiner & van der Kogel 2018]. HR and NHEJ are processes to repair DSBs. HR uses an identical or very similar undamaged DNA molecule that invades the space between damaged strands to act as a template for reconstructing the lesion

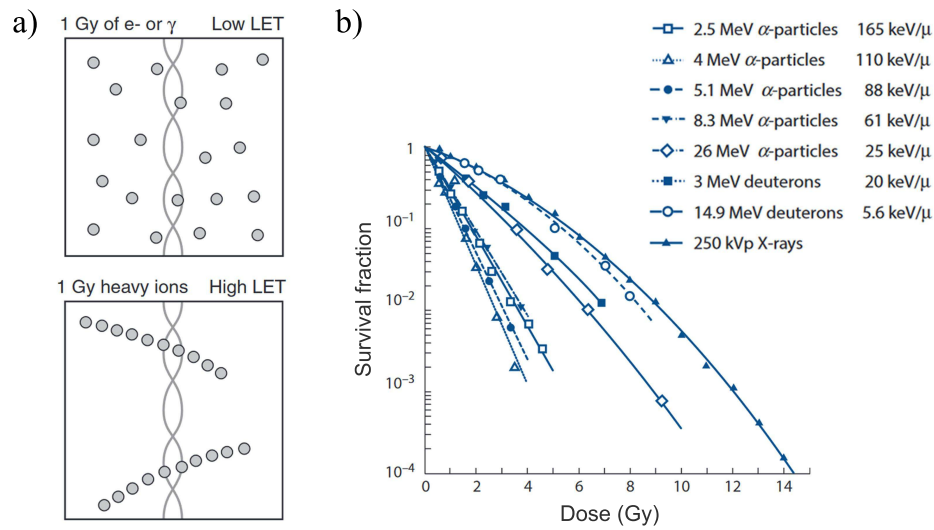


**Figure 1.13:** (a) Distribution of ionization events (represented by circles) of low- and high-LET radiation and (b) survival fraction for different LET particles. Adapted from [Symonds *et al.* 2012] and [Joiner & van der Kogel 2018], respectively.

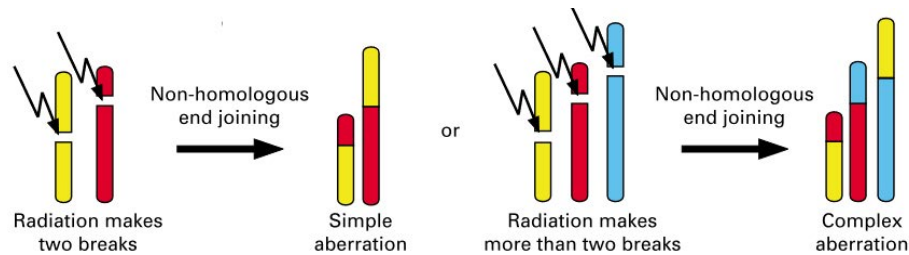


**Figure 1.14:** Examples of DNA damage mis-repair and chromosome aberration formation. Adapted from [Sachs *et al.* 2004].

[Li & Heyer 2008]. In the NHEJ process, the broken ends are directly ligated by different proteins that reconstruct the damaged part of the strands. It does not use another DNA molecule as a template, which may lead to mutations in the repaired chromosomes. NHEJ is the main DSB repair pathway in mammalian cells [Chang *et al.* 2017]. The efficacy of DNA repair may depend on different factors, such as cell condition and dose rate. In general, normal cells are more capable of repairing DNA lesions than tumor cells since cancer cells may present mutations affecting the damage identification. Lower dose rates tend to lead to reduced cell killing due to the repair of sublethal damage over the longer irradiation time [Podgorsak *et al.* 2005].

The radiation-induced damage at the cellular scale may also have an effect at tissue and organ levels. These effects are classified into acute and late effects. Acute effects (e.g., inflammation or skin damage) are caused by cell death in rapidly-proliferating tissues and are reverted relatively quickly after irradiation. Late effects (e.g., ulceration, fibrosis, or cancer development) are produced in slowly-

regenerating tissues by the reduction of cell populations or mutations caused by the incorrect DNA repair. Late effects appear months or years after the exposure [Podgorsak *et al.* 2005].

### Radiosensitivity

Cells may have different inherent radiosensitivity, i.e., their predisposition to harmful effects of radiation differs [Steel *et al.* 1989]. Radiosensitivity is defined as the steepness of survival curves for a given type of cell and radiation. The survival curve is the relationship between the dose and the number of cells that survive after radiation exposure (see Figure 1.15). This relationship is generally plotted as the logarithm of survival rate versus dose [Withers 1975]. The concept of survival curve is explained in more detail in Section 1.2.4.7. A steeper curve means a higher radiosensitivity, i.e., the tissue is more responsive to RT. The initial slope of the curve is typically evaluated by the survival fraction at 2 Gy, which correlates to the probability of tumor eradication [Steel *et al.* 1989].

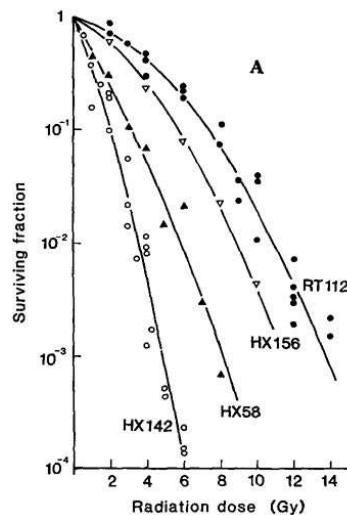


**Figure 1.15:** Cell survival curves for different human tumor cell lines: HX142, HX58, HX156, and RT112 (from more to less radiosensitive) at a dose rate of 1.5 Gy/min. Adapted from [Steel *et al.* 1989].

### Redistribution of cells in the cell cycle

The radiosensitivity of cells also varies significantly with the stage of the cell within the cell cycle [Withers 1975], as Figure 1.16 illustrates. This phenomenon is also known as the age-response function. These differences are explained by the different types of DNA damage produced through the process of cell replication and the distinct damage evaluation checkpoints of each phase.

The most sensitive phases are the G2/M phases. In contrast, cells in the S-phase are more likely to survive [Joiner & van der Kogel 2018]. After exposition

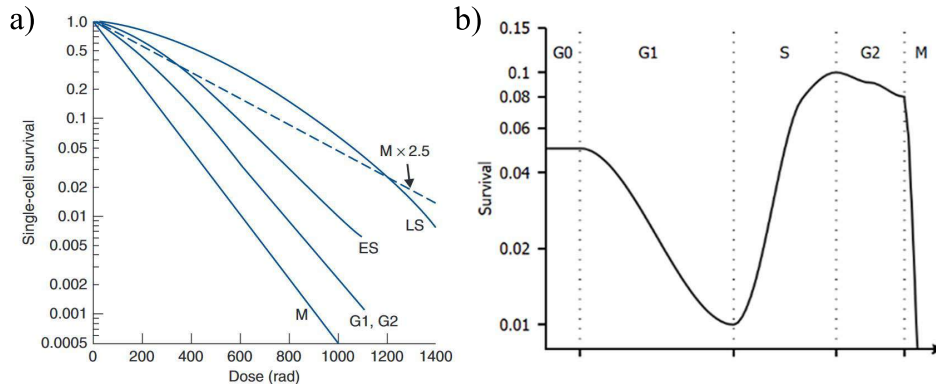


**Figure 1.16:** (a) Survival curves of cells at different phases of the cell cycle, and (b) variation of cell survival (i.e., radiosensitivity) through the cell cycle. Taken from [Joiner & van der Kogel 2018] and [McMahon 2018], respectively.

to radiation, cells tend to be blocked in the S-phase, prior to the M-phase. This blockage is caused because damaged cells may have lost their replication ability, and they cannot proceed to M-phase, the stage where cells divide. This synchrony is progressively lost after irradiation by the redistribution of stem cells (cells that preserve their reproductive ability) over the cell cycle. This process is important in treatments delivered in several sessions because cells in radioresistant phases may transit to more sensitive cell cycle phases before the following irradiation [Joiner & van der Kogel 2018, Withers 1975].

### The role of oxygen

Since a significant proportion of DNA damage is caused by ROS, the availability of oxygen in tissues to create free radicals greatly influences the cell response to radiation [Joiner & van der Kogel 2018]. Hypoxic (low concentrations of oxygen) tumors are more radioresistant than oxic (normal concentration of oxygen) tissues, as Figure 1.17a shows. Thus, oxygen enhances the radiation damage. This effect is quantified by the oxygen enhancement ratio (OER), which is the ratio of doses that leads to the same level of survival in hypoxic and oxic tissues:

$$OER = \frac{D(s_i, hypoxic)}{D(s_i, oxic)}, \quad (1.7)$$

where  $D$  is the dose to obtain a survival fraction  $s_i$  in hypoxic and oxic conditions.

OER values depend on the type of radiation. Low-LET radiation exhibit a OER of around 2.8, while values of 2.5 to 1 are observed for high-LET radiation (e.g., low-energy protons and heavy ions) (see Figure 1.17b) [Wenzl & Wilkens 2011]. This reduced oxygen dependence as LET increases arises from the greater proportion of DNA damage caused by direct effects, which do not imply oxygen reactions.

Tumor tissues tend to be hypoxic due to their chaotic vasculature, which hinders the normal oxygen supply. This effect magnifies as the tumor size increases since the inner part of tumors is beyond the diffusion distance of oxygen from surrounding

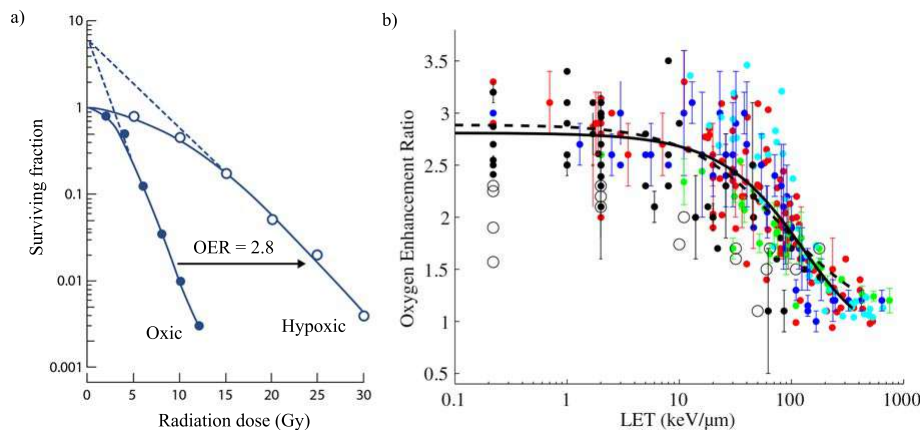


**Figure 1.17:** (a) Survival curves of tissues exposed to radiation under hypoxic and oxic conditions and (b) experimental determination of the OER dependence with LET. Adapted from [Joiner & van der Kogel 2018] and [Wenzl & Wilkens 2011], respectively.

tissues. When tumors are irradiated, surviving cells are predominantly hypoxic cells. As a consequence of the death of outer tumor layers, which were well-oxygenated, oxygen can flow to hypoxic parts of the tumor, which recover normal concentrations of oxygen, becoming more radiosensitive for a re-irradiation. This process is known as reoxygenation and plays an essential role in the rationale for delivering treatments in several fractions (see Section 1.2.4.4) [Joiner & van der Kogel 2018].

### Regeneration and repopulation

Tissues respond to the loss of cells by regenerating, i.e., cells reproduce to achieve the regular quantity of cells in the tissue. After irradiation, the total population of cells decreases due to cell death, and consequently, stem cells proliferate to repopulate both normal and tumor tissues. Therefore, the repopulation of tumors when the treatment is delivered in several sessions needs to be considered since it may counteract the effect of cell killing. The repopulation ability can be defined as the cloning doubling time, i.e., the time of a cell colony to double its population. Tissues differ in their ability, and rate of repopulation [Joiner & van der Kogel 2018]. Also, increased cell loss implies decreased repopulation since fewer stem cells survive in the damaged tissue [Hessel *et al.* 2003].

### Activation of the anti-tumor immune response

Radiation induces immune-mediated anti-tumor responses [Boustani *et al.* 2019]. Radiation can prompt physiological alterations in the TME (e.g., induction of immunogenic cell death and alterations of cancer cell immunophenotype) by triggering phenotypic changes in cancer and normal stromal cells [Portella & Scala 2019]. The radiation-induced cell death and damage can lead to the release of damage-associated molecular patterns (e.g., adenosine triphosphate or High-Mobility-Group-Protein B1), the surface exposure of immunogenic molecules,

and secretion of tumor antigens and cytokines that activates the innate and adaptive anti-tumor immunity. The anti-tumor response can be local or systemic and may play an important role in the non-targeted effects of radiation (see Section 1.2.4.6). For instance, the irradiation of tumor cells could serve as an “in situ vaccine” (i.e., immune primer) by activating the anti-tumor immunity [Portella & Scala 2019].

The anti-tumor immune response depends on the dose and number of sessions of treatments (see Section 1.2.4.4). The optimum irradiation schemes in terms of activation of the immune system are not yet well-established; however, the activation of the immune response to radiation should be considered when designing combined immune-radiotherapy treatments.

Some studies also suggested increased immunogenicity (i.e., the ability of cells/tissues to induce an immune response) by charged particles as compared to conventional X-ray RT [Durante *et al.* 2016, Durante & Flanz 2019b].

*Previous subsections present the 6Rs of radiobiology, which influence tissue responses. In the following section, a strategy largely employed in RT to maximize the effectiveness of treatments exploiting such responses is presented.*

#### 1.2.4.4 The temporal fractionation of the dose

Most RT treatments are delivered in several sessions (fractions) over a few weeks. This approach is called temporal fractionation of the dose. The rationale behind fractionating treatments is: (i) the repair of DNA damage and repopulation of cells in normal tissues, (ii) the reoxygenation of tumors, which makes them more radiosensitive, and (iii) the redistribution of tumor cells to more radiosensitive phases of the cell cycle between fractions. Fractionation increases the tolerance dose of normal tissues, as illustrated in Figure 1.18. However, it also promotes the repopulation and repair of tumor tissues; thus, a higher dose is required to eradicate tumors. Overall, fractionation schemes aim to balance the response of tumors and normal tissues. The selection of the fractionation schedule depends on the radiosensitivity of normal tissues and treated tumors [Podgoršak *et al.* 2006]. The three main types of fractionation regimes used clinically are conventional, hyper-, and hypo-fractionation.

The conventional scheme, the most used in clinics, delivers 2 Gy per fraction, one fraction per day, and five days per week during several weeks. Such a low dose per fraction favor the sparing of late-responding tissues, i.e., most of the normal tissues. Hyper-fractionation uses slightly lower doses per fraction than conventional schemes, but sessions are given two to three times daily. For such shorter intervals between fractions (6 h), the repopulation of normal tissues is not significant, but surviving tumor cells redistribute partially to more sensitive stages of the cell cycle, which promotes tumor cell killing [Withers 1975]. In hypo-fractionation regimes, treatments are delivered in few weekly fractions of high-dose ( $> 5$  Gy). This type of fractionation is beneficial in very conformal treatments of small targets, where normal tissues receive relatively small doses.

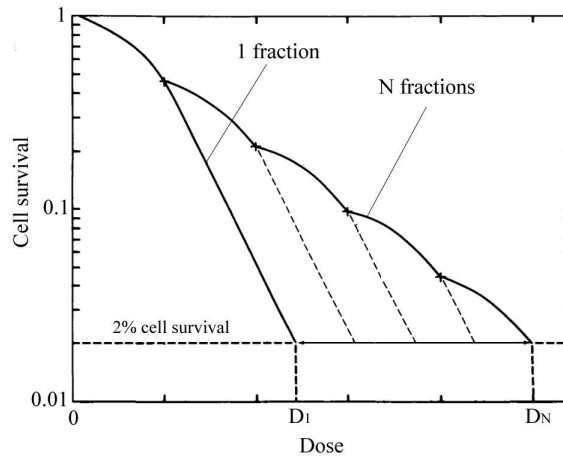


**Figure 1.18:** Survival fraction curves of a treatment fractionated in  $N$  sessions and a single session schedule.  $D_1$  and  $D_N$  correspond to the dose of the 1- and  $N$ -fraction treatments to produce the same effect (2 % cell survival). The shoulders in the survival curve indicate the tissue repair and repopulation after each fraction. Adapted from [Withers 1975].

As described in Section 1.2.4.3, recent evidence suggests the influence of the immune system on treatment outcomes. Preclinical data suggest an increased anti-tumor immune response in hypo-fractionated treatments, with an optimal dose per fraction of 10 to 13 Gy [Poleszczuk & Enderling 2018]. A deeper understanding of the influence of temporal fractionation on the immune response is needed to optimize RT treatments, and their combination with immune therapy [Arnold *et al.* 2018].

*Previous sections have presented the main radiobiological considerations in conventional RT modalities and fractionation regimes. However, other effects may contribute to tissue responses in RT techniques involving non-conventional treatment parameters. The following two sections present two of these effects: dose-volume and non-targeted effects.*

#### 1.2.4.5 Dose-volume effects

Dose-volume effects, firstly observed by Zeeman and Curtis [Curtis 1967, Zeman *et al.* 1959, Zeman *et al.* 1961], refer to the relationship between the quantity of volume irradiated and the overall tissue response. In particular, normal tissue tolerance dose increases as the volume exposed to radiation decreases [Hopewell *et al.* 1986, Hopewell *et al.* 1987, van der Kogel 1993] (see Figure 1.19). For instance, decreasing the diameter of the radiation field from 22.5 to 5 mm leads to an increase of more than 50 Gy in the tolerance dose for skin moist desquamation [Hopewell & Trott 2000]. The decrease in the radiation-induced damage increases sharply below a specific irradiated area. Above this threshold, which differs for

different tissues, the tolerance dose seems to be independent of the volume exposed to radiation.

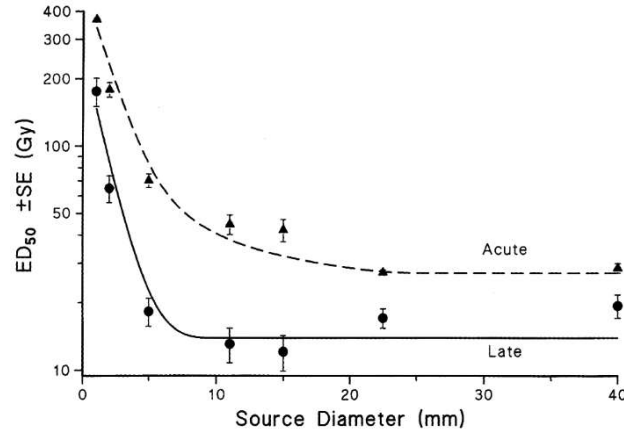


**Figure 1.19:** Tolerance dose, defined as the dose that produces a 50 % probability of acute and late skin damage (isoeffective dose ( $ED_{50}$ )), as a function of the field size (irradiated area). Adapted from [Withers 1975].

The radiobiological mechanism underlying this effect was hypothesized to be the migration of non-irradiated or surviving stem cells from the margins of the irradiated volume to the exposed tissue. These cells assist in repairing and repopulating damaged tissues [Hopewell & Trott 2000]. Thus, the relevance of the dose-volume effect might depend on the presence of stem cells in different tissues. In addition, the increased tolerance depends on the dose received by those cells at the margins of the high-dose volumes, i.e., the sub-tolerance dose bath (low doses within a large normal tissue volume) influences the dose-volume effect [Bijl *et al.* 2003]. The type of tissue organization also determines the dose-volume effect in organs. Parallel organs may benefit from the dose-volume effect, while in serial organs, it may be masked and have a reduced impact on the organ viability.

#### 1.2.4.6 Non-targeted effects

As described previously, cell responses, such as DNA damage or cell death, may be produced by the direct interaction of radiation and cell structures, i.e., the so-called targeted effects (TE). However, non-irradiated cells can also be affected by the irradiation of other cells. The cellular responses not directly associated with DNA damage are the non-DNA-targeted effects (NTE) of radiation. Contrarily to TE, the dose-response of NTE is not linear, having a higher impact at low doses [Mothersill & Seymour 2022]. NTE includes genomic instability, bystander effects, abscopal effects, and cohort effects [Desouky *et al.* 2015].

The radiation-induced genomic instability refers to the appearance of radiation-induced chromosome aberrations in daughter cells due to the irradiation of their progenitors, causing the development of radiation-induced cancers. This phenomenon can also be observed in different generations, where genomic mutations

are caused by the exposure to radiation of parents [Kadhim *et al.* 2013].

Radiation-induced bystander effects are defined as the cellular response of unexposed cells due to the irradiation of neighbor cells [Desouky *et al.* 2015]. A wide variety of bystander responses have been observed, such as DNA damage, mutations, chromosome aberrations, cell death, or differentiation. The mechanism underlying bystander effects is the intracellular communication produced by cell-to-cell contact or by soluble factors released into the culture medium. In addition, other agents released by irradiated cells, such as proteins or ROS, may mediate these effects [Mothersill *et al.* 2018]. Some studies suggest an increased bystander response to high-LET radiation as compared to low-LET particles [Asur *et al.* 2012].

The abscopal effect refers to responses of tissues distant from the irradiated volume, e.g., the tumor regression of distant metastases after irradiation of the primary tumor mass. This phenomenon is hypothesized to be mediated by cytokines and chemokines that regulate the differentiation of immune cells and invasion of the tumor microenvironment [Craig *et al.* 2021]. Abscopal effects are rarely observed and mainly occur at high doses per fraction ( $> 5$  Gy) [Joiner & van der Kogel 2018], e.g., in local hypofractionated RT.

Finally, cohort effects are the overresponse of irradiated cells, i.e., cells exposed to low doses present biological effects associated with higher doses. It results in a reduction in neighbor cells' survival within the irradiated volume. Cell communication mediated by signals produced by irradiated cells is responsible for this phenomenon. This effect is commonly observed in irradiated volumes with a non-uniform dose distribution [Wang *et al.* 2018], and it is likely to be relevant in spatially fractionated radiotherapy.

*As described in the previous sections, tissues may respond differently to radiation depending on several factors. Thus, biological responses need to be described and quantified by dedicated models and quantities. The next section presents the main models and quantities employed to characterize the radiobiological effects in RT.*

#### 1.2.4.7 Radiobiological modeling and dosimetric quantities

The characterization and quantification of tissues' responses to radiation exposure are essential in RT to compare different treatment regimes, modalities, and dose distributions.

*This section presents the main radiobiological models and quantities commonly used in RT to describe the (iso)effects of radiation on tissues: the relative biological effectiveness (RBE), linear-quadratic (LQ) model, biologically effective dose (BED), equivalent total dose (EQD) and equivalent uniform dose (EUD).*

### Relative biological effectiveness

The relative biological effectiveness (RBE) is a measure of how different radiation qualities (type and energy) lead to distinct biological damages. As described in Section 1.2.4.3, the energy deposition pattern of different particles influences the complexity of DNA damage. For instance, high-LET radiation creates more clustered damage to the DNA than low-LET particles, resulting in higher rates of cell death. Consequently, the dose required to cause the same biological damage is lower with high-LET than with low-LET particles. RBE is defined as the ratio of the dose required to produce a given biological effect by a reference radiation type ( $^{60}\text{Co}$   $\gamma$ -rays) and the dose to produce the same effect with the radiation under consideration [Podgorsak *et al.* 2005]:

$$RBE_{\text{test radiation}} = \frac{\text{dose from reference radiation to produce a biological endpoint}}{\text{dose from test radiation to produce a biological endpoint}}. \quad (1.8)$$

When the radiation considered differs from the reference one, the dose is usually prescribed as Gy[RBE] [ICRU 2007]. This notation indicates that, for example, a dose of 2 Gy deposited by megavoltage photons (reference radiation) corresponds to 1 Gy[RBE] of a particle with a RBE of 2.

As a general rule, RBE increases with LET from 1 up to a maximum of 3 to 8 when the LET reaches 200 keV/ $\mu\text{m}$  (see Figure 1.20). For higher LET values, RBE decreases due to an overkill effect, i.e., the radiation deposits in a cell more energy than the required to produce the cell death, leading to a decreased biological effectiveness per unit dose. RBE increases significantly from 10 keV/ $\mu\text{m}$ , which is the value used to divide low- and high-LET radiation. Generally, the optimum LET for cell killing is around 100 keV/ $\mu\text{m}$  [Joiner & van der Kogel 2018].

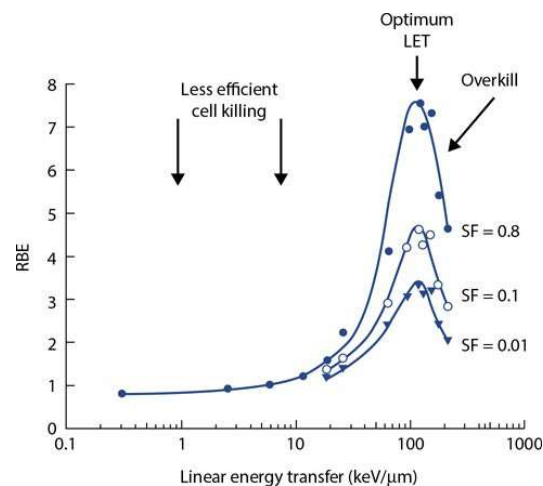


**Figure 1.20:** RBE-LET relationship at different cell surviving fractions (SF). Taken from [Joiner & van der Kogel 2018].

Besides the type of radiation and biological endpoint, RBE may depend on several other factors, such as the tissue oxygenation [Lee *et al.* 2008], tissue type

[Paganetti *et al.* 2000], fractionation regime [Gueulette *et al.* 2001] and particle energy [Wambersie 1999].

### Linear-quadratic model and survival curve

The linear-quadratic (LQ) model describes the cell death caused by radiation [McMahon 2018]. It considers non-repairable DNA damage created by large ionizing events (called single-hit damage or  $\alpha$  term) and cell killing by accumulation of repairable lesions (called multi-hit damage or  $\beta$  term). The  $\alpha$  and  $\beta$  terms can be considered radiosensitivity coefficients related to these two types of damage. In the LQ model, the probability of cell survival,  $S$ , after exposure to  $n$  fractions of dose  $d$  (total dose  $D = nd$ ) is defined as:

$$S = e^{-\alpha D - \beta D^2} = (e^{-\alpha d - \beta d^2})^n = e^{-D(\alpha + \beta d)}. \quad (1.9)$$

When this relationship is plotted on a logarithmic scale as a function of the dose, the survival rate shows a quadratic response curve (see Figure 1.21). This representation is called the survival curve. The  $\alpha$  component refers to the initial slope of the curve, while the  $\beta$  component refers to its bendiness [Symonds *et al.* 2012].

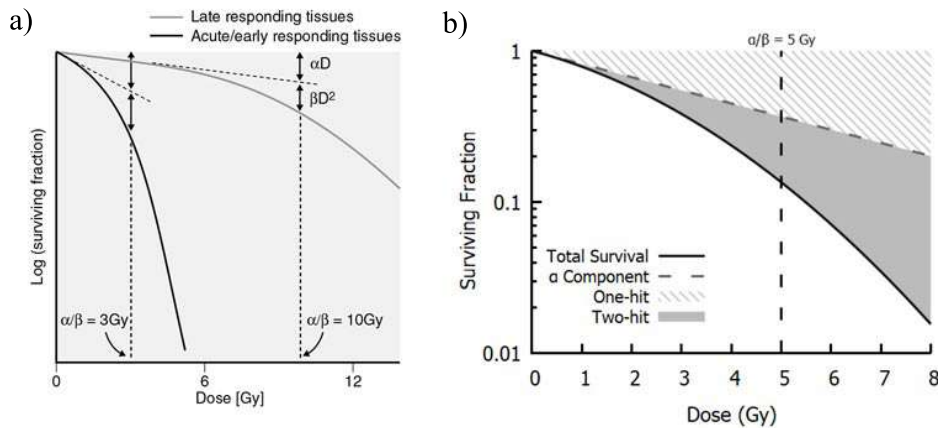


**Figure 1.21:** (a) Dose-response of early and late responding tissues and (b) representation of the contribution of single-hit and multi-hit events to cell death. Taken from [Symonds *et al.* 2012] and adapted from [McMahon 2018], respectively

The value of the ratio between  $\alpha$  and  $\beta$  coefficients, which is the dose at which both components contribute equally to cell killing [McMahon 2018], depends on whether the tissues are early or late responding to radiation. Late-responding tissues have a low  $\alpha/\beta$  (around 3), while early-responding tissues exhibit a high  $\alpha/\beta$  (around 10). Therefore, this ratio may be considered a measure of the sensibility of tissues to fractionation. Low  $\alpha/\beta$  tissues are more sensitive to the temporal dose fractionation than tissues exhibiting high  $\alpha/\beta$ . In general, normal tissues have a low  $\alpha/\beta$  (except for a few tissues such as the spinal cord), and tumors have a high  $\alpha/\beta$  (except for prostate and breast tumors).

The LQ model is widely used in conventional RT due to its simplicity and proven efficacy in conventional techniques and regimes. It enables adjusting the fractionation schedules to obtain a relative level of cell killing in different populations [McMahon 2018]. However, it does not consider the different biological responses of tissues to radiation, but only the effects of DNA damage (clonogenic cell death). Tissue responses to radiation may also be modulated by stromal and vascular effects, immune-system activation, and cell-to-cell signaling effects. Therefore, the clinical use of this model may not be adequate for non-conventional dose delivery techniques or fractionation schemes (e.g., hypofractionated treatments), where these radiation responses play a relevant role [McMahon 2018]. In conventional RT, the range of applicability of this model, in terms of dose per fraction, is from 2 to 18 Gy [Brenner 2008]. In addition, the LQ model only describes the response of a specific cell population state, for example, an asynchronous cell population within the cell cycle. In extreme cases where the radiosensitivity of a cell population is modified, survival curves may differ from the predicted by the model. Although it was a mechanistic model in its earliest applications, due to the lack of consideration of the underlying mechanism of tissue responses to radiation, it has become a phenomenological model due to a good fit to experimental data in conventional fractionation regimes [McMahon 2018].

### Biological effective dose

The biologically effective dose (BED) measures the biological response to a given temporal fractionation scheme. BED is the dose delivered with a given fractionation scheme that causes the same biological endpoint (e.g., cell kill or organ failure) as another fractionation schedule. It is based on the LQ model, i.e., it is directly related to cell survival caused by DNA damage [Fowler 1989]. It can be calculated as follows:

$$BED = n d \left(1 + \frac{d}{\alpha/\beta}\right), \quad (1.10)$$

where  $n$  is the number of fractions,  $d$  is the dose per fraction, and  $\alpha/\beta$  is defined in the previous section.

### Equivalent total dose

The equivalent total dose (EQD) or normalized total dose (NTD) refers to the dose given in 2-Gy fractions that leads to the same biological endpoint of a given fractionation schedule [Flickinger & Kalend 1990]. It is also derived from the LQ model. NTD is calculated as:

$$NTD_{2.0} = n d \left(1 + \frac{d}{\alpha/\beta}\right) \left(1 + \frac{2 \text{ Gy}}{\alpha/\beta}\right)^{-1}, \quad (1.11)$$

where  $n$  is the number of fractions,  $d$  is the dose per fraction, and  $\alpha/\beta$  is defined in the previous section.

### Equivalent uniform dose

The equivalent uniform dose (EUD) is a concept, based on the LQ model, that considers non-uniform distributions within a target volume. EUD is defined as the biologically equivalent dose that, if delivered uniformly, leads to the same biological effect, in terms of cell killing, as a given non-uniform dose distribution [Niemierko 1997].

### Other models

Biological quantities and models presented in this section are based on the assumption that biological effects of radiation mainly depend on the DNA damage and repair. Also, they are mainly derived from in-vitro data. Therefore, they do not consider the impact of the tumor microenvironment on tissue responses [Boustani *et al.* 2019]. Other models that include responses from non-targeted effects have been proposed. For instance, Serre *et al.* [Serre *et al.* 2018] introduced the concept of immunologically effective dose (IED). This quantity characterizes the intrinsic immunogenicity of radiotherapy schedules. IED is defined as the dose that, given an infinitely low dose rate, leads to the same abscopal effect as the fractionation regime under consideration. IED can be considered an extension of the classical BED formula, including a time-dimensional term that describes the immune response to RT.

*Further to the radiobiological models that characterize tissue responses to radiation, models to quantify the effectiveness of complete treatments have been proposed. The following section describes two quantities that evaluate the two main goals of RT, i.e., the maximization of tumor control and the minimization of radiation-induced side effects on normal tissues.*

#### 1.2.5 Tumor control probability and normal tissue complication probability

The fundamental goal of RT is to deliver a dose high enough to eradicate the malignant tumor while minimizing the damage to normal tissues. These two objectives can be assessed individually by the tumor control probability (TCP) and normal tissue complication probability (NTCP). TCP refers to the probability of eradicating the tumor cells at a given dose, and the NTCP is based on tolerance doses of tissues and the probability of developing a specific side effect. Therefore, both depend on the individual tissue radiosensitivity. TCP and NTCP exhibit a sigmoid dependence with dose (see Figure 1.22) [Chang *et al.* 2014].

As illustrated in Figure 1.22, high doses lead to a high TCP but also a considerable increase in the NTCP. Contrarily, at low doses, sparing of normal tissues is expected, but tumor control is not likely to be achieved. Since the increase in TCP occurs at lower doses than in NTCP for most tumor types, a range of intermediate doses may exhibit a high TCP and relatively low NTCP.

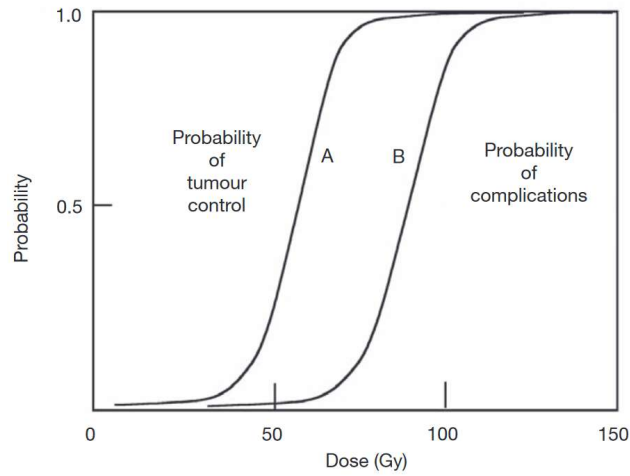


**Figure 1.22:** Example of TCP (curve A) and NTCP (curve B) in a RT treatment. Taken from [Podgorsak *et al.* 2005].

This dose range, where the probability of uncomplicated cure is maximized, is called the therapeutic window. The larger the window is, the safest the treatment. The therapeutic index (TI), or therapeutic ratio (TR), quantifies the size of the therapeutic window. Several methodologies to calculate the TI have been proposed:

$$TI = TCP \times (1 - NTCP), \quad (1.12)$$

at a given dose, or

$$TI = \frac{50\% \text{ probability of a given complication}}{50\% \text{ probability of tumor control}}, \quad (1.13)$$

The TI depends on the definition of complication (i.e., the acceptable level of toxicity), RT technique (i.e., dose rate, LET and precision), the treatment plan, and the state of the patient [Podgorsak *et al.* 2005].

*Prior to delivering RT treatments, a treatment planning process for each patient is necessary. In this procedure, the objective is the maximization of the therapeutic index. The steps of the treatment planning process in EBRT are detailed in the next section.*

### 1.2.6 Treatment planning in EBRT

The delivery of RT treatments is preceded by a process of treatment planning (TP). Computer systems, called treatment planning systems (TPS), are commonly used in clinical practice to perform the different steps of the TP process. The stages of the TP process in EBRT are described hereafter.

## 1. Imaging and volume delineation

The first step in the TP process involves the acquisition of images for various purposes: (i) the delineation of targets and organs involved in the treatment by using MRI, PET, or CBCT techniques, and (ii) the dose calculation, which requires the use of CT data containing the information about the physical characteristics of tissues [Chang *et al.* 2014]. Imaging must be performed in the patient's position during treatment and include all the components present in the dose delivery (e.g., immobilization devices).

The target volume delineation involves several steps. The ICRU [ICRU 1999] defines different tumor, target, and planning volumes. The gross tumor volume (GTV) is the visible tumor, i.e., tumor mass visible on imaging. The clinical target volume (CTV) consists of the GTV plus an additional region to account for the microscopic spread of tumor cells outside the GTV. This margin depends on the degree of infiltration of each tumor. The internal target volume (ITV) accounts for the motion of tumors or other anatomical variations during dose delivery. Then, the ITV is defined as the CTV plus a margin, which is determined by the predicted internal motion depending on the tumor's location. The planning target volume (PTV) is the prescription volume, i.e., it is the volume that must receive the prescribed dose. It consists of the ITV plus a margin to account for setup uncertainties in the patient positioning during treatment. GTV and CTV are oncological concepts independent of the treatment modality, while ITV and PTV depend on the treatment characteristics. Figure 1.23 presents a schematic representation of these volumes.

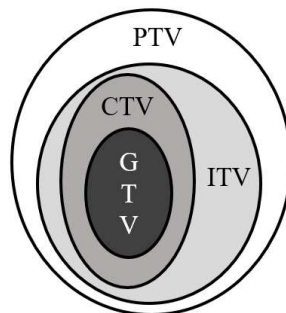


**Figure 1.23:** Schematic representation of the volumes considered for target delineation.

Finally, organs-at-risk (OAR), defined as organs in or near the PTV, are also delineated by considering a planning risk volume (PRV) to compensate for the effects of movement and setup uncertainties.

## 2. Dose prescription and definition of OAR constraints

The selection of treatment modality, dose prescription, and fractionation scheme

depends upon the tumor type, size and location, and patient condition. This choice is based on published reports, recommendations by ICRU, and clinical studies. ICRU reports recommend different methodologies to prescribe treatments depending on the treatment modality [ICRU 2004, ICRU 2007, ICRU 2010, ICRU 2019], such as a maximum level of heterogeneity within the PTV (e.g. + 7 % to - 5 %) or the dose that a percentage of the PTV must receive (e.g.,  $D_{95\%} > 54 \text{ Gy}$  indicates that at least 95 % of the PTV must receive 54 Gy).

At this step, the dose-volume constraints to OAR are also specified. Usual dose constraints for serial organs are a maximum dose to any point or to small volumes (e.g., the brain stem should receive less than 64 Gy to any point, and the dose to volumes of up to 10 cc should not exceed 59 Gy [Emami 2013]). The limiting factors for parallel organs are typically a maximum mean dose or a proportion of tissue receiving a given dose (e.g., more than 1500 cc of the lung should receive less than 7 Gy [Emami 2013]). Such tolerances are also determined by the level of toxicity acceptable for each specific case (i.e., the acceptable frequency of expected complications) and the organ and patient condition.

### 3. Optimization of treatment plans and dose calculation

Treatment plans can be optimized by using two different techniques, forward or inverse planning [Pawlicki *et al.* 2016]. Forward planning involves the selection of the number and angle of beams depending on the patient geometry and PTV and OAR location. Then, the dose is calculated, and, depending on the dose distributions obtained, the planner virtually modifies the treatment plan to meet the plan objectives. Common modifications involve the arrangement, weighting, and fluence of the beam. This treatment plan strategy is used mainly for 3D conformal RT. Contrarily, inverse planning is an automated method. Firstly, the planner chooses the number and angle of the beams and sets the plan objectives and constraints. The TPS iteratively adjusts the weight of the beam segments until the plan meets the objectives. Then, dose distributions are calculated using the result of the optimization. This technique is used in IMRT, SRT, and PT.

TPSs use different algorithms for dose calculations. Calculation algorithms are typically analytical. A detailed description of these models can be found in the literature [Paganetti 2018, Symonds *et al.* 2012]. Monte Carlo-based algorithms, described in detail in Chapter 2 of this thesis, have also been implemented into some TPSs recently.

TPSs also use CT data as an input for the simulation of radiation interaction with matter since it contains physical information (e.g., the density of anatomical tissues). CT images consist of gray values (commonly expressed as Hounsfield units or CT numbers) that correlate to the physical density, attenuation coefficient (for photon therapy), or relative stopping power (for charged particle therapy) of body tissues. This relation is typically expressed as a CT calibration curve.

#### 4. Evaluation of dose distributions

Finally, dose distributions are evaluated. A standard methodology is to condense the large amount of 3D data calculated by TPSs into a 2D graph that presents the dose distribution within a given volume. These graphs are called dose-volume histograms (DVH), and they represent the volume receiving a certain dose against a set of equally spaced dose intervals [Symonds *et al.* 2012]. Then, it is straightforward to assess the dose uniformity within the target volume, the presence of hot or cold spots (high and low dose areas, respectively), and other quantities of interest, such as the dose received by a percentage of organ volume ( $D_{V\%}$ ) or the volume receiving a given dose ( $V_D$ ). In addition, dose distributions from different plans can be compared easily. However, this method has some limitations, such as the dose-volume matrix resolution, which may mask the regions of high dose gradient. DVHs are usually used in combination with other evaluation tools, such as isodose curves or dose statistics [Symonds *et al.* 2012], which can be found in the ICRU reports for each RT modality.

*Previous sections present a general overview of RT treatments. Due to the central role of proton therapy in this thesis, the following chapter provides a more detailed description of the distinct physical, technical, radiobiological, and clinical aspects of this technique.*

### 1.3 Proton therapy

The use of proton beams for treating cancer has evolved and increased substantially since its conception by Wilson in 1946 [Wilson *et al.* 1946]. Nowadays, proton therapy (PT) is a well-established modality for treating several tumor types (see Section 1.3.4). According to the Particle Therapy Co-Operative Group (PTCOG), in 2022, 101 facilities were in operation [PTCOG 2022b], 31 under construction [PTCOG 2022c], and more than 30 in the planning stage [PTCOG 2022a].

The rationale behind using fast protons for treating deep-seated targets is their finite range and the improved dose conformity to the target [Suit *et al.* 1975]. These more favorable dose distributions lead to relevant clinical implications, such as the sparing of normal tissues. The sections below describe the physical characteristics of dose distributions created by proton beams, the technical aspects of their generation, the mechanisms that underlay their radiobiological effect, and their clinical use.

#### 1.3.1 Physical aspects

As briefly described in Section 1.2.1.1, the main interactions of protons with matter are Coulomb interactions with atomic electrons, Coulomb scattering with nuclei, and inelastic collisions with nuclei. These three interaction mechanisms are responsible for the main features that characterize the dose distributions produced

by proton beams: the Bragg peak, range straggling, and lateral beam spread (see Table 1.2). Proton dose and LET distributions are described in more detail in the following subsections.

Interaction type	Interaction target	Principal ejectiles	Influence on projectile	Dosimetric manifestation
Inelastic Coulomb scattering	Atomic e-	Primary p+, ionization e-	Quasi-continuous energy loss	Determines range
Elastic Coulomb scattering	Atomic nucleus	Primary p+, recoil nucleus	Change in trajectory	Determines lateral penumbra sharpness
Non-elastic nuclear reactions	Atomic nucleus	Secondary ions, n, and $\gamma$ rays	Removal of p+ from beam	Primary fluence and generation of n and $\gamma$ rays
Bremsstrahlung	Atomic nucleus	Primary p+, photons	Energy loss, trajectory change	Negligible

**Table 1.2:** Summary of proton interactions, targets, secondary particles produced, influence on incident particles, and effect on dose distributions. p+, e-, and n stand for proton, electron, and neutron. Adapted from [Newhauser & Zhang 2015].

### 1.3.1.1 Depth-dose distributions and Bragg peak

Protons transfer most of their kinetic energy to an absorber medium by Coulomb interactions with atomic electrons (i.e., ionization and excitation). This energy transfer is characterized by the electronic mass stopping power, which can be described by the Bethe-Bloch formula [Bethe 1930, Bloch 1933]:

$$\frac{S}{\rho} = -\frac{dE}{\rho dx} = 4\pi N_A r_e^2 m_e c^2 \frac{Z z^2}{A \beta^2} \left[ \ln \frac{2m_e c^2 \gamma^2 \beta^2}{I} - \beta^2 - \frac{\delta}{2} - \frac{C}{Z} \right], \quad (1.14)$$

where  $N_A$  is the Avogadro's number,  $r_e$  and  $m_e$  are the electron radius and mass,  $z$  is the proton charge,  $Z$  and  $A$  the atomic number and weight of the material,  $c$  and  $v$  the speed of light and incident proton,  $\beta = v/c$ ,  $\gamma = (1 - \beta^2)^{-1/2}$ ,  $I$  the mean excitation potential of the material, and  $\delta$  and  $C$  correction factors [Newhauser & Zhang 2015].

The stopping power depends on the charge of the incident particle and the atomic number of the absorber material. Also, it increases as the kinetic energy (i.e., velocity) of charged particles decreases, with a  $v^{-2}$  dependency. Thus, the energy deposition (i.e., dose) increases in-depth as protons slow down, reaching a maximum at the end of their penetration depth. After this point, the dose decreases rapidly due to the steep reduction in the beam fluence, which is defined as the number of protons traversing a sphere of a given cross-sectional area. This reduction is caused by the complete stop of protons at the end of their range. At shallow depths, the beam fluence decreases monotonously due to the removal of protons from the beam by inelastic nuclear interactions [Newhauser & Zhang 2015]. Overall, the increase in the stopping power and decrease in the beam fluence produce a sharp dose increase followed by a rapid dose fall-off at the end of the proton range. This characteristic

dose depth profile is called the pristine Bragg peak (BP). Figure 1.24 illustrates the dose, fluence, and stopping power variation as a function of depth.

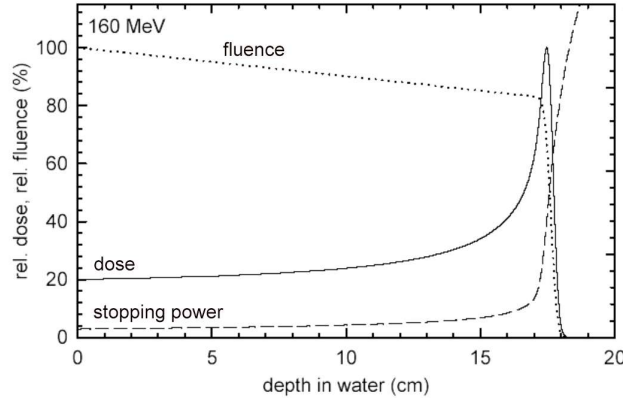


**Figure 1.24:** Relative dose (solid line), fluence (dotted line), and stopping power (dashed line) profiles in-depth in water for a 160 MeV proton beam. Adapted from [Garutti 2013].

A pristine BP typically denotes the BP produced by a monoenergetic beam. In the longitudinal direction, its width is of a few millimeters, much smaller than most tumors' diameter ( $> 1$  cm). Thus, a wider uniform dose region in the longitudinal direction must be created. This flat dose region, called spread-out Bragg peak (SOBP), is obtained by adding pristine BPs shifted in depth (i.e., shifted in energy) with a specific weight (see Figure 1.25a). The number of peaks determines the extension of the SOBP [Paganetti 2018]. As Figure 1.25b shows, the generation of the SOBP by the addition of pristine BP involves the increase in dose at shallow depths; the wider the SOBP, the larger the dose at proximal depths.

Depth-dose curves at the entrance of the absorber material exhibit a buildup region, described in Section 1.2.3. It is caused by the lack of charged particle equilibrium due to the forward emission of secondary electrons and protons, set in motion by incident protons [Paganetti 2018]. This buildup effect is relatively non-significant compared to the buildup region of photon beams.

### 1.3.1.2 Range straggling

As mentioned in Section 1.2.3, protons have a finite penetration depth inside an absorber material, called range. The proton range increases approximately with the square of the initial proton energy. For instance, 70 and 230 MeV beams have a range of 4 and 35 cm in water, respectively. Each proton of a monoenergetic beam has a slightly different range. This phenomenon is called range straggling. This effect is caused by (i) variations in the energy loss of individual protons due to the statistical fluctuations in the number of interactions that each proton undergoes and (ii) the initial energy of each proton of a "monoenergetic" beam may be slightly different due to acceleration and delivery methods. The range-straggling effect increases with the penetration in the material, i.e., the initial energy of the beam (see Figure 1.26). The dose spread at the end of the proton range (distal penumbra) and the width

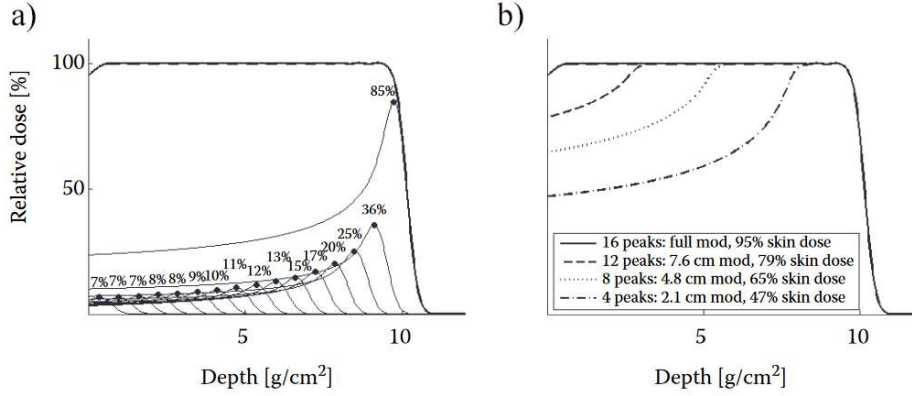


**Figure 1.25:** (a) Generation of the SOBP by adding pristine BP at different depths and weights, and (b) SOBP of different widths as a function of the number of pristine BP. Taken from [Paganetti 2018].

of pristine BPs are mainly determined by the range straggling [Paganetti 2018]. The width of the BP is typically defined as the distance between the depth at the proximal and distal 80 % of the maximum dose [Newhauser & Zhang 2015].

Due to the straggling effect, the range of a nearly-monoenergetic proton beam can be defined in several ways. The mean projected range is typically defined as the depth at which half of the protons traveling along its initial direction come to rest (i.e., the fluence is reduced by 50 %), or equivalently, the depth at the distal 80 % of the maximum dose [Paganetti 2018]. Another approach to defining the range is to assume that protons lose their energy continuously (continuous-slowing-down approximation, CSDA) and express the range as:

$$R_{CSDA} = \int_0^{E_0} \frac{dx}{dE} dE = \int_0^{v_0} \frac{dx}{dv} dv, \quad (1.15)$$

where  $E_0$  and  $v_0$  are the initial kinetic energy and speed of the proton. The CSDA range is usually expressed in g·cm<sup>-2</sup> due to the integration of the mass density in the stopping power. Differences between both definitions are lower than 0.13 % for clinical proton beam energies above 100 MeV [Grimes *et al.* 2017].

### 1.3.1.3 Lateral beam spread

As protons traverse a material, they are deflected by the repulsive force from the positive charge of atomic nuclei (Coulomb interactions with nuclei). These changes in the proton trajectory are typically modeled by combining the individual deflections into a single net angle. This combined effect is called multiple Coulomb scattering (MCS) and causes the lateral spread of the beam [Newhauser & Zhang 2015]. For practical purposes, the MCS angular distribution

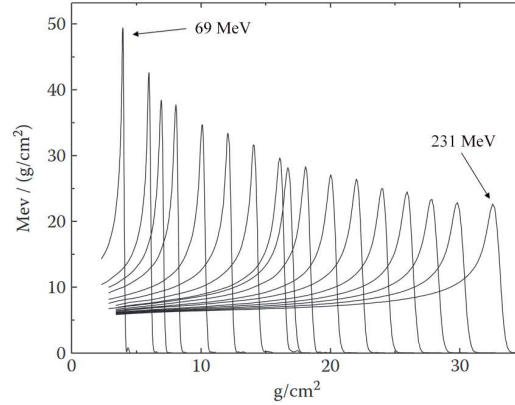


**Figure 1.26:** Range (in  $\text{g}\cdot\text{cm}^{-2}$ ) of a set of proton beams with incident energy from 69 to 231 MeV). Taken from [Paganetti 2018]).

of protons can be approximated by a single Gaussian with a standard deviation  $\theta_0$ :

$$\theta_0 = \frac{14.1 \text{ MeV}}{p v} \sqrt{\frac{L}{L_R}} \left[ 1 - \frac{1}{9} \log\left(\frac{L}{L_r}\right) \right] \text{ [rad]}, \quad (1.16)$$

where  $p$  and  $v$  are the momentum and speed of the incident proton,  $L$  is the target thickness, and  $L_R$  the radiation length of the absorber material. Lateral penumbras of protons beam are much sharper than MV photon beams [Paganetti 2018], which is often beneficial since a sharp lateral penumbra is essential for sparing critical organs adjacent to the target volume. The lateral spread (or penumbra) increases in depth as protons slow down (see Figure 1.27). In addition, the beam widening is more significant as the initial beam energy and the atomic number of the absorber material increase.

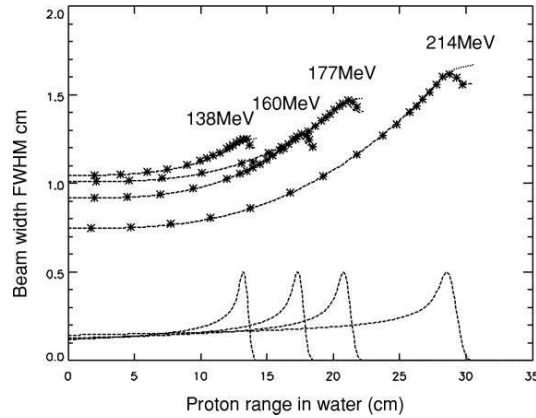


**Figure 1.27:** Evolution of the beam width as a function of depth and beam energy. FWHM states for full-width at half maximum. Adapted from [Pedroni *et al.* 2005].

Besides the lateral dose spread caused by MCS, the products of nuclear interactions along the beam range produce a dose beam halo around the primary beam path [Pedroni *et al.* 2005]. This halo is a broad region of very low doses.

### 1.3.1.4 LET distributions

The LET of a proton beam is calculated by averaging LET values of all the individual protons (see Section 1.2.1.2). The LET increases from around  $1 \text{ keV}/\mu\text{m}$ , at the entrance, to  $8\text{--}12 \text{ keV}/\mu\text{m}$ , at the end of the proton range (see Figure 1.28) [Grassberger *et al.* 2011]. This increment is caused by the increased rate of energy transfer as protons slow down. Secondary particles produced by primary protons may also contribute to the total LET distribution [Grassberger *et al.* 2011], as shown in Figure 1.28. The LET of a proton beam increases even beyond the BP. This phenomenon is produced because only protons at very low energies (high LET) contribute to the LET at distal depths.

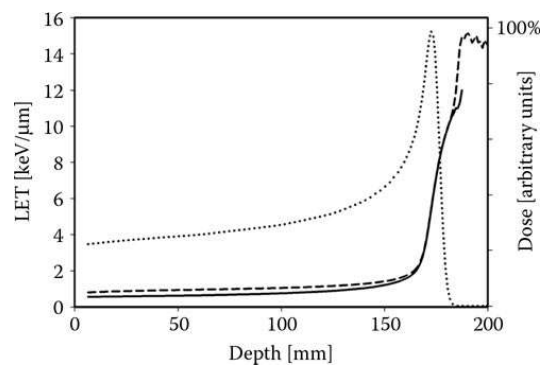


**Figure 1.28:** Dose (dotted line) and total dose-averaged LET (dashed line) and dose-averaged LET for primary protons only (solid line). Taken from [Paganetti 2018].

## 1.3.2 Technical aspects

Proton beams of clinical energies cannot be accelerated and delivered by systems used to produce clinical electron beams (i.e., conventional LINACs) due to their higher mass. The production and delivery of clinical proton beams require dedicated acceleration and delivery techniques. Such methods are presented in the following subsections.

### 1.3.2.1 Particle accelerators

Two types of particle accelerators are typically used in the context of proton therapy: cyclotrons and synchrotrons. Other methods have also been proposed, such as proton LINACs or laser-driven accelerators [Schippers *et al.* 2018], but they are not yet clinically available.

#### Cyclotrons

Cyclotrons consist of five major components: a radiofrequency (RF) system, two or four electrodes, a magnet, a proton source, and an extraction system (see Figure 1.29) [Paganetti 2018]. Electrodes (also called Dees) are separated by a

certain distance and connected to a voltage generated by a RF system, which changes its polarity with a fixed frequency of 50 to 100 MHz. The Dees are made of highly conductive metal; thus, the electric field within them is nil. These electrodes are placed between two electromagnets, which generate a homogeneous magnetic field. The ion source is at the center of the cyclotron and produces protons by ionizing hydrogen gas.

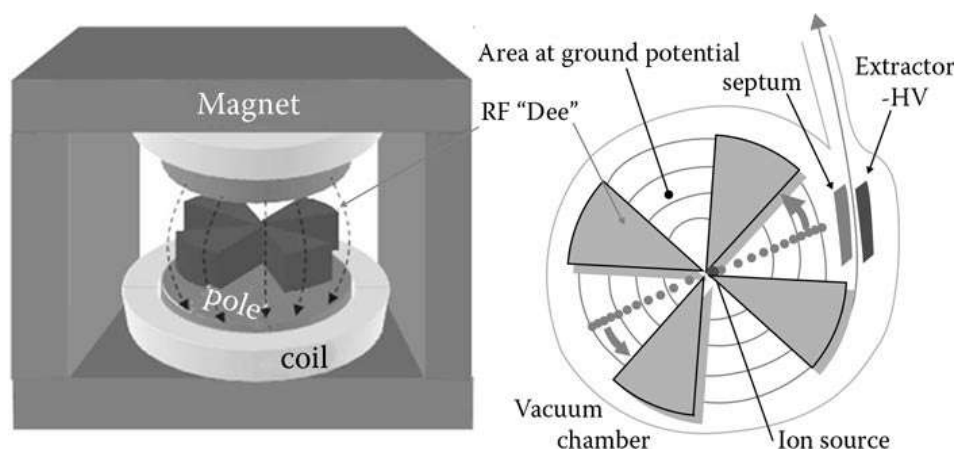


**Figure 1.29:** Schematic representation of a cyclotron. Taken from [Paganetti 2018].

Protons are accelerated every time they cross the gap between electrodes due to the voltage difference. When they traverse the electrode (region free of an electric field), the polarity of the applied electric field changes, so protons continue being accelerated within the gap between that Dee and the following one. Due to the magnetic field inside the electrodes, protons describe a circular orbit (Lorentz force), whose radius increases with the particle's kinetic energy. When the orbit radius reaches the edge of the magnet, protons are extracted by an extractor system.

The main characteristic and advantages of cyclotrons are that they operate at a constant frequency and magnetic field and can create a continuous and high-intensity beams. However, cyclotrons can only produce beams of fixed energy since protons are only extracted when they reach a given orbit (i.e., energy). Also, this system can only accelerate protons up to 230 to 250 MeV [Paganetti 2018]. Above this energy, the mass of protons increases significantly due to relativistic effects, and the orbit frequency would change with energy; then, protons would not be further accelerated in fixed frequency and magnetic field conditions. Other approaches, such as modifying the magnetic field (isochronous cyclotrons) or the frequency (synchrocyclotrons) as a function of the energy, may be adopted to reach larger proton energies. Most clinical centers nowadays employ standard cyclotrons.

The strength of the magnetic field determines the size and weight of cyclotrons since as the magnetic field increases, the orbit radius of the proton's trajectories decreases. The diameter of most commercially available cyclotrons is between 3.5 m (100 tons) and 5 m (200 tons), and their magnetic field strength is 2 to 3.5 T [Paganetti 2018].

### Synchrotrons

Synchrotrons consist of a ring-like evacuated tube that contains several RF cavities, bending (dipole) and focusing (quadrupole or sextupole) magnets, and a proton injector (see Figure 1.30a) [Paganetti 2018].

Synchrotrons operate with varying magnetic fields and frequencies. The RF cavities accelerate protons within the ring, and the swapping voltage frequency of the cavities is modified as a function of the proton energy. Then, protons can be accelerated at energies higher than 250 MeV, unlike cyclotrons. As particles are accelerated, the strength of the magnetic field increases to keep the radius of the orbit approximately constant. Overall, the operation of synchrotrons consists of the injection of low-energy protons (2 to 7 MeV) into the ring, their acceleration, their extraction, and the deceleration of the non-extracted protons by restoring the initial configuration of the magnets (see Figure 1.30b).

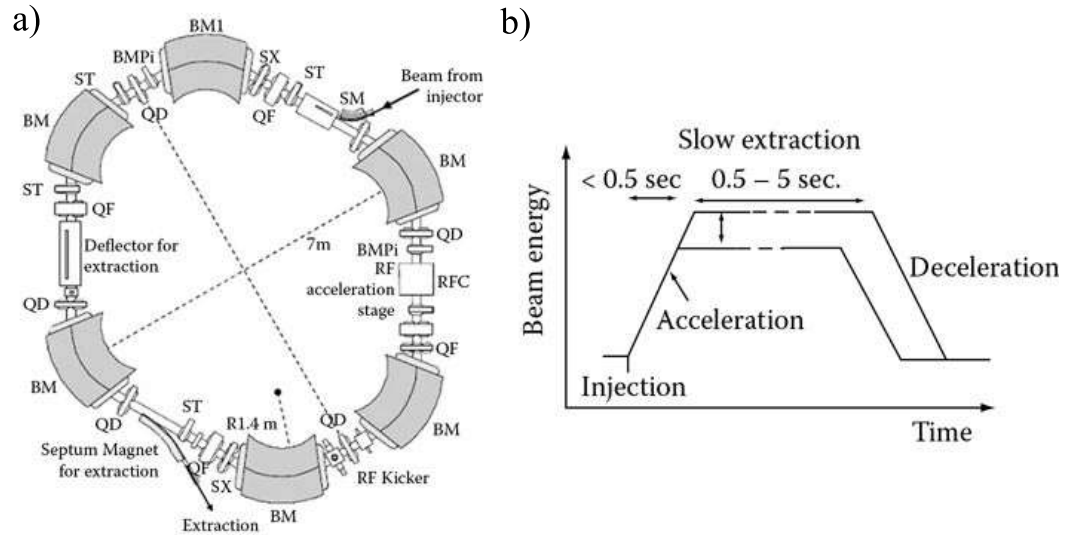


**Figure 1.30:** Schematic representation of (a) a synchrotron and (b) its operating mode.

BM: bending magnet, BMPi: bump magnet for injection, QF: quadrupole focusing magnet, QD: quadrupole defocusing magnet, RFC: radiofrequency cavity, ST: steering magnet, SX: sextupole magnet. Taken from [Paganetti 2018].

The main advantage of synchrotrons, compared to cyclotrons, is that they can produce proton beams of variable energy (even above 250 MeV). However, the synchrotrons cannot produce continuous beams since the magnetic field variation is only effective at one point in the acceleration process, i.e., for protons with a specific energy. Thus, protons are accelerated and extracted by pulses of up to 7 seconds [Paganetti 2018].

### 1.3.2.2 Beam delivery systems

After the acceleration, proton beams are transported to the treatment room through a system consisting of a series of dipole and quadrupole magnets, components to monitor the characteristics of the beam, and energy selection system (ESS). ESSs mainly consist of a graphite degrader in the form of wedges or wheel blocks of different thicknesses. These degraders scatter and attenuate the beam to modulate its energy and intensity according to the treatment requirement. ESSs are used when proton beams are accelerated using a cyclotron since cyclotrons can only produce beams at a fixed energy [Qin *et al.* 2021].

In the treatment room, the beam direction is modified by the gantry. Gantries are rotating transport lines. They are composed of a mechanical structure that allows the gantry arm to rotate  $360^\circ$  in a horizontal plane, dipole and quadrupole magnets to bend and focus the beam, and other beamline components (e.g., correctors or beam diagnostic systems). Gantries focus and direct proton beams from the desired direction onto a point in the treatment room (i.e., the patient). The gantry rotation plus the rotation of the patient table support allow complete geometrical flexibility during treatments. Figure 1.31 illustrates the main components and dimensions of a gantry.

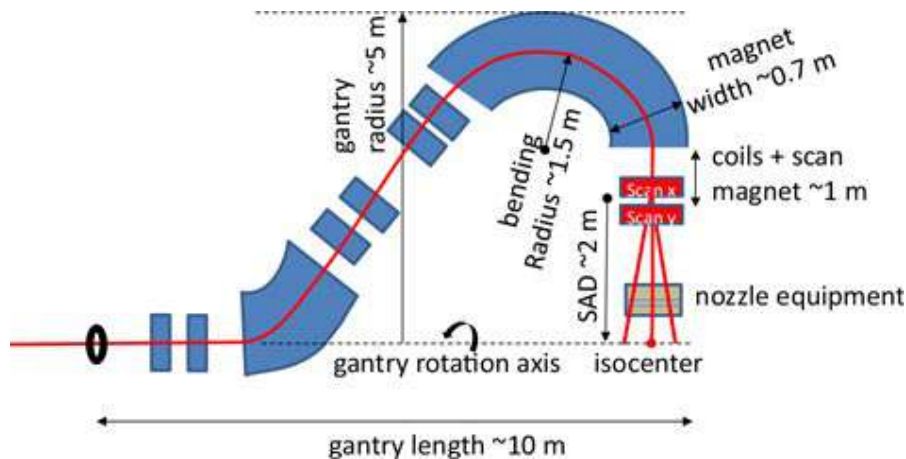


**Figure 1.31:** Schematic representation of a gantry and its dimensions. Taken from [Schippers *et al.* 2018].

Gantries can be built in different configurations in terms of their topology (isocentric, excentric or exocentric gantries) and position of scanning magnets (upstream or downstream scanning gantries) [Schippers *et al.* 2018]. Isocentric downstream-scanning gantries are the standard layout in radiotherapy; the nozzle always points at a fixed position in the treatment room (isocenter), and scanning magnets are located downstream of the nozzle. The treatment head (or nozzle) is the final part of the proton beamline. It contains several components that monitor and shape the beam to obtain the required beam parameters before being delivered to the patient. For instance, several (typically two) ionization chambers are placed along the beamline in the nozzle to provide information about the size, position,

and intensity of the beam. Some gantry and nozzle designs also include devices for in-room CBCT imaging [Landry & Hua 2018]. There are two main types of nozzles dedicated to the different delivery techniques: passive scattering and dynamic spot scanning [Ma & Lomax 2012]. These delivery techniques are described in the following section. Nozzles that allow using both modes are called universal nozzles [Paganetti 2018]. The part of the nozzle closest to the patient is called the snout, and it is where additional components to modify the beam are placed.

Beam transport systems in gantries are optimized for a specific range of proton beam energies. The minimum deliverable energy from a clinical facility is 70 to 100 MeV (which corresponds to a range of 4 to 8 cm in water). Thus, the treatment of targets at shallower depths may require using a range shifter (RS). A RS is a block of low-Z material inserted into the beam path (in the snout), which reduces the beam's energy at the patient surface and brings the BP to shallower depths (see Figure 1.32). The use of RSs increases the beam's scattering, i.e., the spot size, divergence, and lateral penumbra [Lin *et al.* 2021]. The effect of the RS on lateral beam size can be minimized by reducing the air gap between the RS and the patient [Lin *et al.* 2021] when possible (i.e., in pencil-beam scanning beamlines with a telescopic snout).

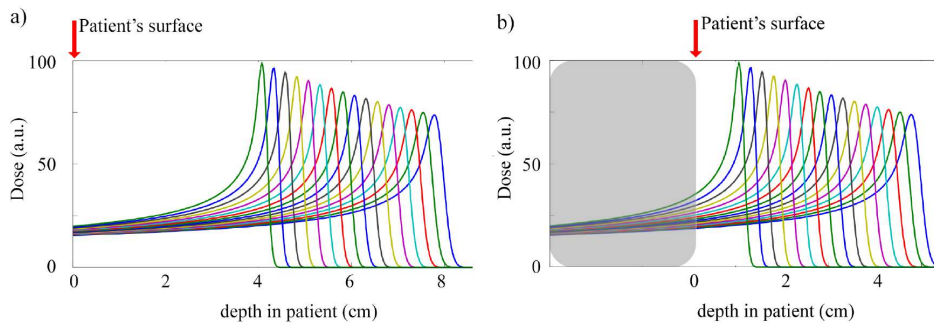


**Figure 1.32:** Representation of the depth in the patient of 70-100 MeV proton beams (a) without and (b) with a range shifter (represented by a grey rectangle).

### 1.3.2.3 Beam delivery techniques

As mentioned in the previous subsection, two main techniques are used for beam delivery in clinics: passive scattering and dynamic spot scanning. These two approaches and their advantages and drawbacks are described hereafter.

#### Passive scattering

The passive scattering (or passive spreading) technique involves spreading out the beam size to cover the target volume [Hang *et al.* 2010]. This is achieved by dispersing the beam in the lateral direction using high-Z scattering foils (typically two; double scattering) and in-depth by spreading the beam energy using a range modulation wheel. The range modulation involves adding pristine Bragg peaks at

different energies and weights to obtain an SOBP (see Section 1.3.1.1). The simplest method to spread the energy of a proton beam is to combine rotating wheels of different thicknesses to selectively modify the energy (i.e., range) according to the tumor thickness (see Figure 1.33a) [Paganetti 2018]. The shifting of the distal part of the SOBP to the target depth is achieved by a range shifter, which consists of several slabs of variable thickness that degrade the beam energy. Then, the beam is shaped to the target silhouette from each beam direction by apertures and brass collimators. Finally, a range compensator conforms the dose to the target in depth for each beam direction, accounting for patient surface curvature, inhomogeneity, and target depth (see Figure 1.33b). This effect is achieved by counterbalancing the depth variation by modifying the thickness of a low-Z absorbed material within the lateral beam distribution [Paganetti 2018]. Figure 1.33c shows a range compensator and a brass collimator, which are specific for each treatment field. Figure 1.34a illustrates a schematic representation of a passive scattering beamline.

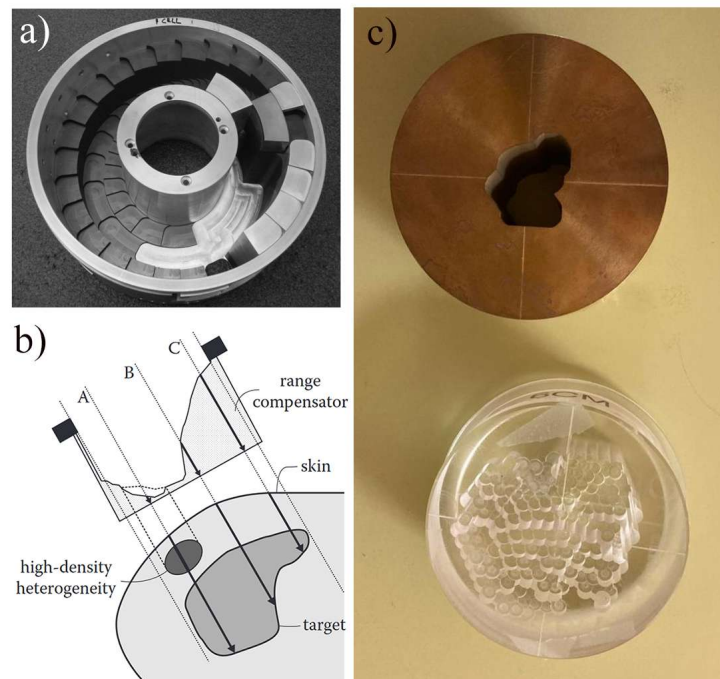


**Figure 1.33:** (a) Range modulator wheel composed of three different tracks and (b) a schematic representation of the principle of a range compensator. Taken from [Paganetti 2018]. (c) Range compensator (down) and brass collimator (top).

The main advantage of this technique is the delivery of dose to the entire target simultaneously, which minimizes the uncertainties in dose distributions for moving targets. Also, passive-scattering provides a sharp lateral dose fall-off due to the beam collimation. However, field-specific hardware (e.g., collimators and compensators) is needed for each treatment, which may be an additional source of neutron dose and imply individual manufacturing, increasing the difficulty of adapting treatments.

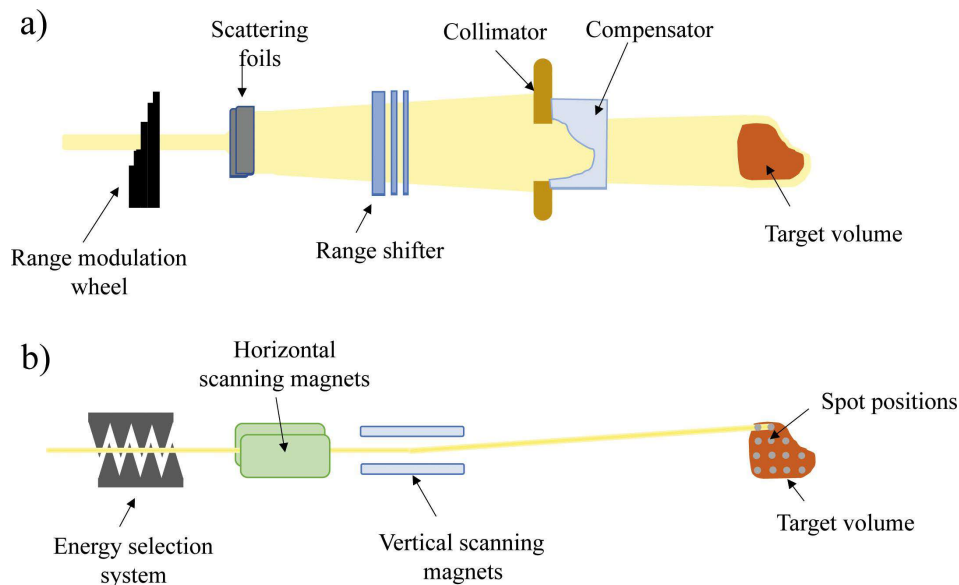


**Figure 1.34:** Schematic representation of a nozzle operating in (a) passive scattering and (b) active scanning mode.

### Dynamic beam scanning

The dynamic beam scanning (or active scanning) technique spreads the dose deposited to the target volume by moving the beam using scanning magnets. The most common form of active scanning in clinical practice is the so-called pencil beam scanning (PBS) mode, which involves scanning an unmodified beam (pencil beam). When produced by a cyclotron, the beam is degraded by ESSs (e.g., wedge-like beam degraders) to change its range and move the beam in the longitudinal direction within the patient. The horizontal and vertical movements are achieved by deflecting the proton beam with dipole magnets. Therefore, the target volume is typically scanned transversally in different iso-energy layers, from the deeper to the shallowest. In the PBS mode, the beam is switched off between each pencil beam position, and the intensity of each pencil beam is modified individually. PBS nozzles are simpler than scattering nozzles since they involve fewer hardware components (see Figure 1.34b) [Paganetti 2018].

The main benefits of PBS systems are the improved ability to conform the dose to the complex target geometries, the versatility to adapt treatments due to the lack of field-specific hardware, and the increased dose rate [Paganetti 2018]. However, treating moving targets may be challenging since the dose is delivered to a sub-volume of the target at a time, and the movement of the target may degrade dose distributions. In addition, the lateral penumbra is less sharp for shallow targets than when using the passive scattering technique [Safai *et al.* 2008].

### 1.3.3 Radiobiological aspects

Recent evidence indicates that protons lead to different biological responses from those observed in conventional X-ray techniques due to their distinct dose deposition pattern [Girdhani *et al.* 2013]. In addition to their ballistic advantages, proton irradiation (i) down-regulates the pro-angiogenic factors, inhibiting angiogenesis signaling, (ii) causes a reduction of inflammatory factors, and (iii) triggers an anti-invasion and anti-migratory behavior, leading to anti-metastatic responses, compared to low-LET photons. These responses may be a consequence of the distinct regulation of gene expression. Increased apoptotic cell death is observed at a cellular level after proton irradiation due to the activation of different apoptotic pathways. Proton beams also produce differential immune effects, compared to X-ray irradiations [Girdhani *et al.* 2013]. In addition, protons are more efficient in producing ROS, inducing oxidative stress cell death and increasing the inactivation of cancer stem cells [Tommasino & Durante 2015].

At the DNA level, different distributions of DNA damage following high doses of irradiation with protons versus photons have been observed [Miszczyk 2021]. The damage produced by protons is more clustered and, therefore, more complex and less repairable than that induced by photons, even at the same LET [Goodhead *et al.* 1993]. This increased complexity arises from the distinct track structures, i.e., the spatial distribution of the energy deposition at the nanoscale [Henthorn *et al.* 2018]. DNA damage misrepair (incorrect DNA re-joining) also strongly depends on the increased density of lesions with LET (Figure 1.35), being more critical at the distal edge of the SOBP. This is a consequence of the proximity effects, i.e., the increased probability of misrejoining when the DSBs are more clustered [Sachs *et al.* 1997]. The misrepaired DSBs, which lead to chromosomal structural changes, are highly toxic, leading to mutations and an increased lethality after proton irradiation compared to photons [Henthorn *et al.* 2018].

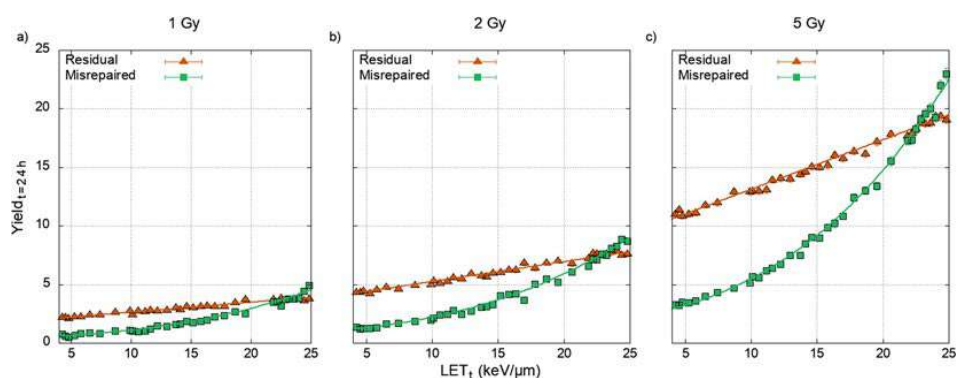


**Figure 1.35:** Predicted yield of misrepaired and residual DSBs as a function of LET at doses of (a) 1, (b) 2, and (c) 5 Gy. Taken from [Henthorn *et al.* 2018].

Those distinct responses due to the proton track structure and LET variation along the proton range can be quantified by the RBE (see Section 1.2.4.7). A constant RBE of 1.1 is typically used in clinics. This value is inferred from

several *in vitro* and *in vivo* studies [Dalrymple *et al.* 1966, Tepper *et al.* 1977, Urano *et al.* 1980], averaging multiple endpoints for a specific dose (2 Gy) and homogeneous dose distributions [Paganetti 2014]. The main advantage of using a generic RBE value is the easy conversion of dose between protons and photons [Paganetti 2018]. However, several studies showed an RBE variation as a function of various factors. RBE varies along the SOBP from 1.1 (entrance region) to 1.7 (distal fall-off) due to the LET increment. The increased LET and RBE at the distal fall-off of the SOBP give rise to an extension by 1 to 2 mm of the biologically effective range (Figure 1.36), which is not included in the current RBE description [Paganetti *et al.* 2002]. Also, the RBE depends on the dose per fraction, increasing as the dose decreases [Paganetti 2014], and tissue type, increasing with decreasing  $\alpha/\beta$  ratio [Paganetti 2018, Underwood & Paganetti 2016]. Other dependencies have been reported, such as cells' genetic background [Girdhani *et al.* 2013]. Then, using the generic RBE may lead to misinterpretation of biological effects in different tissues [Paganetti 2015]. At the nanoscale, the limitations of the RBE become greater since this parameter is based on macroscopic considerations. As Löbrich *et al.* [Löbrich & B. Rydberg 1996] argued, RBE is usually derived as a function of LET, ignoring the complete deposition patterns. Also, the break complexity and proximity effects are not included in LET or RBE descriptions, not considering the DNA misrepair and residual damage, i.e., increased chromosome aberrations and mitotic catastrophe cell death, respectively. Some studies have demonstrated the potential benefits of using a variable RBE in clinics, such as the output improvement of brain treatments [Carabe *et al.* 2013] and the reduction in toxicity in pediatric patients [Peeler *et al.* 2016].

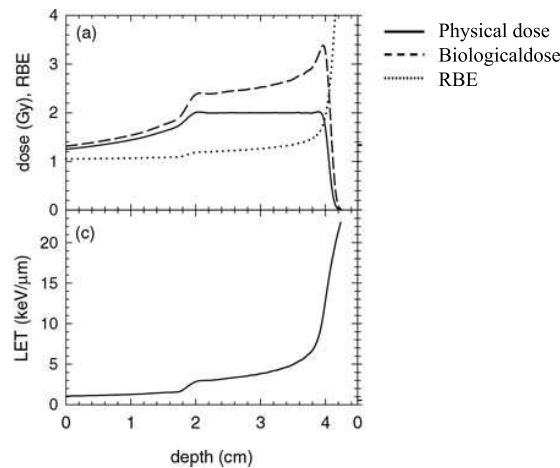


**Figure 1.36:** Physical dose, biological dose considering a variable RBE (RBE-weighted dose), and LET for a 70 MeV proton beam. Adapted from [Wilkens & Oelfke 2004].

In addition, different responses in terms of genotoxicity, inflammatory response, and gene expression have been observed following irradiations with scattered and scanned proton beams [Chaouni 2020, Leduc *et al.* 2021], presumably, due to the differences in dose rate between the two delivery techniques.

### 1.3.4 Clinical aspects

The rationale for using proton therapy in clinics is the sparing of critical structures behind the target due to the finite range of protons. Also, the dose increase at the end of the range (i.e., Bragg peak) allows an enhanced dose escalation [Paganetti 2018]. Overall, reducing the integral dose to the patient may imply reducing morbidity and the likelihood of developing secondary radiation-induced malignancies [Dracham *et al.* 2018].

The finite depth of penetration into tissues, one of the main advantages of proton beams, also implies a significant drawback; the uncertainty in the proton range. Systematic uncertainties arise from inaccurate analytical dose calculation algorithms used by treatment planning systems (TPSs) when computing MCS through large tissue inhomogeneities [Paganetti 2012]. Another source of uncertainty is calculating the proton relative stopping power from X-ray CT images, which implies inaccurate assumptions to correlate the distinct fundamental interactions of imaging and treatment particles [Paganetti 2012]. Random uncertainties related to patient setup also affect the range determination, such as the motion of internal structures, tumor shrinkage, or anatomical changes in the patient. Table 1.3 summarizes the sources of range uncertainty and associated magnitudes.

In clinics, several approaches have been proposed to minimize the range uncertainty, such as Monte Carlo-based TPSs [Paganetti 2012], proton CTs [Schulte & Penfold 2012], or *in vivo* range verification through the measurement of photons produced by the interaction of incident protons with tissues [Knopf *et al.* 2011]. Also, several techniques are used in clinics to minimize its impact on treatments, such as beam angles to avoid beam directions implying OARs behind the target, the definition of beam-specific PTVs accounting for tissue heterogeneities [Park *et al.* 2012], or a robust optimization process considering several error scenarios [Liu *et al.* 2012].

The effect of proton range uncertainty in treatments is not negligible when complex geometries and small fields are involved [Paganetti 2012]. Therefore, this aspect needs to be considered when selecting clinical cases that would benefit from PT. In general, situations where the range degradation changes unpredictably may be unsuitable for PT due to the range uncertainty and risk of irradiating critical structures behind the target and undershooting the targets. Some examples are moving targets or scenarios where beams pass through inhomogeneities, dense targets surrounded by low-density tissue (e.g., lung), or cavities that may fill with gas or liquid. The suitability for PT may also depend on the dose delivery technique used. Dose distributions of treatments involving moving targets are more sensitive to the PBS delivery since the energy of each spot is calculated for traversing a specific path in the initial configuration and the movement of structures may modify the predicted range. Then, using the passive scattering mode may be more suitable since the dose is delivered simultaneously to the entire target. Contrarily, PBS is preferably used for treating tumors close to critical structures due to the high dose conformity to the target.

Source of range uncertainty	Uncertainty without Monte Carlo	Uncertainty with Monte Carlo
Independent of dose calculation:		
Measurement in water for commissioning	$\pm 0.3$ mm	$\pm 0.3$ mm
Compensator design	$\pm 0.2$ mm	$\pm 0.2$ mm
Beam reproducibility	$\pm 0.2$ mm	$\pm 0.2$ mm
Patient setup	$\pm 0.7$ mm	$\pm 0.7$ mm
Dose calculation:		
Biology †	+ 0.8 %	+ 0.8 %
CT imaging and calibration	$\pm 0.5$ %	$\pm 0.5$ %
CT conversion to tissue	$\pm 0.5$ %	$\pm 0.2$ %
CT grid size	$\pm 0.3$ %	$\pm 0.3$ %
Mean excitation energy in tissues	$\pm 1.5$ %	$\pm 1.5$ %
Range degradation; complex inhomogeneities	− 0.7 %	$\pm 0.1$ %
Range degradation; local lateral inhomogeneities *	$\pm 2.5$ %	$\pm 0.1$ %
Total (excluding *,†)	2.7 % + 1.2 mm	2.4 % + 1.2 mm
Total (excluding †)	4.6 % + 1.2 mm	2.4 % + 1.2 mm

**Table 1.3:** Sources of range uncertainty and magnitudes. Adapted from [Paganetti 2012].

The American Society for Radiation Oncology (ASTRO) [ASTRO 2022] defines the recommendations for reimbursement by dividing different clinical indications into three groups. The treatment of clinical indications of Group 1 is supported by published clinical data. Disease sites of this group include ocular tumors, tumors at the base of the skull (e.g., chondrosarcomas), primary or metastatic tumors in the spine, hepatocellular cancer, and pediatric tumors. The treatment of head and neck tumors is challenging due to the critical structures close to the target volume. The irradiation of such OARs (e.g., brainstem, central nervous system (CNS) structures, or chiasm) can result in irreversible functional loss, such as hearing and ocular loss or neurocognitive deficits. Thus, the improved dose conformity and sharp penumbra of protons may result in the dose reduction to some of those structures compared to photon treatments [Holliday *et al.* 2015, McDonald *et al.* 2016, Romesser *et al.* 2016, Swisher-McClure *et al.* 2016, Ares *et al.* 2009, Morimoto *et al.* 2014] (see Figure 1.37). Moreover, large volumes of the brain receiving radiation in pediatric and young adult patients may increase the risk of side effects since their neurocognitive structures are still in development. PT may be beneficial for reducing the integral dose to this organ. Examples of pediatric tumors typically treated with PT are medulloblastomas [Kahalley *et al.* 2020] and gliomas [Indelicato *et al.* 2019]. In addition, radioresistant tumors, such as sarcomas or high-grade gliomas, may benefit from PT since the dose to the tumor can be increased without exceeding the tolerance dose to normal tissues thanks to the inverse depth dose profile of proton beams [Hu *et al.* 2018].

Other indications that may be suitable for PT but still need more evidence from

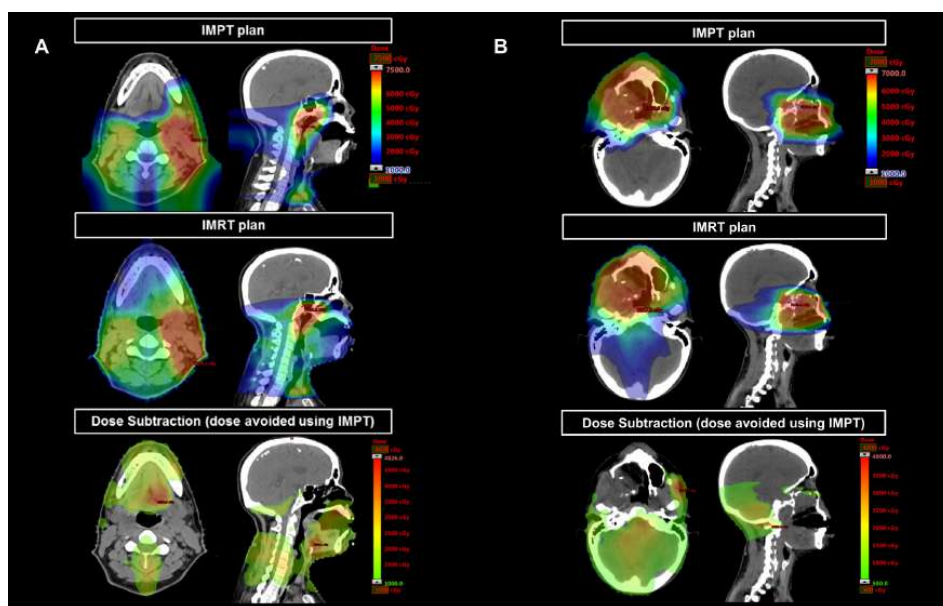


**Figure 1.37:** Dose distributions in intensity-modulated proton (IMPT) and photon (IMRT) therapy and dose differences between them. Treatments of (A) nasopharyngeal carcinoma and (B) adenoid cystic carcinoma of the hard palate. Taken from [Blanchard *et al.* 2018].

clinical trials are included in Group 2. Examples of clinical indications of this group are thoracic, abdominal, and pelvic malignancies, non-metastatic prostate cancer, and breast cancer. The use of PT for treating these disease sites may decrease the risk of radiation-induced late effects, compared to photon therapy, thanks to the sparing of critical structures [Fagundes *et al.* 2015, Fontenot *et al.* 2009, Ntentas *et al.* 2019].

Clinical indications not included in those two groups are considered not suitable for PT due to the insufficient evidence of its efficacy, for instance, the treatment of prostate cancers after prostatectomy. The need for randomized clinical trials is intensely discussed in the community for such indications.

Besides the use of static proton fields, other approaches have been suggested, such as proton arc therapy (PAT) [Ding *et al.* 2016]. The concept of PAT is delivering proton beam treatments through arcs. This technique has the potential to enhance dose conformity within the target volume while reducing the integral dose delivered to the patient, improving the adoption of dose escalation and hypofractionation [Seco *et al.* 2013]. PAT also improves the quality and robustness of treatments since the proton range uncertainty is diffused at distal and proximal regions due to the rotating arc beam, reducing the impact of range uncertainty [Seco *et al.* 2013]. Furthermore, proton arc beams may allow the LET painting (i.e., optimization of the LET distribution), which can be used for optimizing and increasing the biological effectiveness within the target [Carabe *et al.* 2020, Toussaint *et al.* 2019]. This technique has demonstrated

its potential in several disease sites and indications, such as a reduced dose to organs-at-risk, compared to intensity-modulated proton therapy and VMAT, for pediatric cancers [Toussaint *et al.* 2019], adult brain tumors [Ding *et al.* 2019], breast [Chang *et al.* 2020], and lung [Li *et al.* 2018], among others. Regarding its implementation in clinics, the first prototype of spot-scanning arc therapy (SPArc) delivery has already been performed on a clinical proton beam therapy machine [Li *et al.* 2019].

*Despite the advances in RT described in the previous sections, the normal tissue's morbidity remains the main limiting factor in RT treatments, compromising the treatment of radioresistant tumors, for instance. The use of distinct dose delivery methods, such as the spatial fractionation of the dose, can increase the sparing of normal tissues. Due to its central role in this thesis, the concept of spatially fractionated radiotherapy is presented in the following section.*

## 1.4 Spatially-fractionated radiotherapy

This chapter presents the fundamentals of spatially fractionated radiotherapy (SFRT), current knowledge of its distinct radiobiology, as well as the characteristics of each SFRT technique. Since the focus of this thesis is proton minibeam radiation therapy, the dosimetric, technical, and clinical aspects of this technique are described in more detail in a dedicated section (Section 1.4.4).

### 1.4.1 Fundamentals of spatially-fractionated radiotherapy

Spatially fractionated radiotherapy (SFRT) uses several narrow beamlets separated by small gaps (usually 1 - 4 times the beamlet width) [Prezado 2022]. Radiation beams may be spatially fractionated in one or two dimensions, as Figure 1.38 illustrates. The center-to-center (c-t-c) distance defines the separation between the centers of two beamlets in any of those dimensions. This dose delivery method results in non-uniform dose distributions, contrary to conventional techniques. SFRT dose profiles are characterized by a succession of high-dose regions, called peaks, and areas of low dose, called valleys (see Figure 1.39). The peaks correspond to the path of the primary beam, while valley doses result from the leakage and scatter of radiation in the collimator systems and the scatter of particles out of the primary beam axis [Billena & Khan 2019]. This dose pattern appears to activate biological mechanisms different from those involved in standard RT, leading to superior tissue sparing [Prezado 2022]. A detailed description of the biological responses to SFRT can be found in Section 1.4.3.

The fractionation of the dose in SFRT is typically described by the ratio between peak ( $D_{peak}$ ) and valley ( $D_{valley}$ ) doses, called the peak-to-valley dose ratio (PVDR):

$$PVDR = \frac{D_{peak}}{D_{valley}}. \quad (1.17)$$

This quantity is assumed to be a biologically relevant parameter [Dilmanian *et al.* 2002]; high PVDRs, together with low valley doses [Smyth *et al.* 2018], are considered to increase the normal tissue's tolerance dose, while low PVDRs and high valley doses lead to higher toxicities [Dilmanian *et al.* 2002]. However, a recent retrospective analysis showed no significant correlation between the PVDR and an increased life span in tumor-bearing animals [Fernandez-Palomo *et al.* 2022].

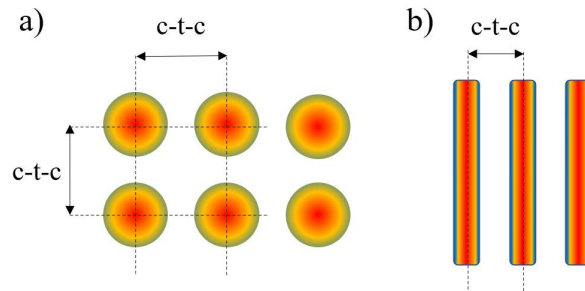


**Figure 1.38:** Schematic representation of beamlets spatially fractionated in (a) two and (b) one dimensions. The center-to-center (c-t-c) distance defines the distance between the center of two beamlets in each of those dimensions.

The concept of SFRT (or fractionation of the x-ray dosage in space) was first introduced by Köhler in 1909 [Köhler 1909]. The main purpose of this approach was to overcome the skin toxicities (i.e., increase the tolerance dose) when deep-seated tumors were treated with the existing orthovoltage X-ray beams. At that time, delivering curative doses to deep tumors resulted in large doses to the skin due to the low penetration of low-energy beams. Therefore, skin toxicity entailed the main limitation of the treatments.

First treatments in SFRT employed grids of steel or lead with apertures of 3 cm in diameter [Liberson 1933]. The resulting reduction of irradiated volume led to an increase in the skin's toxicity, allowing an increment in the delivered dose by 10 to 20 times compared to seamless irradiations. In addition, the lateral scattering of low-energy radiation resulted in quasi-homogeneous dose distributions in depth [Mohiuddin *et al.* 1990]. In 1952, Marks *et al.* [Marks 1952] proposed the use of lead-rubber grids to reduce the irradiation of skin tissue from secondary rays produced in lead collimators. Adopting this methodology, two hundred patients with advanced carcinoma were treated with palliative intent. They responded more readily to the treatment than when conventional roentgen radiation was applied. This favorable response was hypothesized to be a consequence of the dose escalation, i.e., lower absorption of dose by normal tissues and increased transmission to target volumes. In addition, a healing process was observed in areas receiving scattered radiation (valleys), which extended to irradiated areas through the apertures of the grid (peaks).

The clinical use of SFRT was abandoned in the 1950s following the advent of LINACs. LINACs are able to produce megavoltage X-rays beams, which provide

better skin sparing than orthovoltage X-rays. However, the use of SFRT was renewed in the 1970s and 1990s when it was adapted to megavoltage photon beams produced by 60-Co machines [Barkova & Kholin 1971, Muth *et al.* 1977] and LINACs [Mohiuddin *et al.* 1990]. The spatial fractionation of the dose provided an additional normal tissue sparing potential (i.e., increased tissue tolerance dose) besides the achieved by MV photon beams, enabling the use of more aggressive treatment schemes [Gholami *et al.* 2016]. In the first pilot study on the use of SFRT using megavoltage photon beams generated by a LINAC [Mohiuddin *et al.* 1990], twenty-two patients with massive or recurrent tumors (gastrointestinal, liver, and miscellaneous tumors, and sarcomas) were treated with palliative purposes. A grid containing 141 holes arranged in a hexagonal pattern, blocking 50 % of the irradiated area, was used as a collimator. After the treatment, 18 in 22 patients showed no acute side effects and none of them developed long-term complications, even though they previously received tolerance doses of radiation. Regarding the palliative response, 91 % of patients showed palliation of symptoms (including 22 % showing complete relief). The authors of that study concluded that MV photon SFRT improved the quality of life of the treated patients without causing additional normal tissue toxicity, which could not have been possible with open-field techniques.

In the last three decades, the concept of the spatial fractionation of the dose has evolved and, nowadays, SFRT can be classified into four main techniques: GRID therapy [Köhler 1909], LATTICE radiotherapy (LRT) [Wu *et al.* 2010], minibeam radiation therapy (MBRT) [Dilmanian *et al.* 2006], and microbeam radiation therapy (MRT) [Slatkin *et al.* 1992]. A more detailed description of these techniques is given in the following section (Section 1.4.2).

### 1.4.2 Spatially-fractionated radiotherapy techniques

One of the main differences among the various SFRT techniques is the geometry and scale of the irradiation patterns (i.e., beamlet width and spacing). GRID and LRT typically use 1 to 2 cm diameter pencil-shaped beamlets arranged in 2D- or 3D-grid geometry, respectively. The c-t-c distance between beamlets is 2 to 4 cm. In MBRT, arrays of 0.5 to 1 mm-width planar beamlets are employed and the separation between minibeamlets is typically 1 to 4 mm. Finally, MRT uses micrometric (50 to 100  $\mu\text{m}$ ) beamlets in the form of planar or pencil-shaped microbeams separated by 200 to 400  $\mu\text{m}$  c-t-c distance.

The different irradiation geometries lead to a different degree of spatial fractionation. Figure 1.39 illustrates the differences in the dose distributions between GRID, MBRT, and MRT. The PVDR in GRID and LRT ranges from 2 to 5, whereas in MBRT and MRT can be up to 20 and 50, respectively. This also influences the therapeutic doses employed in each technique. Peak doses in GRID and LRT are usually 10 to 20 Gy (typically delivered in one fraction or in hypofractionation regimes). The smaller beamlet sizes in MBRT and MRT allow the use of doses up to 100 and 600 Gy, respectively, due to the increase in the normal tissue tolerance dose produced by the dose-volume effect (see Section 1.2.4.5).

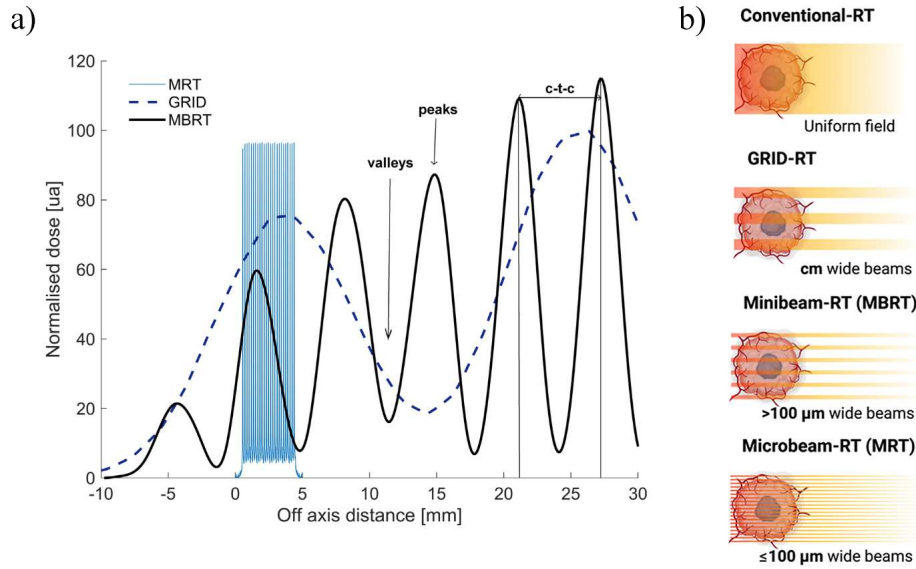


**Figure 1.39:** Representation of (a) lateral dose profiles and (b) dose distributions of different SFRT techniques, i.e., GRID therapy, MBRT, and MRT. The center-to-center (c-t-c) distance refers to the distance between two adjacent peak regions. Taken from [De Marzi *et al.* 2019b] and [Fernandez-Palomo *et al.* 2022].

The main application of each technique also differs. Whereas GRID and LRT are mainly used for palliative purposes, MBRT and MRT clinical applications are expected to be radical treatments.

In addition, the different beam sizes, degrees of modulation, and prescribed doses may induce distinct biological responses [Prezado 2022], as described in more detail in Section 1.4.3.

The main characteristics of these four techniques are summarized in Table 1.4.

Technique	Beamlet width	Beamlet spacing	Irradiation pattern	Peak dose (Gy)	PVDR	Main applications
GRID therapy	1-2 cm	2-4 cm	2D-grid of pencil-shaped beamlets	10-20	2-5	Palliative and curative
LRT			dose hotspots			
MBRT	0.5-1 mm	1-4 mm	Array of planar beamlets or grid of pencil-shaped beamlets	up to 100	10-20	Radical preclinical and potential clinical
MRT	50-100 μm	200-400 μm		300-600	50	

**Table 1.4:** Summary of the main characteristics of GRID therapy, LRT, MBRT, and MRT. Adapted from [Prezado 2022].

The combination of SFRT with different particles, such as X-rays, electrons, protons, or heavier ions, has been explored, and their suitability for each technique will be discussed in the sections hereafter.

## 1.4.2.1 GRID therapy

Megavoltage X-ray GRID therapy [Mohiuddin *et al.* 1990] is the most common form of SFRT in clinics [Billena & Khan 2019], mainly for palliative purposes. GRID therapy is usually delivered in the form of individual non-confluent 2D arrays of pencil-shaped megavoltage photon beams. Hence, it corresponds to a two-dimensional dose delivery (see Figure 1.40a). Beamlets may be arranged in orthogonal or hexagonal patterns (see Figure 1.40b). These patterns are obtained by collimating a broad-based photon field into smaller beamlets. Standard collimation devices are attenuation blocks with equally spaced apertures (see Figure 1.40c), MLCs, or a combination of both. GRID results in the fractionation of the dose only in the two dimensions orthogonal to the beam direction (Figure 1.40e), while depth dose profiles show the characteristic fall-off of MV X-ray beams (Figure 1.40d) [Billena & Khan 2019].

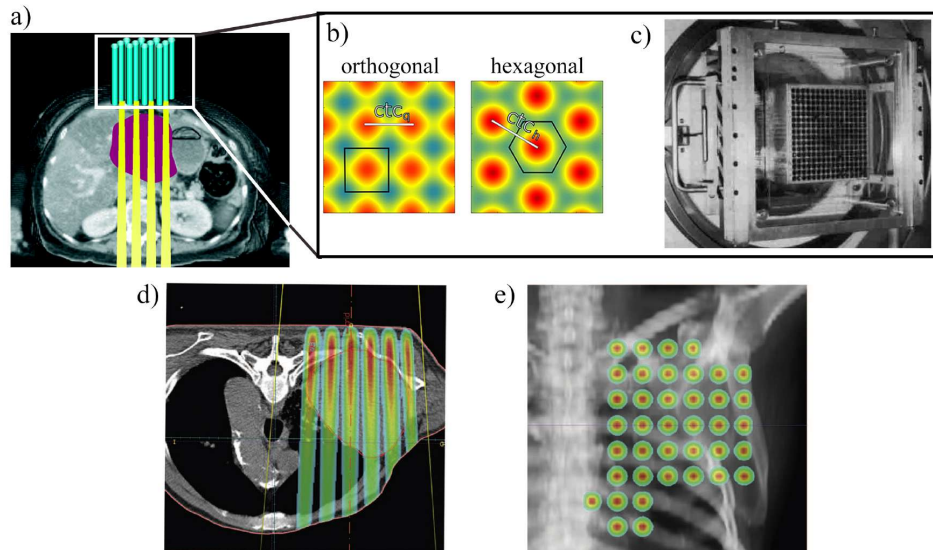


**Figure 1.40:** (a) Conceptual representation of a 2D-GRID treatment delivery. Blue cylinders represent the beam collimation and the path of the resulting individual beamlets is displayed in yellow. (b) Representation of the fluence of beamlets arranged in orthogonal and hexagonal patterns. (c) Example of attenuation block attached to a LINAC head acting as a collimator. (d) and (e) shows examples of dose distributions in a GRID therapy treatment in the view orthogonal to the beam direction and in the beam-eye view, respectively. Adapted from (a) [Wu *et al.* 2010], (b) [Sammer *et al.* 2017], (c) [Mohiuddin *et al.* 1996], and (d and e) [Almendral *et al.* 2013].

Photon beams used in GRID therapy are typically produced by conventional LINACs. Novel approaches using VMAT or helical tomotherapy (TOMOGRID) [Zhang *et al.* 2016] have also been proposed to modulate the dose three-dimensionally and improve tumor conformity [Grams *et al.* 2021]. Martínez-Rovira *et al.* [Martínez-Rovira *et al.* 2017b] also suggested the use of flattening filter-free (FFF) photon beams to obtain a higher degree of dose modulation and thinner

beams, which may lead to a higher therapeutic index.

In GRID therapy, beamlet sizes range from 1 to 2 cm, and the separation between beamlets, defined as the *c-t-c* distance, is typically of 2 - 4 cm [Billena & Khan 2019, Prezado 2022]. Gholami *et al.* [Gholami *et al.* 2016] reported that aperture diameters of 1.0 - 1.25 cm and *c-t-c* of 1.8 cm might lead to the optimum clinical results for treating radioresistant tumors, i.e., the therapeutic ratio is maximized for a given equivalent uniform dose. The degree of spatial dose fractionation in GRID treatments is relatively low (the PVDR ranges from 2 to 5 [Prezado 2022]) due to the dose deposited in valley regions resulting from the important lateral scattering of MV X-rays.

GRID therapy is generally delivered in one fraction of 10 - 20 Gy maximum dose, alone or in combination with conventional EBRT [Yan *et al.* 2020]. The potential of GRID therapy for increasing the therapeutic index has been proven in several studies treating advanced head and neck cancers [Huhn *et al.* 2006, Peñagaricano *et al.* 2010, Edwards *et al.* 2015] and other disease sites, such as pelvis, abdomen, thorax, skin, or liver [Mohiuddin *et al.* 1990, Mohiuddin *et al.* 1996, Mohiuddin *et al.* 1999, Kudrimoti *et al.* 2002, Mohiuddin *et al.* 2009, Neuner *et al.* 2012, Mohiuddin *et al.* 2014]. Despite the limitations of these studies, i.e., lack of control arms, heterogeneity in the study population, and non-consistent dose prescription, GRID therapy showed a reduction in the toxicity (i.e., pain improvement and mass effect) along with higher control rates than the obtained historically with conventional techniques (76 % to 100 %) [Billena & Khan 2019]. Moreover, some data showed a reduced rate of distant metastases following GRID therapy, which may be related to abscopal effects [Edwards *et al.* 2015].

GRID therapy using protons (proton GRID) has also been proposed [Gao *et al.* 2018, Henry *et al.* 2017]. Proton GRID provides several advantages over conventional photon GRID. The lateral scattering of protons in depth produces a more uniform dose distribution within the target volume while maintaining the beneficial spatial fractionation in normal tissues. In addition, the use of protons provides more conformal dose distributions (i.e., the negligible dose deposited after the Bragg peak position and the increase in dose at the end of the proton range). Mohiuddin *et al.* [Mohiuddin *et al.* 2020] reported the first proton GRID therapy trial. Ten patients with large tumors (sarcomas and carcinomas) were treated with palliative intent. These tumors could not be treated with X-ray GRID since the excessive entrance and exit doses would lead to prohibitive doses to normal tissues. Proton GRID resulted in a decrease in the entrance dose, an increased dose uniformity within the target, and the sparing of normal tissues and critical structures due to the enhanced dose conformity of protons.

#### 1.4.2.2 LATTICE radiotherapy

LATTICE radiotherapy (LRT) [Wu *et al.* 2010] is based on modulating the dose in 3D, contrary to conventional GRID techniques, where the dose is two-

dimensionally fractionated. LRT consists of creating localized high-dose spheres, called vertices, within the tumor volume. The diameter of the vertices is typically 1 to 2 cm and are separated by 2 to 6 cm c-t-c distance [Prezado 2022]. These high-dose spots are produced by converging multiple beams within the tumor volume. LRT can be delivered with intensity-modulated or volumetric-arc techniques [Wu *et al.* 2010]. Figure 1.41 illustrates the concept of LRT and examples of dose distributions.

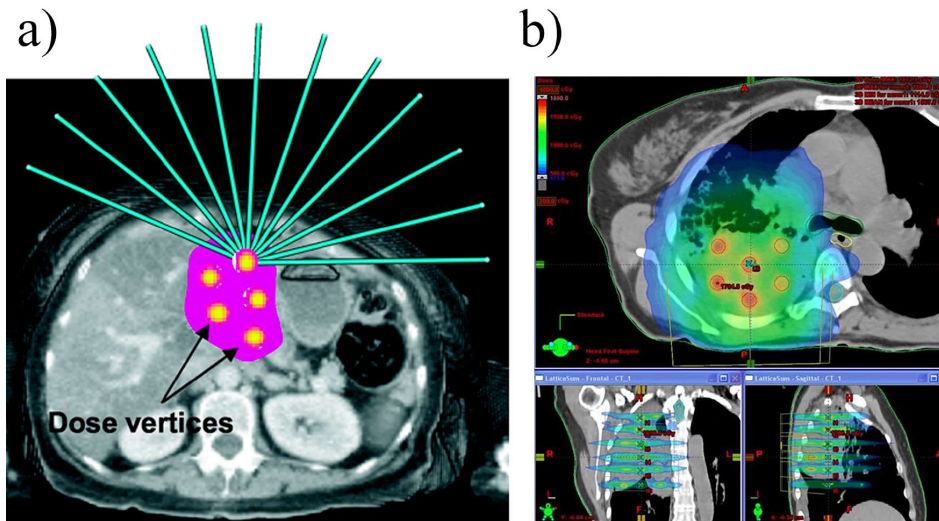


**Figure 1.41:** (a) Conceptual representation of a LRT treatment delivery. Blue lines represent individual fields converging on a small volume within the tumor to create high-dose vertices (displayed in yellow). (b) Example of dose distributions of a LRT treatment. Taken from [Wu *et al.* 2010].

One of the main advantages of LRT, as compared to GRID therapy, is that peak doses are limited to within the tumor volume, reducing the dose delivered to normal tissues [Billena & Khan 2019]. However, normal tissues may not benefit from the sparing potential of SFRT due to the lack of a dose fractionation pattern outside the target volume. Its main applications are the treatment of advanced large tumors, palliative tumor debulking, and boost treatments. LRT can be used alone or in combination with conventional EBRT, chemotherapy, or immunotherapy. LRT efficacy in clinics has been reported for several tumor types, such as gynecological [Amendola *et al.* 2010], ovarian [Suarez *et al.* 2015], prostate [Pollack *et al.* 2020], and advanced non-small cell lung cancers [Amendola *et al.* 2018, Amendola *et al.* 2019]. The therapeutic doses and fractionation regimes varied notably from study to study (from 48 Gy in 22 fractions to 18 Gy vertex dose in one fraction [Billena & Khan 2019]). The response to LRT treatments also varied significantly depending on the clinical condition. A summary of clinical outcomes can be found in the review paper of Wu *et al.* [Wu *et al.* 2020]. As an example, in the first phase I clinical trial using LRT as a boost followed by conventional EBRT for treating prostate cancer, no toxicity was observed after

66 months of follow-up [Pollack *et al.* 2020].

The feasibility of implementing proton and carbon-ion LRT has also been studied. A treatment plan evaluation of a sinonasal malignancy, performed by Yang *et al.* [Yang *et al.* 2022], showed no significant differences in dose modulation within the target between photon, proton, and carbon ion LRT plans. However, the use of charged particles enables the protection of OAR, as compared to photon plans.

*Due to the centimeter-size beamlets used in GRID and LRT, the spacing between dose hotspots needs to be relatively large, limiting the application of these techniques to large tumors. Furthermore, the dose-volume effect (see Section 1.2.4.5) is not fully exploited for such beam sizes. MRT and MBRT aim to overcome these limitations by using submillimeter-fractionated beamlets.*

### 1.4.2.3 Microbeam radiotherapy

Microbeam radiation therapy (MRT) [Slatkin *et al.* 1992] is the most extreme form of SFRT. It originated in 3rd generation synchrotrons in the 90s [Slatkin *et al.* 1994]. MRT uses arrays of quasi-parallel microplanar beams (called microbeams) produced by means of multislit collimators [Bartzsch *et al.* 2020]. Microbeams are 25- to 50- $\mu\text{m}$ -wide and are separated by a c-t-c distance of 200 to 400  $\mu\text{m}$  [Prezado 2022]. MRT is considered to provide a relatively high degree of spatial dose fractionation (PVDRs of 50 or above can be achieved). To preserve such high-spatial modulation of the dose, MRT requires minimal beam divergence (i.e., sharp penumbra), kilovoltage beams [Prezado *et al.* 2009b] and very high dose rates [Prezado 2022]. The use of divergent beams or higher beam energies would result in a significant reduction of the spatial dose modulation [Prezado 2022]. In addition, therapeutic doses need to be delivered in a very narrow time window (fractions of seconds) to prevent the blurring of the microbeam pattern due to any movement of the patient on a submillimeter scale [Grotzer *et al.* 2015, Schültke *et al.* 2017], e.g., the cardiosynchronous pulsations [Manchado de Sola *et al.* 2018]. Thus, very high mean dose rates (around 100 Gy/s) are required.

Historically, producing beams with these features (i.e., low beam divergence and high dose rates) has only been achievable by 3rd generation synchrotrons. Examples of synchrotrons facilities that have implemented MRT are the Brookhaven National Laboratory (USA) [Slatkin *et al.* 1994], Canadian Light Source (Canada) [Chicilo *et al.* 2020], European Synchrotron Radiation Facility (ESRF) (France) [Laissue *et al.* 1999], SPring-8 (Japan) [Crosbie *et al.* 2010], and the Australian Synchrotron (Australia) [Sprung *et al.* 2012]. The development of MRT has been limited by the restricted beam time in this type of facility [Prezado 2022]. Some approaches have been proposed to produce high-dose microbeams using compact systems. For instance, Hadsell *et al.* [Hadsell *et al.* 2013] developed a compact system based on carbon nanotube (CNT) field emission technology. Also, Winter [Winter *et al.* 2020] proved the feasibility of implementing a line-focus X-ray tube

that produces most of the beam features required in MRT. However, the dose rates in those systems (up to 100 Gy/s) are still much lower than those at synchrotrons.

Preclinical trials showed the effectiveness of MRT. Several studies in rodents reported an increase in the tolerance dose of the brain [Bräuer-Krisch *et al.* 2010, Laissue *et al.* 2007, Schültke *et al.* 2008, Serduc *et al.* 2008a, Slatkin *et al.* 1994], vasculature [Bouchet *et al.* 2015, Serduc *et al.* 2008b, Serduc *et al.* 2006, Van Der Sanden *et al.* 2010], spinal cord [Laissue *et al.* 2013], and skin [Zhong *et al.* 2003] up to 300 to 600 Gy peak doses in one fraction. Similar results have also been achieved in other animals, such as insects [Schweizer *et al.* 2000], birds [Dilmanian *et al.* 2001], dogs [Adam *et al.* 2022], and pigs [Laissue *et al.* 2001]. For instance, in the work by Laissue *et al.* [Laissue *et al.* 2001], the cerebellum of immature pigs was irradiated using a microbeam array. Animals treated with MRT did not show behavioral, neurological, or developmental problems at peak doses of 600 Gy in a single fraction, contrary to seamless irradiations at 29 Gy [Van den Aardweg *et al.* 1994]. These data suggest that MRT may be a promising therapeutic option for treating pediatric patients. The efficacy of MRT in tumor control has also been proven for various tumor types, such as gliomas [Bouchet *et al.* 2016], melanomas [Potez *et al.* 2019], and squamous cell carcinomas [Miura *et al.* 2006]. These studies showed a similar or increased survival and tumor regrowth delay after MRT irradiations compared to conventional radiotherapy. Another relevant study for the clinical transfer of MRT successfully treated large animals (dogs) with spontaneous brain tumors using synchrotron-generated microbeams under clinical conditions [Adam *et al.* 2022]. A complete summary of results in MRT tumor studies can be found in the review article by Fernandez-Palomo *et al.* [Fernandez-Palomo *et al.* 2020].

Relevant clinical indications that might benefit from MRT are adult and pediatric patients with radioresistant tumors, lung cancer, or malignant tumors in the musculoskeletal system [Schültke *et al.* 2017] due to the increase in the tolerance dose of normal tissues. Schültke *et al.* [Schültke *et al.* 2017] proposed the use of MRT as a boost for conventional EBRT, where peak doses would be used to enhance tumor control. MRT could also be used as a microsurgical tool for treating non-malignant neurological diseases, such as epilepsy [Fardone *et al.* 2018, Pouyatos *et al.* 2016, Romanelli *et al.* 2013] due to the size and precision of microbeams and the high tolerance of the central nervous system to MRT [Fernandez-Palomo *et al.* 2020]. In addition, Sabatasso *et al.* [Sabatasso *et al.* 2011] proposed MRT as a primer for drug delivery since microbeams temporarily increase vascular transpermeability.

Despite the potential clinical benefits of MRT, its translation to clinical trials is hindered by three main limitations: the need for large synchrotrons to produce such high-dose-rate beams or its clinical implementation into other systems (e.g., carbon nanotube devices or a line-focus X-ray tubes), the lack of suitable dosimetric protocols for such narrow and intense beams, and the requirement for an accurate patient positioning at submillimeter scale [Prezado 2022, Yan *et al.* 2020]. Another

drawback of the clinical use of MRT is that the use of low-energy X-rays restricts this technique to superficial tumors.

The feasibility of using other types of particles different from X-rays has been studied. Martinez-Rovira *et al.* [Martínez-Rovira *et al.* 2015] showed that proton- or VHEE-MRT is not adequate for treating deep-seated tumors. The lateral scattering of these particles results in the widening of microbeams in depth, significantly decreasing the spatial dose modulation. This results in an unfavorable ratio between the primary and scatter doses. Monte Carlo results showed that the peak and valley pattern is only preserved up to very shallow depths (around 50 mm for a 120 MeV proton beam) [Kłodowska *et al.* 2015]. Zlobinskaya *et al.* [Zlobinskaya *et al.* 2013], proved the efficacy of proton microbeams in the protection of skin tissue, i.e., maintenance of cell viability and reduction of inflammatory response. However, as just explained, proton MRT is limited to superficial targets. The use of thicker beams, as in minibeam radiation therapy, can be an effective solution.

#### 1.4.2.4 Minibeam radiotherapy

Minibeam radiation therapy (MBRT) [Dilmanian *et al.* 2006] was proposed to overcome the main limitations of MRT while preserving the advantages of the spatial fractionation of the dose. It represents a compromise between GRID therapy and MRT in terms of beamlet sizes. MBRT uses arrays of 300 to 1000  $\mu\text{m}$ -wide planar beamlets [Prezado 2022] typically separated by 1 to 3 mm c-t-c distance [Yan *et al.* 2020]. Minibeams are generated by multislit collimators or beam choppers [Prezado *et al.* 2009b]. These larger beamlets are less sensitive than microbeams to the blurring of the peak-and-valley pattern due to cardiosynchronous pulsations [Manchado de Sola *et al.* 2018]. Thus, lower dose rates are needed, allowing the implementation of MBRT in more cost-effective facilities, e.g., small animal irradiators [Bazyar *et al.* 2017, Prezado *et al.* 2017b]. The increase in the beam size and c-t-c distance also allows using beams with larger divergences than in MRT. Then, the use of higher energies than kV X-ray beams, different particle types, and irradiators is feasible [Prezado *et al.* 2009a]. In addition, minibeams require less challenging dosimetry and positioning procedures [Dilmanian *et al.* 2006, Prezado *et al.* 2009b].

Like MRT, MBRT was born in synchrotron facilities. First experiences with minibeams [Dilmanian *et al.* 2006, Prezado *et al.* 2015] showed that, despite the increment in the beam size, the tolerance dose of brain tissue increased significantly compared to conventional RT (no apparent damage was observed in normal tissue at 120-150 Gy). Similar results were found in other studies performed in small animal irradiators [Bazyar *et al.* 2017, Prezado *et al.* 2017a]. For instance, in the work of Prezado *et al.* [Prezado *et al.* 2017a], no significant brain damage was observed following MBRT at peak doses of 60 Gy, contrary to standard RT. MBRT also resulted in reduced skin damage at 100 Gy peak doses. Preclinical studies also reported a significant tumor control effectiveness in glioma-bearing

rats (up to 60 % long-term survival), suggesting the efficacy of MBRT in terms of tumor control, even when delivering highly heterogeneous dose distributions to the target [Deman *et al.* 2012, Prezado *et al.* 2012b, Sotiropoulos *et al.* 2021]. Similar outcomes were found for quasi-homogenous dose distributions to the target when interlacing minibeam arrays [Deman *et al.* 2012, Dilmanian *et al.* 2006, Prezado *et al.* 2012b].

The use of kV X-ray minibeam arrays limits the clinical applicability of MBRT to superficial tumors (e.g., ocular tumors). To overcome this limitation, the use of higher energies (e.g., megavoltage X-ray beams) and different types of radiation (e.g., charged particles) has been proposed. Kundapur *et al.* [Kundapur *et al.* 2022] performed a phase III trial using 6 MV photon 1 mm-thick minibeam arrays for treating large animals (dogs) with brain tumors. This study reported high rates of tumor control and fewer long-term toxicities than in conventional treatments. Alternatively, the combination of charged particles (i.e., protons and heavy ions) with minibeam arrays may further increase the therapeutic index in MBRT due to the higher relative biological effectiveness of protons and heavy ions and their more advantageous dose distributions (i.e., Bragg peak) [Prezado 2022]. For the same geometry of the arrays, dose distributions of X-ray, proton, and carbon minibeam arrays differ significantly (see Figure 1.42). Contrary to X-rays, charged particles (i.e., protons and carbons) exhibit the characteristic Bragg peak, being more pronounced with respect to the entrance dose in the case of carbon ions. Regarding the spatial modulation of the dose, the degree of fractionation decreases in depth for the three types of radiation. However, in the case of protons, the rapid increase of valley doses in depth creates a quasihomogeneous lateral dose distribution at the end of the range, contrary to X-ray and carbon beams.

The use of proton minibeam arrays is called proton minibeam radiation therapy (pMBRT) [Prezado & Fois 2013]. In terms of the spatial fractionation of the dose, the main advantage of proton minibeam arrays compared to X-ray minibeam arrays is the widening of minibeam arrays in depth due to the lateral scattering of protons. Thus, the dose modulation decreases in depth, allowing combining a high spatial fractionation in healthy tissues and a homogeneous dose distribution in the target using only one array. However, the lateral scattering also represents two drawbacks in pMBRT: the rapid reduction of the PVDR and the decrease in Bragg-peak-to-entrance dose ratio (BEDR) with respect to broad beam conditions. Due to its relevance in this thesis, pMBRT is presented in more detail in a dedicated section (Section 1.4.4).

Aside from protons, using heavier ions, such as carbon [Dilmanian *et al.* 2012], lithium [Eley *et al.* 2021], and neon [Prezado *et al.* 2021] has been suggested. Heavy-ion MBRT provides several dosimetric advantages over X-ray and proton minibeam arrays since they are less affected by the MCS. Consequently, heavy-ion minibeam arrays exhibit higher PVDR, lower valley doses, reduced lateral penumbras and higher BEDR (see Figure 1.42) [Martínez-Rovira *et al.* 2017a, Peucelle *et al.* 2015a]. However, reducing the distance between minibeam arrays, which decreases the PVDR, or interlacing several arrays [Dilmanian *et al.* 2012] may be required to obtain

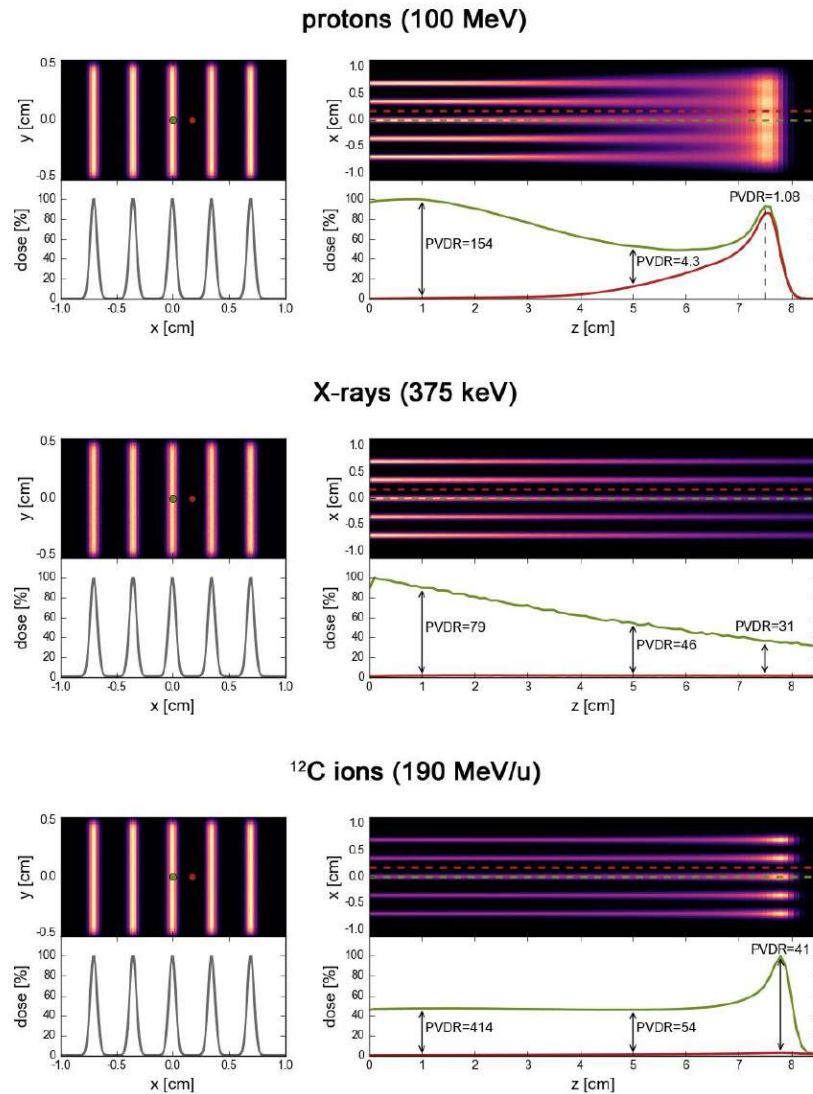


**Figure 1.42:** Lateral and depth dose profiles produced by an array of five (a) X-ray, (b) proton, and (c) carbon minibeams (0.7 mm wide minibeams separated by 3.5 mm c-t-c distance) in a water phantom. Green and red dots illustrate the position of the peak and valley, respectively. Taken from [Schneider 2020].

homogeneous dose distributions within the target due to the reduced lateral scattering of these particles. In terms of biological properties, the reduced oxygen enhancement effect of heavy ions favors the treatment of radioresistant tumors [Prezado 2022]. Also, the higher RBE may be exploited to increase the tumor cell killing, although the large variation in LET and RBE in depth should be considered. The normal tissue-sparing potential of heavy-ion MBRT has already been shown in preclinical studies. Dilmanian *et al.* [Dilmanian *et al.* 2012] used four interleaved carbon minibeam arrays to treat a 6.5 mm target in a rabbit brain.

After the treatment, little damage was observed to the brain tissue surrounding the target, and the animal exhibited normal behavior during the following 6 months. Regarding neon minibeam, the work of Prezado *et al.* [Prezado *et al.* 2021] reported a significant skin tissue sparing after Ne-MBRT irradiations (only reversible dermatitis was observed), compared to broad beam Ne irradiations. However, experiences with lithium have not shown any gain in tissue sparing, as compared with seamless lithium RT [Eley *et al.* 2021], probably linked to the high biological peak doses delivered (62.4 Gy times RBE).

*The more favorable tissue response to SFRT, compared to seamless irradiations, may be explained by the involvement of distinct biological mechanisms. The biological responses that may be activated by the spatial fractionation of the dose are described in the following section.*

### 1.4.3 Biological responses in spatially fractionated radiotherapy

Although the efficacy of SFRT has been proven in several preclinical studies, the basis of the biological response of normal and tumor tissues is not fully understood yet. Some data suggest that the spatial fractionation of the dose triggers different biological mechanisms from the observed in conventional techniques, i.e., differential vascular effects [Bouchet *et al.* 2015], dose-volume effects and migration of undamaged cells [Dilmanian *et al.* 2002], signaling effects [Fernandez-Palomo *et al.* 2013], the production of free radicals and its diffusion to low-dose areas [Dal Bello *et al.* 2020], and inflammation and immunomodulatory effects [Bertho *et al.* 2022]. Differential responses of normal and tumor tissues to these effects have also been observed. The biological mechanisms involved in normal and tumor tissue response to SFRT are described in more detail hereafter and summarized in Figure 1.4.3.

The role of vascular effects has been mainly studied in MRT, where a prompt vascular repair in normal tissues and increased radioresistance of mature blood vessels have been observed [Bouchet *et al.* 2015, Serduc *et al.* 2006, Van Der Sanden *et al.* 2010]. Contrarily, immature vasculature is more sensitive to MRT [Sabatasso *et al.* 2011], which may explain the higher sensitivity of tumors to MRT with respect to normal tissues [Bouchet *et al.* 2010, Fontanella *et al.* 2015]. This preferential effect on tumor vasculature may also prevent the blood supply and create hypoxic regions [Bouchet *et al.* 2013], which may explain the debulking effect of GRID therapy [Yan *et al.* 2020]. The fast regeneration of microvasculature of normal tissues may be promoted by the assistance of undamaged angiogenic cells from low-dose areas [Dilmanian *et al.* 2005].

The migration of undamaged stem cells from the valleys to peak areas to repair tissues exposed to high doses was hypothesized to contribute to the sparing effect of SFRT techniques [Dilmanian *et al.* 2002]. Preclinical data show a differential migration effect in normal and tumor tissues. Crosbie *et al.* [Crosbie *et al.* 2010] observed a coordinated repair response over the irradiated normal tissue due to cell

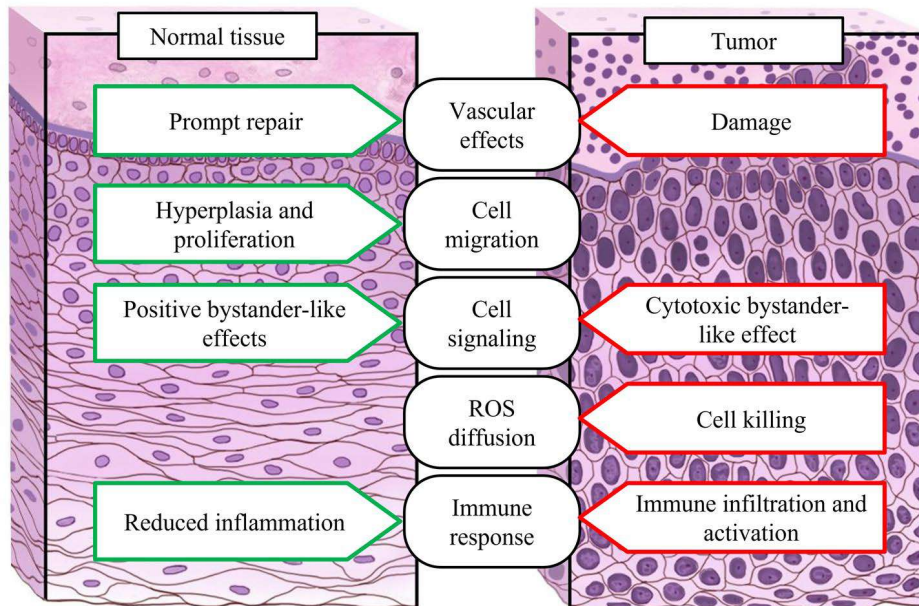


**Figure 1.43:** Summary of the effects in normal and tumor tissues caused by the distinct biological responses observed in SFRT.

migration after MRT irradiation. Contrarily, in the tumor, the migration of cells irradiated at peak doses caused a mixing of lethally irradiated cells with undamaged cells. As described in Section 1.2.4.5, the size of the peak dose-irradiated region (i.e., beamlet size) influences the efficacy of the repair response due to cell migration (dose-volume effect) [Hopewell & Trott 2000]. As Figure 1.44 illustrates, tissue preservation increases drastically as the beamlet size decreases.

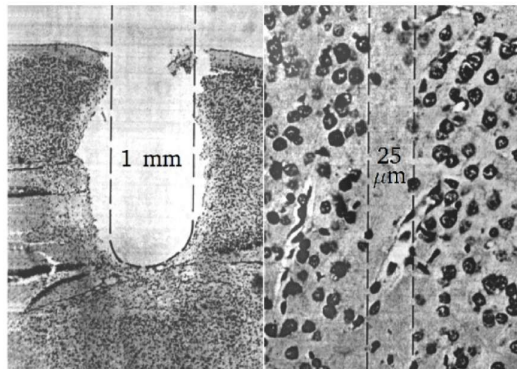


**Figure 1.44:** Histological analysis of mice brain tissue irradiated with 1-mm and 25- $\mu\text{m}$ -wide deuteron beams. A increased tissue preservation is observed following the 25- $\mu\text{m}$ -wide beam irradiation as compared to 1-mm-wide beam. Taken from [Zeman *et al.* 1961].

Non-targeted effects produced by cell signaling, described in Section 1.2.4.6, may also contribute to the tumor response to SFRT. Bystander-like effects have

been reported in LRT [Kanagavelu *et al.* 2014] and GRID therapy [Asur *et al.* 2012]. In the work by Asur *et al.* [Asur *et al.* 2012], significant cell killing was observed in unirradiated murine mammary cells after exposure to medium obtained from cells exposed to GRID irradiation (10 Gy peak dose), suggesting bystander-like responses. Cells receiving scattered radiation at valley regions (1 Gy) also exhibit cohort effects. In addition, mice treated with two LRT vertices exhibit a higher reduction of local tumor growth compared to animals irradiated with a single vertex, which may indicate intra-tumor bystander effects [Kanagavelu *et al.* 2014]. Similar effects have been observed following MRT irradiations [Lobachevsky *et al.* 2015, Lobachevsky *et al.* 2021]. Regarding the role of bystander-like effect in normal tissues, Dilmanian *et al.* [Dilmanian *et al.* 2007] suggested that this mechanism may assist the initiation of migration, proliferation, and differentiation of progenitor glial cells, which may be responsible for the tissue repair. In addition, an antitumorigenic and protective (radioresistance-like) bystander effect was observed in a nonirradiated brain hemisphere of rats treated with MRT [Smith *et al.* 2018]. Other studies also observed abscopal effects in LRT. Kanagavelu *et al.* [Kanagavelu *et al.* 2014] reported a growth delay in an unirradiated tumor implanted in the left lung of mice after the treatment of a tumor in the right lung. These effects have also been observed in rats after MRT [Fernandez-Palomo *et al.* 2013]. The bladder and the non-irradiated hemisphere of a rat exhibit a decrease in clonogenic survival following the irradiation of the other hemisphere with microbeams, independently of the presence of a tumor in the irradiated volume.

ROS produced by radiation, particularly hydrogen peroxide, may also contribute to the tumor cell killing in MRT and MBRT. ROS production is involved in DNA damage and cell killing, as described in Section 1.2.4.2. These molecules can migrate from peak regions, where they are produced, to valley areas, resulting in quasi-homogeneous distributions [Dal Bello *et al.* 2020].

Finally, immunomodulation and immune system activation is hypothesized to be one of the main participants in tissue responses to SFRT [Prezado 2022]. Studies on MRT concluded that the early tissue response depends on inflammation and the innate and adaptative immune response [Sprung *et al.* 2012]. In the work by Bouchet *et al.*, [Bouchet *et al.* 2013], more than half of the genes expressed after MRT irradiations were associated with immunity and inflammation (67 % and 64 % in tumor and normal tissues, respectively). Some of these genetic pathways were related to natural killer cells and CD8+ T-cells, suggesting the participation of the immune system in the efficacy of MRT. Other preclinical studies also hypothesize that the increased immune cell activation after MRT, compared to conventional irradiations, is involved in tumor response [Bouchet *et al.* 2016]. In addition, Bertho *et al.* [Bertho *et al.* 2022] proved the determinant role of immune activation in the antitumoral response to MBRT. That study aimed to compare the response of immunocompetent and immunodeficient glioma-bearing rats to minibeam. Immunodeficient animals did not respond to the treatment (no difference was found with respect to the control group). In contrast, a percentage of 33 % of

immunocompetent rats survived long-term. These results suggest the participation of T-cells in the mechanism of tumor control in MBRT. Immunodeficient rats treated with seamless irradiation responded to the treatment (62.5 % long-term survival free of tumor), which suggests a fundamentally distinct mechanism of tumor control between conventional RT and MBRT. Furthermore, differences in the immune cell population and T-cell infiltration were observed, with a higher proportion of cytotoxic T-cells in the MBRT-irradiated group with respect to the conventional RT one at 48 h after irradiation. Similar results, in terms of response to the treatment of immunocompetent and immunodeficient rats, were found following pMBRT [Bertho *et al.* 2021a]. Also, an increased proportion of infiltrating CD4+ T-cells was detected in the tumor after pMBRT, compared to conventional proton therapy. The determinant role of the immune system in the response to SFRT techniques opens the door to the combination of these techniques with immunotherapy [Prezado 2022]. Preclinical studies showed that gene-mediated immunotherapy increases the efficacy of MRT in the treatment of central nervous system tumors [Smilowitz *et al.* 2006]. A percentage of 44 % of glioma-bearing rats treated with MRT combined with immunotherapy survived for a year after therapy, which represents a 2-fold increase with respect to the group treated with MRT alone. The combination of immunotherapy (immune checkpoint blockade) with LRT also resulted in greater effects than traditional debulking results (i.e., complete tumor eradication) [Jiang *et al.* 2021].

*Due to the central role of proton minibeam radiation therapy in this thesis, the dosimetric, technical, clinical, and biological aspects of this technique are described in detail in the following section.*

#### 1.4.4 Proton minibeam radiotherapy

Proton minibeam radiation therapy (pMBRT) was first proposed in 2013 by Prezado and Fois [Prezado & Fois 2013] and represents the most explored combination of MBRT with charged particles so far. This approach combines the spatial fractionation of the dose with submillimetric proton beams. The rationale behind this alliance is the increase in the therapeutic index with respect to MBRT. Proton minibeam presents several advantages, in terms of dose modulation, compared to X-ray minibeam: i) a significant spatial modulation is maintained at clinically relevant energies; thus, the treatment of deep-seated tumors is possible; ii) no dose is deposited after the Bragg peak; and iii) the widening of minibeam in-depth creates a homogeneous dose distribution at the end of the range with only one array while preserving the pattern of peak and valleys at shallow depths (see Figure 1.42). In addition, the distinct biological properties of protons compared to X-rays, e.g., more clustered and less repairable DNA damage (see Section 1.3.3), may trigger a more favorable tumor response.

*The next subsections of this chapter aim to describe in more detail the dosimetric, technical, preclinical, and clinical aspects of this technique.*

#### 1.4.4.1 Dosimetric aspects

Dose profiles in pMBRT differ from dose distributions in standard PT. Regarding the depth dose profile of a proton minibeam, the ratio between the dose at the Bragg peak (BP) and the entrance dose is reduced compared to seamless conditions [Prezado & Fois 2013], i.e., the BEDR decreases. This is caused by the scattering of primary protons away from the minibeam axis, reducing the fluence and hence the dose at the peak region in depth. Contrary to seamless conditions, the amount of protons removed from the beam axis is not compensated by in-scattered particles. Then, the maximum dose is located at shallow depths and not at the end of the range. This phenomenon, called Bragg peak degradation, was documented by Larsson in 1967 [Larsson 1967] for beams smaller than 3 cm in diameter. Figure 1.45a shows a PDD profile along the minibeam axis. The magnitude of the reduction in BEDR depends on the shape of the minibeam; pencil-shaped minibeam exhibit a lower BEDR than planar minibeam of the same width due to the lack of lateral scattering equilibrium in two directions instead of only one. This effect also depends on the minibeam size; wider minibeam show a higher BEDR [Peucelle *et al.* 2015b]. As opposed to peaks, valley doses exhibit an increase in depth, reaching a maximum at the end of the range (see Figure 1.45a) [Peucelle *et al.* 2015b]. This increment is caused by the contribution of protons scattered from minibeam paths to the dose in valley regions. When the dose is integrated over all the irradiated area (i.e., minibeam and space between them), the PDD profile resembles seamless irradiation dose distributions, exhibiting a maximum at the BP position [Prezado & Fois 2013]. Regarding the dose modulation, the decrease in the peak dose and increase in the valley dose causes the reduction of the PVDR in depth (see Figure 1.45b). The scattering also leads to a broadening of minibeam, i.e., peak full-width at half maximum (FWHM) increases in depth [Peucelle *et al.* 2015b], as illustrated in Figure 1.45c.

The composition of peaks and valleys, in terms of the type of particle contributing to the dose, also varies in depth. Dose at peak regions is mainly deposited by primary protons along the minibeam range. Secondary particles ( $\delta$ -rays before the BP and nuclear products at the vicinity of the BP) only contribute up to 10 % to the peak dose [Peucelle 2016]. Figure 1.46a and Figure 1.46b illustrate the composition of peaks in-depth and the contribution to the peak dose of different species of secondary particles, respectively. Regarding valley regions, secondary particles are the main contributor to the dose at shallow depths (up to 3 cm depth in water for a 100 MeV beam). At deeper positions, primary protons fill out valley regions due to the Coulomb scattering, being the main responsible for the increase in the valley dose [Peucelle 2016]. Figure 1.46c shows the contribution of primary and secondary particles to valley dose as a function of depth. Species of secondaries that contribute the most to valley doses are fragmentation products (e.g., secondary

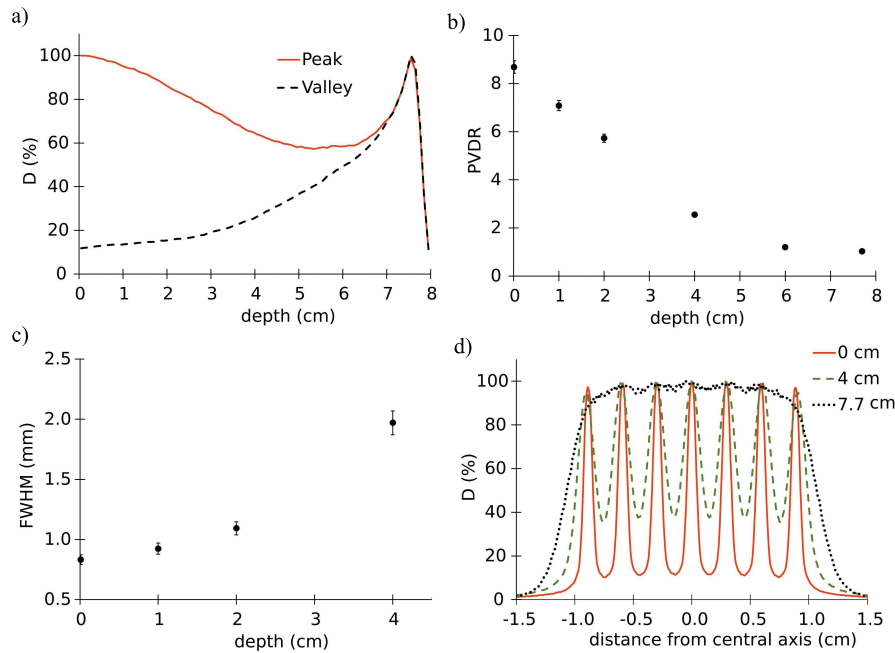


**Figure 1.45:** (a) Depth dose profile in water at peak and valley regions, (b) PVDR and (c) peak FWHM as a function of depth in water, and (d) lateral dose profiles at several depths in water of an array of seven 100 MeV minibeam arrays. The slit width of the collimator considered is  $400 \mu\text{m}$ , and the c-t-c distance 2.8 mm.

protons) (see Figure 1.46d). However, a significant proportion of the secondary particles at the proximal edge of the Bragg peak are  $\delta$ -electrons produced by the interaction of fragments with the medium. The different composition of peaks and valleys may lead to slight differences in the LET and, consequently, in the RBE. In the study by Lansonneur *et al.* [Lansonneur *et al.* 2020], the LET at peaks and valleys at 5 cm depth in a human head for 115 to 150 MeV beams was 3 and 1  $\text{keV}\cdot\mu\text{m}^{-1}$ , respectively. The derived RBE, calculated using models for conventional PT [McNamara *et al.* 2015] with a dose per fraction set at 2 Gy, varied from 1.1 to 1.4 at peak and valleys, respectively. However, models adapted to the distinct biological mechanisms triggered by pMBRT irradiations need to be developed to extract reliable conclusions about the different biological doses at peaks and valleys.

pMBRT lateral dose profiles are characterized by a succession of high-dose (peak) and low-dose (valley) areas. The degree of heterogeneity decreases in-depth, as Figure 1.45d shows, due to the lateral scattering of primary protons. Therefore, the combination of protons and MBRT allows to achieve homogeneous dose distributions at the BP position (target volume) and a high spatial dose fractionation at shallow depths (normal tissues) using only one minibeam array (see Figure 1.47). This may represent an advantage over X-ray minibeam arrays, where interlacing multiple arrays is needed to obtain uniform dose distributions in-depth, increasing the complexity of treatments [Prezado & Fois 2013].

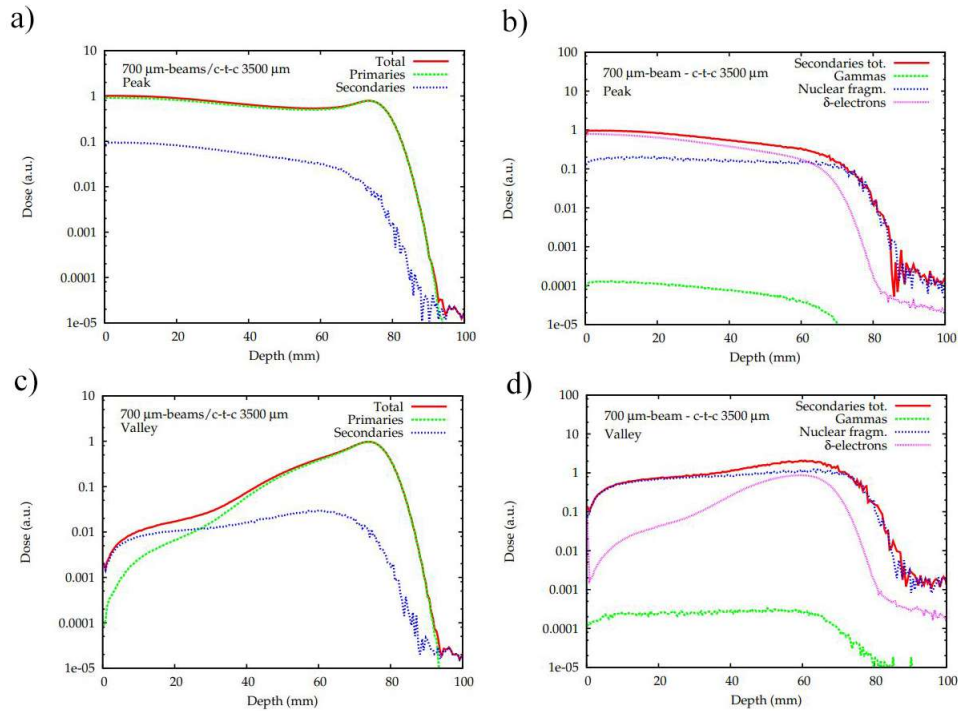


**Figure 1.46:** Contribution of primary and secondary particles to (a) peak and (c) valley doses in-depth, and proportion of different species of secondary particles at (b) peaks and (d) valleys. An array of five minibeam (0.7 mm width; 3.5 mm c-t-c distance) and a monoenergetic 100 MeV field were considered. Taken from [Peucelle 2016].

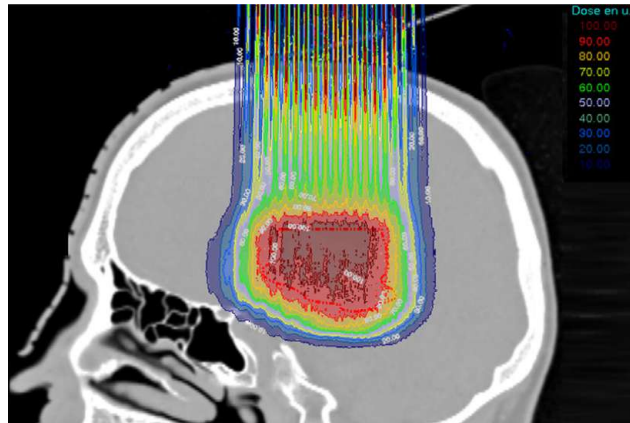


**Figure 1.47:** Dose distribution of a pMBRT plan for the treatment of a glioma. Adapted from [De Marzi *et al.* 2019b].

Besides the dosimetric advantages of pMBRT over MBRT described above, the more favorable ballistics of protons, i.e., their inverse depth dose profile, prevents the irradiation of normal tissue located behind the Bragg peak.

#### 1.4.4.2 Technical aspects

The first worldwide technical implementation of pMBRT was performed in 2014 at one of the passive beamlines of the Institut-Curie Proton Therapy Center (ICPO) in Orsay, France [Peucelle *et al.* 2015b]. Four years after, in 2018, this technique was also implemented at the PBS beamline of the same center [De Marzi *et al.* 2018]. Regarding the implementation of pMBRT, the PBS mode provides several advantages over the passive scattering technique: higher-dose rates (up to several grays per second) can be achieved, neutron production is reduced, and the dose conformity is improved due to possibility of using the intensity modulation [De Marzi *et al.* 2019b]. In the following years, three other institutions implemented pMBRT: the Technical University in Munich, Germany (preclinical facility) [Girst *et al.* 2016], the University of Maryland/MD Anderson, USA [Dilmanian *et al.* 2015a], and the University of Washington in Seattle, USA [Lee *et al.* 2016]. A summary of the research with proton minibeam performed in those facilities can be found in the review of Meyer *et al.* [Meyer *et al.* 2019].

Proton minibeam at clinical centers are typically produced by mechanical collimators placed at the nozzle exit. These collimators contain several submillimetric apertures that shape the minibeam from a broad beam field created at the collimator entrance (see Figure 1.48a).

Two main types of collimator geometries may be used: pinhole (pencil-shaped) [Charyyev *et al.* 2020] and planar [De Marzi *et al.* 2018, Guardiola *et al.* 2017] minibeam collimators. Figure 1.49 presents a schematic design of planar and pinhole minibeam collimators. Pencil-shaped minibeam are characterized by a submillimetric FWHM in two dimensions, while planar minibeam are a few millimeters to a few centimeters long in one direction. Pinhole minibeam are organized in two-dimensional patterns (e.g., hexagonal), whereas the arrangement of planar minibeam is a one-dimensional array. Planar minibeam offer an easier collimator custom manufacturing and higher production yield (collimator's transmission) than pinhole minibeam, making them more suitable for clinical translation [Dilmanian *et al.* 2015a]. In addition, as described in Section 2.1.3, planar minibeam provide higher BEDR and less degraded dose distributions at peak regions. However, they offer lower spatial dose fractionation (i.e., lower PVDR) [Schneider 2020]. Planar minibeam collimators are typically designed according to the methodology described in Guardiola *et al.* [Guardiola *et al.* 2017]. However, the design may need to be adapted to the beam delivery method. Generally, collimators need to be divergent, i.e., the slit tilt follows the beam divergence. This is especially relevant for PBS nozzles due to the large beam divergence (small source-to-isocenter distance). De Marzi *et al.* [De Marzi *et al.* 2018] showed that divergent collimators in a PBS beamline provide a higher degree of homogeneity in peak doses along the lateral dose profile and smaller lateral penumbra. In passive-scattering beamlines with a low beam divergence, the tilt of the slits does not significantly affect dose distributions [Guardiola *et al.* 2017].

Regarding other collimator specifications, the influence on dose distributions of

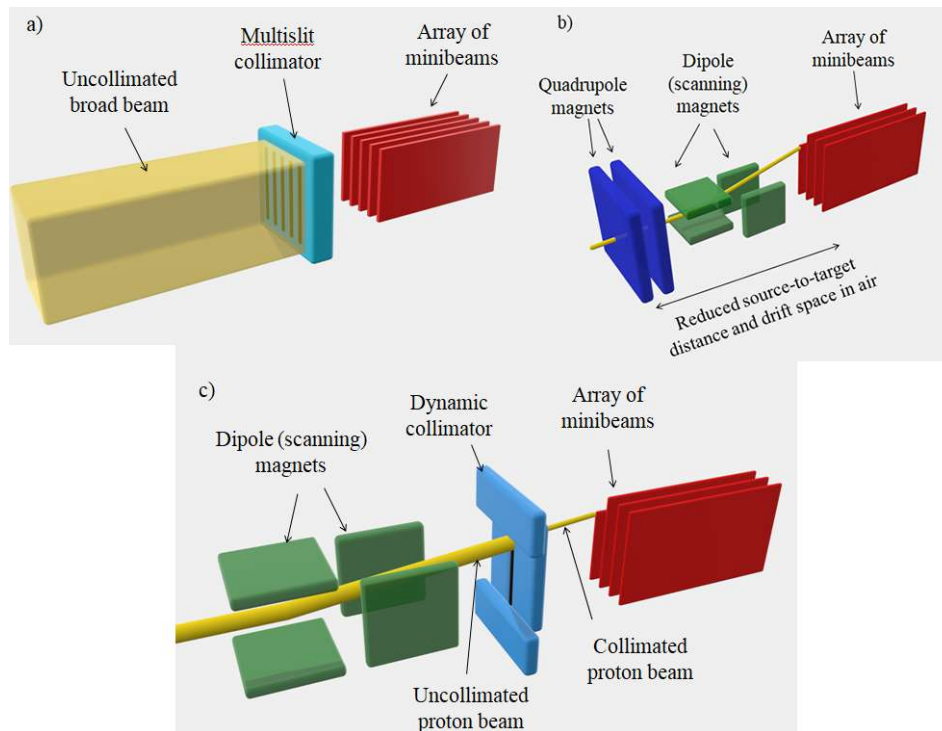


**Figure 1.48:** Schematic representation of three methods for producing minibeam arrays. (a) Multislit collimator: A collimator with several submillimetric apertures is placed in front of a seamless field to shape minibeam arrays. (b) Magnetic focusing: A pair of quadrupole magnets, a reduced source-to-target distance, and a shorter drift space in the air allow focusing the proton beam up to submillimeter beamlet sizes. (c) Dynamic scanning collimator: A dynamic collimator creates single slits of the required shape and then moves a given distance ( $c$ - $t$ - $c$  distance) to produce other minibeam arrays. In this method, the beam spot follows the shape of each aperture.

the  $c$ - $t$ - $c$  distance between minibeam arrays, slit width, and collimator thickness has been studied theoretically and experimentally [Guardiola *et al.* 2017, Lee *et al.* 2016, Peucelle *et al.* 2015b]. For instance, higher PVDRs result from a reduction in the slit width and an increase in the collimator thickness and  $c$ - $t$ - $c$  distance. Therefore, collimator characteristics may also influence the biological response of tissues [Meyer *et al.* 2019]. Irradiation and treatment requirements influence the selection of collimator specifications. For instance, the compromise between dose homogeneity in the target and the spatial fractionation in normal tissues strongly correlates with the slit spacing and width [De Marzi *et al.* 2018]. Collimators employed in pMBRT are commonly made of brass material since it provides the best compromise between manufacturing cost, micro-etching, maximization of PVDR, and minimization of minibeam penumbras and neutron contamination, with respect to other materials such as tungsten, nickel or iron [Guardiola *et al.* 2017]. Guardiola *et al.* [Guardiola *et al.* 2017] showed that the biological neutron dose in the patient remains below 1 % of the total absorbed dose with these collimators.

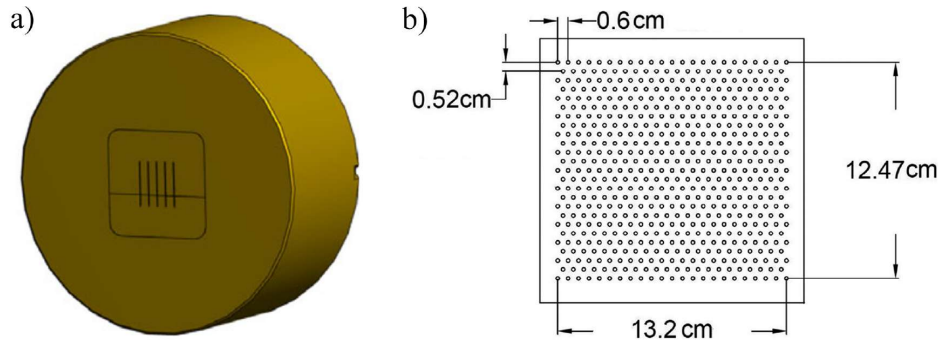


**Figure 1.49:** Schematic representation of a (a) planar and (b) pencil-shaped minibeam collimators. Adapted from [De Marzi *et al.* 2018] and [Charyyev *et al.* 2020], respectively.

Although mechanical collimators are easily implementable in current clinical facilities [Dilmanian *et al.* 2015a], they present several drawbacks, i.e., the reduction of the dose rate [Charyyev *et al.* 2020], the increased production of secondary neutrons, and their inflexibility (a different collimator needs to be manufactured for each irradiation pattern) [Schneider 2020]. Several generation methods have been proposed recently to overcome those limitations, such as dynamic collimators [Sotiropoulos & Prezado 2021] or magnetic focusing [Schneider *et al.* 2020]. The latter consists of generating submillimeter beamlets by using quadrupole magnets to focus down the incoming proton beam. While these focusing magnets are usually part of conventional PBS nozzles, the new nozzle design features a more compact arrangement of the components and, crucially, a significantly reduced focal length (quadrupole-to-target distance) as well as a shorter drift space in air (see Figure 1.48b). This method would allow more flexible and efficient treatments than mechanical collimators since there is no need for specific hardware for each irradiation pattern (i.e., collimators), and the dose rate is increased [Schneider *et al.* 2020]. It also provides lower valley doses and higher PVDRs [Peucelle 2016]. The dynamic scanning collimator consists of a single slit collimator, which can modify the slit width and length dynamically [Sotiropoulos & Prezado 2021]. It can be repositioned to create an array of minibeamlets with the desired *c-t-c* distance. In the PBS mode, the beam spot is positioned within the aperture and moves following its shape (see Figure 1.48c). This method provides increased flexibility as compared to multislit collimators. However, none of these two methods has been implemented in clinical facilities yet.

#### 1.4.4.3 Preclinical results in pMBRT

pMBRT has already proven its efficacy in terms of gain in the therapeutic index, compared to conventional techniques, in several preclinical studies.

Most preclinical evaluations have been performed either in naive or glioma-bearing rats [Bertho *et al.* 2021b, Lamirault *et al.* 2020b, Lamirault *et al.* 2020a, Prezado *et al.* 2018, Prezado *et al.* 2017b, Prezado *et al.* 2019]. These studies

showed an increase in the normal tissue tolerance compared to standard proton therapy (PT). In the long-term (6-month) study by Prezado *et al.* [Prezado *et al.* 2017b], rats treated with pMBRT showed no significant brain damage and only reversible skin epilation at peak doses of 58 Gy and 25 Gy mean dose. Contrarily, animals exposed to PT at the same mean dose exhibited severe moist desquamation and substantial brain damage (necrosis, demyelination, astrogliosis, and microglial activation). In addition, the study by Lamirault *et al.* [Lamirault *et al.* 2020b] showed that pMBRT has no significant impact on the cognitive, motor, or emotional functions of treated rats ten months after irradiation. Studies in mouse models reported similar results in the skin. Contrary to pMBRT treatments, mice irradiated with seamless irradiations presented ear swelling, erythema, desquamation, and loss of sebaceous glands [Girst *et al.* 2016]. A decreased cell death and inflammatory response were also observed in pMBRT irradiations as compared to PT at the same mean dose [Zlobinskaya *et al.* 2013].

Preclinical data have also shown an increase in the survival rate following pMBRT irradiation, as compared to PT at the same mean dose, suggesting equivalent or superior tumor control effectiveness [Lamirault *et al.* 2020a, Prezado *et al.* 2018, Prezado *et al.* 2019]. pMBRT irradiations using one array of minibeam in one fraction resulted in 67 % long-term survival rates in RG2 glioma-bearing rats, a 3-fold increase compared to treatments with standard PT (see Figure 1.50a) [Prezado *et al.* 2019]. Even higher rates of free-tumor survival rates (up to 83 %) were achieved in the work by Bertho and Ortiz *et al.* [Bertho *et al.* 2021b] when the dose was delivered in two fractions using a crossfire geometry. In these studies, tumor ablation was achieved by delivering a heterogeneous dose distribution to the target (see Figure 1.50b), i.e., a significant fraction of the volume received non-tumorcidal doses (valley doses). However, higher tumor control was achieved in pMBRT [Prezado *et al.* 2019]. These results seem to contradict the paradigm of conventional PT, which assumes that a lethal dose of radiation needs to be deposited in each tumor cell to control the tumor. The mechanisms involved in this distinct tissue response to minibeam were presented in Section 1.4.3.

#### 1.4.4.4 Future clinical implementation

The promising data reported in preclinical studies (see Section 1.4.4.3) support the preparation of clinical trials [Prezado 2022].

At the time of writing this manuscript, Phase I/II clinical trials are being planned at our institution (ICPO). The trials are designed in two phases. Phase I will assess the acute and late (6-month) neurotoxicity (e.g., radiation necrosis (RN)) following pMBRT irradiations at different doses. The second one will evaluate the control rates at 6 months of recurrent glioblastoma multiforme (GBM). The inclusion criteria for these investigations are based on three main points: (i) patients must have radiographic evidence by MRI of brain metastases outside the brainstem, (ii) patients must have at most four metastases (one of them must have its longest diameter larger than 2 cm and smaller than 4.0 cm), and (iii) their Performance

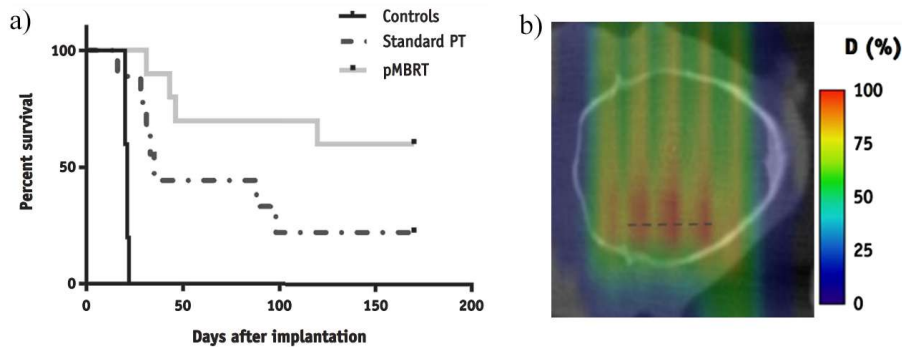


**Figure 1.50:** (a) Survival curves of non-irradiated (controls) rats, and groups treated with standard proton therapy and pMBRT. (b) Example of dose distributions in a pMBRT treatment. The dotted black line represents the tumor depth. Taken from [Prezado *et al.* 2019].

Score should be 0-2 and the life expectancy larger or equal than 3 months.

The aim of these studies is to prove the safety and efficacy of pMBRT for treating unresectable large ( $> 3$  cm in diameter) brain metastases (BM) and focal recurrence of GBM. These two types of cancer develop frequently in adults; GBM accounts for 80 % of all malignant brain tumors [Goodenberger & Jenkins 2012] and BM occur in up to 50 % of cancer patients [Schouten *et al.* 2002]. The treatment of these two clinical indications with conventional RT techniques (e.g., stereotactic radiosurgery [Mitchell *et al.* 2022]) has a poor prognosis. The median survival for GBM is 12 to 15 months [Kudulaiti *et al.* 2021] and 6 to 12 months for BM [Mitchell *et al.* 2022]. The rationale behind the poor outcome of RT treatments is that the requested dose escalation to reach higher local control rates is compromised by the risk of toxicities to surrounding organs and the normal brain. The major complication is RN, occurring in 25 to 34 % of patients treated with conventional RT [Ali *et al.* 2019]. RN could lead to neurological dysfunction. The improvement of the prognosis using other conventional modalities (e.g., proton therapy) may be limited due to the large tumor volumes. For instance, the study by Atkins *et al.* [Atkins *et al.* 2018] reported similar rates of local recurrence, acute toxicity, and RN as photon-based radiosurgery when treating BM with proton therapy. pMBRT seems to be a promising candidate to treat these indications since it drastically reduces the neurotoxicity in the normal brain while providing equivalent to or superior tumor control than conventional techniques (according to preclinical data). This would allow increasing the therapeutic index by using more aggressive schemes, which would increase the rates of tumor control without significant toxicity. Also, the reduced neurotoxicity of proton minibeam may allow the irradiation of large brain volumes, which may improve the rates of eradication of infiltrative tumors such as gliomas [Prezado 2022] and the treatment of multiple BM [Meyer *et al.* 2019].

In the context of the preparation of these clinical trials, Lansonneur *et al.* [Lansonneur *et al.* 2020] performed the first treatment plan evaluation in glioma and meningioma cases using a clinical setup. This study proved the feasibility

of obtaining dose distributions within the target recommended for standard PT (homogeneous dose distributions with  $\pm 7\%$  variation) while maintaining high spatial dose fractionation in normal tissues (see Figure 1.51). Therefore, a similar gain in the therapeutic index as obtained in preclinical studies could be expected in the clinical treatment of those malignancies.

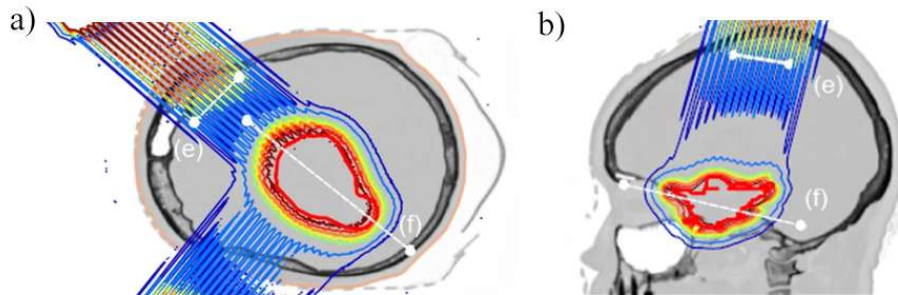


**Figure 1.51:** Dose distributions in a pMBRT treatment plan for (a) glioma and (b) meningioma cases. The planning target volume (PTV) is displayed in red color. Taken from [Lansonneur *et al.* 2020].

A part of the work of this PhD thesis deals with the preparation of Phase I clinical trials in brain metastases. This preparation includes a treatment plan comparison between conventional RT techniques and pMBRT, the optimization of the irradiation setup, and proposing dosimetric protocols adapted to pMBRT. A summary of the work outline in this thesis can be found in Section 1.5.

Besides BM and GBM, other indications whose local control could be improved with more aggressive treatments but nowadays are limited by the significant normal tissue toxicity may benefit from pMBRT. This is the case of highly radio-resistant tumors such as osteosarcoma, chordoma, chondrosarcoma, locally advanced bronchial cancer, or unresectable Ewing's sarcoma [Meyer *et al.* 2019]. Another clinical application of pMBRT might be the treatment of low-risk tumors (e.g., lymphomas, low-grade gliomas, or benign lesions), which may benefit from the reduced side effects of pMBRT [Meyer *et al.* 2019]. In addition, pMBRT could reduce skin toxicity in RT treatments thanks to the high spatial fractionation of the dose at shallow depths [Meyer *et al.* 2019]. Acute radiation dermatitis remains a side effect in up to 95 % of patients that receive RT [Rosenthal *et al.* 2019]. Moreover, indications suitable for MRT [Fardone *et al.* 2018], such as trigeminal neuralgia, epilepsy, or other neurological diseases, may also be treated with pMBRT. Dilmanian *et al.* [Dilmanian *et al.* 2015a] suggested the use of proton minibeam also for current hypofractionated treatments, particularly for lung and liver tumors.

Radioprotection calculations considering the clinical setup that will be used in the potential pMBRT clinical trial have also been performed. Leite *et al.* [Leite *et al.* 2021] assessed the secondary neutron dose contribution of pMBRT collimators to different organs in clinically relevant intracranial treatments. Results from that work conclude that the neutron ambient equivalent dose in pMBRT is higher than in conventional PBS treatments but lower than in passive scattering

PT. In addition, the neutron dose to organs close to the target is higher in pMBRT than in conventional PT, however, organs situated furthest from the target receive a larger quantity of neutrons in passive-scattering PT treatments than in pMBRT. Overall, the study provides the first insight into performing epidemiological studies of the long-term effects of pMBRT treatments.

## 1.5 Work outline

The main work performed during this PhD thesis focused on defining new dosimetry standards for pMBRT preclinical and clinical trials.

The dosimetry for preclinical investigations involved both experimental acquisitions and Monte Carlo simulations. As the starting point of these studies, the suitability of different dosimeters to measure pMBRT dose distributions and the good parametrization of our Monte Carlo codes were tested by comparing measured and simulated dosimetric quantities (Section 3.2). Once the performance of detectors and simulation codes was assessed, different studies were performed with the objective of establishing a set of guidelines and protocols to ensure reproducible dosimetry in the current preclinical trials performed at our institution. These investigations consisted of a robustness analysis of the sensitivity of pMBRT dose distributions to different setup and irradiation parameters (Section 3.3). Based on the results obtained, a methodology to optimize the irradiation parameters was designed (Section 3.4). In addition, guidelines and a dosimetric protocol were proposed to perform robust and reproducible dosimetry in *in vivo* preclinical trials (Section 3.5 and 3.6). Then, dose distributions in preclinical studies performed at our institution were computed and evaluated (Section 3.7).

Whereas the first part of the thesis focused on preclinical conditions, the second segment investigated the clinical potential of pMBRT. Firstly, the potential benefits of treating brain, liver, and lung metastases (some of the clinical indications candidates for the potential clinical trials) were evaluated by comparing dose distributions in pMBRT plans with the standard of care for these malignancies in our institution (i.e., stereotactic radiotherapy) and PT treatments (see Chapter 4). Secondly, the possibility of combining pMBRT and arc therapy for the treatment of brain lesions was evaluated in a treatment plan study by assessing the potentially improved dose and LET distributions when delivering proton minibeam through arcs (see Chapter 5). In those investigations, the influence of pMBRT plan parameters on dose distributions was also studied to provide a first insight into the treatment plan optimization possibilities in pMBRT.

# Materials and methods

---

## Contents

---

<b>2.1</b>	<b>Experimental dosimetry</b>	<b>89</b>
2.1.1	Description of ICPO facility	89
2.1.2	Implementation of pMBRT at ICPO	90
2.1.3	pMBRT dosimetry	92
2.1.4	Preclinical dosimetry in pMBRT	100
<b>2.2</b>	<b>Monte Carlo simulations</b>	<b>107</b>
2.2.1	The Monte Carlo method	108
2.2.2	TOPAS simulations toolkit in medical physics	109
2.2.3	Simulation details	111
<b>2.3</b>	<b>Treatment planning studies</b>	<b>116</b>
2.3.1	Software	117
2.3.2	Treatment planning in pMBRT	117

---

*This chapter describes the materials and methods employed in this PhD thesis. It is divided into three main parts: experimental dosimetry, Monte Carlo simulations, and treatment planning for pMBRT dosimetric studies. They are described in detail in the three following sections.*

## 2.1 Experimental dosimetry

*An important part of this thesis involves experimental measurements for different pMBRT studies at the Orsay Proton Therapy Center (ICPO). This section briefly describes this facility and the implementation of pMBRT at it. In addition, the challenges of minibeam dosimetry are discussed, and the detectors and adapted dosimetry protocols employed are described. Finally, it presents the details of the experimental campaigns performed during this thesis.*

### 2.1.1 Description of ICPO facility

The Institut Curie Orsay Proton Therapy Center (Institut Curie - Centre de Protonthérapie d'Orsay, ICPO) is a clinical facility initially built in 1991 in Orsay (France). The center is equipped with a C235 isochronous cyclotron (IBA, Belgium) which supplies three treatment rooms. Two rooms have horizontal

fixed beamlines operating in a passive scattering delivery mode. They are mainly devoted to intracranial [Noel *et al.* 2003] and ocular [Dendale *et al.* 2006] treatments. Maximum beam energies in these rooms are 201 and 76 MeV, corresponding to proton ranges of 26 and 4 cm in water, respectively. The third room consists of an isocentric 360° rotating gantry designed for beam energies between 100 and 230 MeV. The gantry is equipped with a IBA ProteusPlus universal nozzle (i.e., it can operate in passive scattering and PBS delivery mode). This room is primarily dedicated to pediatric treatments nowadays. In this thesis, the PBS beamline was considered since it provides several advantages in generating minibeam using mechanical collimators compared to the passive scattering mode, such as higher dose rates and reduced neutron production [De Marzi *et al.* 2018]. The main components of the PBS beamline are presented in Figure 2.1. The function of such elements is described in Section 1.3.2.

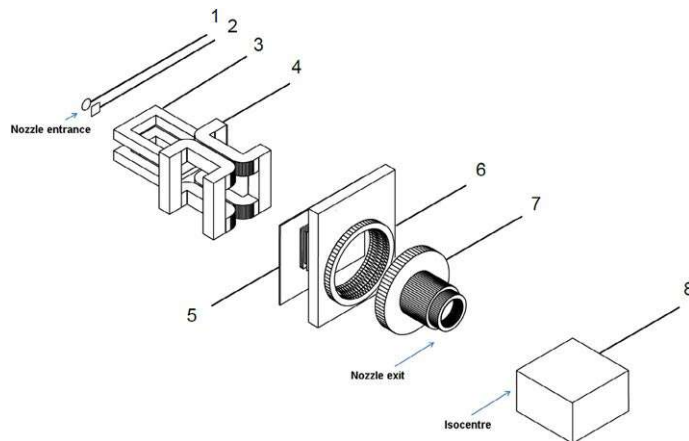


**Figure 2.1:** ICPO PBS beamline: (1) exit window, (2) first ionization chamber, (3)-(4) scanning magnets, (5) second ion chamber, (6) snout holder, (7) snout, and (8) target volume. Taken from [De Marzi *et al.* 2019a].

*The following subsection describes the implementation of pMBRT at this facility for preclinical studies and clinical trials.*

### 2.1.2 Implementation of pMBRT at ICPO

pMBRT was implemented at the PBS beamline of the ICPO in 2018 [De Marzi *et al.* 2018]. At this facility, proton minibeam are shaped by means of mechanical collimators. These collimators consist of a 6.5-cm-thick brass cylinder with a rectangular insert of one (single-slit) or several (multi-slit)  $400 \pm 50\text{-}\mu\text{m}$ -wide slits. The thickness of these collimators was chosen to resemble the apertures used in the clinical routine at this beamline. pMBRT collimators were designed in a divergent geometry, i.e., the slit tilt follows the beam divergence, which depends on the virtual source-axis, pencil beam transverse position, and collimator-axis distances [De Marzi *et al.* 2018]. The slit divergence is defined as the angle of a

given slit with respect to the line orthogonal to the collimator surface. The rationale behind the use of this design has been described in Section 1.4.4.2. Collimators used in this work can be classified depending on their primary purpose: small-animal preclinical studies or future clinical trials.

For small-animal irradiations, collimators with various center-to-center (*c-t-c*) distances were manufactured to study tumor and tissue responses as a function of beam spacing and peak and valley doses. The number of slits also differs from collimator to collimator to study the effect of the total irradiation area. In all cases, the slit height was 2 cm since it allows the irradiation of the entire rat's brain (animal model chosen for *in vivo* studies). Table 2.1 presents the collimator specifications and an example of these collimators can be found in Figure 2.2a. In addition to pMBRT collimators, a broad beam aperture was also manufactured to compare pMBRT with conventional PT (see Figure 2.2b). The size of this aperture is  $1.6 \times 2.0 \text{ cm}^2$  to cover the same area as pMBRT arrays.

The collimator prototype designed for human treatments consists of 15 slits separated by a *c-t-c* distance of 4 mm, covering a  $5.6 \times 5.64 \text{ cm}^2$  area (see Figure 2.2c). This collimator was designed for a potential pMBRT clinical trial (see Section 1.4.4.4), where the target volume will be metastases of 2 to 4 cm in diameter. *In vitro* studies [Bertho 2022] also use this collimator because the larger area allows the irradiation of several cell wells simultaneously, which notably reduces the study's total irradiation time. All the pMBRT collimators presented in this section were manufactured by means of electrical discharge machining, which is described elsewhere in the literature [Ho & Newman 2003].

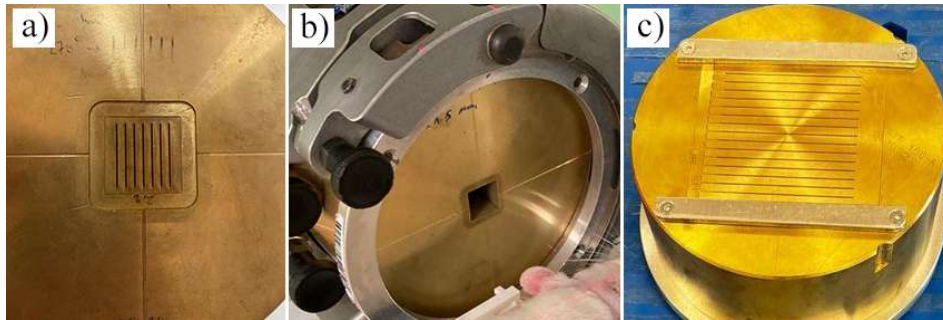


**Figure 2.2:** Examples of collimators used in this work. (a) Five slit-collimator with 2.8 mm *c-t-c* distance (collimator 2 in Table 2.1), and (b)  $16 \times 20 \text{ mm}^2$  broad beam collimator (collimator 7 in Table 2.1), both for small animal irradiations. (c) Collimator with fifteen slits and 4 mm *c-t-c* distance for clinical purposes (collimator 8 in Table 2.1).

Collimators for *in vivo* preclinical studies (collimators 1 to 7 in Table 2.1) were designed to be placed in the upstream part of the snout (i.e., the downstream surface of the collimator and snout match). This is the position where the collimators are typically located in the clinical routine. Then, the range shifter (RS) in pMBRT irradiations had to be placed after the collimator in the beamline (see Figure 2.3a). This configuration significantly reduces the spatial fractionation of the dose in the target due to the additional amount of material minibeam pass through if a RS

Purpose	Collimator number	Number of slits	c-t-c * distance	Slit width	Irradiation area
Small-animal irradiation	1	1	-	400 $\mu\text{m}$	400 $\mu\text{m}$ x 2 cm
	2	5	2.8 mm	400 $\mu\text{m}$	1.16 x 2 cm <sup>2</sup>
	3	7	2.8 mm	400 $\mu\text{m}$	1.72 x 2 cm <sup>2</sup>
	4	5	2.0 mm	400 $\mu\text{m}$	1.04 x 2 cm <sup>2</sup>
	5	5	4.0 mm	400 $\mu\text{m}$	1.64 x 2 cm <sup>2</sup>
	6	9	2.0 mm	400 $\mu\text{m}$	1.64 x 2 cm <sup>2</sup>
	7	Broad beam collimator			
Clinical trials/ cell irradiations	8	15	4.0 mm	400 $\mu\text{m}$	5.64 x 5.6 cm <sup>2</sup>

**Table 2.1:** Specifications of collimators employed in the implementation of pMBRT at the ICPO. \*c-t-c stands for centre-to-centre.

needs to be used (often the case for human patients). The collimator design for clinical purposes (collimator 8 in Table 2.1) was optimized to place the pMBRT collimator as close as possible to the patient in order to minimize the air gap and lateral penumbra, and thus obtain higher PVDRs. In this configuration, the collimator was located at the downstream part of the snout. Then, the RS could be placed at the position of clinical collimators in the snout (see Figure 2.3b). This setup allows the degradation of the beam energy without reducing the dose modulation in the patient.

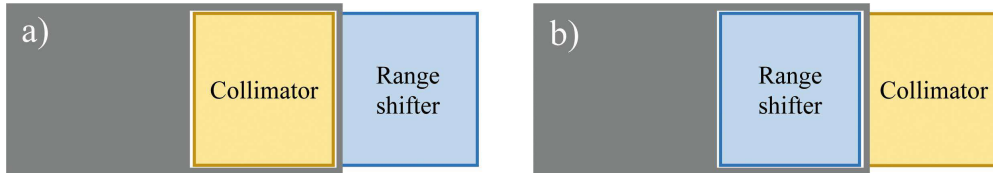


**Figure 2.3:** Representation of the collimator attachment into the snout for collimators dedicated to (a) small-animal irradiations (collimator 1 to 7 in Table 2.1) and (b) clinical trials (collimator 8 in Table 2.1).

*The dosimetry for such narrow beams requires using detectors and protocols different from the ones employed in conventional broad beam RT. The next section discusses these additional considerations.*

### 2.1.3 pMBRT dosimetry

*The very small beam sizes (400 to 1000  $\mu\text{m}$ ) used in pMBRT frame the technique within the small-field dosimetry domain. This section discusses the dosimetric challenges associated with those narrow beams, as well as suitable dosimeters and protocols.*

### 2.1.3.1 Small-field dosimetry

A *small irradiation field* is defined as a treatment field that meets at least one of the following three physical conditions: (i) there is a lack of lateral charged particle equilibrium on the beam axis, (ii) there is a partial occlusion of the primary source by the collimating device, or (iii) the beam dimension is similar or smaller than the size of the detector [IAEA 2017]. In these situations, the field size is commonly defined as the full-width-at-half-maximum (FWHM) at the measurement point [IAEA 2017]. Small-field dosimetry involves additional challenges and considerations with respect to dose measurements in large-field (also called broad beam) conditions.

Beam sizes comparable to or smaller than the range of secondary particles contributing measurably to the absorbed dose lead to the loss of lateral charged particle equilibrium (LCPE), i.e., more charged particles scatter out of the field than in-scatter. In this situation, radiation detectors may introduce non-negligible perturbations to the non-equilibrium state [Das *et al.* 2008], which may require applying correction factors [Sotiropoulos & Prezado 2022].

Another challenge in small-field dosimetry is related to the collimation of a field from a source with a finite width into submillimetric beamlets. The collimation device typically produces a partial blocking of the source leading to pronounced and overlapping penumbras [Das *et al.* 2008]. The extension of the geometrical penumbra over the primary beamlet area causes a volume-averaging effect within the detector. The volume averaging effect refers to the measurement of the mean absorbed dose over the sensitive volume of the radiation detector without considering the field's heterogeneity within that area (see Figure 2.4) [IAEA 2017]. This effect is also observed when the detector's active area is larger than the radiation field.

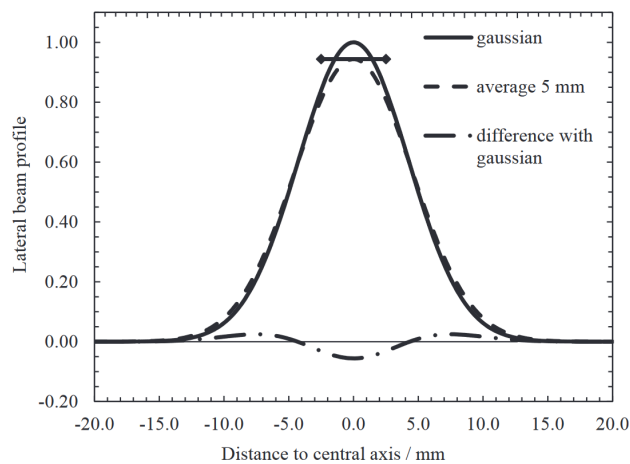


**Figure 2.4:** Illustration of the volume-averaging effect in small-field conditions. The measurement over the sensitive area of the detector (5 mm) misrepresents the small-field dose distribution. Taken from [IAEA 2017].

### 2.1.3.2 Dosimetry protocols in small-field conditions

The physical aspects of small-field dosimetry (described in the previous section) are not considered in the Codes of Practice (COP) for dosimetry in conventional broad beam conditions, e.g., the Technical Report Series (TRS) 398 (described in Section 1.2.1.3). Therefore, some assumptions in these COPs tend to be valid to a lesser extent in small-field conditions. Consequently, adapted COPs have been developed for dosimetry in small-field RT, such as stereotactic treatments, IMRT, or flattening-filter-free (FFF) techniques. A relevant example of those adapted COPs is the IAEA's report for "Dosimetry of Small Static Fields Used in External Beam Radiotherapy" (TRS-483) [IAEA 2017].

Similar to the TRS-398 for broad beam conditions, the TRS-483 provides formalisms for reference and non-reference dosimetry and recommendations on the types of detectors and phantoms to use in small-field dosimetry. The guidelines proposed for determining the absorbed dose to water are based on a two-step protocol: (a) reference dosimetry using ionization chambers (IC) with calibration coefficients provided by primary standard laboratories, and (b) relative dosimetry for the determination of field output factors.

Regarding reference dosimetry, using graphite calorimeters employed in broad beam conditions as a primary standard instrument may be unsuitable due to their large cores compared to field sizes. Those calorimeters rely on core sizes orders of magnitude larger than the millimeter size. In small-field conditions, small-scale calorimeters may need to be used [IAEA 2017]. Millimeter-size graphite core calorimeters have already been used for small-field dosimetry, e.g., Renaud *et al.* [Renaud *et al.* 2018] measured absolute outputs of FFF photon beams with the Aarrow probe (6.1 mm in diameter and 10 mm long core) [Renaud *et al.* 2013], and Christensen *et al.* [Christensen *et al.* 2020] used a graphite calorimeter with a 5 x 7 mm<sup>2</sup> core for measuring 2 x 2 cm<sup>2</sup> proton fields.

Concerning the second step in the protocol, the assumption that dosimetric quantities are independent of the field size when computing output factors is not valid [IAEA 2017]. Therefore, output correction factors may need to be applied.

Regarding suitable detectors, the TRS-483 recommends using ICs for field sizes where the volume averaging effect is not significant and smaller detectors for smaller fields. ICs employed for dosimetry in broad beam conditions are typically not appropriate due to the volume-averaging effect produced by the high dose gradients within their sensitive volume and substantial perturbations in the absence of LCPE [IAEA 2017]. Suitable detectors in these conditions are nearly tissue equivalent radiochromic film, diodes, diamond detectors, vented ICs of a volume smaller than 0.6 cm<sup>3</sup>, and liquid ICs. However, volume-averaging corrections may be required in some cases (e.g., for FFF beams) due to the non-homogeneity of the lateral profile [IAEA 2017]. Volume-averaging correction factors are defined as the ratio of the absorbed dose to water at the reference point in the absence of the detector and the mean absorbed dose to water over the sensitive volume of the detector. In addition, the orientation and alignment of detectors (e.g., diodes and diamond detectors)

should be considered. COPs recommend the detector to be oriented such that the smallest dimension of its sensitive volume is perpendicular to the scanning direction and aligned in such a way that the radiation fluence is approximately uniform over the sensitive volume [IAEA 2017].

The use of detectors different from those considered in conventional RT also involves employing phantoms adapted to hold these detectors and provide high spatial resolution measurements and accurate positioning [IAEA 2017].

Finally, reference measurement conditions may need to be adapted to the distinct physical aspects of small-field dosimetry depending on the technique and machines employed [IAEA 2017]. For instance, the TRS-483 suggests referring dosimetry calculations to 10 g/cm<sup>2</sup> depth for photon beams in LINACs, tomotherapy, and CyberKnife machines, whereas the center of the hemisphere of a given phantom is recommended as reference measurement depth for Gamma Knife machines.

### 2.1.3.3 Dosimetry protocols in pMBRT

Although pMBRT is framed within the small-field dosimetry domain, the smaller beamlet sizes employed (400-1000  $\mu\text{m}$ ) compared to techniques considered in the TRS-483 report (centimeter-size fields) may require additional considerations. As stated in the motivation for developing the TRS-483 report,

*“It is prudent to assume that a detector used for dosimetry in large fields will not perform well in small fields until the contrary is proven by its adequate characterization specifically for use in small fields.”*

Following this rationale, developing new protocols may be required for the clinical implementation of pMBRT. In this context, our team (New Approaches to Radiotherapy, NARA) established a collaboration with the National Physical Laboratory (NPL) (London, United Kingdom) and the ICPO (Orsay, France) to develop an absolute dosimetry method for pMBRT. This work was initiated in the framework of a European project (INSPIRE) and is based on the use of a small-core (16 mm in diameter and 2 mm thickness) calorimeter and ICs to create a protocol for traceable absolute dosimetry. The data analysis of this study will be made by other members of the collaboration and will not be presented in this PhD thesis.

Other protocols for MBRT dosimetry have also been proposed. Prezado *et al.* [Prezado *et al.* 2011] designed an adapted two-step protocol for preclinical trials in white-beam MBRT, inspired by the TRS-483. It consists of, firstly, measuring the reference (absolute) dose in broad beam conditions with ionization chambers following recommendations of the TRS-398 report [IAEA 2001]. Then, peak and valley doses are determined by multiplying/dividing the reference dose by the associated output factor/PVDR (computed by Monte Carlo simulations or relative dosimetry methods) [Prezado *et al.* 2012a].

Regarding dosimeters, some of the detectors recommended by the TRS-483 report have been proven suitable for dose measurements in minibeam conditions,

i.e., radiochromic films, high-resolution diodes, and microdiamond detectors [Guardiola & Prezado 2020, Peucelle *et al.* 2015b]. For instance, De Marzi *et al.* [De Marzi *et al.* 2018] reported a good agreement between pMBRT measurements with the RAZOR diode and Monte Carlo results. In the work by Livingstone *et al.* [Livingstone *et al.* 2016], similar PVDRs were measured with a synthetic diamond detector and Gafchromic films in submillimetric kV X-ray beam conditions. These detectors have an active area smaller than pMBRT field dimensions, which is required to resolve those highly heterogeneous dose distributions. A detailed description of the specific detector models used in this thesis can be found in Section 2.1.3.4.

A part of this thesis focuses on developing dosimetry protocols for pMBRT preclinical trials. The rationale behind the development of these protocols is to ensure robust and reproducible dosimetry, imperative to reliably correlate physical quantities and biological endpoints of treatments in the preclinical stage. A description of the protocol proposed in this thesis for pMBRT preclinical dosimetry can be found in Chapter 3.

#### 2.1.3.4 High-spatial resolution detectors employed in this work

The detectors employed for pMBRT dosimetry in this thesis are:

- i. the PTW-60019 microdiamond detector (PTW, Germany),
- ii. the RAZOR diode (IBA Dosimetry, Germany),
- iii. radiochromic films, in particular, EBT-XD GAFchromic films (Ashland, USA) and Orthochromic OC-1 films (OrthoChrome, 2022),
- iv. and the Lynx detector (IBA Dosimetry).

A general definition of these detector types can be found in Section 1.2.1.4, and the specifications of the precise models employed in this work are presented hereafter.

#### Microdiamond detector

The PTW-60019 microdiamond detector [PTW 2022a] consists of a synthetic diamond with an active cylindrical volume of 1.1 mm radius and 1  $\mu\text{m}$  thickness. When placed perpendicular to the beam (on-edge), as recommended in the TRS-483 [IAEA 2017], the detector's resolution is 1  $\mu\text{m}$  (see Figure 2.5). In the parallel direction to the beam, the dose is averaged over 2.2 mm, not allowing the precise characterization of pMBRT dose profiles due to the steep dose gradients in the dose distributions. In this work, the microdiamond detector was uniquely used to measure lateral dose profiles in the on-edge orientation.

Prior to pMBRT measurements, the microdiamond detector was cross-calibrated in that orientation against a calibrated ppc05 plane-parallel ionization chamber (IBA Dosimetry, Germany) [IBA Dosimetry 2022c] in broad beam conditions (5 x 5  $\text{cm}^2$  field). The obtained calibration factor was 1.0642 nC/Gy, which is comparable

to the nominal response reported by the manufacturer ( $\sim 1$  nC/Gy) [PTW 2022a]. Although the possible impact of the loss of LCPE and the perturbation effects in small-field dosimetry are not fully considered under the broad beam condition employed for this measurement, this method serves as the first approximation for dose determination in pMBRT.

As described in Section 2.1.3.1, perturbation effects in small-field dosimetry arise from the volume-averaging effect and density perturbation. The volume-averaging effect is not expected to significantly affect dose measurements with the solid-state detectors used in this thesis due to their small active area. However, the change in density with respect to the surrounding medium may play a significant role; whereas density perturbation factors are constant in broad beam conditions, they diverge for small fields since the energy spectrum along the profile varies due to the fluctuating energy spectrum [Cervantes *et al.* 2021, Sotiropoulos & Prezado 2022].

Uncertainties in dose measurement with the microdiamond detector arise from the electrometer reproducibility (1 %), the scanning system accuracy ( $\pm 0.1$  mm) (see Section 2.1.4.1), and the standard deviation in the average dose in the peak and valley regions (2 %). A conservative overall uncertainty of 3 % was adopted, following the methodology used by Peucelle [Peucelle 2016].

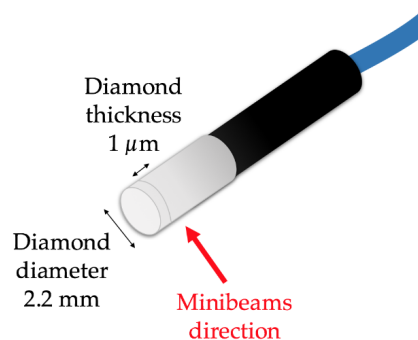


**Figure 2.5:** Representation of the microdiamond orientation for measuring pMBRT lateral dose profiles. The detector is placed on-edge (perpendicular to the minibeam direction) to take advantage of the micrometric size of the active area in this orientation. Taken from [Peucelle 2016].

### Razor diode

The RAZOR diode [IBA Dosimetry 2022d] has a cylindrical active volume of 0.6 mm in diameter and 20  $\mu$ m in length. Like the microdiamond detector, it was placed on-edge to take advantage of the micrometric size of the active volume in this orientation. The RAZOR detector was also used to measure pMBRT lateral dose profiles. The cross-calibration process of this detector reproduced the same methodology used for the microdiamond. The calibration factor for the RAZOR diode employed was 3.425 nC/Gy. The manufacturer reports a sensitivity in the other measurement orientation (i.e., parallel direction to the beam) of 4.1 nC/Gy

[IBA Dosimetry 2022d]. The same uncertainty in dose measurements as for the microdiamond detector was considered for the RAZOR diode.

### Radiochromic films

Radiochromic films (RCF) are a well-established detector for small-field dosimetry due to their high spatial resolution in two dimensions [Carnicer *et al.* 2013] and wide dynamic dose range. According to manufacturers, the films used in this work, i.e., EBT-XD [Gafchromic 2022] and OC-1 [OrthoChrome 2022] films, can effectively measure doses of 0.1 to 40 Gy and 0.1 to 100 Gy, respectively. This allows measuring peak and valley doses simultaneously in pMBRT, contrary to MRT. In MRT, the high dose variations in the beam entrance region may require separate measurements for peak and valley doses due to the limited dynamic range of radiochromic films [Sammer *et al.* 2019].

As described in Section 1.2.1.4, RCFs require post-processing, i.e., their reading using flatbed scanners and posterior conversion of the scanning output to dose using calibration curves. In this work, films were read by an Epson Expression 1200XL scanner at 300 dpi resolution and following the recommendations by Devic *et al.* [Devic *et al.* 2005]. EBT-XD and OC-1 films were scanned using the transmission and reflective modes, respectively, following the manufacturer's instructions. Then, the reading output was the transmittance and reflectance, respectively. The rationale behind using a different methodology to read these two film types is that the EBT-XD coating is transparent, whereas the protective layer of OC-1 films is opaque (see Figure 2.6). Films were scanned in the same orientation as they were irradiated to not introduce variations in the reading due to the film coating.

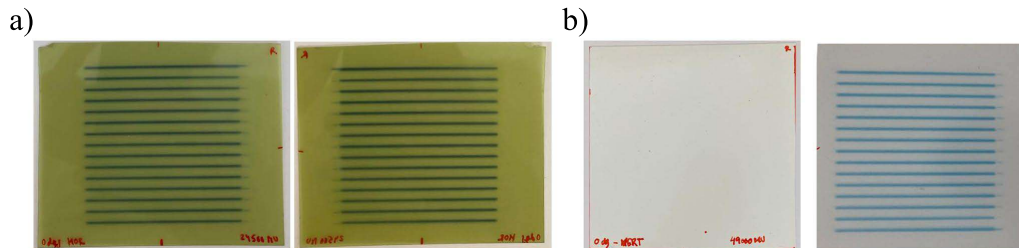


**Figure 2.6:** Examples of irradiated (a) EBT-XD and (b) OC-1 films. Films are presented in two orientations (facing up and down) to illustrate the transparency and opacity, respectively, of their protective coating.

The process of polymerization of the RCF active layer (i.e., colorization) could last several hours after exposure (up to 24 h) [Shima *et al.* 2012]. Then, a non-negligible increase in the optical density, called post-exposure density growth (PEDG), may be expected post-irradiation [Cheung *et al.* 2005]. In this work, the readout of films was performed 43 h after exposure to minimize the uncertainty in PEDG.

The calibration of both film types consisted of irradiating films at a reference position (1 cm depth in solid water) and at different doses along their dynamic

range in broad beam conditions. Three measurements per dose were performed to reduce possible uncertainties due to film inhomogeneities. Then, the reading outputs (transmittance or reflectance) were converted to optical density (OD):

$$OD = -\log_{10} \left( \frac{I}{I_0} \right), \quad (2.1)$$

where  $I$  and  $I_0$  are the readings of the exposed and unexposed (0 Gy) films, respectively. Only the red channel was considered due to its increased sensitivity compared to the green and blue channels. The equivalence of the red-channel reading with the three-channel method has been verified in previous works of the team [Peucelle 2016]. The rational function, recommended by Devic *et al.* [Devic *et al.* 2016], was employed to fit the calibration curve dose-OD. This function can be expressed as:

$$D = a OD + b OD^n, \quad (2.2)$$

where  $D$  is dose,  $OD$  the optical density, and  $a$ ,  $b$ , and  $n$  the fitting coefficients. A calibration was performed for each film lot employed. Examples of calibration curves for EBT-XD and OC-1 films are presented in Figure 2.7.

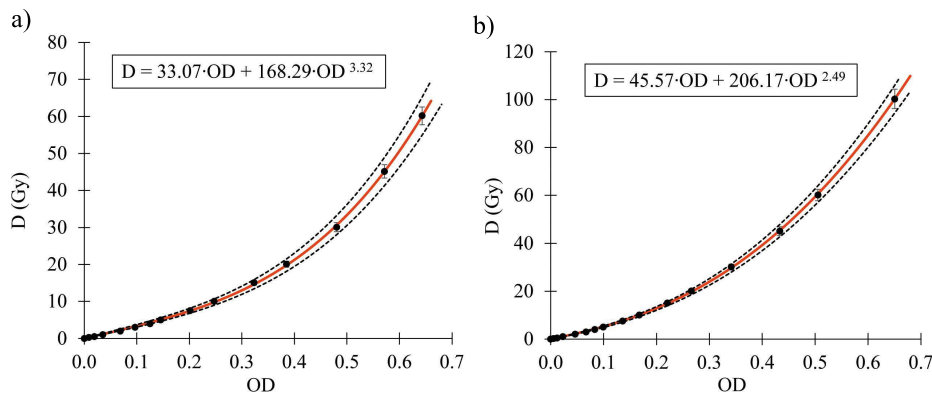


**Figure 2.7:** (a) Examples of calibration curves for (a) EBT-XD and (b) OC-1 films in the red channel (with their associated 95 % confidence band). The corresponding functions are also presented at the top of the figure.

Once films were calibrated, the procedure to extract the dose values from irradiated films consisted of using equation 2.2 to convert reading outputs to optical density and then apply the corresponding calibration curve. A non-irradiated film was stored together with each batch of irradiated films to check for possible changes in  $I_0$ .

Uncertainties in film measurements were computed following the methodology proposed by Sorriaux *et al.* [Sorriaux *et al.* 2013], which considers as sources of uncertainty the measurement of the OD (1 %), film calibration (2 %), the standard deviation in the average dose in the peak and valley regions (2 %), and misalignment in films/phantom positioning. A conservative value of 5 % was used in this work.

## Lynx detector

The Lynx detector [IBA Dosimetry 2022b] is a scintillation device of gadolinium-based material with an effective spatial resolution of 0.5 mm. Although this spatial resolution is not high enough to accurately resolve proton minibeam employed in this work (400 to 1000  $\mu\text{m}$ ), this detector was used to optimize the experimental setup by comparing peak, and integral dose values in different configurations (see Section 3.4) since it provide two-dimensional real-time dosimetric information. Its performance has already been found suitable for proton beam measurements [Russo *et al.* 2017].

*Previous sections have described the general considerations in experimental pMBRT dosimetry. The following section presents the details of the measurements performed in this work.*

### 2.1.4 Preclinical dosimetry in pMBRT

*The experimental campaigns in this thesis were devoted to two main purposes: the validation of dosimeters and our Monte Carlo codes in pMBRT conditions and dosimetry for preclinical experiments. General irradiation details are presented hereafter. Specifics on the materials and configurations employed in the different studies are presented in the following subsections.*

In all the measurements performed in this work, a homogeneous field was delivered at the collimator entrance to shape proton minibeam. The field size was 5 x 5 cm<sup>2</sup> for preclinical collimators (numbers 1 to 7 in Table 2.1) and 10 x 10 cm<sup>2</sup> for the larger collimator (number 8 in Table 2.1) to ensure a homogeneous peak-valley pattern along the lateral dose profile. In all cases, monoenergetic 100 MeV proton beams were considered.

The irradiation parameters were optimized after a robustness analysis, which was one of the main objectives of this thesis. Optimum values for different parameters and the guidelines to obtain them can be found in Sections 3.3 and 3.5.

#### 2.1.4.1 Validation of Monte Carlo simulations and dosimetric protocols

A series of experimental campaigns were devoted to validating our Monte Carlo simulations and the dosimetric protocols employed. For this purpose, the water tank BluePhantom2 (IBA Dosimetry, Germany) [IBA Dosimetry 2022a] and the RW3 Slab Phantom (PTW, Germany) [PTW 2022b] were used as target volumes. In these measurements, the collimator exit-to-isocenter distance (CID) was 8.66 cm, and the air gap between the collimator and the target volume was 7 cm. The gantry angle was 0° to avoid the tank wall.

Measurements with solid-state dosimeters (microdiamond detector and RAZOR diode) were performed in the water tank. Lateral profiles were acquired using the tank scanning system with step sizes of 0.2 and 0.4 mm at peak and valley regions,

respectively. Field irradiations ( $5 \times 5 \text{ cm}^2$  field) were repeated for each data point. Measurement depths were 0 and 1 cm in water. The monitor units (MU) employed were adjusted to obtain valley doses above 0.1 Gy in all cases. The crosscheck measurements with radiochromic films were also performed in the water tank under the same conditions described above.

Additional measurements were performed in the solid water phantom due to its easier handling compared to the water tank. The solid water phantom consisted of a stack of ten  $20 \times 20 \times 1 \text{ cm}^3$  slabs. Films were placed at several depths between slabs. When several films were used simultaneously, the depth of the films in the solid phantoms ( $z_w$ ) was corrected by a depth scaling factor ( $C_m$ ) following IAEA recommendations [IAEA 2001]:

$$z_w = z_m C_m \frac{\rho_m}{\rho_w}, \quad (2.3)$$

where  $z_m$  is the phantom thickness, and  $\rho_m$  and  $\rho_w$  the water and solid phantom densities, respectively.  $C_m$  is the ratio between the phantom material and the water mass stopping powers. Following the methodology adopted by Peucelle [Peucelle 2016] for 100 MeV proton beams,  $\rho$  and  $C$  values were  $1.045 \text{ g/cm}^3$  and 0.980, respectively, for solid water, and  $1.2 \text{ g/cm}^3$  and 0.961 for radiochromic films.

MU delivered were adapted to obtain doses within the appropriate range for each film type. Specifically, a valley dose higher than 1 and 3 Gy for EBT-XD and OC-1 films, respectively, was delivered to minimize the impact of uncertainties in the very low dose region of the calibration curve caused by the steep slope of the curve.

Measurements were performed using multislit collimators in the two orthogonal directions to the beam direction, which will be referred to as vertical and horizontal orientations in the rest of the manuscript. The vertical orientation refers to the rotation of the collimator in which, at  $270^\circ$  gantry angle, the slits point to the floor-ceiling direction. The horizontal orientation is defined as a rotation of  $90^\circ$  with respect to the vertical orientation. Figure 2.8 illustrates the two pMBRT collimator orientations considered.

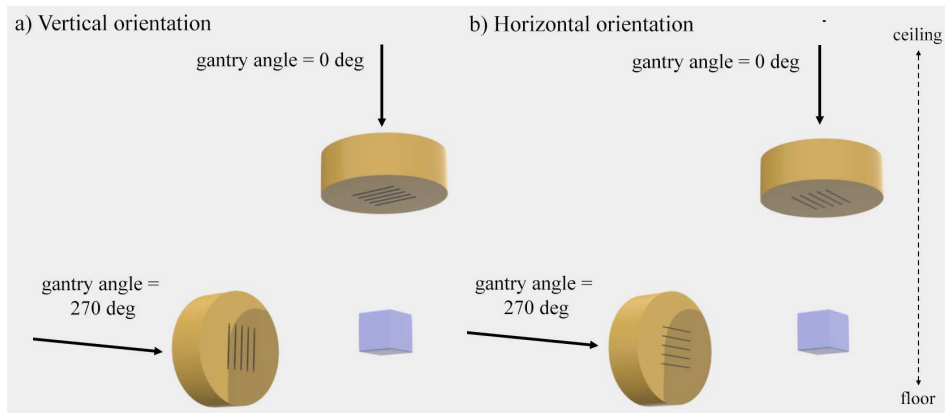


**Figure 2.8:** Representation of the vertical and horizontal orientations of pMBRT collimators.

Besides homogeneous phantoms, a heterogeneous rat head's phantom was used to validate our Monte Carlo simulations. It was designed within a collaboration between the *Institut de Radioprotection et de Sûreté Nucléaire* (IRSN) (France) (Morgane Dos Santos, Miray Razanajatovo, Yoann Ristic, and François Trompier) and *Commissariat à l'énergie atomique* (CEA) (France) (Véronique Menard) as part of the *FantoMICE* project for the development of a phantom for dosimetric studies. The phantom was manufactured using a molding technique. A mold was created in alginate using a euthanized rat (displayed in pink in Figure 2.9). Then, a tissue equivalent material (MXD) was poured into the mold along with the skull of an adult rat. The position of the bone in the phantom was verified in CT images.

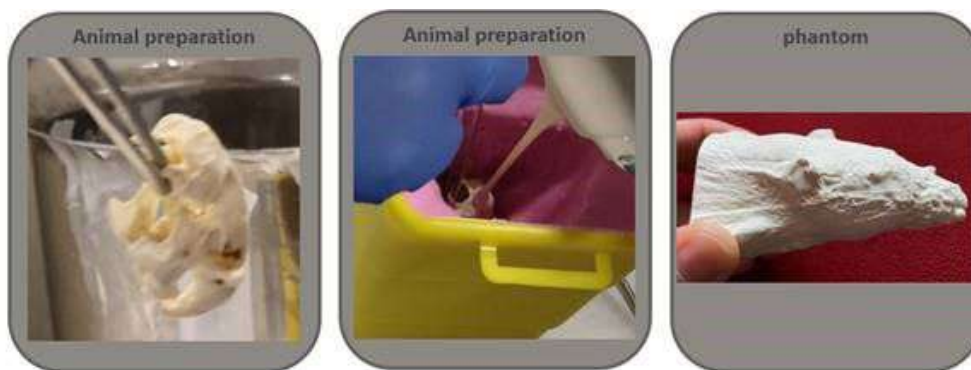


**Figure 2.9:** Illustration of the skull extracted from an adult rat, preparation of the mold and pouring of tissue equivalent material, and rat phantom (from left to right images).

Images courtesy of Dr. Dos Santos.

The phantom was cut in two parts at 1.6 cm depth (tumor implantation location) in the lateral direction (see Figure 2.10a) to allow the insertion of a detector within the rat's head. Radiochromic films were placed on the phantom surface and in the aperture between the two phantom pieces to measure lateral dose profiles. Before irradiations, planar X-ray images were taken using the in-room CT imaging device for the correct positioning of the phantom (see Figure 2.10b), as in rat irradiations (see Section 2.1.4.2). Collimator 2 (five slits and 2.8 mm *c-t-c* distance; see Table 2.1) was used for these measurements. In all cases, the air gap and CID were 7 cm and 8.66 cm, respectively. The gantry was rotated to  $270^\circ$  (horizontal irradiation), and the orientation of the slits was vertical (see Figure 2.10c).

Experimental and simulated lateral dose profiles were compared by computing the main parameters that characterize pMBRT dose distributions, i.e., the peak-to-valley dose ratio (PVDR) and peak full-width-at-half-maximum (FWHM). For the sake of comparison, lateral dose profiles were normalized to the maximum dose in the profile.

#### 2.1.4.2 Dosimetry for preclinical trials

Experimental dosimetric studies performed during this thesis involved *in vivo* and *in vitro* preclinical trials.

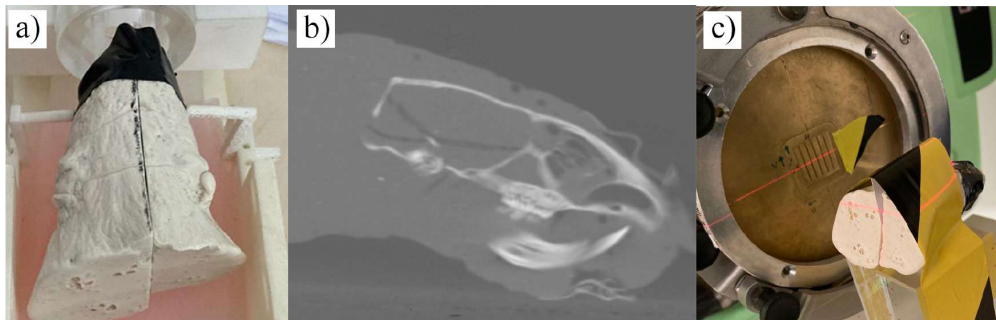


**Figure 2.10:** (a) Rat phantom, (b) CT of the phantom in the sagittal plane, and (c) experimental setup for the irradiations.

### *In vivo* studies

In *in vivo* studies, either the whole rat's brain or the implanted tumor were considered the target volumes. Three different setup configurations were evaluated.

Setup 1 refers to one lateral (unilateral) irradiation with the slits in the vertical orientation. Collimators 2 to 7 (see Table 2.1) were employed. The entrance port of the pMBRT field was the contralateral brain hemisphere (opposite hemisphere to that on which the tumor was implanted) to evaluate the response of the normal brain and tumor simultaneously. Figure 2.11a illustrates this configuration. In this configuration, the air gap between the collimator's exit and the rat's skin was 7 cm to allow including beam modifier components after the collimator if required. Since the beam energy considered was 100 MeV (i.e., proton range of 7.7 cm in water), the rat's brain was irradiated in the plateau region of the depth dose profile of proton beams (the size of the rat's head was around 3 cm).

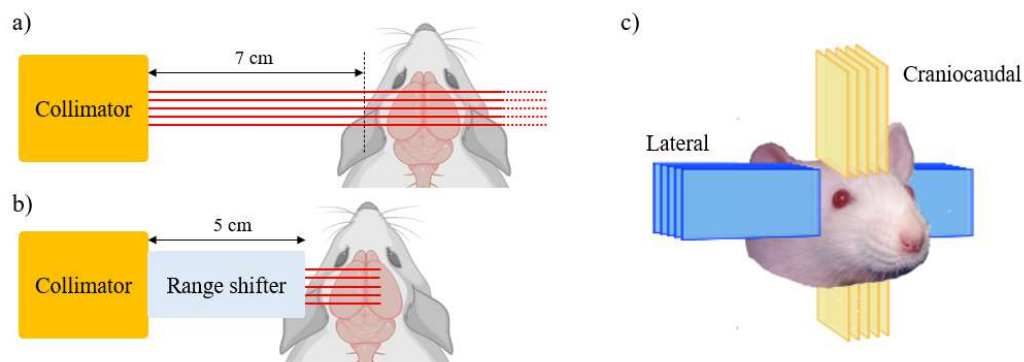


**Figure 2.11:** Representation of setups (a) 1, (b) 2, and (c) 3 for preclinical *in vivo* studies. Setups 1 and 2 consist of a unilateral array of proton minibeam. In setup 1, the tumor was irradiated at the plateau of the proton beam depth dose profile, whereas in setup 2, the Bragg peak was positioned at the tumor position. Setup 3 refers to a crossfire irradiation using two orthogonal arrays.

Setup 2 involved the unilateral irradiation of the target (i.e., tumor) at the Bragg peak position. Since the minimum deliverable energy in the experimental room was

100 MeV, a PMMA block was used as a range shifter (RS). The PMMA block was 5 cm-wide in the direction of the beam to shift the Bragg peak to the center of the tumor (1.6 cm in depth). The size of the RS in the beam direction was calculated by employing Monte Carlo simulations. The dimension in the other two directions was chosen to allow the block to be in contact with the rat's skin when the rat was on the treatment couch. The RS was placed between the collimator and the rat without separation between these elements (i.e., no air gap) (see Figure 2.11b). The collimator used for this configuration was collimator 4 (five slits separated by 4 mm *c-t-c* distance; see Table 2.1) to obtain a quasihomogeneous dose distribution in the target (PVDR  $\sim$  1.2). As in Setup 1, the treatment was delivered considering the vertical orientation of the slits and the entrance port was the contralateral brain hemisphere. Figure 2.12 shows an example of a treatment considering this experimental setup.

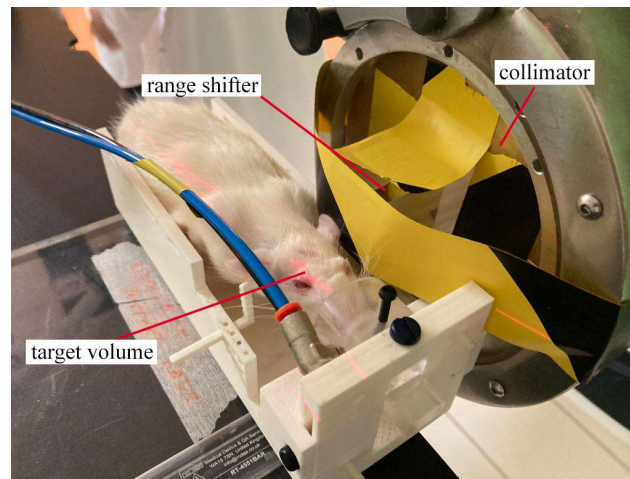


**Figure 2.12:** Rat treatment in setup 2, i.e., unilateral irradiation of the tumor at the Bragg peak position.

All configurations already described involved one-array lateral irradiations. Setup 3 refers to an orthogonal crossfire irradiation (see Figure 2.11c). The field arrangement consisted of a lateral (gantry at  $270^\circ$ ) and a craniocaudal (gantry at  $0^\circ$ ) irradiation in a crossfire geometry (vertical and horizontal orientation of the slits in the lateral and craniocaudal irradiations, respectively) to avoid the blurring of the characteristic peak-valley pattern. No range shifter was used in this configuration, i.e., the rat's brain was irradiated at the plateau region. The collimator 2 (five slits separated by 2.8 mm *c-t-c* distance; see Table 2.1) was employed for both beam directions and the air gap was 7 cm and 6.5 cm in the lateral and craniocaudal irradiations, respectively.

Table 2 summarizes the irradiation configurations for pMBRT *in vivo* studies presented in this section.

In all rat irradiations, the CID was 8.66 cm, and the rat was moved in the longitudinal direction to set the required air gap. The position of rats in the

Setup number	Collimator number	Air gap (cm)	Range shifter thickness (mm)	Number of arrays	Depth dose profile region within target
1	2, 3, 4, 5, 6, 7	7	0	1 (unilateral)	plateau
2	5	0	50	1 (unilateral)	Bragg peak
3	2	7 and 6.5	0	2 (crossfire)	plateau

**Table 2.2:** Description of the configurations considered in small-animal preclinical studies. Collimators are described in Table 2.1.

orthogonal directions to the beam was adjusted using the in-room CT. In lateral irradiations, the field was restricted to the brain volume, avoiding the irradiation of critical OARs (e.g., the spinal cord and the olfactory bulb) (see Figure 2.13a). The back of the skull was considered the reference point where the last slit in the longitudinal rat plane should be located. In craniocaudal irradiations, the rat was moved to avoid the irradiation of the hemisphere where the tumor was not implanted (left hemisphere) (see Figure 2.13b).

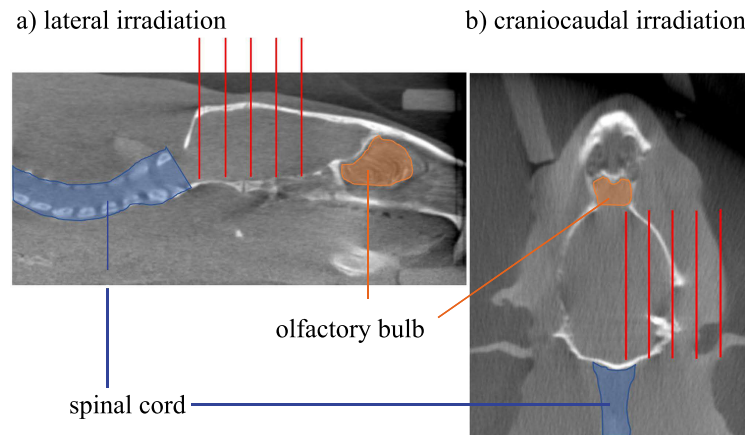


**Figure 2.13:** Organs-at-risk considered in rat treatments in the (a) lateral and (b) craniocaudal irradiations. The proton minibeam paths are represented in red color.

The dosimetry prior to *in vivo* treatments involved experimental and Monte Carlo data. Figure 2.14 illustrates the workflow for dose prescription divided into four main steps.

- Step 1. Experimental measurements were performed at 1 cm depth with radiochromic films in a solid water phantom to determine the dose per MU, i.e., the dose rate,  $\dot{D}_{1cm}^{SW}$  [Gy/MU], was measured. For these measurements, pMBRT collimators for preclinical irradiations (numbers 1 to 7 in Table 2.1) were employed.
- Step 2. Monte Carlo simulations, performed in a model of the solid water phantom and a rat (see Section 2.2.3.1), were used to find the correlation factor  $f$  between the mean dose at 1 cm depth in solid water,  $D_{1cm}^{SW}$ , and the mean dose at the target position in the rat (1.6 cm depth),  $D_{1.6cm}^{rat}$ , for the

same number of primary particles:

$$f = \frac{D_{1.6cm}^{rat}}{D_{1cm}^{SW}}. \quad (2.4)$$

- Step 3. The factor  $f$  was applied to the measured dose rate  $\dot{D}_{1cm}^{SW}$ , as detailed in Figure 2.14, to obtain the dose rate at the target position,  $\dot{D}_{1.6cm}^{rat}$ .
- Step 4. The prescribed MU for each treatment were determined by dividing the mean dose required at the target,  $D_{prescribed}$ , by the dose rate  $\dot{D}_{1.6cm}^{rat}$  (see Figure 2.14).

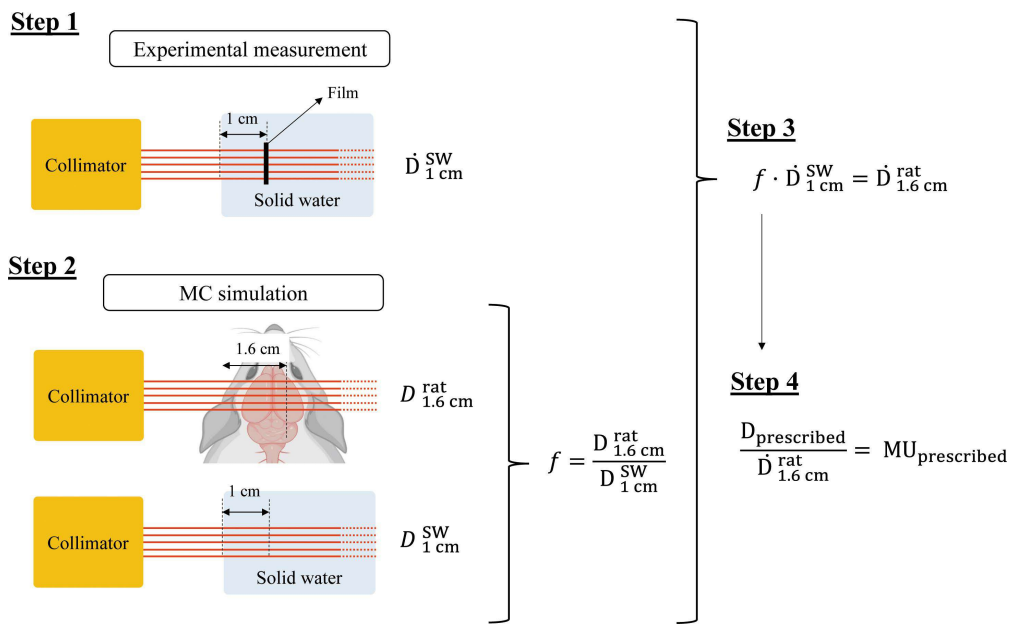


**Figure 2.14:** Example of the workflow for dose prescription in rat treatments.

A more detailed description of the dosimetric protocols and guidelines for preclinical studies involving small animals will be provided in Chapter 3. The rat phantom, presented in Section 2.1, was not used for experimental dosimetry since it was not available at that time.

Finally, quality assurance (QA) measurements were performed during treatments by placing radiochromic films on the rat's skin. OC-1 films were used since their dynamic range was suitable for the high doses delivered to rats (up to 80 Gy peak doses), contrary to EBT-XD films. The dose delivered to all irradiated animals during this PhD thesis was measured and checked to correspond to the expected prescribed dose.

### *In vitro* studies

*In vitro* studies (i.e., cell irradiations) were performed using 24-well plates. The collimator 8 (fifteen slits separated by 4 mm c-t-c distance; see Table 2.1) was

employed to irradiate several well plates simultaneously. For broad beam irradiation, the collimator was removed.

Plates were placed on the top of a solid water phantom consisting of four 1-cm slabs. The solid water surface was at 9.66 cm from the collimator exit, the CID was 8.66 cm, and the gantry was at  $0^\circ$  (see Figure 2.15). The dosimetry for these experiments was performed using a plate with the same amount of medium as for cell irradiations. Radiochromic films were placed under the plate to measure the dose per MU received by cells since cells typically lie at the bottom of the well. During cell irradiations, films were also placed in the same position for QA and identifying regions of the cell culture receiving peak and valley doses. EBT-XD and OC-1 films were employed depending on the doses delivered to the cells in each experiment, as detailed in Section 3.7.2.

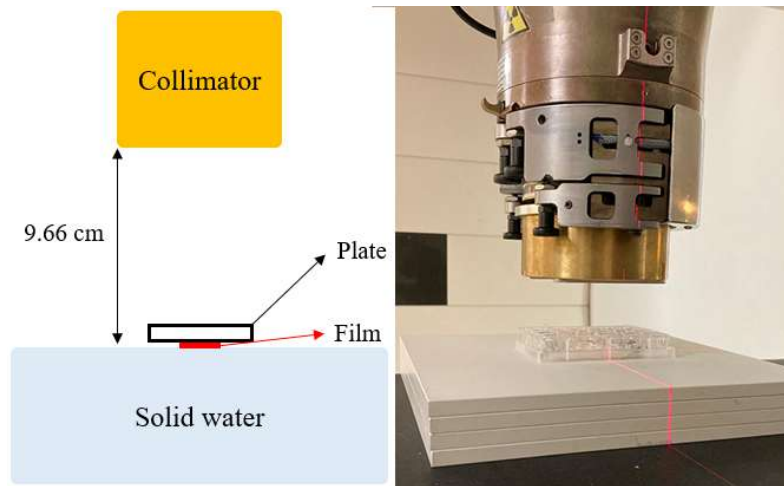


**Figure 2.15:** Setup for cell irradiations.

For the dosimetry of broad beam irradiations in *in vivo* and *in vitro* studies, a ppc05 ionization chamber was also used to measure the dose per MU at reference positions. This allowed crosschecking film measurements.

In the studies performed during this thesis, lateral dose profiles were evaluated by computing the parameters that define pMBRT dose distributions and influence the biological responses, i.e., PVDR, peak FWHM, and peak, valley, and mean doses. Unless otherwise stated, the PVDR was computed as the ratio of the central peak dose and the dose in the valley to the left of the central peak. Mean doses were calculated as the average dose between the first and last peak of the profile.

## 2.2 Monte Carlo simulations

*This section aims to introduce the concept of Monte Carlo (MC) simulations, with special emphasis on the MC-based software used in this thesis, the TOPAS toolkit. The details of the simulations are also provided.*

### 2.2.1 The Monte Carlo method

The Monte Carlo (MC) method, first introduced by Metropolis and Ulan in 1949 [Metropolis & Ulam 1949], is a class of numerical methods based on the use of random numbers. This method is typically used to solve mathematical and physical problems involving multiple independent variables [Salvat 2015].

The idea behind the MC method is to use a probabilistic approach instead of explicitly solving analytical equations. This stochastic process involves creating a sequence of states whose evolution is determined by random events [Kalos & Whitlock 2009]. Due to the probabilistic nature of this method, the calculations do not provide an exact solution; they approximate the true value with a certain statistical uncertainty. The uncertainty decreases as the number of random events increases [Salvat 2015]. A more detailed description of the basis of the MC method can be found elsewhere in the literature [Kalos & Whitlock 2009, Salvat 2015].

The MC method is used in a wide variety of physical problems, such as radiation transport, statistical physics, chemistry, and even quantum mechanics [Kalos & Whitlock 2009]. The most relevant application of the MC method in RT is the simulation of radiation transport. This application is especially suited to the MC method since radiation transport is a natural stochastic process [Kalos & Whitlock 2009].

The MC simulation of radiation transport starts with a set of initial particles (called histories) represented by a set of numbers defining their properties (e.g., nature of the particle, position, momentum, and energy). From this series of numbers, different random processes (e.g., energy loss, scattering, or production of secondary particles) are initiated when the particle is transported through a medium. These processes are determined by probability distributions described in the underlying physical models. This step leads to determining a new set of values for these particles and daughter ones. The process is repeated iteratively until a particular condition, indicating each history's completion, is met. This condition includes particle absorption or particle energy below a threshold [Metropolis & Ulam 1949].

The MC method has been used in medical physics since the 1970s. Its first application was calculating the conversion factor of an ionization chamber for electron beams [Berger *et al.* 1975]. Since the 1980s, the use of the MC method for medical purposes has grown significantly with extended applications in nuclear medicine [Zaidi 1999], modeling of external electron [Ma & Jiang 1999] and photon EBRT [Verhaegen & Seuntjens 2003], treatment planning system [Chetty *et al.* 2006b], or dose verification [Hoshida *et al.* 2019]. Its increased use triggered the development of various MC codes. The most used codes in the medical physics community are MCNP [Forster & Godfrey 1985], EGSnrc [Kawrakow & Rogers 2000], Geant4 [Agostinelli *et al.* 2003], and FLUKA [Böhlen *et al.* 2014]. Two Geant-4 simulation toolkits widely employed are GATE [Jan *et al.* 2011] and TOPAS [Perl *et al.* 2012].

Among all the available MC codes, TOPAS has been widely used in this thesis. Its features and applications are described in the following section.

### 2.2.2 TOPAS simulations toolkit in medical physics

TOPAS (TOol for PArticle Simulation) [Perl *et al.* 2012] is a MC simulation platform mainly dedicated to applications in medical physics. It is freely distributed for educational and research purposes by TOPAS MC Inc at [TOPAS MC Inc. 2022].

TOPAS is based on the Geant4 code. The Geant4 code [Agostinelli *et al.* 2003] is a MC-based toolkit for simulating the transport and interactions of particles traversing matter. It is implemented in C++ and is organized in predefined classes utilizing object-oriented technology [Apostolakis *et al.* 2007]. Geant4 consists of three modules: the kernel, physics processes, and interfaces modules. The kernel module initializes, manages run configurations, enables the simulation of processes, and handles particles, tracks, and materials. The physics processes module contains a large set of physics models and cross-sections to simulate the interactions of particles with matter across a vast energy range (0.1 keV to 10 PeV [Allison *et al.* 2016]). Finally, the interfaces module handles visualization and input/output features allowing the user to guide the application.

In Geant4, the physics interactions of particles with matter are simulated using a set of general class categories: track, trajectory, step, process, event, and run [Allison *et al.* 2016]. A *track* is the state of a particle at a particular point along its path, including its energy, momentum, position, time, mass, charge, lifetime, and other quantities. Tracks are grouped in *trajectories*. A *step* consists of two associated endpoints in time and space and represents the change in track properties between them. The user can define the size of the steps for each transportation and physics process. A *process* is a class that implements physical interactions. Processes are constructed of physics lists, which define particle and interaction mechanisms. These lists are organized into modules defining physics processes, e.g., electromagnetic (EM) or hadronic models. Modules must be selected according to the particular problem to be simulated and the involved energy regime. Detailed information on Geant4 physics lists and modules can be found elsewhere [Geant4 Collaboration 2021]. An *event* is the basic unit of a simulation and consists of a particle decay or interaction of a primary particle with the medium, its subsequent interactions, and the produced secondary particles. Finally, a *run* is a collection of events. An extensive list of all the class categories in Geant4 and their definition can be found in [Agostinelli *et al.* 2003].

Geant4 has been widely validated against published results based on other MC codes (e.g., MCNP and EGS4nrc) and experimental data [Carrier *et al.* 2004]. A compilation of results from validation and regression tests can be found in the repository of the Geant4 Collaboration [Geant4 Collaboration 2022]. Moreover, benchmarking and validation studies have been performed for specific applications in RT, such as proton therapy [Pinto *et al.* 2016], carbon ion therapy

[Bolst *et al.* 2017], BNCT [Chen *et al.* 2019], and photon and electron EBRT [Poon & Verhaegen 2005].

Despite their accuracy and efficacy, MC codes such as Geant4 are usually underutilized due to their complexity, i.e., their use is limited to research groups with deep MC expertise. The rationale behind the development of TOPAS was to introduce a user-friendly MC platform to the clinical proton therapy community to reduce the uncertainty margins in treatment plans [Perl *et al.* 2012].

TOPAS is layered on top of Geant4. Then, it encapsulates its libraries plus additional code to extend its functionality and provide easier control without the need to write C++ code [Perl *et al.* 2012]. The main feature of TOPAS is the preservation of the underlying Geant4 code and its full capabilities in terms of speed, accuracy, and flexibility, offering benchmarked underlying physics. Also, it can be run by users with limited or no programming experience, contributing to the widespread use of MC in the proton therapy community.

In TOPAS, the Geant4 code is extended by creating a high-level macro language (*parameter control system*) that allows the user to specify the simulation components [Perl *et al.* 2012]. The parameter control systems consist of a set of user input *parameter files*. Each parameter file is a text file consisting of one or more lines that define the parameter type, name, and value (Parameter\_Type : Parameter\_Name = Parameter\_Value). The parameter type can be a string (*s*), boolean (*b*), integer (*i*), double (*d*), or a double vector (*dv*). Parameter names are grouped in several categories indicating whether the parameter corresponds to a geometry (*Ge/*), particle source (*So/*), physics (*Ph/*), scoring (*Sc/*), time feature (*Tf/*), or a TOPAS overall control (*Ts/*) component, among others. Such notation precedes the name of the parameter as a prefix. For instance, to describe that the half-length in the X direction (*HLX*) of a box called *MyBox* is 50 cm, the parameter command is written as follows:

$$d : Ge/MyBox/HLX = 50.0 \text{ cm}. \quad (2.5)$$

TOPAS also expands Geant4 by including additional predefined modules (called *scorers*) for scoring different quantities. More details on the parameter control systems and all the parameter files included in TOPAS can be found in the TOPAS user guide [TOPAS MC Inc 2021]. Besides the predefined simulation components already implemented in TOPAS, user can create their own simulation objects in C++ code and use them in TOPAS as extensions.

Since TOPAS is layered on top of Geant4, the testing of the Geant4 code serves as validation. However, TOPAS has been further validated in various configurations [Perl *et al.* 2012, Testa *et al.* 2013, Perl 2014, Shin *et al.* 2017, Huang *et al.* 2018].

*The details of simulations performed in this thesis are given in the next section.*

### 2.2.3 Simulation details

All the MC simulations in this thesis were performed using the TOPAS version 3.5 (based on Geant4.10.7). Simulations were dedicated to two main purposes: (i) optimization of the experimental setup of current pMBRT preclinical trials and computing dose distributions for these studies (results presented in Chapter 3), and (ii) dosimetric calculations for theoretical studies involving human patients to evaluate the clinical potential of pMBRT (results presented in Chapters 4 and 5).

*The following subsections describe the geometry, particle source, physics parameters, scoring, and output post-processing of simulations.*

#### 2.2.3.1 Geometry

The ICPO PBS beamline (described in Section 2.1.1) was considered in all the simulations presented in this work. A model of the nozzle-equipped gantry of the ICPO (see Figure 2.16) was used as described in the work by De Marzi *et al.* [De Marzi *et al.* 2019a]. The components included in the modeling of the beamline are the vacuum window (located at 290 cm from the isocenter), two ionization chambers (at 283 and 116 cm), two scanning magnets (at 233 and 193 cm), and the snout holder and snout (their position depends on the irradiation setup, detailed below). pMBRT collimators, described in Section 2.1.2 were also modelled in TOPAS. *TsCylinder* and *G4GTrap* were the geometry components employed to model the external rim of the collimator and the slits, respectively. Collimators were placed in the snout in the arrangement described in Section 2.1.2. The position of the collimator from the isocenter differs from study to study. In studies related to preclinical studies, the upstream part of the collimator (and snout) was at 8.66 cm from the isocenter (as in experimental measurements). In simulations involving human patients, the collimator position depends on the specific treatment and the distance from the collimator exit to the skin (detailed hereafter).

Different target volumes were modeled in TOPAS: a water tank, solid water phantom, rat's head phantom, rat's head, and several human patients. The geometry of the water tank and slab phantoms were as described in Section 1.4.4.3. The materials used to model water and the tank wall were *G4\_WATER* and *G4\_PLEXIGLASS*, respectively. The solid water (RW3 model) was defined according to the manufacturer specifications (composition: hydrogen (7.59 %), carbon (90.41 %), titanium (1.2 %) and oxygen (0.8 %); density = 1.045 g/cm<sup>3</sup>) [PTW 2022b]. Both volumes were placed as in experimental irradiations; the distance between the surface of the volume and the downstream part of the collimator was 7 cm (the isocenter was at 1.66 cm depth in the target volume). The rat's head phantom, rat's head, and human patients were included in TOPAS as CT images. TOPAS allows importing CT images as DICOM files. The method developed by Schneider *et al.* [Schneider *et al.* 2000] (implemented in TOPAS) was adopted to convert image values (i.e., CT numbers or Hounsfield Units) to materials.

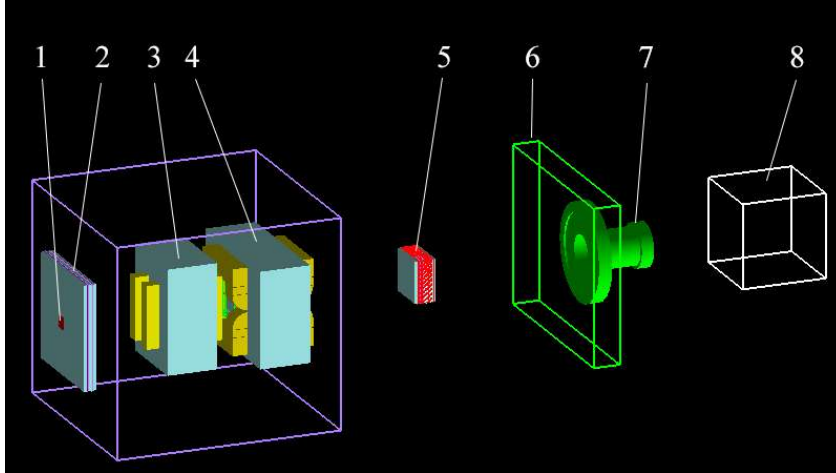


**Figure 2.16:** TOPAS visualization of the ICPO PBS beamline. The components shown in the image are (1) vacuum window, (2) first ion chamber, (3)-(4) scanning (dipole) magnets, (5) second ion chamber, (6) snout holder, (7) snout and (8) target volume.

The rat used to model the phantom and perform the CT scans was the same age as the irradiated ones in preclinical studies (7 weeks-old). The resolution of the rat phantom, rat, and human images was  $0.05 \times 0.05 \times 0.05 \text{ mm}^3$ ,  $0.1 \times 0.1 \times 0.1 \text{ mm}^3$ , and  $1.2 \times 1.2 \times 1.2 \text{ mm}^3$ , respectively. In all simulations, the center of the target (i.e., tumor) was placed at the isocenter. The gap between the collimator's exit and the skin of rats was as in experimental irradiations (see Section 1.4.4.3) and 5 cm for human patients.

### 2.2.3.2 Particle source

A particle beam can be defined as a set of individual particles whose momentum points to a common direction ( $z$  in this work) [Reiser 2008]. However, in practice, individual particles show a spread in their position ( $x$  and  $y$ ) and momentum direction ( $x'$  and  $y'$ ) in the plane transversal to the beam axis. These spreads can be modeled as Gaussian distributions, especially for pencil beams. These distributions resemble an ellipse when plotted in the space of the particle's positions and momentum direction [Schneider 2020]. In TOPAS, this type of beam can be produced by the emittance source type with two-dimensional elliptical Gaussian distributions per axis. The characteristics of this beam source are described by six parameters ( $\sigma_x$ ,  $\sigma_y$ ,  $\sigma'_x$ ,  $\sigma'_y$ ,  $r_x$ , and  $r_y$ ).  $\sigma_x$  and  $\sigma_y$  refer to the standard deviation of the Gaussian that describes the horizontal and vertical spread of particle positions.  $\sigma'_x$  and  $\sigma'_y$  describe the spread in the momentum trajectory in both directions perpendicular to the beam direction. Finally,  $r_x$  and  $r_y$  refer to the correlation coefficient of the beam ellipses.

The particle source parametrization of the nozzle entrance (i.e., vacuum window) and its parameters defined by De Marzi *et al.* [De Marzi *et al.* 2019a] were used except  $\sigma_x$  and  $\sigma_y$ . De Marzi *et al.* adjusted the spot size of the beam source

( $\sigma_x$  and  $\sigma_y$ ) by averaging the major and minor axes of the spot shape, neglecting possible differences between them. This approximation was proven correct for broad beam conditions. However, this adjustment significantly affects pMBRT lateral dose profiles. In this work, the effect of spot size variation on pMBRT dose distributions was evaluated by means of MC simulations. From the results of this study (presented in Section 3.3), I concluded that the spot size that leads to an agreement with all the tested experimental conditions could be better characterized by using  $\sigma_x$  and  $\sigma_y$  values of 15 and 10 mm. The proton energy and energy spread at the source were also extracted from the work by De Marzi *et al.* [De Marzi *et al.* 2019a]. Monoenergetic proton beams of 100 MeV (at the isocenter) were considered for all simulations linked to preclinical studies, whereas beam energies in studies involving human patients depend on the treatment plan (see Sections 4.3 and 5.2). Regarding the beam steering, the magnetic field values of dipole magnets were also modeled as defined in [De Marzi *et al.* 2019a].

The whole nozzle geometry was considered in all simulations. De Marzi *et al.* [De Marzi *et al.* 2018] showed that the parameterization of the source at the nozzle exit leads to a significant underestimation of valley doses, whereas a good agreement with experimental data is obtained with the complete modeling.

In simulations considering collimators for preclinical investigations (numbers 1 to 7 in Table 2.1), a homogeneous 5 x 5 cm<sup>2</sup> field, composed of 324 regularly spaced (3 mm) pencil beam spots, was created at the collimator entrance. For studies involving human patients, the field size and spot configuration depend on the treatment and beam specifications (see Sections 4.3 and 5.2).

The total number of histories simulated differs from case to case. In all cases, the value was adjusted to obtain a maximum value for the statistical uncertainty (detailed in Section 2.2.3.6).

### 2.2.3.3 Physics parameters

All the TOPAS simulations of this work were run using the *Geant4\_Modular* option and the modules recommended for proton therapy (*g4em-standard\_opt3*, *g4h-phy\_QGSP\_BIC\_HP*, *g4decay*, *g4ion-binarycascade*, *g4h-elastic\_HP*, *g4stopping*, and *g4radioactivedecay*) [Grevillot *et al.* 2010]. The parameters for the minimum and maximum electromagnetic (EM) range were set to 100 eV and 230 MeV. The resolution of the tables containing the mean free path, stopping power range, and inverse range values for EM processes (*EMBinsPerDecade*) was set to 100 (above 15 bins/decade fluctuations in dose calculations are not significant [Grevillot *et al.* 2010]). A relevant parameter for MC calculations is the range cut (i.e., production threshold for secondary particles after EM interactions). I performed a test to evaluate the effect of this parameter in pMBRT lateral dose distributions and find an appropriate value for our simulation setups. I found that, for our minibeam sizes, cut values larger than 0.01 mm lead to an under- and over-estimation of peaks and valleys, respectively. For values of 0.01 mm or below, fluctuations become negligible. Figure 2.17 illustrates the dependence of

peak and valley doses on the range cut value in-depth and the simulation time as a function of the cut value. Since the reduction of the range cut is associated with an increase in the simulation time, the range cut in all the simulations of this thesis was 0.01 mm, representing, at maximum, 10 % of the smallest scoring voxel dimension. All other parameters used default options. Although the maximum step length may be a critical parameter in MC simulations, this parameter was not tuned in our simulations since it is related to range cut and, for sufficient low cut values (as is the case), the effect of a fixed step limitation becomes negligible [Grevillot *et al.* 2010].

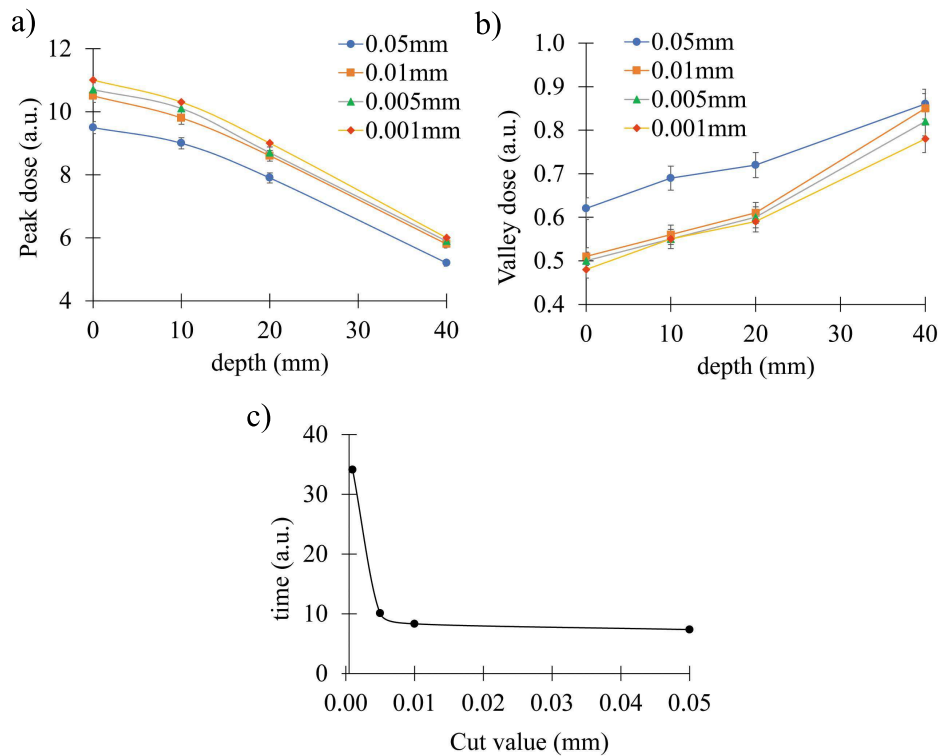


**Figure 2.17:** Variation of the (a) peak dose, (b) valley dose, and (c) simulation time as a function of the range cut.

### 2.2.3.4 Scoring

Two volume scoring actors were employed in the simulations of this work: *DoseToWater* (calculated from energy-dependent stopping power conversion) and *ProtonLET* (calculated as the dose-averaged-LET of primary and secondary protons and associated secondary electrons). The technique that TOPAS uses to score LET is described in [Cortés-Giraldo & Carabe 2015, Granville & Sawakuchi 2015]. In TOPAS, the dose and LET are calculated on a voxel basis.

Scoring volumes, defined as parallel worlds, were created in the region of interest of target volumes (i.e., the volume containing voxels receiving any dose).

Parallel worlds overlapped geometry mass components with no effects on physics. The scoring grid resolution of scoring volumes differs depending on the study. The voxel size may affect the scoring of quantities, especially in the direction of peaks and valleys, since relatively large voxels may lead to a possible volume averaging effect due to the submillimetric size of minibeam arrays [Schneider *et al.* 2022a, Charyyev *et al.* 2020]. In simulations for preclinical studies involving only one planar minibeam array, the dose scoring grid was 0.1 mm in the direction of peaks and valleys, 2 mm along the planar minibeam arrays, and 1 mm in depth. When interlacing arrays (see Section 2.1), the voxel size was 0.2 x 0.2 x 0.2 mm<sup>3</sup> to resolve minibeam arrays in the two array directions effectively. For purely theoretical studies involving human patients and several minibeam arrays, the scoring grid size was increased to 0.5 x 0.5 x 0.5 mm<sup>3</sup> for the sake of computation time and memory. This resolution was considered enough for those theoretical evaluations.

### 2.2.3.5 Hardware and parallelization

Simulations were performed on the Joliot Curie-SKL computational cluster with 48 CPU cores Intel Skylake@2.7 GHz (AVX512) at *Commissariat à l'énergie atomique et aux énergies alternatives* (CEA). The maximum simulation time in this cluster was 24 h.

Due to the stochastic nature of MC simulations, a large number of initial histories is required to achieve a relatively low statistical uncertainty. Due to the time limit in the computational cluster employed, the number of particle histories needed to be divided into several computing units. TOPAS, as Geant4, allows the parallelization of the simulation job in multiple cores (multithreading) and combines the results in a single output file. In addition, several jobs of the same simulation were run with different initial random seeds. At the end of the calculation, the results from all independent simulations were combined as described in the following section (Section 2.2.3.6). This approach is feasible when the individual tracks and histories are independent (e.g., for dose and LET calculations).

### 2.2.3.6 Data post-processing

As stated in Section 2.2.3.5, MC simulations were divided into several jobs and their results were collated. For cumulative quantities, i.e., dose, results of each job were added up voxel by voxel:

$$D_k = \sum_i^N D_{k,i}, \quad (2.6)$$

where  $D_k$  is the total dose in voxel  $k$ ,  $D_{k,i}$  is the dose in the voxel  $k$  in the  $i$ -th job, and  $N$  the total number of jobs. For LET, the results of each parallelized simulation were averaged:

$$LET_k = \frac{1}{N} \sum_i^N LET_{k,i}, \quad (2.7)$$

where  $LET_k$  is the total LET in voxel  $k$ ,  $LET_{k,i}$  is the LET in the voxel  $k$  in the  $i$ -th job, and  $N$  the total number of jobs. From the resulting total dose and LET distributions, several parameters were investigated, such as peak, valley, maximum, and mean doses, peak-to-valley dose ratio (PVDR), peak full-width-at-half-maximum (FWHM), biological effective dose (BED), normalized total dose (NTD), dose homogeneity indexes, dose-volume histograms (DVH) and other dose-volume indexes.

Regarding the statistical uncertainty of simulations, TOPAS reports statistical measures (such as the variance and standard deviation) of the scored quantities. For cumulative quantities (i.e., dose) the uncertainty of the total dose in each voxel was calculated using the method described by Chetty et al. [Chetty et al. 2006a]:

$$u_{d_k} = \sqrt{\frac{1}{N-1} \left( \frac{\sum_i D_{k,i}^2}{N} - \left( \frac{\sum_i D_{k,i}}{N} \right)^2 \right)}, \quad (2.8)$$

where  $u_{d_k}$  is the uncertainty of the total dose in the voxel  $k$ ,  $D_{k,i}$  the dose in the  $k$ -th voxel produced by the independent repetition  $i$ , and  $N$  the total number of primary histories. The statistical uncertainty associated with LET values was calculated as recommended by TOPAS developers, i.e., as the standard deviation of the LET values of each simulated job divided by the square root of the number of independent jobs [Ramos-Méndez 2022]. The uncertainty of quantities derived from dose and LET was calculated by propagating the uncertainties of each independent variable following the equation:

$$\Delta X(a, b, \dots, z) = \sqrt{\left( \frac{dX}{da} \right)^2 \Delta a^2 + \left( \frac{dX}{db} \right)^2 \Delta b^2 + \dots + \left( \frac{dX}{dz} \right)^2 \Delta z^2}, \quad (2.9)$$

where  $\Delta X$  is the uncertainty of the derived quantity  $X$  and  $\Delta a$ ,  $\Delta b$ , ...,  $\Delta z$  are the uncertainties of the variables  $a$ ,  $b$ , ...,  $z$ .

The global uncertainty of lateral dose profiles was calculated as the average statistical uncertainty of voxels with a dose higher than 50 % of the maximum dose, as considered in other pMBRT works [Peucelle 2016]. The global uncertainty was kept below 1 % in simulations linked with preclinical studies. The global uncertainty of the entire scoring volume in theoretical studies involving human patients was calculated as the average statistical uncertainty of voxels with a dose higher than 90 % of the maximum dose, as considered in similar studies [Lansonneur et al. 2020]. In these scenarios, the uncertainty was below 3 % in all cases.

## 2.3 Treatment planning studies

The work in this PhD thesis involved the calculation of pMBRT dose distributions in human patients (Chapters 4 and 5). For these cases, a treatment planning process was required. The treatment planning process consists of four

steps, as described in Section 1.2.6: (i) imaging and volume delineation, (ii) dose prescription and OAR constraints definition, (iii) optimization of treatment plans, and (iv) plan evaluation. The work performed in this thesis regarding treatment planning focused on the three latter steps.

*The following subsections describe the software employed for treatment planning and the specific procedures adopted in this work.*

### 2.3.1 Software

As described in Section 2.2.3, pMBRT dose distributions in this work were calculated by means of MC simulations using the TOPAS toolkit. The clinical software ECLIPSE treatment planning system (TPS) (Varian Medical Systems, Palo Alto, CA, USA) [Varian 2022] was employed for the usual treatment planning steps (volumes delineation, beam arrangements, spot optimization, dose constraints and prescription). The Nonlinear Universal Proton Optimized algorithm (NUPO) (v.15.6.05) with pencil beam scanning algorithm and delivery was considered for the spot optimization. However, ECLIPSE was not used for computing final pMBRT dose distributions since, as of October 2022, (i) it does not allow the simulation of pMBRT mechanical collimators, (ii) the scoring resolution ( $1 \times 1 \times 1 \text{ mm}^3$  at maximum) is not high enough to resolve the minibeam [Charyyev *et al.* 2020], and (iii) the calculation models employed for seamless irradiations may be not adequate for minibeam calculations.

To tackle this issue, Institut Curie established a collaboration agreement with Varian Medical Systems (Palo Alto, USA) in the context of developing a dedicated TPS for pMBRT (ongoing project).

*The distinct dose delivery in pMBRT and the lack of adapted commercial treatment planning systems require adopting distinct planning strategies departing from those employed in conventional RT. The details of the methodologies for treatment planning used in this work are presented in the following section.*

### 2.3.2 Treatment planning in pMBRT

As mentioned in the previous section, clinical TPSs, and ECLIPSE in particular, are not tailored to the distinct dose delivery method in pMBRT. Therefore, the spot configuration of all treatment plans presented in this thesis was performed considering seamless conditions (i.e., conventional proton therapy). These optimized spot configurations were used as input for MC simulations. Pencil beam spot weights, expressed in monitor units (MU), were converted to the number of protons per spot following the methodology described in [Fracchiolla *et al.* 2015]. This translation was performed using an in-house code developed by the ICPO's team. All the ICPO lines are modeled in TOPAS and a graphical user interface has been developed to allow the transit of data between TPSs and TOPAS, in particular the

generation of simulation files with PBS beam parameters, the automated choice of HU-material conversion parameters, and the positioning of dose matrices in DICOM format. Using that code, a good agreement between standard PT plans computed by ECLIPSE and TOPAS was obtained in previous studies (see Figure 2.18) [Lansonneur *et al.* 2020], proving its good performance.

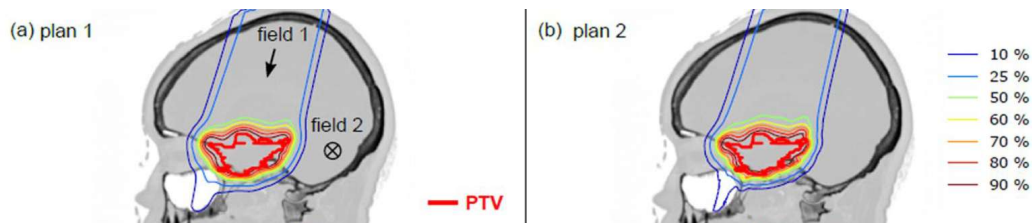


**Figure 2.18:** Dose distributions computed by (a) ECLIPSE and (b) TOPAS for the same treatment plan. Taken from [Lansonneur *et al.* 2020].

The use of a spot configuration optimized in broad beam conditions does not consider the lack of lateral equilibrium in pMBRT dose distributions. Therefore, when this spot optimization is applied to pMBRT conditions, the dose homogeneity within the SOBP may be reduced, especially in its distal part, as illustrated in Figure 2.19c.

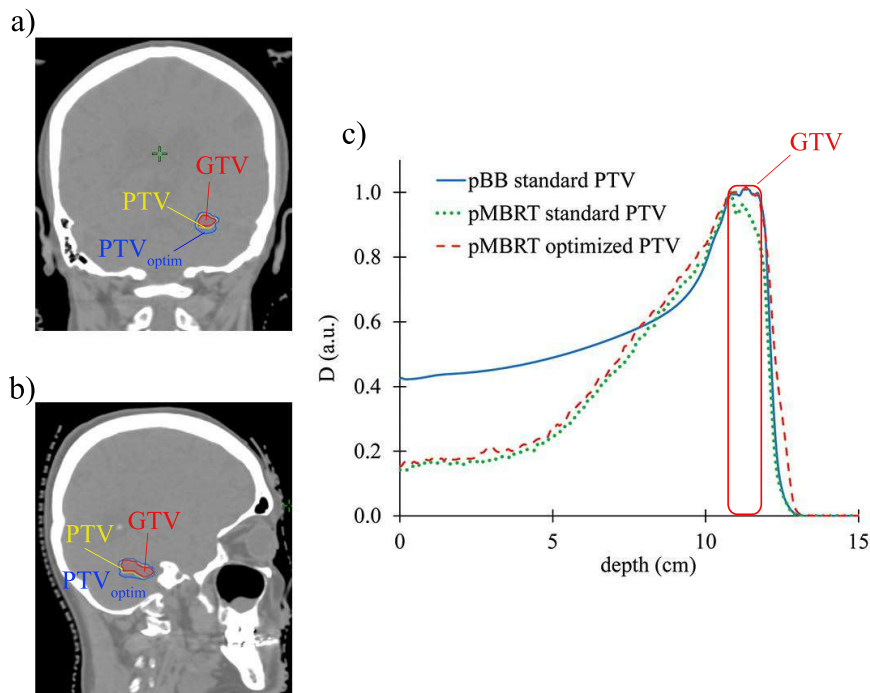


**Figure 2.19:** (a, b) Representation of the standard PTV delineation (in yellow color) and specific PTV definition,  $PTV_{optim}$ , for pMBRT plan optimization (in blue color). (c) Resulting dose distributions of the plan optimization using the standard PTV and specific PTV ( $PTV_{optim}$ ).

In this thesis, a few adjustments had to be made in order to address that issue. A straightforward strategy to mitigate this effect consists of defining a specific planning target volume ( $PTV_{\text{optim}}$ ) for pMBRT plan optimization. This volume was elongated in the direction of the beam at the PTV location (see Figure 2.19). Considering this new PTV in the spot optimization process, a dose homogenization within the SOBP was achieved when the pMBRT collimator was added during MC dose calculations (see Figure 2.19c). Although this strategy may slightly worsen the dose conformity of treatment plans, it serves as a surrogate of an optimization module adapted to the dose delivery method of minibeam.

Other parameters specific to pMBRT treatments (e.g., the position and orientation of the minibeam) to consider in the optimization process will be discussed in Section 4.6.

Regarding optimization objectives, PTV and OAR constraints were specific to each clinical case. In order to conduct a treatment plan comparison study under clinical conditions between pMBRT and conventional RT techniques, the reports, and recommendations for small-field treatment planning were followed (e.g., TG-101 for stereotactic radiotherapy [Benedict *et al.* 2010]). Details will be given in Chapters 4 and 5.

*The following three chapters are devoted to presenting the results obtained during this thesis. Chapter 3 is dedicated to dosimetric studies in pMBRT preclinical trials, Chapter 4 presents a treatment plan study to evaluate the potential of pMBRT for treating several clinical indications, and Chapter 5 explores the benefits of combining pMBRT with proton arc therapy.*



# Dosimetry for pMBRT preclinical trials

## Contents

<b>3.1</b>	<b>Rationale</b>	<b>121</b>
<b>3.2</b>	<b>Validation of Monte Carlo codes and dosimetric protocols</b>	<b>122</b>
<b>3.3</b>	<b>Robustness analysis</b>	<b>130</b>
3.3.1	Collimator tilt	132
3.3.2	Collimator translation	132
3.3.3	Target volume tilt	133
3.3.4	Collimator specifications	134
3.3.5	Air gap and collimator-isocenter distance	134
3.3.6	Spot shape	136
<b>3.4</b>	<b>Optimization of the experimental setup</b>	<b>139</b>
<b>3.5</b>	<b>Guidelines for pMBRT dosimetry in preclinical studies</b>	<b>141</b>
<b>3.6</b>	<b>Dosimetric protocol for pMBRT preclinical trials</b>	<b>143</b>
3.6.1	Determination of absorbed dose under reference conditions	143
3.6.2	Determination of absorbed dose under pMBRT conditions	144
<b>3.7</b>	<b>Dosimetry for <i>in vivo</i> and <i>in vitro</i> studies</b>	<b>146</b>
3.7.1	<i>In vivo</i> experiments	146
3.7.2	<i>In vitro</i> experiments	153
<b>3.8</b>	<b>Discussion and conclusions</b>	<b>155</b>

*This chapter presents the work performed and results obtained in the context of the pMBRT preclinical investigations carried out during this PhD thesis.*

## 3.1 Rationale

As described in Section 2.1.3, the dosimetry for pMBRT is a challenging and error-prone task due to the small beam sizes and the high dose gradients employed. The use of high-spatial-resolution detectors, which are not typically employed in clinical routines, is necessary to characterize pMBRT dose distributions. However, the uncertainty in dose measurements with those detectors may mask small variations in pMBRT dosimetric quantities. Therefore, MC simulations may

be used as a complementary tool in pMBRT dosimetric studies. In this work, the performance of the simulation codes and experimental protocols (including the detector choice) presented in Chapter 2 was tested in pMBRT conditions by comparing dose distributions measured experimentally and computed using MC simulations (see Section 3.2).

An additional challenge in pMBRT is the increased impact on dose distributions of very small uncertainties in the irradiation and setup configurations, compared to conventional seamless techniques. Along this line, a robustness analysis on the dosimetry for pMBRT preclinical experiments was performed by evaluating the influence of different irradiation and geometry parameters on dose distributions (see Section 3.3). Based on the results obtained, a series of guidelines and an adapted dosimetric protocol for optimizing the experimental setup and performing reproducible dosimetry were proposed (see Sections 3.4, 3.5 and 3.6).

Finally, once the experimental setup and protocols were optimized, the dosimetry for the pMBRT preclinical trials held at our institution (ICPO) during this thesis was performed (see Section 3.7).

## 3.2 Validation of Monte Carlo codes and dosimetric protocols

The MC codes and some of the detectors employed in this work have been previously validated for pMBRT dosimetry [De Marzi *et al.* 2018, Guardiola & Prezado 2020, Peucelle *et al.* 2015b]. However, the modification of some of the simulation parameters and irradiation conditions in this work (as described in Chapter 2) required an additional extensive validation prior to our biological experiments. The validation was mainly performed in the first four centimeters of the proton range since it is the range of depths mostly considered in preclinical trials. To do so, simulation results were compared with experimental data measured using different dosimeters. This comparison considered the overall shape of dose profiles as well as the dosimetric quantities that define pMBRT lateral dose distributions, i.e., full width at half maximum (FWHM) of the peaks, and peak-to-valley dose ratios (PVDR). In addition, relative dose measurements were performed at the Bragg peak depth since, as described in Section 2.1.4.2, some preclinical investigations considered the tumor irradiation at that position.

Firstly, I compared simulated lateral dose distributions with experimental data measured with solid-state detectors at 0 and 1 cm depth in water. As stated in the IAEA's COP for small-field dosimetry (TRS-483) [IAEA 2017]:

*“As no ideal detector exists, it is advised to use two or three different types of detectors suitable for a particular measurement so that redundancy in the results can provide more confidence and assurance that no significant dosimetry errors are being made.”*

Following this recommendation, two detectors that had already been proven suitable for pMBRT measurements (i.e., the microdiamond detector and the RAZOR diode) were used [De Marzi *et al.* 2018, Guardiola & Prezado 2020]. Collimator 3 (seven slits separated by 2.8 mm c-t-c distance; see Table 2.1) was employed in this case. A good agreement between MC results and measured data with both detectors was found in terms of the overall shape of lateral dose profiles (see Figure 3.1). The mean relative difference (considering peak and valleys doses) between MC and measured profiles with the microdiamond detector and the RAZOR diode was 2.8 % and 4.0 %, respectively. In addition, calculated and measured PVDRs and peak FWHM also agreed (see Table 3.1). These results suggest the appropriate modeling of our MC simulations regarding the parametrization of the source, selection of physics lists, and geometry modeling.

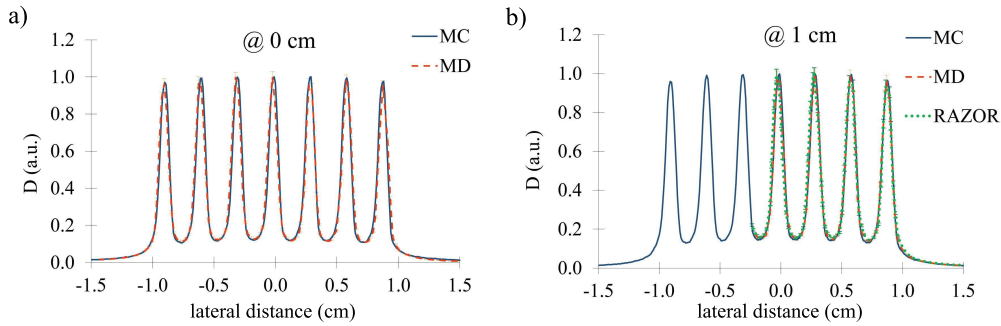


**Figure 3.1:** Relative lateral dose profiles at (a) 0 and (b) 1 cm depth in water computed using MC simulations and measured with the microdiamond (MD) detector and the RAZOR diode.

	0 cm depth		1 cm depth		
	MC	MD	MC	MD	RAZOR
<b>PVDR</b>	$8.3 \pm 0.1$	$8.5 \pm 0.3$	$6.9 \pm 0.1$	$6.7 \pm 0.3$	$6.6 \pm 0.3$
<b>FWHM<sub>peak</sub> (<math>\mu\text{m}</math>)</b>	$900 \pm 50$	$950 \pm 100$	$1000 \pm 50$	$1000 \pm 100$	$950 \pm 100$

**Table 3.1:** PVDR and peak FWHM of pMBRT lateral dose distributions simulated by MC codes and measured with the RAZOR diode and microdiamond (MD) detector at 0 and 1 cm depth in water.

Secondly, the suitability of radiochromic films for measuring pMBRT lateral dose profiles was evaluated. To do so, I first assessed the LET dependence of the films in broad beam conditions. As Figure 3.2 illustrates, the films employed in this thesis (i.e., EBT-XD and OC-1) do not exhibit quenching effect in the region of the proton beam depth dose profile considered in this study (four first centimeters of the proton range in water). Quenching correction factors (QCF) in that region were, on average,  $1.01 \pm 0.04$  and  $0.98 \pm 0.04$  for EBT-XD and OC-1 films, respectively. Figure 3.3 shows the QCF as a function of depth and LET. QCFs were computed as the ratio of dose read by films and the dose measured with the ppc05 ionization chamber

(IBA Dosimetry, Germany) [IBA Dosimetry 2022c]. In addition, the LET variation along pMBRT lateral profiles does not result in a significant quenching effect in film measurements. Figure 3.4 compares lateral dose profiles measured with films and the microdiamond detector. Mean QCFs at the peaks were  $1.03 \pm 0.06$  and  $1.05 \pm 0.06$  for EBT-XD and OC-1 films, respectively, whereas at the valleys were  $1.04 \pm 0.06$  and  $0.97 \pm 0.06$ .

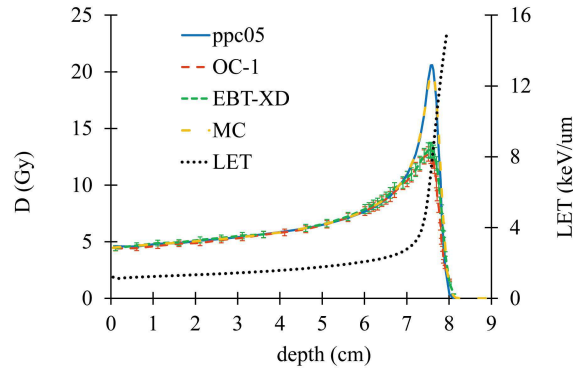


**Figure 3.2:** Depth dose profiles of a 100 MeV proton beam in water calculated by MC and measured with the ppc05 ionization chamber and radiochromic films (EBT-XD and OC-1), and LET depth distribution calculated by MC. Broad beam conditions were considered for those measurements.

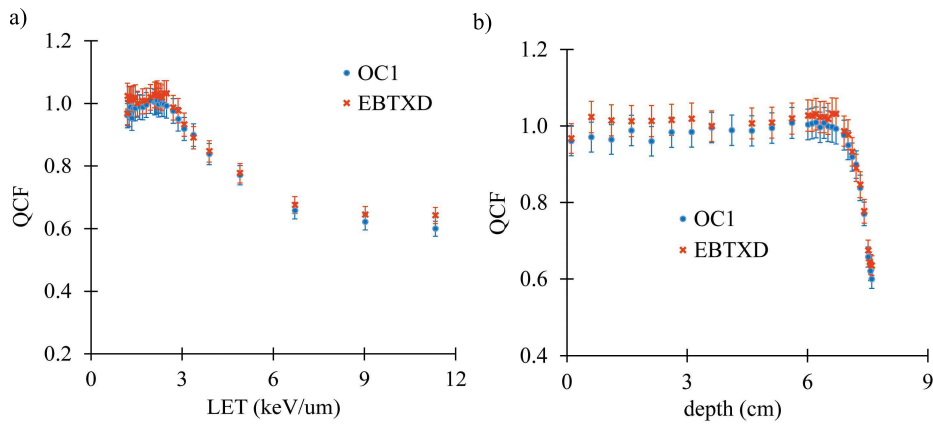


**Figure 3.3:** Quenching correction factors (QCF) as a function of (a) LET, and (b) depth for EBT-XD and OC-1 films. A 100 MeV proton beam and broad beam conditions were considered for those measurements.

Once the LET dependence in the film response was evaluated, measurements using OC-1 films were compared with the previously validated MC results and experimental data measured with the RAZOR and microdiamond detectors. Figure 3.5 and Table 3.2 show the agreement between lateral profiles at 0 cm depth in water measured with the different detectors and MC data, proving the good performance of OC-1 films in pMBRT conditions. The mean relative difference (considering peak and valley doses) of film measurements with respect to the

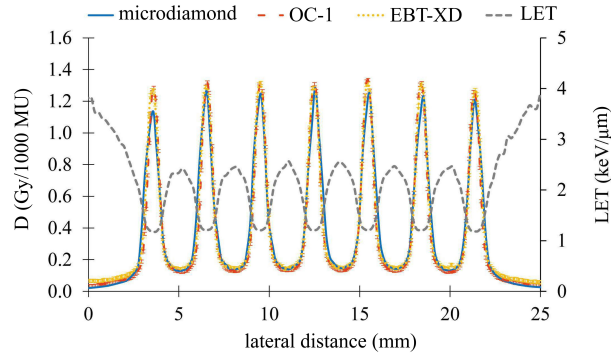


**Figure 3.4:** Lateral dose profiles at 0 cm depth in water measured with the microdiamond detector and EBT-XD and OC-1 films. The dose is expressed as Gy per 1000 MU for the sake of comparing the detectors employed at different dose ranges. The LET along the lateral profile is also displayed.

microdiamond detector, the RAZOR diode, and MC data was 3.8 %, 2.9 %, and 1.2 %, respectively.

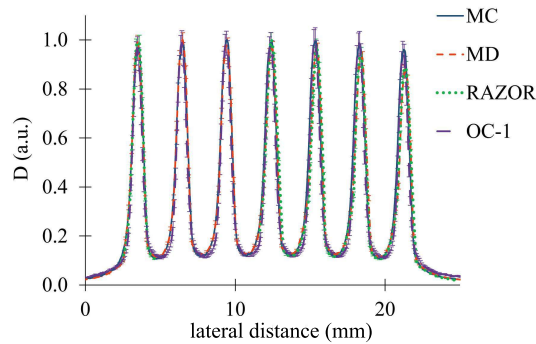


**Figure 3.5:** Lateral dose profiles at 0 cm depth in water simulated with MC and measured with the microdiamond (MD) detector, RAZOR diode, and OC-1 films.

	MC	MD	RAZOR	OC-1
<b>PVDR</b>	$8.2 \pm 0.1$	$8.0 \pm 0.3$	$8.3 \pm 0.3$	$8.1 \pm 0.5$
<b>FWHM<sub>peak</sub> (<math>\mu\text{m}</math>)</b>	$900 \pm 50$	$950 \pm 100$	$900 \pm 100$	$850 \pm 50$

**Table 3.2:** PVDR and peak FWHM at 0 cm depth in water calculated by MC and measured with OC-1 films, the RAZOR diode, and the microdiamond (MD) detector.

OC-1 and EBT-XD films were further tested by comparing MC results and experimental measurements at several depths in a solid water phantom with different collimators and under several conditions. As an example of the agreement between measured and simulated data, Figure 3.6 illustrates a comparison between lateral dose profiles in an extreme situation where the collimator 3 (seven slits separated by 2.8 mm c-t-c distance; see Table 2.1) was tilted by  $0.350^\circ$  with respect to the beamline. The relative difference (considering peak and valley doses) between

calculated and measured data was below the uncertainty in dose measurements with the films (5 %). Table 3.3 compares those lateral profiles in terms of the PVDRs. MC results and experimental data agree for all the depths investigated (from 0 cm to 7 cm). In addition, experimental and calculated peak FWHMs are also compatible. For instance, at 1 cm depth in solid water,  $\text{FWHM}_{\text{exp}}$  and  $\text{FWHM}_{\text{MC}}$  were  $1100 \pm 50 \mu\text{m}$  and  $1150 \pm 50 \mu\text{m}$ , respectively. These results demonstrate the suitability of these film types for pMBRT relative dosimetry. In addition, the agreement in the overall shape of lateral profiles further confirms the appropriate parametrization of the MC codes employed, even in situations where the collimator is tilted.

Depth (cm)	MC	OC-1	EBT-XD
0	$5.8 \pm 0.1$	$5.5 \pm 0.4$	$5.8 \pm 0.5$
1	$4.9 \pm 0.1$	$4.8 \pm 0.4$	$4.7 \pm 0.4$
2	$4.07 \pm 0.05$	$3.9 \pm 0.3$	$4.0 \pm 0.3$
3	$2.93 \pm 0.04$	$3.0 \pm 0.2$	$2.9 \pm 0.2$
4	$2.08 \pm 0.03$	$2.0 \pm 0.2$	$2.0 \pm 0.2$
5	$1.50 \pm 0.02$	$1.4 \pm 0.1$	$1.4 \pm 0.1$
6	$1.21 \pm 0.01$	$1.17 \pm 0.09$	$1.10 \pm 0.09$
7	$1.08 \pm 0.01$	$1.06 \pm 0.08$	$1.05 \pm 0.08$

**Table 3.3:** PVDR measured with EBT-XD and OC-1 films and simulated by TOPAS (MC) at 0, 1, 2, 3, 4, 5, 6, and 7 cm depth in solid water.

The performance of films for measuring relative lateral dose profiles at the Bragg peak position was also evaluated. For this validation, the setup considered in *in vivo* studies where the tumor is irradiated at the Bragg peak position (see Setup 3 in Section 2.1.4.2) was employed. This configuration involved a 5 cm-thick range shifter and the solid water phantom described in Chapter 2. Lateral profiles were evaluated at 1.6 cm depth in solid water (BP position). Measurements with both film types (EBT-XD and OC-1) were in agreement with MC data, as illustrated in Figure 3.7. In addition, calculated ( $1.63 \pm 0.05$ ) and measured ( $1.6 \pm 0.1$ ) PVDR values were compatible within their respective uncertainties.

Besides the validation of our simulations in homogeneous phantoms (i.e., solid water phantom and water tank), I compared MC results and film measurements in a heterogenous rat phantom. The description of the rat phantom can be found in Section 2.1.4.1. Measured and simulated lateral dose profiles at the rat's skin and 1.6 cm depth were considered. A good agreement in terms of the overall shape of dose distributions (see Figure 3.8), PVDRs, and peak FWHM (see Table 3.4) was found between MC results and data measured with OC-1 and EBT-XD films. The mean relative difference (considering peak and valley doses) of measured and simulated profiles was 3.2 % for both film types. The measurement points considered are relevant in *in vivo* preclinical investigations since 1.6 cm depth is

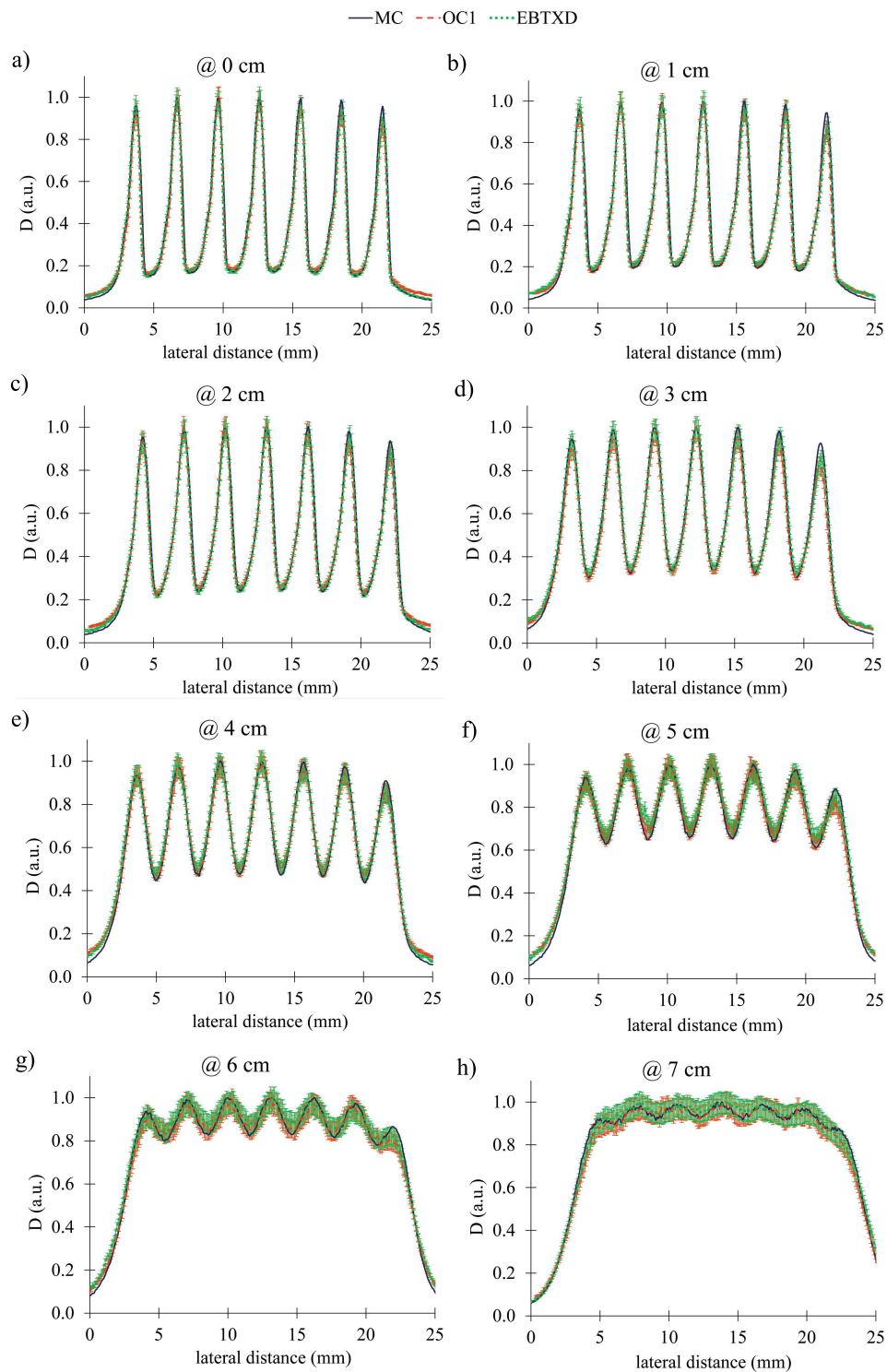


**Figure 3.6:** Relative lateral dose profiles computed by MC simulations and measured with EBT-XD and OC-1 films at 0, 1, 2, 3, 4, 5, 6, and 7 cm depth in solid water.

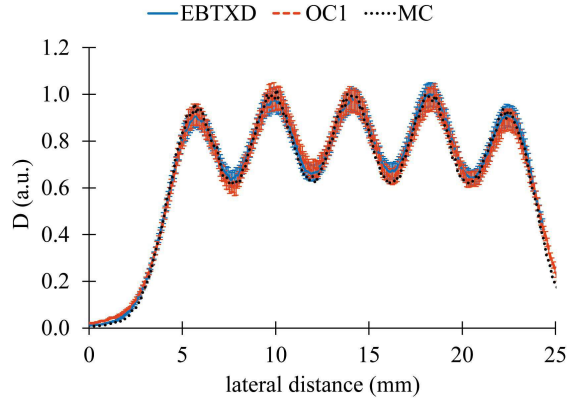


**Figure 3.7:** Relative lateral dose profiles computed by means of MC simulations and measured with EBT-XD and OC-1 films at the Bragg peak position.

the tumor implantation location in the rat's brain. It is important to remark that the rat phantom employed resembles the rats irradiated in preclinical trials (see Section 2.1.4.1). Therefore, the agreement between measured and simulated data at this depth suggests that MC simulations can be used in the process of dose estimation and prescription (see Section 3.6), which typically considers the mean dose to the tumor as a figure of merit. In addition, these results illustrate the suitable performance of our MC codes in situations involving heterogeneities.

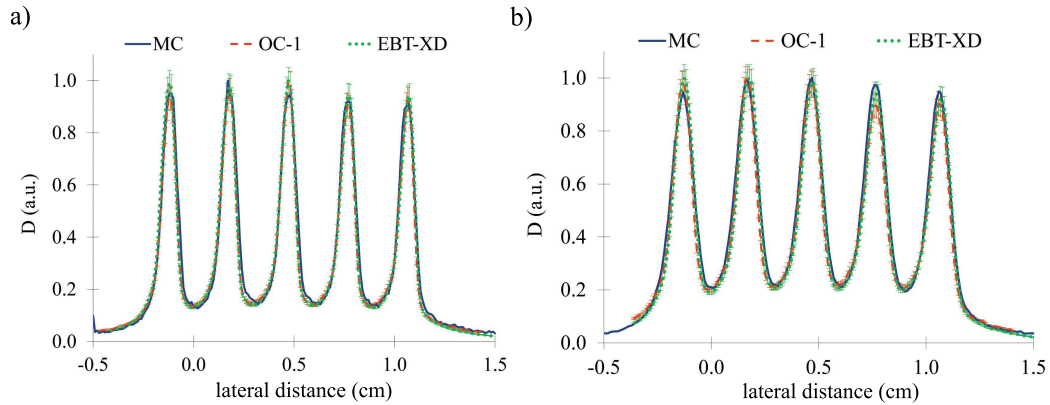


**Figure 3.8:** Relative lateral dose profiles measured with OC-1 and EBT-XD films and calculated by MC at the rat's skin and 1.6 cm depth in the rat phantom.

	0 cm depth			1.6 cm depth		
	MC	OC-1	EBT-XD	MC	OC-1	EBT-XD
PVDR	$6.7 \pm 0.1$	$6.9 \pm 0.5$	$7.1 \pm 0.5$	$4.7 \pm 0.1$	$4.6 \pm 0.3$	$4.7 \pm 0.3$
$\text{FWHM}_{\text{peak}} (\mu\text{m})$	$950 \pm 50$	$900 \pm 50$	$900 \pm 50$	$1150 \pm 50$	$1200 \pm 50$	$1200 \pm 50$

**Table 3.4:** PVDR and peak FWHM at the rat's skin (0 cm depth) and 1.6 cm depth in the rat phantom calculated by MC and measured with OC-1 and EBT-XD films.

A good agreement was also found between measured dose rates with EBT-XD and OC-1 films, which were independently calibrated (see Figure 3.9 and Table 3.9). The relative difference between those measurements was below 7 %. This result suggests the suitability of these films for dose estimation in the pMBRT measurements considered in preclinical trials (lateral profiles at depths between 0 cm and 2 cm). The calibration of these films was further validated by comparing the dose rate measured with films and the ppc05 ionization chamber in broad beam conditions, i.e., using collimator 7 (16 x 20 mm<sup>2</sup> aperture; see Table 2.1) (see Table 3.5).

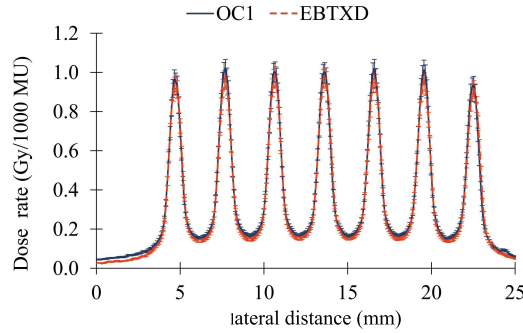


**Figure 3.9:** Lateral dose distributions in terms of Gy per 1000 MU measured with OC-1 and EBT-XD films at 1 cm depth in water.

	pMBRT		BB		
	OC-1	EBT-XD	IC	OC-1	EBT-XD
$\dot{D}_{\text{peak}}$ (Gy/1000 MU)	1.00 ± 0.05	0.97 ± 0.05	-	-	-
$\dot{D}_{\text{valley}}$ (Gy/1000 MU)	0.17 ± 0.01	0.15 ± 0.01	-	-	-
$\dot{D}_{\text{mean}}$ (Gy/1000 MU)	0.41 ± 0.02	0.39 ± 0.02	3.7 ± 0.1	3.7 ± 0.2	3.5 ± 0.2

**Table 3.5:** Dose rates (as Gy per 1000 MU) at peak and valley regions and on average over the whole profile. Dose rates were measured with a ppc05 ionization chamber (IC) and OC-1 and EBT-XD films in pMBRT and broad beam (BB) conditions.

Overall, the suitability of the detectors employed in this PhD thesis for our purposes of pMBRT preclinical dosimetry has been proven. In addition, our MC codes have been validated in terms of the appropriate modeling of the experimental setup and physics parameters for simulating pMBRT lateral dose profiles.

*Once the suitability of detectors and the good parametrization of MC codes was proven, they were used to carry out different dosimetric studies, presented in the following sections.*

### 3.3 Robustness analysis

In this study, the sensitivity of pMBRT dose distributions to variations in different irradiation and geometry parameters was evaluated. The greater influence of those variations on dose distributions, compared to conventional techniques, arises from the smaller beamlet sizes and higher dose gradients employed in pMBRT. This study focused on the dosimetry for preclinical investigations (lateral profiles from 0 cm to 4 cm depth). In this work, the parameters that, based on our experience, are easily fluctuating and relevant in proton minibeam irradiations were considered:

1. The tilt of the collimator with respect to the PBS beamline ( $\theta$  in Figure 3.10). The angle between the beamline and the collimator entrance may influence dose distributions since the divergence of the slits is optimized to be collinear with the beam divergence in all cases (see Section 2.1.2).
2. The translation of the collimator in the two directions perpendicular to the beamline ( $\Delta X$  in Figure 3.10). The displacement of the collimator from the beam axis may affect the homogeneity of the peak heights along the profile since some of the slits may be underirradiated.
3. The tilt of the target volume (i.e., phantom/detector axis in this case) with respect to the beamline ( $\alpha$  in Figure 3.10).
4. The collimator specifications, i.e., the c-t-c distance between slits, divergence angles of the slits, and slit width (c-t-c distance,  $\gamma$ , and  $w$  in Figure 3.10). The manufacturing process of submillimeter-width (400  $\mu\text{m}$ ) and divergent ( $w = 0.06^\circ$  to  $0.9^\circ$ ) multislit collimators may introduce new sources of uncertainty to the collimator specifications, influencing the irradiation parameters and lateral dose profiles.
5. The air gap between the collimator exit and the target volume, and the collimator-isocentre distance (CID). The distance between the surface of the target volume and the downstream part of the collimator may impact the lateral dose profiles since, as the air gap increases, the distance scattered protons may travel before reaching the target do so. Also, the proximity of the collimator entrance to the source may affect dose profiles.
6. Pencil beam spot shape and size. The proton source's size and shape may impact pMBRT dose distributions since the collimator's slits are not symmetrical in the two dimensions perpendicular to the beamline. In our MC simulations, the spot size is defined by the standard deviation of the Gaussian that describes the horizontal and vertical spread of particle positions at the nozzle entrance ( $\sigma_x$  and  $\sigma_y$ ) (see Section 2.2.3.2). The impact of variations in these parameters was evaluated.

Figure 3.10 shows a schematic representation of the parameters evaluated.

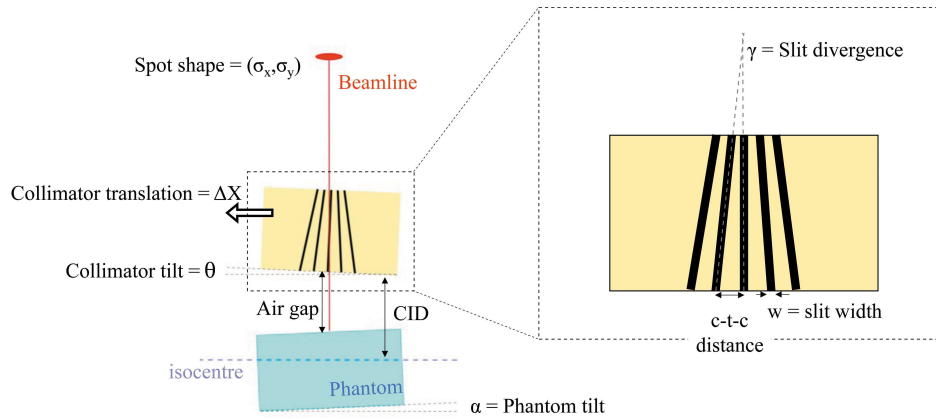


**Figure 3.10:** Schematic representation of the parameters studied in the robustness analysis.

MC simulations were employed to study how variations in these parameters might affect lateral dose profiles. Table 3.6 describes the set of parameters considered and the values assessed. The value of each parameter was modified individually to evaluate its effect on dose distributions independently. Unless otherwise stated, reference values were utilized (see Table 3.6). Collimators 3 and 5 (seven slits separated by 2.8 mm c-t-c distance, and five slits separated by 4 mm c-t-c distance; see Table 2.1) were considered for this study.

Parameter	Values evaluated
Collimator tilt	$0^*$ , $\pm 0.125$ , $\pm 0.250$ , and $\pm 0.500^\circ$
Collimator translation	$0^*$ and $\pm 2$ mm in X and Y directions
Target volume tilt	$0^*$ , $\pm 1$ , and $\pm 3^\circ$
c-t-c distance	3.86, 3.93, and $4.00^*$ mm
Slit divergence	0.100, 0.120 and $0.125^* \text{ }^\circ$
Slit width	$400^*$ and $450 \mu\text{m}$
Air gap	$5^*$ , 6, and 7 cm
CID	$8.66^*$ and 38.66 cm
Spot size $(\sigma_x, \sigma_y)$	$(11,11)^*$ , (8,14), (9,13), (9,16), (10,15), (10,12), (13,9), (15,9), (15,10), (16,9), (16,10), (17,10.5), (19, 11) mm

**Table 3.6:** Values considered for the parameters evaluated. \* indicates the reference values. c-t-c and CID stand for center-to-center and collimator-isocenter distance, respectively.

For each configuration (i.e., sets of values in Table 3.6), the peak FWHM, PVDR, and peak, valley, and mean doses were evaluated. Depths from 0 cm to 4 cm were analyzed since it is the region of the proton range considered for irradiations in preclinical trials. In all cases, mean doses were calculated as the

average dose between the first and last peak of the profile, and PVDRs as the ratio of the central peak dose and the dose in the valley to the left of the central peak.

*The following subsections present the robustness analysis results for each parameter considered.*

### 3.3.1 Collimator tilt

**A rotation of the collimator in the longitudinal direction of the slits significantly disturbs the lateral dose profiles.** PVDR decreases by 5 % to 50 % for tilt angles of  $\pm 0.125^\circ$  to  $\pm 0.5^\circ$ , as compared to the  $0^\circ$ -tilt situation. This variation is mainly caused by the decrease in peak doses (by 3 % to 50 %). Valley doses are also affected by the collimator inclination; a maximum reduction of 20 % was found for tilt angles of  $\pm 0.5^\circ$ . In addition, the average dose decreases significantly (up to 35 % for a  $\pm 0.5^\circ$ -tilt). Similar values were found experimentally. These changes in lateral dose profiles, relative to the reference scenario ( $0^\circ$ -tilt), are illustrated in Figure 3.11a. An increasing tilt also reduces the homogeneity of the peak height along the profile by 6 % to 48 % for tilt angles of  $\pm 0.125^\circ$  to  $\pm 0.5^\circ$  (see Figure 3.11b). In this case, the homogeneity of the lateral profile is defined as the relative difference between the maximum and minimum peak doses.

Regarding the size of minibeam, peak FWHM increases up to 50 % for tilt angles of  $\pm 0.5^\circ$ . In addition, the profile is displaced with respect to the center of the phantom (see Figure 3.11b).

Contrarily, a collimator tilt in the perpendicular direction of the slits (along the peak-valley pattern) does not influence lateral dose profiles for the angles studied.

The alteration of lateral dose profiles due to the collimator-beamline tilt is mainly caused by the loss of collinearity between the divergence of each slit and the divergence of the PBS beamline. This results in a lesser number of protons passing through each slit, considerably decreasing the peak and valley doses.

It is important to highlight that the tilt angles considered in this study are not easily detectable in clinical QA routines and are typically below tolerance levels in conventional techniques. Therefore, the technical implementation of pMBRT in clinics should consider updated and adapted QA protocols, including this parameter's effect.

### 3.3.2 Collimator translation

It was observed that a translation of the beam, up to  $\pm 2$  mm, with respect to the collimator axis in the two directions perpendicular to the beamline, has no impact on the overall shape of the lateral dose profiles (apart from displacing their position) (see Figure 3.12a). This may be caused because the broad beam field created at the collimator entrance in our experimental setup (see Section 2.1.4.2) is relatively large ( $5 \times 5 \text{ cm}^2$ ) compared to the pMBRT irradiation area ( $1.6 \times 2 \text{ cm}^2$ ) and the collimator translation considered (2 mm). In other setups where the broad

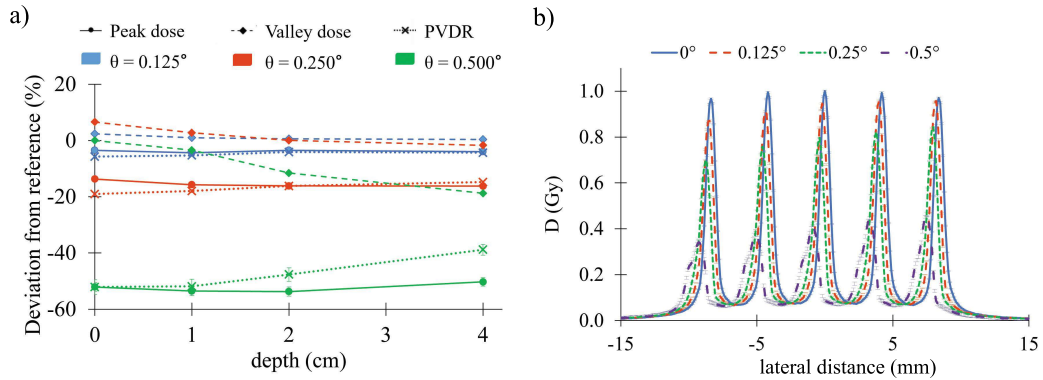


**Figure 3.11:** (a) Variation in peak-to-valley dose ratios (PVDRs) and peak and valley doses with respect to the reference scenario ( $0^\circ$ -tilt) as a function of the collimator tilt ( $\theta$ ). (b) Lateral dose profiles at a 1 cm depth in water for different collimator tilts with respect to the beamline.

beam field dimension is comparable to the minibeam irradiation area, the collimator translation may affect dose distributions.

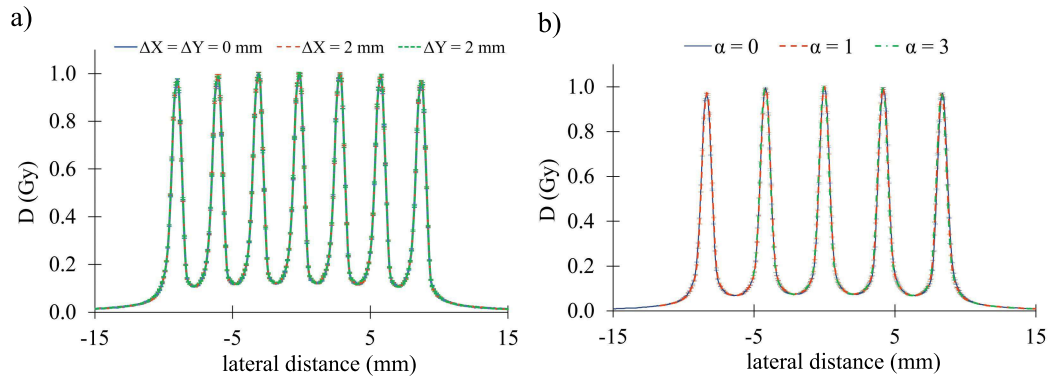


**Figure 3.12:** Lateral dose profiles at a 1 cm depth in water for (a) different collimator translations with respect to the beamline and (b) different phantom tilt angles with respect to the collimator exit. Profiles were overlapped for the sake of comparing them.

### 3.3.3 Target volume tilt

A target volume (e.g., phantom) tilt, up to  $\pm 3^\circ$ , with respect to the downstream plane of the collimator does not influence the overall shape of the lateral dose profiles (see Figure 3.12b). This suggests that the increased space protons travel in the air on one side of the profile due to the inclination of the target volume is not significant in terms of the dose deposited.

### 3.3.4 Collimator specifications

The manufacturing process of pMBRT collimators (electrical discharge machining), despite being very precise, comes with its own uncertainties. In particular, the slit width has an inherent uncertainty of approximately 50  $\mu\text{m}$ . This also results in uncertainties in the c-t-c distance and slit divergence.

**Slight variations in the c-t-c distance, slit divergence, and slit width caused by the uncertainties in the manufacturing process of collimators significantly affect lateral dose profiles.** Figure 3.13 summarises the results. To cite some examples:

- A reduction of 0.15 mm in the c-t-c distance implies a decrease in PVDR values in an amount of 5 % to 6 % (see Figure 3.13a). This is caused by the increase in valley doses (up to 7 %) due to the greater contribution of scattered protons to this region when minibeam are closer. Contrarily, a 0.15 mm increase in the c-t-c distance leads to an increase in the PVDR and a decrease in valley doses by the same magnitude. In addition, the mean dose increases/decreases up to 13 % for a 0.15 mm c-t-c distance decrease/increase. Conversely, peak doses and peak FWHM are not affected by that variation.
- Regarding the slit divergence, an increase of up to 5 % reduces the PVDR by up to 6 % since valley doses increase by 6 % (see Figure 3.13b) due to the greater contribution of scattered protons to this region. Consequently, the mean dose increases by up to 10 %, whereas peak doses and peak FWHM remain constant.
- Finally, an increase by 50  $\mu\text{m}$  in the slit width leads to the following effects: a reduction of the PVDR by up to 5 %, an increase in the peak and valley doses by up to 19 % (see Figure 3.13c), and an increment in the average dose by up to 15 %. Peak FWHM also increases by 8 %. Reverse effects of the same magnitude were found for a 50  $\mu\text{m}$  reduction in the slit width. These effects are caused by the different number of protons passing through the collimator depending on the width of the slits.

### 3.3.5 Air gap and collimator-isocenter distance

**The air gap between the surface of the target volume and the collimator exit has also a considerable impact on dose distributions** due to the fact that a greater number of scattered protons travel from peak to valley positions as the air gap increases. As an example, an increment of 1 cm in the air gap leads to a decrease by up to 14 % in the PVDR at shallow depths. Peak doses are reduced by up to 11 %, valley doses increase by up to 5 %, and the average dose is decreased by 4 %. These variations decrease as a function of depth, as Figure 3.14 shows. The peak FWHM also increases by 6 % to 9 % for each additional centimeter of air gap.

Regarding the effect of the collimator-isocenter distance (CID), i.e., snout

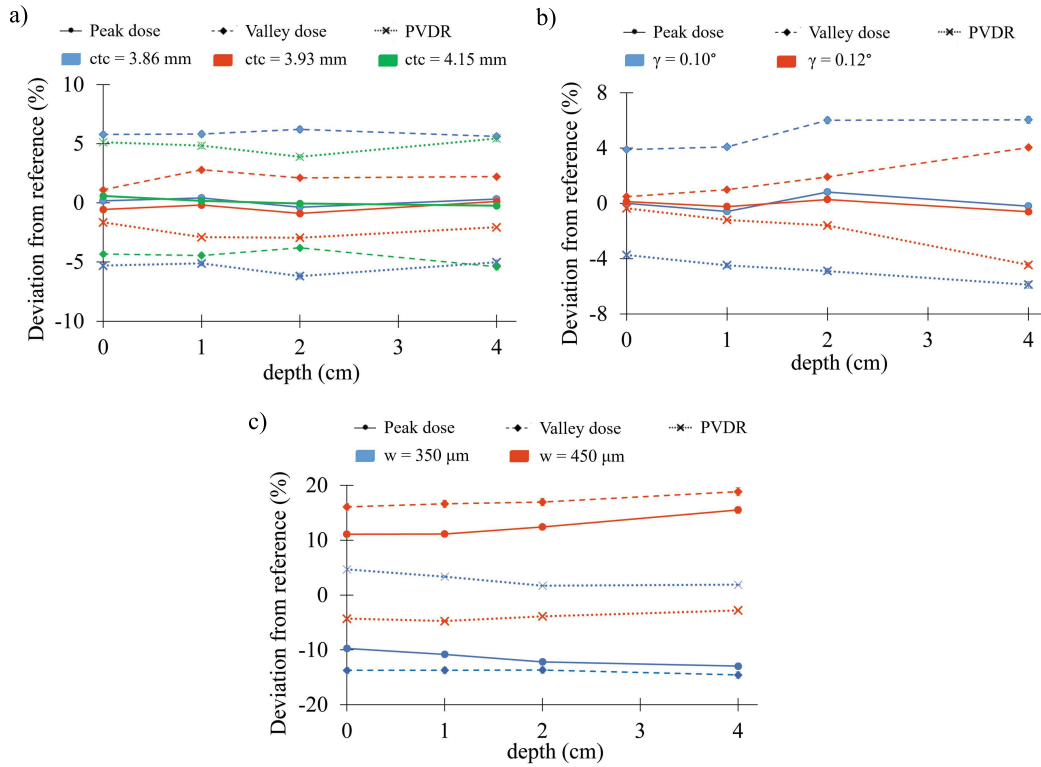


**Figure 3.13:** Variation in peak-to-valley dose ratios (PVDRs) and peak and valley doses with respect to the reference scenario (c-t-c = 4 mm,  $\gamma = 0.125^\circ$ , and  $w = 400 \mu\text{m}$ ; see Table 3.6) as a function of depth and (a) center-to-center (c-t-c) distance, (b) slit divergence ( $\gamma$ ), and (c) slit width (w).

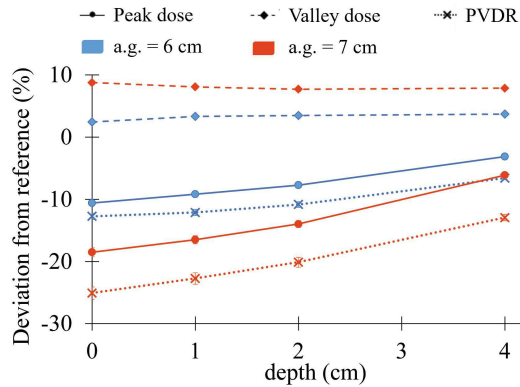


**Figure 3.14:** Variation in peak-to-valley dose ratio (PVDRs) and peak and valley doses as a function of depth and air gap (a.g.) with respect to the reference scenario (5 cm a.g.).

extension, a reduction of this parameter may affect dose distributions since, for a given air gap, the target is closer to the source. Also, the collinearity between the divergent slits and beam divergence is lost as the slit divergence is optimized for a specific CID. To illustrate this effect, I found that a reduction of the CID by 30 cm

leads to an increment in the peak, valley, and average doses by up to 30 % and a decrease by 8 % in the PVDR. Similar results were found experimentally.

### 3.3.6 Spot shape

Variations in the pencil beam spot size in the two dimensions orthogonal to the beamline (i.e., spot shape) considerably influence parameters that characterize pMBRT lateral dose profiles (see Table 3.15).

Condition			Variation (%)				
#	$\sigma_x$ (mm)	$\sigma_y$ (mm)	$D_{\text{peak}}$	$D_{\text{valley}}$	$D_{\text{mean}}$	PVDR	$\text{FWHM}_{\text{peak}}$
1	8	14	17	-9	9	28	-11
2	9	16	9	-12	4	24	
3	9	13	10	-6	6	16	-7
4	10	15	5	-9	2	15	
5	10	12	6	-3	4	9	
6	11	11	-	-	-	-	-
7	13	9	-10	4	-4	-13	
8	15	9	-17	3	-9	-20	
9	15	10	-32	-9	-11	-25	
10	16	9	-21	-2	-13	-19	7
11	17	10.5	-32	-9	-23	-25	
12	19	11	-30	-0	-21	-30	11

**Table 3.7:** Variation of peak, valley, and mean doses, PVDR, and peak FWHM in different spot size conditions compared to reference condition 6, where the pencil beam spot is symmetrical. The spot size is expressed as  $\sigma_x$  and  $\sigma_y$  values. Values in this table correspond to a lateral profile at 0 cm depth.

For instance, a non-symmetrical spot characterized by  $\sigma_x$  and  $\sigma_y$  of 15 and 10 mm reduces by 32 %, 9 %, 11 %, and 25 % the peak dose, valley dose, mean dose, and PVDR, respectively, as compared to the reference condition (i.e., a symmetrical spot of 11 mm  $\sigma_x$  and  $\sigma_y$ ) in the irradiation setup considered (vertical orientation of the slits).

A spot size that reproduces experimental lateral dose profiles in all the configurations studied in this PhD thesis can be defined by  $\sigma_x$  and  $\sigma_y$  of 15 and 10 mm. These values were used in all the MC simulations performed in this thesis.

Variations of the spot size in each direction affect peak and valley doses independently. For example, a variation in  $\sigma_y$  (conditions 2 and 3 in Table 3.15) only significantly affects the valley dose, whereas a change in  $\sigma_x$  (conditions 7 and 8

in Table 3.15) influences only the peak dose. To further correlate the shape of the pencil beam spot and its effect on peak and valley doses, more data and a more exhaustive evaluation, which is out of the scope of this thesis, are needed.

These results suggest a significant dependence of the mean dose on the shape and reproducibility of the spots as they enter (and therefore are transmitted through) the collimator. In other words, the dose and monitor units may need to be checked (typically done by a monitor chamber) after the beam has passed through the collimator and not before, as typically done in conventional techniques

In addition, lateral dose profiles differ significantly depending on the slit orientation for a given spot size. For instance, for a beam spot of 9 and 13 mm  $\sigma_x$  and  $\sigma_y$ , the peak dose, valley dose, mean dose, and PVDR differ by 19 %, 13 %, 10 %, and 30 % in the vertical and horizontal slit orientation (see Figure 3.15).

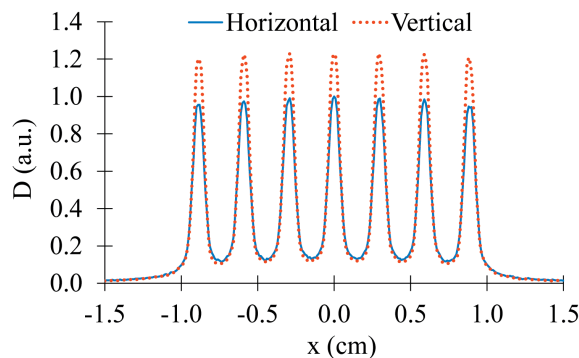


**Figure 3.15:** Simulated lateral dose profiles at 0 cm depth in water for the vertical and horizontal orientation of the slits and a given pencil beam spot size.

A summary of the impact on dose distributions of variations in irradiation and setup parameters is presented in Table 3.8.

**The sensitivity of lateral dose distributions in pMBRT to slight variation in the setup and irradiation parameters affects not only dosimetric quantities, e.g., peak and valley doses or PVDR, but also the biological responses directly correlated with those physical quantities.** The increased normal tissue sparing of minibeam may be reduced by a decrease in the PVDR since higher PVDRs (higher spatial dose fractionation) are assumed to favor normal tissue sparing [Dilmanian *et al.* 2002]. A variation in the peak width (i.e., peak FWHM) also influences the response of normal tissues since one of the participants in the decreased radiation-induced toxicity of pMBRT is the so-called dose-volume effect (the smaller the field size is, the higher the tolerance of normal tissues)[Curtis 1967, Hopewell & Trott 2000]. The increase or reduction in peak and valley doses also plays a crucial role in normal tissue sparing, especially valley doses, since strong indications suggest that these low-dose regions are responsible for the preservation of normal tissue architecture and survival of

Parameter	Variation	Maximum variation (%)				
		PVDR	Peak dose	Valley dose	Mean dose	FWHM
Collimator tilt	↗ 0.5°	↘ 50	↘ 50	↗ 20	↘ 35	↗ 50
Collimator translation	↗ 2 mm	0	0	0	0	0
Phantom tilt	↗ 3°	0	0	0	0	0
c-t-c distance	↗ 0.15 mm	↘ 6	0	↗ 7	↗ 13	0
Slit divergence	↘ 5 %	↘ 6	0	↗ 6	↗ 10	0
Slit width	↗ 50 μm	↘ 5	↗ 19	↗ 19	↗ 15	↗ 8
Air gap	↗ 1 cm	↘ 14	↘ 11	↗ 5	↘ 4	↗ 9
CID	↗ 30 cm	↘ 8	↗ 30	↗ 30	↗ 30	0
Spot size	± 5 mm	± 24	± 21	± 12	± 13	± 10

**Table 3.8:** Maximum variation of the peak-to-valley dose ratio (PVDR), peak FWHM, and peak, valley, and average doses for a given variation in the evaluated parameters.

progenitor cells [Dilmanian *et al.* 2002]. Also, a recent study concluded that valley doses to the tumor correlate with the increased lifespan in pMBRT preclinical trials [Fernandez-Palomo *et al.* 2022]. In addition, an unforeseen variation in the mean dose may also affect the comparison of pMBRT with conventional broad beam PT since this is the quantity commonly used as the dose prescription parameter in preclinical investigations [Prezado *et al.* 2018, Prezado *et al.* 2019, Lamirault *et al.* 2020b, Lamirault *et al.* 2020a, Bertho *et al.* 2021b]. Variation in parameters that cause a translation of the lateral profile may also affect the overall response of animals to treatments since normal tissue volumes and tumors may be irradiated or underirradiated, respectively, which is especially relevant in pMBRT due to the high doses per fraction employed. Other studies also reported some of these dependencies [Rivera *et al.* 2020].

Therefore, **the accurate knowledge and reporting of the physical parameters of pMBRT irradiations are imperative to extract reliable conclusions from preclinical studies when correlating physical quantities and biological endpoints.** Given the significant and unexpected effect that variations in setup and irradiation parameters may have on dose distributions and biological responses to pMBRT, adapted protocols and methodologies for this technique are needed since these fluctuations may be overlooked in protocols for conventional techniques.

*In the following sections, a methodology to optimize the experimental setup (Section 3.4) and guidelines for a reproducible dosimetry in preclinical trials (Section 3.5) are proposed.*

### 3.4 Optimization of the experimental setup

As discussed in the previous section, an exhaustive optimization of the experimental setup for pMBRT may be necessary when this technique is implemented in a clinical beamline due to two main reasons: (i) optimizing the irradiation parameters to fully exploit the benefits of pMBRT and (ii) ensuring the reproducibility of irradiations taking into account the increased sensitivity of dose distributions as compared to conventional seamless techniques.

For those purposes, a methodology to optimize the experimental setup at our institution (ICPO) was developed. Since the setup parameter that influences the most lateral dose profiles is the tilt between the collimator and the beamline (see Section 3.3), the process proposed focused on the alignment of the beam direction to the collimator entrance.

The collinearity between the beamline and collimator could depend on the orientation of the collimator as well as the rotation angle of the gantry. Figure 3.16 shows differences in dose distributions considering the two orientations of the slits for a given incidental beam angle to the collimator entrance. Therefore, **an independent optimization (i.e., alignment between the beamline and the collimator entrance) was done for each irradiation configuration.**

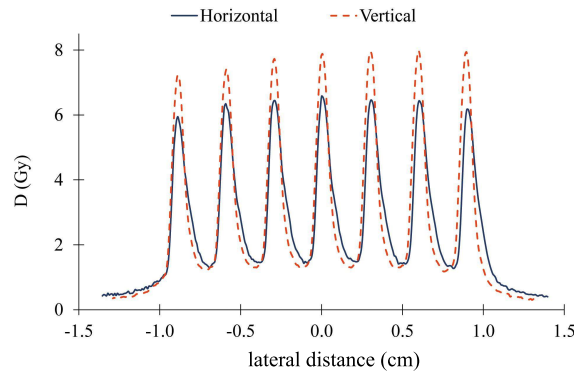


**Figure 3.16:** Lateral dose distributions measured with OC-1 films at 0 cm depth in solid water for the vertical and horizontal orientation of the slits and given incidental beam angle to the collimator entrance.

Firstly, the beam was centered on the collimator entrance. The position of a  $5 \times 5 \text{ cm}^2$  broad beam field was modified until the center of the field matched the collimator axis. The Lynx detector was employed to measure the 2D dose profile of the field.

Following the centering of the beam with respect to the collimator, the beamline was aligned to the orthogonal direction to the collimator entrance by varying the incidental beam angle. In the PBS beamline employed, the point where the beam crosses the two ionization chambers of the gantry (see Section 2.1.1) can be modified. This points will be referred to as IC offset hereafter. A variation of these points leads to a change in the beamline angle, as Figure 3.17 illustrates. We modified

the beam alignment parameters at their passage over these two chambers (internal procedure of the IBA system) in order to make the beam and collimator collinear at the isocentre.

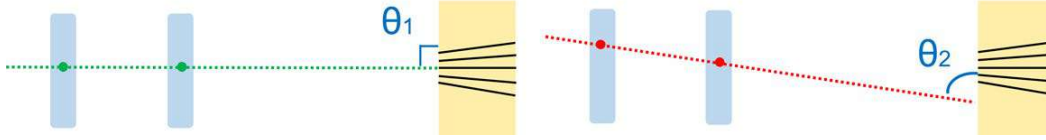


**Figure 3.17:** Schematic representation of how the ionization chamber offsets influence the beamline angle with respect to the collimator.

For each incidental beam angle (i.e., set of IC offsets), peak doses were measured with a Lynx detector at 7 cm from the collimator exit. The peak dose was chosen as a figure of merit for the beam alignment since this quantity is significantly reduced by an increasing beamline-collimator tilt (see Section 3.3.1). Therefore, the maximum peak dose was sought to find the minimum tilt angle. A non-divergent single-slit collimator (collimator 1 in Table 2.1) was employed to minimize uncertainties due to the divergence of the slits.

This study found the optimum beam parameters for each irradiation configuration. They were used in all pMBRT irradiations performed after this study. As an example of the results of the optimization for a given configuration (horizontal orientation of the slit and collimator of seven slits separated by 2.8 mm c-t-c distance), the tilt angle was reduced from  $0.35 \pm 0.05^\circ$  prior to the optimization to  $0.0 \pm 0.1^\circ$  when using the optimized beam configuration. Figure 3.18 illustrates simulated and measured lateral profiles prior to and post-optimization. As a result of the beam alignment, the PVDR increased from  $5.5 \pm 0.3$  and  $4.8 \pm 0.3$  at depths of 0 and 1 cm, respectively, to  $9.0 \pm 0.5$  and  $7.5 \pm 0.4$ . After the optimization, a higher dose homogeneity between slits (by 10 %) was also observed (see Figure 3.18).

In this study, it has been shown that conventional alignment techniques (including beam-snout-collimator collinearity control) are not accurate enough for pMBRT. Therefore, adapted methodologies, such as the one presented in this section, are necessary to optimize the pMBRT irradiation setup and enhance the beam transmission through the final collimator.

It is important to note that even if the collimator entrance and beamline are well aligned, the collimator insert containing the slits may not fit perfectly in the external frame of the collimator (see Section 2.1.2), which could also introduce a loss of collinearity between the slits and beamline. This defect in the collimator insert, caused by the manufacturing process, can be revealed when measured profiles with the optimum beam configuration, found for the single-slit collimator, do not agree with MC simulations considering the 0-tilt scenario. The systematic tilt between the slit insert and the external frame of the collimator needs to be characterized, as detailed in the following section.

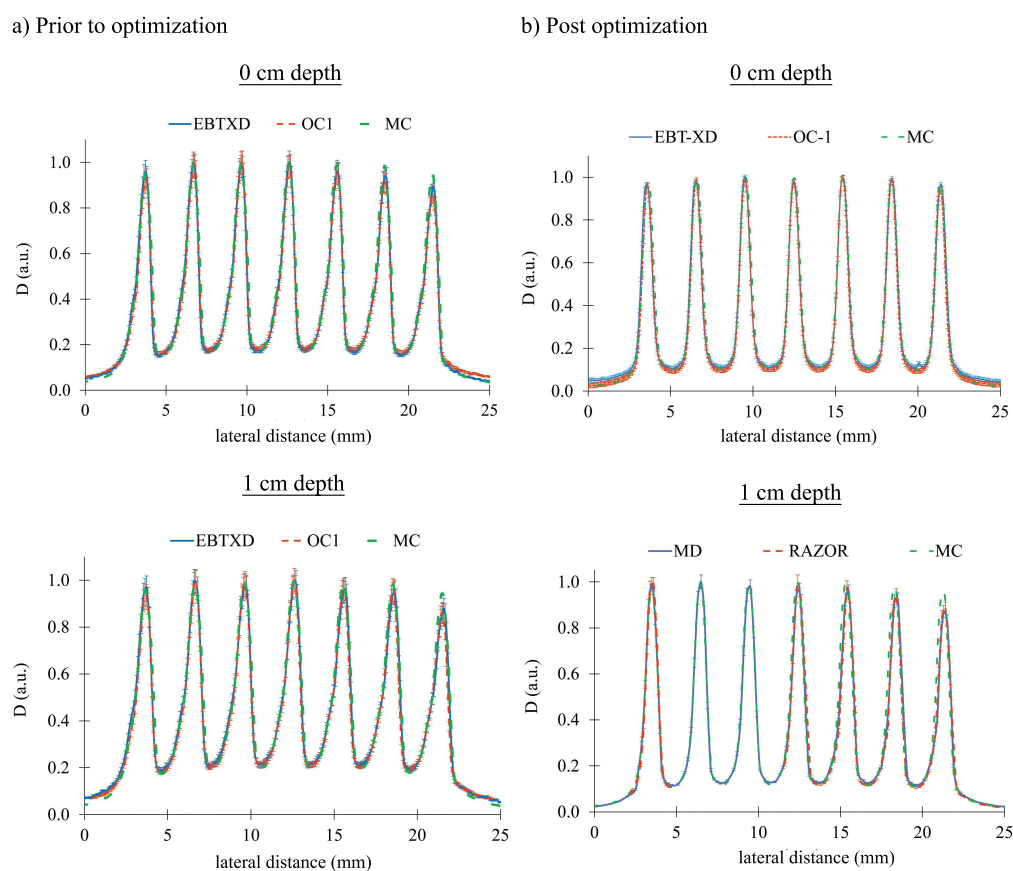


**Figure 3.18:** Lateral dose profiles at 0 and 1 cm depths in water (a) before and (b) after the beam alignment. Dose profiles were calculated by Monte Carlo (MC) codes and measured with EBT-XD and OC-1 films, the RAZOR diode, and the microdiamond detector.

### 3.5 Guidelines for pMBRT dosimetry in preclinical studies

The guidelines proposed for performing reproducible and robust dosimetry in pMBRT small-animal preclinical studies consist of four steps. They are detailed hereafter and summarized in Table 3.9.

1. Quality assurance (QA) of collimator manufacturing. To characterize collimator specifications that define irradiation parameters (i.e., c-t-c distance, slit divergence, and slit width), dose measurements with high-resolution detectors (e.g., radiochromic films, microdiamond detector, or RAZOR diode) should be performed. Then, they should be compared to results from validated MC codes or treatment planning systems (TPS). The collimator specifications in MC codes that lead to dose distributions compatible with experimental measurements should be found. This process should be repeated for each

Objective	Method
Prior to treatment	
QA of the collimator manufacturing	Experimental measurements and MC/TPS calculations.
Selection of the experimental setup	MC/TPS calculations.
Dose determination	Experimental measurements.
During and post-treatment	
QA of the irradiation	Experimental measurements

**Table 3.9:** Synopsis of the dosimetry guidelines.

collimator since the specifications of each one may be slightly different due to manufacturing uncertainties. At this step, the possible tilt of the slit inserts with respect to the external collimator frame (described in Section 3.4) should also be also characterized.

2. Selection of the experimental setup. MC or TPS simulations using animal CTs should be used to calculate dose distributions in the target volume. Then, depending on prescribed dose distribution parameters (e.g., PVDR or average doses), the experimental setup (e.g., the CID, air gap, or gantry angle) and irradiation parameters (i.e., collimator specifications) should be chosen. The selection of the experimental setup conditions should consider the sensitivity of dose distributions to setup parameters (see Section 3.3) to minimize the potential uncertainties in dose distributions. The experimental setup needs to be reproducible, i.e., it could be adopted in all phantom and animal irradiations planned for a specific study. This step also implies the selection of the optimum beam configuration for each irradiation configuration and slit orientation, following the recommendations in Section 3.4.
3. Dose determination. Dose measurements with high-resolution detectors should be performed at reference positions in a phantom. Slab phantoms of different tissue-equivalent materials are typically employed at this step. Figure 3.19 shows two examples of phantoms used for dose determination prior to animal treatments: a solid water homogeneous phantom and a heterogeneous phantom composed of solid water and lung equivalent materials. A common practice consists of combining dose measurements at reference positions with MC calculations in the animal's CT for dose prescription in terms of monitor units (MU) (see Section 3.6). At this step, a comparison between measurements at the reference position and MC/TPS predictions may be performed to verify the parameters implemented in simulations (e.g., beam parameters and setup conditions).
4. QA of the irradiation. At the time of the treatment, radiochromic films should be placed on the animal's skin to measure lateral profiles. These measurements should be compared with those previously performed for dosimetry as a quality check. The measurement of doses at the time of the experiment may also be helpful in case irradiations were not reproducible and

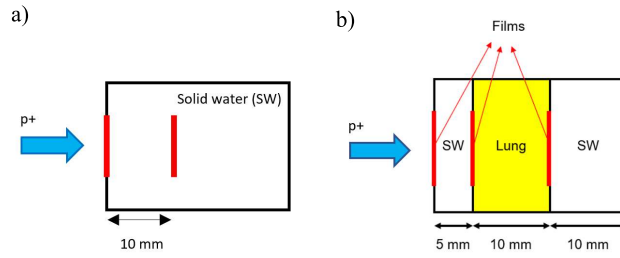


**Figure 3.19:** Schematic representation of experimental setups for dose determination prior to preclinical small-animal treatments using (a) a solid water phantom and (b) a heterogeneous phantom composed of solid water and lung equivalent material.

the dose received by the irradiated animals needs to be traced back by using MC/TPS simulations.

Part of the results presented in Sections 3.3, 3.4 and 3.5 were published in [Ortiz *et al.* 2022] in the form of a research article.

### 3.6 Dosimetric protocol for pMBRT preclinical trials

The protocol presented hereafter describes the methodology proposed for dosimetry in the pMBRT *in vivo* preclinical trials performed at our institution (ICPO) during this PhD thesis. It is based on the absorbed dose to water and inspired by the recommendations provided in the TRS-398 [IAEA 2001], TRS-483 [IAEA 2017] and the dosimetric protocol for MBRT preclinical studies proposed by Prezado *et al.* [Prezado *et al.* 2011].

#### 3.6.1 Determination of absorbed dose under reference conditions

The first step in the protocol is measuring the dose in reference (i.e., broad beam) conditions. The reference field size recommended by the TRS-398 [IAEA 2001] for clinical proton beams is 10 x 10 cm<sup>2</sup> or, for small-field applications, the largest clinically available. In this case, the reference field considered is the one used in our institution for preclinical small-animal investigations, i.e., a 5 x 5 cm<sup>2</sup> open field (no collimators). The TRS-398 also suggests placing the reference point of the ionization chamber (IC) in the middle of the SOBP. However, since most of the preclinical investigations performed in our institution considered irradiations of the target in the plateau region, the reference point employed in this protocol is 1 cm water-equivalent depth. For irradiations of the target at the Bragg peak (BP) position, the reference depth is also 1 cm since, in preclinical investigations, only pristine BPs are employed.

The dose is measured then in these conditions employing the ppc05 ionization chamber following the methodology recommended by the TRS-398. Ideally, measurements should be performed in water, and the irradiation direction should

be the vertical one (gantry at  $0^\circ$ ) to avoid the tank wall.

Once the dose is determined by the reference field detector, detectors not typically used in clinical routine (i.e., the RAZOR diode and the microdiamond detector) are cross-calibrated in the reference conditions described above. Since those detectors will be used afterward to measure pMBRT profiles, their orientation should be the one recommended for small-field conditions, i.e., they should be oriented such that the smallest dimension of its sensitive volume is perpendicular to the scanning direction (on-edge) [IAEA 2017] (see Figure 2.5). A calibration factor, in terms of Gy per nC, is then obtained for each detector in the setup conditions that will be used for pMBRT measurements.

### 3.6.2 Determination of absorbed dose under pMBRT conditions

#### 3.6.2.1 QA of irradiation conditions

As discussed in detail in Section 3.3, relatively small and not easily detectable variations in setup and irradiation parameters may significantly affect dose distributions. Therefore, the appropriate irradiation conditions should be checked before proceeding with measurements in pMBRT conditions. The optimum irradiation parameters should have been previously defined following the optimization process of the irradiation setup, detailed in Section 3.4. These conditions are considered the reference ones and should be reproduced in any pMBRT measurement.

At this stage, the peak dose (quantity most affected by variations in irradiation parameters) is measured with the same equipment and setup as in the optimization process. In this case, the Lynx detector is employed since it provides real-time dosimetric information, and its handling is easier than solid-state detectors or radiochromic films. The measurement point should be such that the peak FWHM is large enough (i.e.,  $> 900 \mu\text{m}$ ) to be resolved by the spatial fractionation of the Lynx detector (0.5 mm). For the collimators employed in our institution (slit width of  $400 \mu\text{m}$ ), the air gap between the collimator exit and the measurement point is 7 cm.

If the measured peak dose is compatible with the value obtained in the optimization process, one can proceed to the next step in the protocol. Contrarily, the irradiation parameters should be optimized following the methodology presented in Section 3.4.

This QA process should also be performed prior to animal treatments.

#### 3.6.2.2 Measurement of lateral dose profiles

At this step, lateral dose distributions are assessed with radiochromic films, e.g., EBT-XD or OC-1 films, and at least one high-spatial-resolution detector, i.e., the RAZOR diode or the microdiamond detector. Measuring with at least two different detectors provide more confidence in measurements in non-reference conditions [IAEA 2017]. Measurements are performed in a water tank with scanning motors.

The scanning step size for solid-state detector measurements should be no larger than 0.2 mm to effectively resolve minibeam dose distributions. The measurement depth for those detectors and radiochromic films is 0 cm and 1 cm. The setup (e.g., air gap, CID, collimator rotation, and gantry angle) should be the same as in the treatments. Measurements with films could be performed in solid water due to its easier handling and more accurate positioning of films, compared to the water tank.

From these measurements, peak, valley, and mean doses are determined in terms of Gy per MU at the reference depths, i.e., 0 and 1 cm. The mean dose is defined as the average of dose points between the first and last peak of the profile and the PVDR as the ratio of the central peak dose and the dose at the valley to the left of the central peak.

Those measurements should be performed for each of the pMBRT collimators that will be used in preclinical investigations.

### 3.6.2.3 Absorbed dose in the rat's head

To determine the dose in the rat's head, the methodology presented in Section 2.1.4.2 should be followed. It is based on combining the experimental measurements described in the previous section and data from benchmarked MC simulations.

From the results of MC simulations in water (or solid water) and in a modelization of the rat's head, the peak, valley, and mean dose at 1 cm depth in water (or solid water),  $D_{1cm}^{water}$ , is correlated to the dose at a depth of interest in the rat's head,  $D_d^{rat}$ , as:

$$f_d = \frac{D_d^{rat}}{D_{1cm}^{water}}. \quad (3.1)$$

The depth of interest in the rat's head for dose prescription is typically the tumor implantation point (1.6 cm depth), and 0 cm (skin tissue) and 1 cm (normal brain tissue) for the dose evaluation in normal tissues.

Then, the peak, valley, and mean dose in the rat's head in terms Gy per MU,  $\dot{D}_d^{rat}$ , are computed by multiplying the correlation factor  $f_d$  by the peak, valley, and mean dose rate at 1 cm depth in water (or solid water) measured experimentally in the previous step,  $\dot{D}_{1cm}^{water}$ :

$$\dot{D}_d^{rat} = f_d \cdot \dot{D}_{1cm}^{water}. \quad (3.2)$$

Finally, from the dose rate in the rat's head,  $\dot{D}_d^{rat}$ , the MU required to deliver the prescribed dose are calculated. This value is also used to calculate the peak, valley, and mean doses delivered to rats in treatments for a given prescribed number of MU.

*The following section presents the results of MC simulations outlined in this protocol to perform the dosimetry the preclinical studies held at our institution.*

## 3.7 Dosimetry for *in vivo* and *in vitro* studies

### 3.7.1 *In vivo* experiments

The dosimetry for *in vivo* preclinical investigations at our institution (ICPO) was performed as part of this PhD thesis. The main objective of those calculations was to evaluate the relative dose distributions in the rat's head considering treatment conditions. They were performed by means of previously validated MC simulations.

As described in Section 2.1.4.2, three main setups were employed for *in vivo* small-animal preclinical studies during this thesis.

Setup 1 consisted of unilateral irradiations of the rat's brain in the plateau region (see Section 2.1.4.2) using collimators for small-animal studies (numbers 2 to 7 in Table 2.1). The field entrance port in this setup was the contralateral brain hemisphere (opposite hemisphere to that on which the tumor was implanted) to evaluate the damage to normal brain tissue and the tumor response simultaneously. Treatments using this setup were delivered in one fraction. Figure 3.20 shows examples of dose distributions in these irradiation conditions for different collimator specifications.

For each configuration, the PVDR, peak FWHM, and peak, valley, and mean doses were evaluated since they are the parameters that may influence the biological responses to minibeam. The mean dose of the profile was calculated as the average dose between the first and last peak of the array. Since the response of both normal tissues and tumor were assessed in each treatment, dosimetric quantities were evaluated at three different depths in the rat's head, i.e., 0 cm (skin), 1 cm (normal brain tissue), and 1.6 cm (tumor implantation location). Table 3.10 presents the evaluated quantities of those profiles for a prescribed dose of 30 Gy mean dose to the target, and Figure 3.21 shows the lateral dose profiles scored at the tumor implantation depth.

Studies using these configurations aim to evaluate several biological endpoints (e.g., lifespan, normal tissue radiation-induced toxicity, tumor control, or immune infiltration within the tumor) following pMBRT. For instance, collimators 2 (2.8 mm c-t-c distance) and 4 (2 mm c-t-c distance) (see Table 2.1) were employed to study the distinct response of glioma-bearing rats to the same valley dose but different peak and average doses. Biological studies using these configurations are still ongoing as of when writing this manuscript.

Setup 2 refers to unilateral irradiations of the rat's brain (i.e., implanted tumor) in the Bragg peak region (see Section 2.1.4.2) using collimator 5 (five slits separated by 4 mm c-t-c distance; see Table 2.1). As in setup 1, the entry port was the contralateral hemisphere, and treatments were delivered in one fraction. Figure 3.22 shows the 2D dose distribution in the rat's head and the lateral dose profile at the tumor implantation depth in this configuration.

As in the previous configuration, the PVDR, peak FWHM, and peak, valley, and

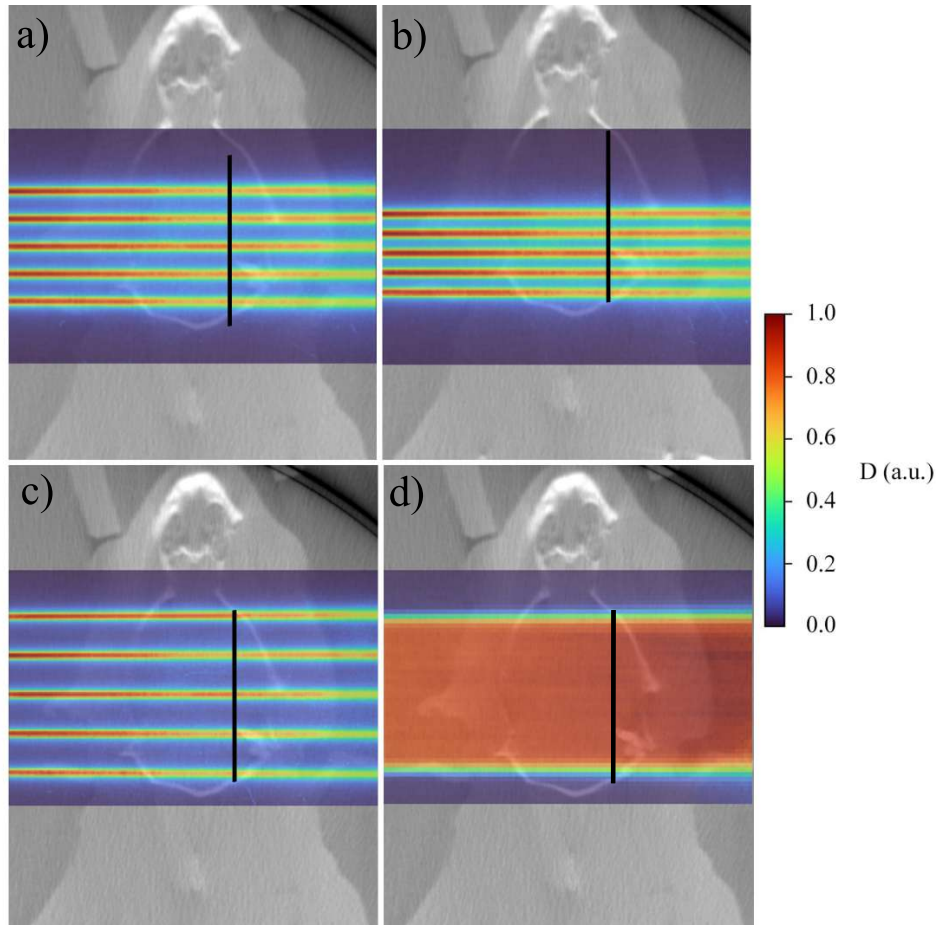


**Figure 3.20:** 2D dose distributions in the rat's head from the craniocaudal view considering setup 1 (unilateral irradiation of the rat's brain in the plateau region; see Section 2.1.4.2) and collimators of (a) five slits and 2.8 mm c-t-c distance, (b) five slits and 2 mm c-t-c distance, (c) five slits and 4 mm c-t-c distance, and (d)  $16 \times 20 \text{ mm}^2$  aperture (collimators 2, 4, 5, and 7 in Table 2.1). The tumor depth is represented by a solid black line.

mean doses were evaluated in the rat's skin (0 cm depth), normal brain tissue (1 cm depth), and tumor implantation location (1.6 cm depth) for a prescribed mean dose of 25 Gy (see Table 3.11).

Treatments considering this setup were compared with studies employing setup 1 (detailed above) to evaluate the different biological endpoints (e.g., tumor control or infiltration of immune cells within the tumor) when the tumor is irradiated within the plateau of the depth-dose profile (setup 1) or at the Bragg peak position (setup 2). The different LET distribution in the plateau and Bragg peak region may lead to distinct tumor responses due to the different proton track structures (see Section 1.2.4.3). Also, the spatial fractionation within the target in this configuration is reduced with respect to Setup 1 (the PVDR is 3.1 to 10.2 in setup 1 and 1.7 in setup 2), and peak/valley doses decrease/increase considerably,

	Collimator 2 (c-t-c = 2.8 mm)			Collimator 4 (c-t-c = 2.0 mm)		
	skin	@ 1 cm	tumor	skin	@ 1 cm	tumor
$D_{\text{mean}}$ (Gy)	$28.8 \pm 0.2$	$29.6 \pm 0.2$	30	$28.7 \pm 0.2$	$29.4 \pm 0.2$	30
$D_{\text{peak}}$ (Gy)	$71.9 \pm 0.4$	$66.2 \pm 0.4$	$62.9 \pm 0.3$	$54.4 \pm 0.3$	$51.0 \pm 0.3$	$48.6 \pm 0.3$
$D_{\text{valley}}$ (Gy)	$9.7 \pm 0.1$	$11.0 \pm 0.2$	$12.3 \pm 0.2$	$11.8 \pm 0.1$	$13.6 \pm 0.1$	$15.1 \pm 0.2$
PVDR (Gy)	$7.4 \pm 0.1$	$6.0 \pm 0.1$	$5.1 \pm 0.1$	$4.6 \pm 0.1$	$3.7 \pm 0.1$	$3.1 \pm 0.1$
FWHM ( $\mu\text{m}$ )	$900 \pm 50$	$1050 \pm 50$	$1200 \pm 50$	$950 \pm 50$	$1100 \pm 50$	$1250 \pm 50$
	Collimator 5 (c-t-c = 4.0 mm)			Collimator 7 (broad beam)		
	skin	@ 1 cm	tumor	skin	@ 1 cm	tumor
$D_{\text{mean}}$ (Gy)	$29.4 \pm 0.2$	$29.7 \pm 0.2$	30	$27.9 \pm 0.2$	$29.3 \pm 0.2$	30
$D_{\text{peak}}$ (Gy)	$107.8 \pm 0.8$	$98.4 \pm 0.6$	$91.4 \pm 0.5$	-	-	-
$D_{\text{valley}}$ (Gy)	$7.7 \pm 0.1$	$8.7 \pm 0.1$	$8.9 \pm 0.1$	-	-	-
PVDR (Gy)	$14.0 \pm 0.3$	$11.3 \pm 0.2$	$10.2 \pm 0.2$	-	-	-
FWHM ( $\mu\text{m}$ )	$850 \pm 50$	$1000 \pm 50$	$1250 \pm 50$	-	-	-

**Table 3.10:** Mean, peak, and valley doses, PVDRs, and peak FWHM at the skin, 1 cm depth in the rat’s head, and the tumor implantation depth for 30 Gy prescribed mean dose. The setup considered was the number 1 (unilateral irradiation of the rat’s brain in the plateau region; see Section 2.1.4.2) and collimator numbers 2, 4, 5, and 7 (see Table 2.1) were employed.

which can also play a role in tumor control. In addition, the outcome of these treatments would provide more realistic information on the possible response of human patients to pMBRT since clinical trials are intended to irradiate the target volume in the Bragg peak region. These treatments also investigate the response of the normal brain to the higher valley doses delivered in this setup (up to 16 Gy), which correlate to the normal tissue sparing in pMBRT [Dilmanian *et al.* 2002]. The studies considering this configuration are still ongoing at the time of writing this manuscript.

Finally, treatments employing setup 3 (crossfire irradiation of the rat’s brain in the plateau region; see Section 2.1.4.2) aimed to study the impact of the temporal fractionation of pMBRT on the response of glioma-bearing animals. For that purpose, different delivery schemes were considered: (i) a crossfire irradiation in one fraction, and crossfire irradiations in two fractions separated by 48 h and delivering (ii) the same physical dose as the single-fraction treatment, and (iii) the same BED. In addition, a group of rats was unilaterally irradiated employing the broad beam aperture ( $16 \times 20 \text{ mm}^2$ ; see Table 2.1) and considering the same dose prescription as in pMBRT treatment (iii). In the crossfire irradiation, two orthogonal arrays of minibeam intersecting at the target were delivered: one in the craniocaudal direction and the other in the lateral direction (see Figure 3.23). Collimator 2 (five

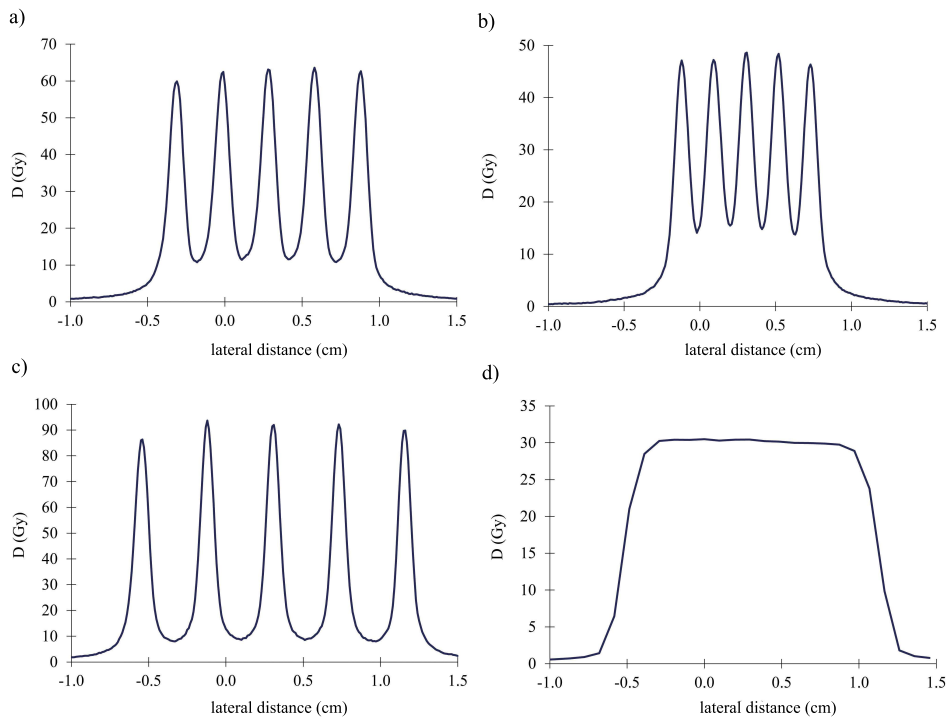


**Figure 3.21:** Lateral dose profiles at the tumor depth (see solid black line in Figure 3.20) considering setup 1 (unilateral irradiation of the rat's brain in the plateau region; see Section 2.1.4.2) and collimator numbers (a) 2, (b) 4, (c) 5, (d) 7 (see Table 2.1). The prescribed dose, in terms of the mean dose in the profile, was 30 Gy.

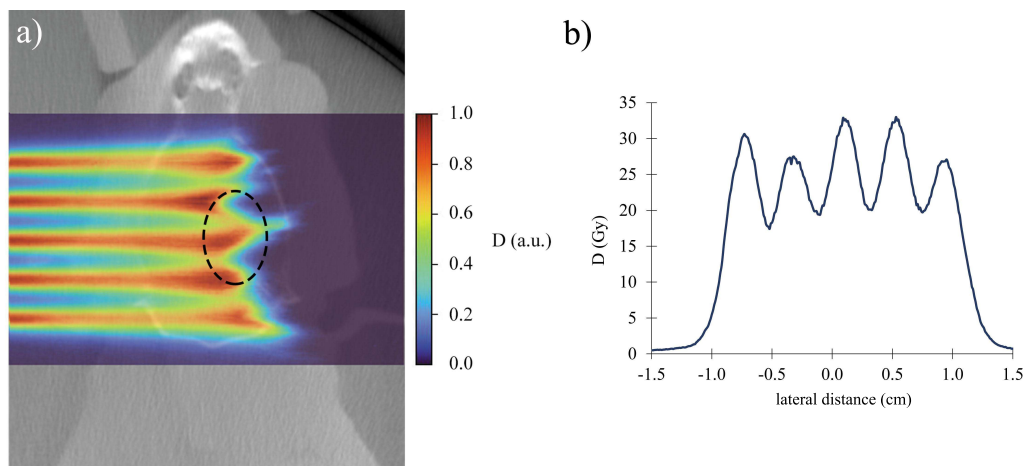


**Figure 3.22:** (a) 2D dose distribution in the rat's head from the craniocaudal view and (b) lateral dose profile at the tumor depth considering configuration 2 (see Section 2.1.4.2) and collimator 4 (see Table 2.1). The tumor position is represented by a dotted black line.

slits separated by 2.8 mm c-t-c distance; see Table 2.1) was employed in this study. Figure 3.23 shows the resulting dose distributions in this irradiation setup.

The results of the first series of irradiations using this configuration were

	skin	1 cm	tumor
$D_{\text{mean}}$ (Gy)	$14.9 \pm 0.2$	$19.4 \pm 0.3$	25
$D_{\text{peak}}$ (Gy)	$23.1 \pm 0.3$	$24.8 \pm 0.3$	$32.9 \pm 0.3$
$D_{\text{valley}}$ (Gy)	$8.4 \pm 0.1$	$16.2 \pm 0.2$	$19.4 \pm 0.2$
PVDR (Gy)	$2.8 \pm 0.1$	$1.5 \pm 0.1$	$1.7 \pm 0.1$
FWHM ( $\mu\text{m}$ )	$2700 \pm 50$	-	-

**Table 3.11:** Mean, peak, and valley doses, PVDRs, and peak FWHM at the skin, 1 cm depth in the rat’s head, and the tumor implantation depth for 25 Gy prescribed mean dose. The setup considered was the number 2 (see Section 2.1.4.2) and collimator 4 (see Table 2.1) was employed.

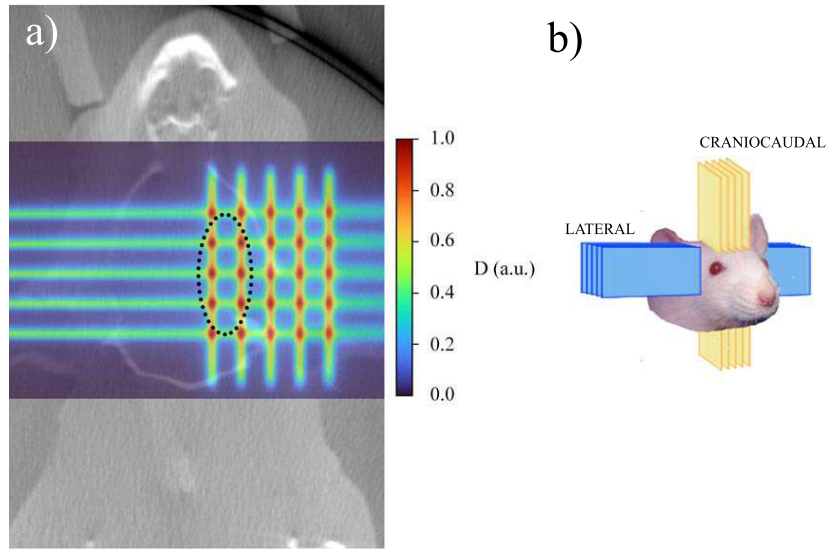


**Figure 3.23:** (a) 2D dose distribution in the rat’s head from the craniocaudal view and (b) beam arrangement in configuration 3 (crossfire irradiation of the rat’s brain in the plateau region; see Section 2.1.4.2) using collimator 2 (five slits separated by 2.8 mm c-t-c distance; see Table 2.1). The tumor implantation depth is represented by a dotted black line.

published in the work by Bertho and Ortiz *et al* [Bertho *et al.* 2021b]. This study showed that (i) when one fraction is used, the same average dose resulted in statistically equivalent survival curves independently of the spatial dose distribution (crossfired, unilateral and broad beam), and (ii) the temporal fractionation of the dose increases the therapeutic index of pMBRT in glioma-bearing rats, i.e., higher rates of tumor control were obtained when delivering the same BED in two fractions (83 %) (group 4 in Figure 3.24) compared to single-fraction treatments (38 %) (group 2 in Figure 3.24), and standard PT (group 5 in Figure 3.24). In addition, pMBRT irradiations, either in one or two fractions, resulted in reduced normal tissue damage as compared to seamless irradiation, as also reported in previous studies [Prezado *et al.* 2017b].

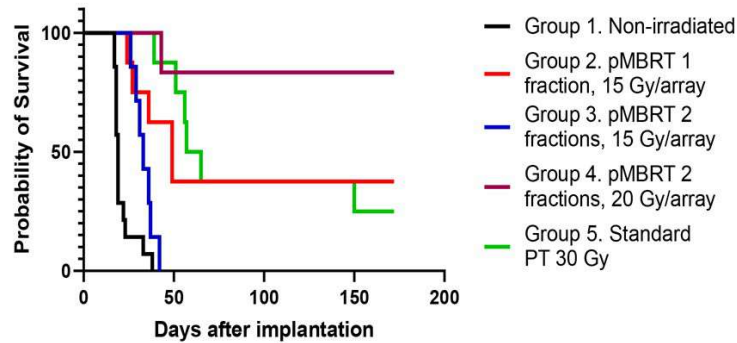


**Figure 3.24:** Comparison of the survival curves of the non-irradiated control (black line), standard proton therapy (green line), pMBRT delivered in one fraction (red line) or in two fractions using the same physical dose (blue line), and pMBRT delivered in two fractions prescribing an equivalent BED (brown line).

Dose distributions at the tumor implantation depth resulting from the combination of lateral and craniocaudal arrays create three different patterns on peaks and valleys within the tumor. The three degrees of spatial fractionation of the dose (i.e., PVDRs), depend on whether they are defined in the intersection of two valleys (PVDR<sub>1</sub> in Figure 3.25), a peak and a valley (PVDR<sub>2</sub> in Figure 3.25), or two peaks (PVDR<sub>3</sub> in Figure 3.25) of different arrays. Figure 3.26 shows the lateral dose profiles at different locations in the tumor volume to further illustrate the different spatial dose fractionation within the intersection between the lateral and craniocaudal arrays.

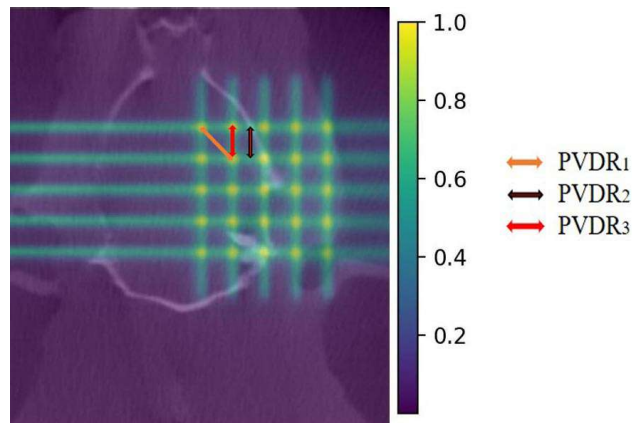


**Figure 3.25:** Representation of three different PVDR definitions, i.e., within the intersection of two valleys (PVDR<sub>1</sub>), a peak and a valley (PVDR<sub>2</sub>), or two peaks (PVDR<sub>3</sub>) of different arrays.

In the situation where the lateral array intersects the valley of the craniocaudal field (Figure 3.26a), the spatial fractionation of the dose is maximized (PVDR<sub>1</sub>), i.e., peak and valley doses are the highest and lower dose points, respectively, within the tumor. This scenario may be relevant to characterize the biological responses

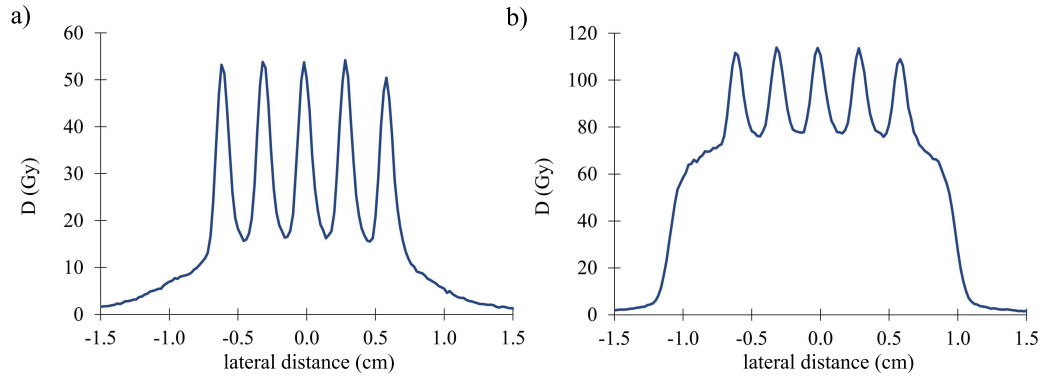


**Figure 3.26:** Lateral dose profiles at the tumor depth for setup 3 (crossfire irradiation of the rat’s brain in the plateau region; see Section 2.1.4.2) and collimator 2 (five slits separated by 2.8 mm c-t-c distance; see Table 2.1). The two profiles illustrate the lateral array intersecting (a) a valley and (b) a peak of the craniocaudal array. The prescribed dose, in terms of mean BED in two fractions, was 120 Gy (40 Gy physical dose).

to treatments since it is assumed that minimum valley doses might determine the increased lifespan in pMBRT [Fernandez-Palomo *et al.* 2022] as well the normal tissue toxicity [Dilmanian *et al.* 2002].

Dosimetric quantities (i.e., PVDR and peak and valley doses) at the skin, normal brain, and tumor are presented in Table 3.12. In this configuration, peak and valley physical doses to the tumor are almost two times higher than when the irradiation consists of a unilateral array (Setup 1) with the same collimator. The PVDR also increases from  $5.1 \pm 0.1$  to  $7.0 \pm 0.3$  in this configuration.

	Lateral		Craniocaudal	Tumor
	skin	1 cm	skin	
$D_{\text{peak}}$ (Gy)	$52.7 \pm 0.4$	$50.8 \pm 0.4$	$112.3 \pm 0.8$	$113.7 \pm 0.8$
$D_{\text{valley}}$ (Gy)	$7.7 \pm 0.2$	$9.0 \pm 0.2$	$18.8 \pm 0.3$	$16.3 \pm 0.3$
PVDR (Gy)	$6.8 \pm 0.3$	$5.7 \pm 0.3$	$6.0 \pm 0.3$	$7.0 \pm 0.3$

**Table 3.12:** PVDRs and peak and valley doses at the skin, 1 cm depth in the rat’s head, and the tumor implantation depth for 120 Gy prescribed mean biological equivalent dose. The setup considered was number 3 (crossfire irradiation of the rat’s brain in the plateau region; see Section 2.1.4.2) and collimator 2 (five slits separated by 2.8 mm c-t-c distance; see Table 2.1) was employed.

For all the treatments described in this section, a QA of the irradiation was performed by measuring dose distributions on the rat skin with radiochromic films. Figure 3.27 shows examples of the agreement between film measurements on the rat’s skin during treatments and MC results. These results prove the reproducibility of pMBRT irradiation when following the guidelines and protocols proposed in Sections 3.5 and 3.6.

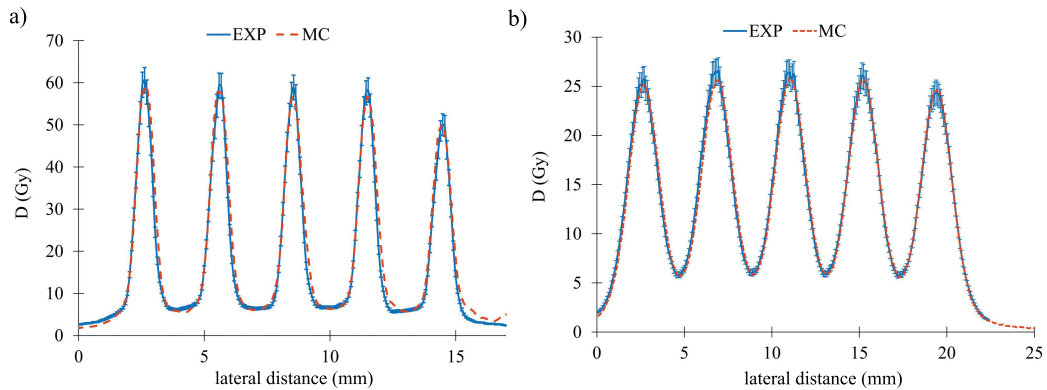


**Figure 3.27:** Lateral dose profiles at the rat's skin measured with OC-1 films during treatments (EXP) and simulated using TOPAS (MC) considering setups 2 and 3.

### 3.7.2 *In vitro* experiments

Dosimetry for *in vitro* (i.e., cell irradiation) experiments only involved experimental data since, contrary to small-animal irradiations, measurements can be performed at the target position (i.e., MC simulations are not required). In cell irradiations, EBT-XD and OC-1 films were placed under the cell plate, where cells are attached. The plates used for dosimetry prior to cell treatments contained the same amount of medium as the plates for cell irradiations. This amount of medium filled the wells to 1 cm in-height to reproduce the beam characteristics in the normal brain tissue (1 cm depth in the rat's head) to reliably correlate *in vivo* and *in vitro* biological data. As in cell irradiations, only the four central wells were filled by medium (see Figure 3.28a). For pMBRT irradiations, collimator 8 (15 slits separated by 4 mm c-t-c distance; see Table 2.1) was used (see Figure 3.28b). For broad beam irradiations, no collimator was employed. A complete description of the experimental setup in these irradiations can be found in Section 2.1.4.2. The mean dose rate (Gy per MU) was measured with radiochromic films for dose prescription. The mean dose was calculated as the average dose of the profile within the center of the well.

In cell treatments, several dose points, i.e., 2, 5, 10, and 20 Gy mean dose, were considered in pMBRT and broad beam conditions. At the time of irradiation, film measurements were performed for QA. For mean doses lower than 5 Gy, EBT-XD films were used, whereas, for higher doses, OC-1 films were employed to keep peak and valley doses within the dynamic dose range of each film type (see Section 2.1.3). Figure 3.29 shows an example of a lateral dose profile measured by films.

Mean, peak, and valley doses, the PVDR, and peak FWHM were computed for each well and configuration. Table 3.13 presents the values for those parameters.

*In vitro* irradiations presented in this section aim to evaluate the differential production of DNA damage at peaks and valleys and perform clonogenic assays. Part of the results of these studies have already been presented in the PTCOG conference 2022 [Bertho 2022].

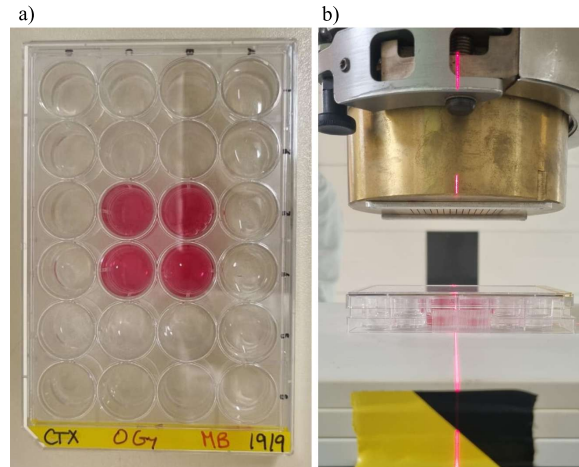


**Figure 3.28:** (a) Example of a cell plate for *in vitro* investigations with only the four central wells filled by medium, and (b) experimental setup for pMBRT irradiations.

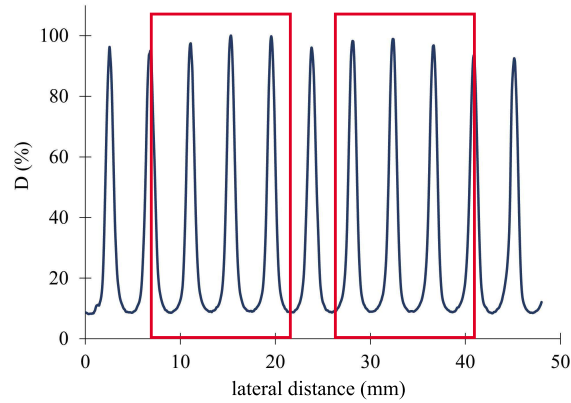


**Figure 3.29:** Relative dose profile at the cells' position in the pMBRT irradiations. The red square represents the area of the irradiated wells.

	$D_{\text{mean}}$ (Gy)	$D_{\text{peak}}$ (Gy)	$D_{\text{valley}}$ (Gy)	PVDR	$\text{FWHM}_{\text{peak}}$ ( $\mu\text{m}$ )
2 Gy - BB	$2.1 \pm 0.1$	-	-	-	-
5 Gy - BB	$5.0 \pm 0.2$	-	-	-	-
10 Gy - BB	$10.3 \pm 0.5$	-	-	-	-
20 Gy - BB	$20 \pm 1.0$	-	-	-	-
2 Gy - MB	$2.1 \pm 0.1$	$6.5 \pm 0.3$	$0.69 \pm 0.05$	$9.4 \pm 0.7$	$930 \pm 50$
5 Gy - MB	$5.2 \pm 0.3$	$15.2 \pm 0.8$	$1.6 \pm 0.1$	$9.8 \pm 0.7$	$930 \pm 50$
10 Gy - MB	$10.3 \pm 0.5$	$32 \pm 1$	$3.2 \pm 0.2$	$10.0 \pm 0.7$	$930 \pm 50$
20 Gy - MB	$20.3 \pm 0.9$	$66 \pm 3$	$5.7 \pm 0.3$	$11.5 \pm 0.8$	$930 \pm 50$

**Table 3.13:** PVDR, peak FWHM, and average, peak, and valley doses in the broad beam (BB) and minibeam (MB) irradiations for 2, 5, 10, and 20 Gy mean dose.

## 3.8 Discussion and conclusions

This chapter presented the work performed during this PhD thesis in the context of dosimetry for pMBRT preclinical investigations.

Dosimetric evaluations in pMBRT conditions (i.e., submillimeter beam sizes and highly heterogeneous dose distributions) involve both experimental data and MC simulations. Although some high-spatial-resolution detectors are able to resolve minibeam dose distributions, their uncertainty in the dose measurement may mask detailed information or small variation in relevant dosimetric parameters (e.g., PVDR, minibeam widths, or peak doses). Therefore, complementary MC data are typically necessary for pMBRT studies.

Since the detectors and simulation codes required for pMBRT dosimetry are not typically used in clinical routine, their performance in pMBRT conditions needs to be validated before proceeding with dosimetric campaigns. Then, the first step in the dosimetric process performed in this thesis was to validate our MC codes and dosimetric protocols (e.g., irradiation setup and detectors employed). The good parametrization of our simulation codes was demonstrated by comparing MC results with experimental data obtained using solid-state detectors previously proven suitable for pMBRT measurements (i.e., the RAZOR diode and microdiamond detector). Once our MC codes were validated, the good performance of radiochromic films (i.e., OC-1 and EBT-XD films) for dose measurement in pMBRT conditions was also demonstrated by comparing film measurements with MC results and solid-state detector data. Those investigations considered lateral dose profiles at different depths in water and solid water. OC-1 and EBT-XD films were also proven suitable for dose determination at shallow depths (from 0 cm to 4 cm). The validation of detectors and simulation codes was performed considering different and independent dosimeters, proving the soundness of the results. Overall, these satisfactory results allowed us to have two different detector types (i.e., solid-state detectors and radiochromic films) and a complementary tool (i.e., MC simulations) for pMBRT dosimetry. Although the two detector types employed are suitable for pMBRT dose measurements, they come with a series of drawbacks. For instance, measurements with solid-state detectors of very small active volumes are sensitive to their orientation with respect to small-field geometries [IAEA 2017], require water tanks or solid phantoms with scanning motors to measure dose profiles, and the measurements of dose distributions are arduous and time-consuming since the dose needs to be measured point-by-point. Regarding film measurements, they need post-processing, not allowing real-time dose measurements. To overcome those limitations, our institution established a collaboration with the *National Physics Laboratory* (London, United Kingdom) to test the performance of a CMOS detector in pMBRT conditions. This detector combines two of the main advantages of solid-state detectors and radiochromic films, i.e., real-time and 2D measurements. The suitability of this detector to perform real-time quality assurance or beam monitoring in pMBRT is still being evaluated by other members of the collaboration. Measurements with the CMOS detector are being compared against measurements

performed with radiochromic films; therefore, their validation performed in this thesis served as a ground framework for the study of the viability of new detectors in the context of pMBRT. In addition, the validation of the detectors used in this thesis permitted proceeding with dosimetric studies needed for the current preclinical investigations, in combination with the also validated MC simulations. This validation provides a high level of confidence in the results of dosimetric studies using the tested detectors and simulation codes.

One of these studies was the evaluation of the sensitivity of pMBRT dose distributions to uncertainties and relatively small variations in irradiation and setup parameters. Results of this robustness analysis showed that the dosimetric quantities that define lateral dose distributions (e.g., peak and valley doses, PVDR, or peak FWHM) are highly influenced by variations in irradiation (e.g., collimator specifications) and setup (e.g., tilt between the collimator entrance and the beamline) parameters, not easily detectable in clinical QA routines. For instance, a collimator-beamline tilt of  $\pm 0.5^\circ$  reduces peak doses and the PVDR by up to 50 %. This increased sensitivity must be considered in pMBRT investigations since it affects not only dosimetric quantities but also the biological responses dependent on these quantities and, consequently, the treatment outcomes. Therefore, these results reveal the importance of accurately reporting irradiation parameters and optimizing the experimental setup to extract reliable conclusions from preclinical studies.

Based on those results, a methodology to optimize the experimental setup was designed. The proposed method is based on the alignment of the beamline with respect to the collimator entrance since it is the setup parameter that affects the most pMBRT dose distributions. This process resulted in the optimization of the irradiation parameters, which would allow to fully exploit the benefits of pMBRT in preclinical investigations. In addition, it set a series of reference values for irradiation parameters to be used to evaluate the reproducibility of irradiation conditions prior pMBRT dosimetric campaigns and treatments.

Along the line of ensuring robust and reproducible dose measurements in preclinical trials, a series of guidelines and a dosimetric protocol were proposed. These series of recommendations considered the results of the robustness analysis and optimization process, which are not taken into account in current protocols. They were published in [Ortiz *et al.* 2022] to guide the implementation of this technique in other institutions.

Adopting the proposed guidelines and protocols, the dosimetry for preclinical trials at our institution was performed. The reproducibility of irradiations during treatments was shown by performing QA measurements of treatments, proving the suitability of the proposed protocols. Dosimetry for these studies also involved calculations in rat models using MC simulations. These dosimetric results allowed to accurately evaluate dose distributions at any point in the rat's head and reliably correlate relevant dosimetric quantities (e.g., PVDR, peak, valley, and mean doses) with the biological outcomes of treatments (e.g., tumor control, normal tissue

toxicities, or immune cell infiltration). This type of analysis is especially relevant at the preclinical stage since these investigations aim to disentangle the biological responses to pMBRT and their dependence on dosimetric quantities, which are not fully characterized yet. Simulations used for those calculations were validated not only in homogeneous conditions (i.e., water and solid water phantoms) but also in a realistic phantom resembling the rat's head of treated animals. Therefore, computed dose distributions in the rat's head were considered to be very accurate.

Further evolutions in the context of dosimetric calculations in *in vivo* studies would involve the development of a treatment planning system (TPS) for pMBRT dosimetry in small animals. Although the MC simulations used in this work are a tool that allows the accurate calculation of dose distributions, they do not consider the geometry of each individual animal. A modelization of a rat of the same age as the irradiated animals was used instead. In addition, simulations did not consider the integral dose to specific internal structures (i.e., tumor or brain) but only lateral dose profiles at the depth of these regions of interest. A dedicated TPS would allow calculating the treatment plans for each animal and evaluating the dose in specific volumes as done in the clinical practice. This would lead to a reduction in the variability of preclinical results.

Finally, dosimetry for *in vitro* preclinical trials was also performed during this thesis. The irradiation conditions for those investigations were designed to obtain in the cell culture a similar degree of fractionation (PVDR) and range of doses as in *in vivo* studies. Therefore, these results allowed to perform biological studies complementary to small-animal irradiations to obtain a more complete picture of the role of different biological mechanisms on the response of tissues to pMBRT.

Overall, the work on preclinical dosimetry performed during this PhD thesis evaluated the different aspects that need to be considered when developing a new radiotherapeutic technique, i.e., the suitability of dosimeters and complementary tools for dose measurements, a robustness analysis to evaluate the potential pitfalls affecting the reproducibility of treatments, and the consequent development of guidelines and protocols. This work allowed the reliable realization of preclinical investigations in our institution and aims to contribute to the initiation of pMBRT studies at other facilities. In addition, the results presented in this section are expected to contribute to the development of protocols and codes of practice for the clinical implementation of this technique.



# Assessment of the potential of pMBRT for treating metastases

---

## Contents

<b>4.1</b>	<b>Rationale</b>	<b>159</b>
<b>4.2</b>	<b>Clinical cases considered</b>	<b>160</b>
<b>4.3</b>	<b>Treatment plans</b>	<b>161</b>
4.3.1	Stereotactic radiotherapy treatments	162
4.3.2	pMBRT treatment plans	162
4.3.3	PT treatment plans	165
<b>4.4</b>	<b>Evaluation of dose distributions</b>	<b>165</b>
4.4.1	Target coverage	167
4.4.2	Mean dose to organs-at-risk	173
4.4.3	Assessment of tolerance dose limits	174
<b>4.5</b>	<b>Evaluation of technical aspects</b>	<b>178</b>
<b>4.6</b>	<b>Influence of plan parameters on dose distributions</b>	<b>179</b>
4.6.1	Orientation and position of the slits	179
4.6.2	Center-to-center distance	180
<b>4.7</b>	<b>Discussion and conclusions</b>	<b>181</b>

---

*This chapter presents a study on the suitability of pMBRT for treating different metastatic sites in the context of preparing the forthcoming clinical trials.*

## 4.1 Rationale

As previously discussed in Section 1.4.4.4, the promising results in pMBRT preclinical studies encourage the preparation of clinical trials for this technique [Prezado 2022]. An indication that may be a suitable candidate for these clinical investigations is brain metastases (BM). Up to 50 % of cancer patients develop this malignancy [Mitchell *et al.* 2022]. The standard of care for this indication is photon stereotactic radiotherapy (SRT) [Minniti *et al.* 2016]. Whereas a local control rate of up to 85 % can be achieved when treating small BM (< 2 cm in diameter), the treatment of large BM (> 2 cm in diameter) has a poor prognosis (i.e., the median survival is 6 to 12 months [Mitchell *et al.* 2022]). An enhanced dose escalation would be needed to improve

the current treatment outcomes; however, the required increase in the dose to the target is compromised by the risk of toxicities to surrounding normal tissues. For instance, neurological damage and radiation-induced necrosis (RN) are reported in 14 % and 50 % of patients treated with SRT [Minniti *et al.* 2011]. The treatment of small BM is also accompanied by RN at a rate of 15 % to 25 %. The radiation-induced necrotic lesion within the tumor volume and surrounding brain tissue may appear with mass effect and neurological dysfunction [Ali *et al.* 2019]. Based on preclinical results, pMBRT could reduce those complications [Prezado *et al.* 2017b, Prezado *et al.* 2019, Lamirault *et al.* 2020a, Lamirault *et al.* 2020b], and be specially beneficial for the treatment of large BM.

Other common metastatic sites that might benefit from hypofractionated pMBRT treatments may be lung and liver [Dilmanian *et al.* 2015b], which are also typically treated with SRT [Aitken & Hawkins 2015, Ricardi *et al.* 2012]. Overall, the development of metastases is one of the leading causes of cancer morbidity and mortality, accounting for up to 90 % of deaths related to cancer [Guan 2015].

The work presented in this chapter is framed in the context of preparing the forthcoming pMBRT clinical trials. It aims to theoretically evaluate the potential benefits of this technique for treating those clinical indications by comparing the dose distribution of pMBRT plans with SRT treatments, the standard of care for those malignancies at our institution. pMBRT plans are also compared to standard proton therapy (PT) treatments to fully disentangle the potential benefits of pMBRT in clinics over conventional techniques (see Sections 4.2 to 4.5).

In addition, this work provides a first insight into the impact on dose distributions of the aspects of the treatment plan optimization process specific to pMBRT, e.g., the position, orientation, and separation between minibeam (see Section 4.6).

## 4.2 Clinical cases considered

As mentioned in the previous section, this study evaluates the suitability of pMBRT for treating three clinical indications, i.e., brain, liver, and lung metastases. Four clinical cases from our institution (Institut Curie - Hôpital) (Saint Cloud, France) were selected: two brain metastases, one at the temporal lobe (Case 1) and one at the frontal lobe (Case 2), a liver (Case 3) and a lung (Case 4) metastases. These cases were previously treated with stereotactic techniques at our institution (see Section 4.3.1). The selection of BM cases meets the criteria for the forthcoming clinical trials. As detailed in Section 1.4.4.4, patients that would be involved in those investigations should have at most four metastases outside the brainstem, and the diameter of at least one of them should be larger than 2 cm and smaller than 4 cm. In addition, the Performance Score and life expectancy of those patients should be 0-2 and greater than 3 months, respectively. Selected target volumes in the lung and liver are also at least 2 cm wide.

The selection criteria for this present study are also based on the target position (i.e., PTV depth and proximity to organs-at-risk (OAR)). Deep-seated tumors are

considered a priority for this study since, in these cases, normal tissues located prior to the target are expected to benefit from a high spatial fractionation of the dose. At the same time, a homogeneous dose distribution within the target could be provided if required. The differential degree of fractionation that can be achieved in normal tissues and the target volume with very few fields (even only one field) is one of the main dosimetric advantages of pMBRT (see Section 1.4.4.1). In addition, target volumes are close to OARs to assess the possibility of sparing these structures regardless of their irradiation at high peak doses. In Case 1, the PTV is adjacent to the acoustic nerve and close to the brainstem. The target volume considered in Case 2 is at the proximity of the brainstem and optic pathway. The OARs situated close to the PTV in Cases 3 and 4 are the liver, lung, heart, and great vessels (i.e., the superior vena cava and the pulmonary artery). Figure 4.1 shows the PTV and OARs location in the clinical cases selected for this study.

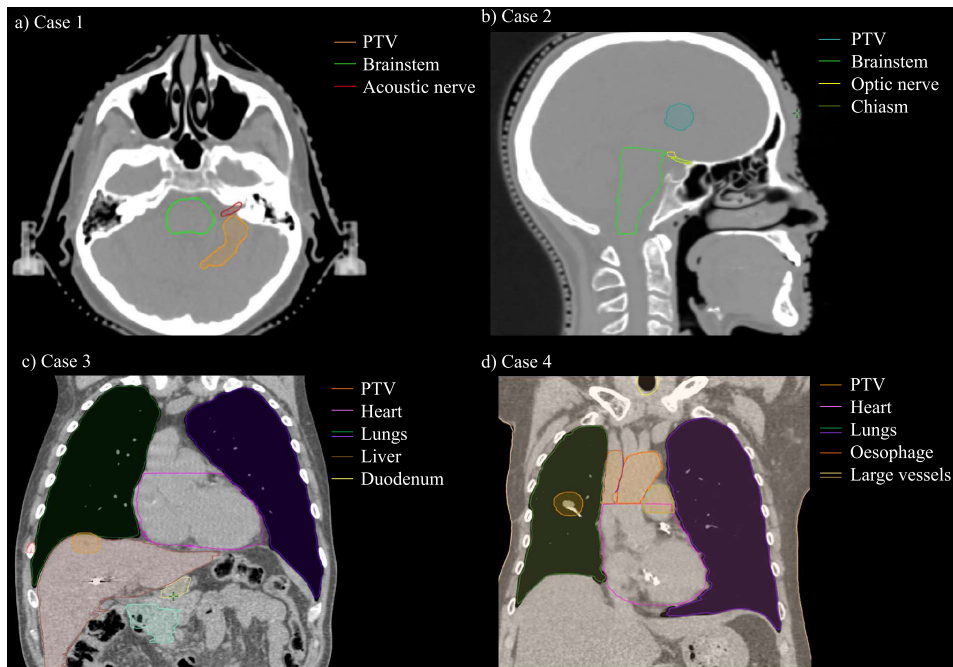


**Figure 4.1:** PTV and relevant OARs in (a) Case 1 (brain metastasis at the temporal lobe), (b) Case 2 (brain metastasis at the frontal lobe), Case 3 (liver metastasis), and Case 4 (lung metastasis).

### 4.3 Treatment plans

As previously mentioned, this study compares pMBRT, PT and SRT dose distributions. This section presents the details of the treatment plans considered for each clinical case.

### 4.3.1 Stereotactic radiotherapy treatments

SRT treatment plans were generated by medical physicists at our institution. These plans were used to treat the clinical cases presented in the previous section with radical intention. Case 1 was treated using the volumetric modulated arc therapy (VMAT) technique with four arcs. In Case 2, VMAT and dynamic conformal arc therapy (DCAT) were combined. Four arcs, two of each technique, were employed. The technique used in Case 3 was a combination of VMAT, using one arc, and DCAT, with two arcs (three arcs in total). Finally, VMAT using three arcs was employed in Case 4. VMAT and DCAT techniques are described in Section 1.2.2.4. Figure 4.2 presents the arrangement of arcs in SRT treatment plans.

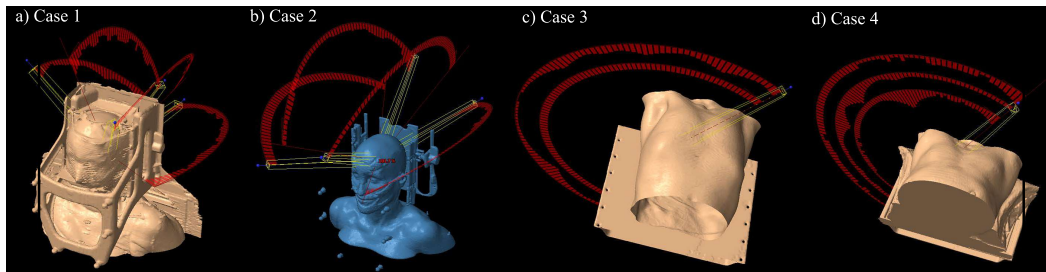


**Figure 4.2:** Field arrangement in (a) Case 1 (brain metastasis at the temporal lobe), (b) Case 2 (brain metastasis at the frontal lobe), Case 3 (liver metastasis), and Case 4 (lung metastasis).

Regarding the dose prescription, a treatment consisting of five fractions of 7 Gy each was chosen to treat Cases 1 and 2. In Case 3, three fractions of 15 Gy each were prescribed. Finally, the prescribed dose in Case 4 was 60 Gy in five fractions.

### 4.3.2 pMBRT treatment plans

pMBRT plans aim to reproduce as much as possible irradiation schemes of *in vivo* preclinical studies (i.e., one or two proton minibeam arrays in one fraction [Prezado *et al.* 2018, Prezado *et al.* 2019, Bertho *et al.* 2021b]) to draw conclusions on the treatment outcome of clinical cases based on preclinical results. Therefore, pMBRT treatment plans consist of one array in Case 1 and two arrays in Cases 2 to 4. Field specifications for each case are summarized in Table 4.1 .

When the treatment is delivered using two fields, the planar minibeam arrays are combined in a crossfire geometry, i.e., the collimator rotation between the two fields is  $90^\circ$  (see Figure 4.3) to avoid blurring the peak-valley pattern due to possible positioning uncertainties. This field arrangement has also been used in preclinical investigations [Serduc *et al.* 2009, Bertho *et al.* 2021b].

For each case, two pMBRT configurations are studied:

- i A narrow center-to-center (*c-t-c*) distance between minibeams to achieve a uniform dose distribution within the PTV, comparable to the one in SRT treatments. Treatments considering this configuration are denoted as plan B.

	Case 1		Case 2	
PTV dimension (cm <sup>3</sup> )	4.0 x 4.0 x 1.0		2.0 x 2.0 x 2.0	
Field name	Field 1		Field 1	Field 2
Number of spots	302		241	229
Energy range (MeV)	125 140		145 165	140 150
Gantry angle (°)	90		230	40
Couch angle (°)	180		0	180
Range shifter thickness (mm)	0		65	65
PTV min.-max. depth (mm)	105 - 120		72 - 92	57 - 77
	Case 3		Case 4	
PTV dimension (cm <sup>3</sup> )	3.0 x 2.5 x 2.0		2.8 x 2.7 x 2.3	
Field name	Field 1	Field 2	Field 1	Field 2
Number of spots	480	407	461	389
Energy range (MeV)	130 147	128 157	120 136	133 143
Gantry angle (°)	315	235	270	310
Couch angle (°)	0	90	90	0
Range shifter thickness (mm)	65	65	65	65
PTV min.-max. depth (mm)	105 - 132	81 - 112	46 - 73	74 - 98

Table 4.1: Field specifications in pMBRT treatments.

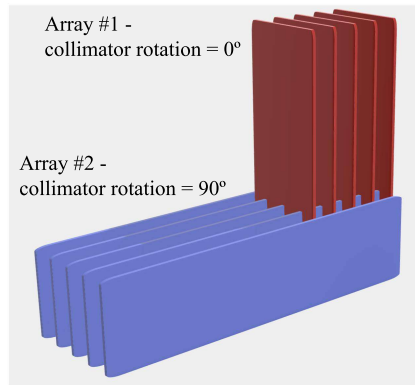


Figure 4.3: Schematic representation of a crossfire geometry. The two minibeam arrays are interlaced, forming an angle of 90° between the two peak-valley patterns.

- ii. A large *c-t-c* distance to create a quasi-uniform dose distribution in the target ( $PVDR = 1.2$  to  $1.3$ ). The rationale behind aiming for this degree of spatial dose fractionation within the target is that, in preclinical trials, dose distributions characterized by a  $PVDR$  of  $1.2$  led to a tumor control rate of  $67\%$  in glioma-bearing rats, representing a 3-fold increase as compared to broad beam irradiation ( $22\%$ ). This type of treatment is referred to as plan C.

The c-t-c distance considered in each case is presented in Table 4.2. The collimator design employed is described in detail in Section 2.1.2 (arrays of 400  $\mu\text{m}$ -width and 5.6 cm-long divergent slits).

Case	Plan	Technique	# of fields	c-t-c distance (mm)	# of fractions	Prescribed dose
1	A	SRT (VMAT)	4 arcs	-	5	35 Gy
	B	pMBRT	1	4.5	1	19.9 Gy[RBE]
	C			6.0		
	D	PT		-		
2	A	SRT (VMAT+DCAT)	4 arcs	-	5	35 Gy
	B	pMBRT	2	3.5	1	19.9 Gy[RBE]
	C			5.0		
	D	PT		-		
3	A	SRT (VMAT+DCAT)	3 arcs	-	3	45 Gy
	B	pMBRT	2	3.5	1	28.9 Gy[RBE]
	C			4.0 and 4.5		
	D	PT		-		
4	A	SRT (VMAT)	3 arcs	-	5	60 Gy
	B	pMBRT	2	3.0 and 3.5	1	31.7 Gy[RBE]
	C			4.0		
	D	PT		-		

**Table 4.2:** Treatment plans evaluated in this study. SRT treatments are denoted by the label A, pMBRT plans considering a uniform dose to the target by the letter B, pMBRT plans delivering a quasi-homogeneous dose distribution to the PTV by the letter C, and PT plans by D. VMAT stands for volumetric modulated arc therapy, DCAT for dynamic conformal arc therapy, and c-t-c for center-to-center.

Since the simulation of treatment plans in this study considered the PBS beamline of ICPO, the minimum deliverable proton energy is 100 MeV (as described in Section 2.1.1). Therefore, treatments involving target depths shallower than 7.7 cm (proton range in water for a 100 MeV beam) require the use of a 65 mm block of PMMA acting as a range shifter. The range shifter is placed before the collimator, as could be done in the clinical routine with proton beams. As discussed in Section 2.1.2, pMBRT collimators for human treatments were designed such that the range shifter can be placed prior to the collimator to minimize the degradation of the spatial fractionation of the dose at the patient’s surface. When the range shifter is placed after the collimator, the degree of spatial dose modulation is reduced due to the widening of proton minibeam as they traverse a material.

Treatment plans were optimized as described in Section 2.3.2. Pencil beam spot weights and positions are calculated by ECLIPSE considering seamless irradiations, and the resulting spot configuration is used in pMBRT conditions.

Concerning dose prescription, all pMBRT treatments are simulated in a

single fraction, as typically done in preclinical trials with satisfactory results in terms of radiation-induced toxicity and tumor control [Prezado *et al.* 2017b, Prezado *et al.* 2018, Prezado *et al.* 2019, Lamirault *et al.* 2020a]. As mentioned above, pMBRT treatments in this study are intended to reproduce treatment schemes in preclinical trials to extrapolate preclinical results to clinical treatment outcomes. The biological equivalent dose (BED) is used as a figure of merit for dose prescription in order to compare pMBRT with SRT plans, which employ different temporal fractionation schemes. The suitability of using this parameter in pMBRT conditions will be discussed in detail in Section 4.7. In pMBRT treatments, the same BED to the PTV as in SRT plans is prescribed, i.e., 59.5 Gy in Cases 1 and 2, 112.5 Gy in Case 3, and 132 Gy in Case 4. The  $\alpha/\beta$  of the tumor volume for the BED calculation is 10 Gy [Qi *et al.* 2006, Steel 2002] as in preclinical trials [Bertho *et al.* 2021b]. Corresponding physical doses in one fraction are 19.9 Gy[RBE] in Cases 1 and 2, 28.9 Gy[RBE] in Case 3, and 31.7 Gy[RBE] in Case 4. The notation Gy[RBE] indicates the equivalent dose that, deposited by the reference radiation type (i.e., photons), leads to the same biological damage as the dose delivered by a radiation type different from the reference one (i.e., protons in this case) (see Section 1.2.4.7). The dose is prescribed in terms of the mean dose to the PTV, as done in preclinical investigations [Prezado *et al.* 2017b, Prezado *et al.* 2018, Prezado *et al.* 2019, Lamirault *et al.* 2020a, Bertho *et al.* 2021b].

### 4.3.3 PT treatment plans

PT plans consist of the same field arrangements and fractionation schedules as the pMBRT treatments presented in the previous section, i.e., one field in Case 1 and two fields in Cases 2 to 4, and a single fraction. However, no collimators are used. In addition, the same range shifters are employed.

PT plans were optimized following the standard clinical practice. As for pMBRT plans, the dose is prescribed in terms of the same BED to the PTV as in SRT treatments. Therefore, 19.9 Gy[RBE] in Cases 1 and 2, 28.9 Gy[RBE] in Case 3, and 31.7 Gy[RBE] in Case 4 are prescribed.

The description of PT plans is summarized in Table 4.2.

## 4.4 Evaluation of dose distributions

pMBRT dose distributions were computed by means of Monte Carlo (MC) simulations using the TOPAS toolkit (see Section 2.2.3). Figures 4.4 to 4.7 show the dose distributions of pMBRT, PT and SRT treatment plans in the four cases evaluated.

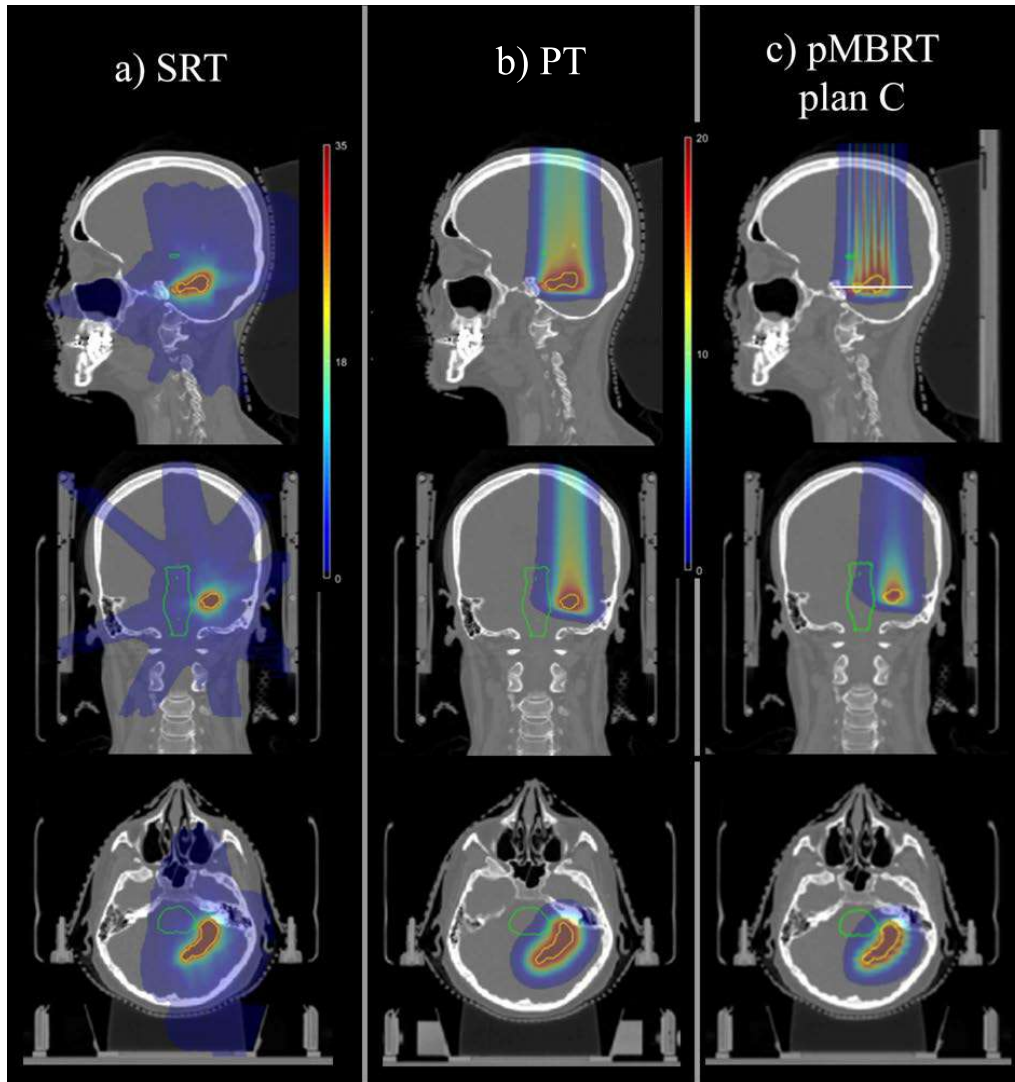


**Figure 4.4:** Examples of dose distributions of the (a) SRT, (b) PT and (c) pMBRT plans in Case 1. The PTV is displayed in yellow, the brainstem in green, and the acoustic nerve in red.

Visually, it is evident that in all pMBRT and PT plans, the dose is confined to a much smaller volume as compared to SRT treatments. However, pMBRT results in volumes outside the PTV that receive similar or even higher doses than the prescribed dose to the target (i.e., peak doses). Contrarily, in SRT and PT plans, the maximum dose is restricted to the target volume. In addition, the dose conformity to the target in pMBRT and PT appears to be degraded with respect to the SRT treatments considered in this study. A more detailed quantitative analysis of dose distributions is provided hereafter.

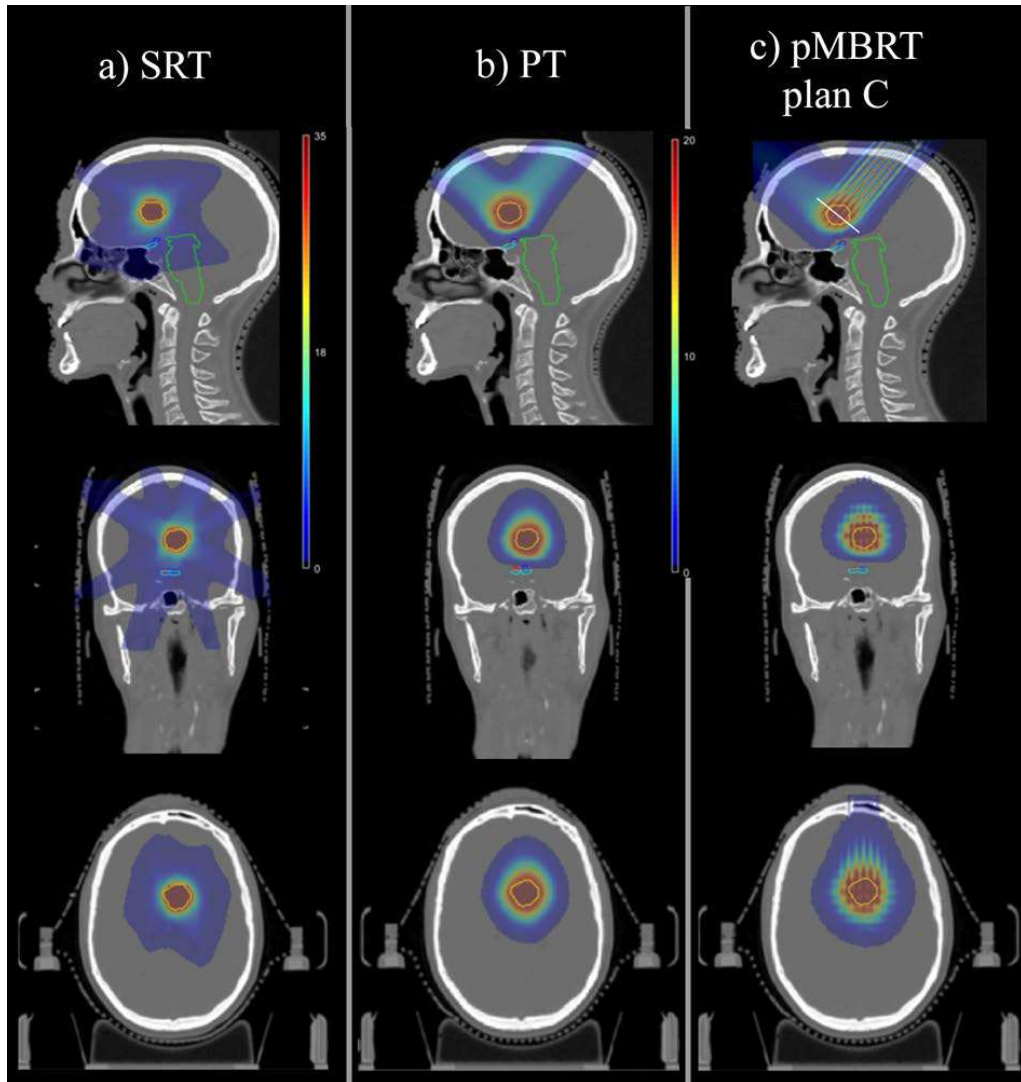


**Figure 4.5:** Examples of dose distributions of the (a) SRT, (b) PT and (c) pMBRT plans in Case 2. The PTV is displayed in yellow, the brainstem in green, and the cochlea in light blue .

pMBRT, PT and SRT plans are evaluated and compared by assessing three main aspects of their dose distributions: the target coverage, mean dose to OARs, and whether the dose to normal tissues remains below tolerance dose limits. These three points are discussed in the three following sections.

#### 4.4.1 Target coverage

The target coverage of the different treatment plans is evaluated by computing the dosimetric homogeneity index  $D_{95\%}$  (i.e., dose received by the 95 % of the PTV), and PTV volume that receives more than 110 % ( $V_{110\%}$ ) and 93 % ( $V_{93\%}$ ) of the prescribed dose.

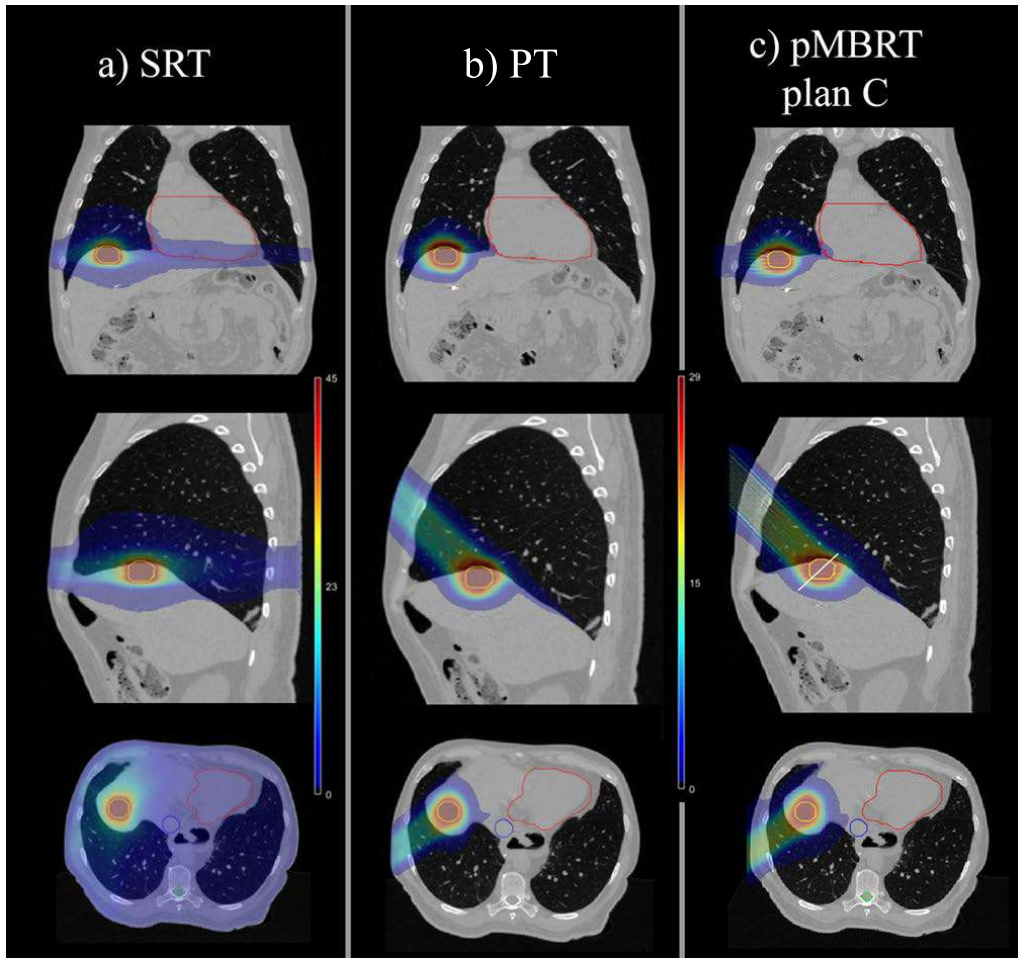


**Figure 4.6:** Examples of dose distributions of the (a) SRT, (b) PT and (c) pMBRT plans in Case 3. The PTV is displayed in yellow, the heart in red, and the superior vena cava in blue.

The type of pMBRT treatment aiming for a uniform dose distribution to the target (plans B) achieve similar or even superior target coverage than SRT plans (see Table 4.3). The equivalent target coverage of SRT and pMBRT (plans B) treatments is illustrated in Figures 4.8 to 4.11, which show the dose-volume histograms (DVH) in Cases 1 to 4. As detailed previously, the mean BED to the target is delivered in both treatment modalities. The concept of BED is derived from the LQ model. Assuming the validity of the LQ model in pMBRT conditions, these results suggest that similar levels of tumor control as in conventional SRT may be expected in pMBRT treatments for a similar target coverage and BED to the PTV. The validity of this assumption will be discussed in detail in Section 4.7.

pMBRT plans provide a lower degree of tumor coverage than PT treatments due to the adoption of several approximations in the optimization of pMBRT plans (see Section 2.3.2). Similar levels of target coverage as PT treatment could be expected

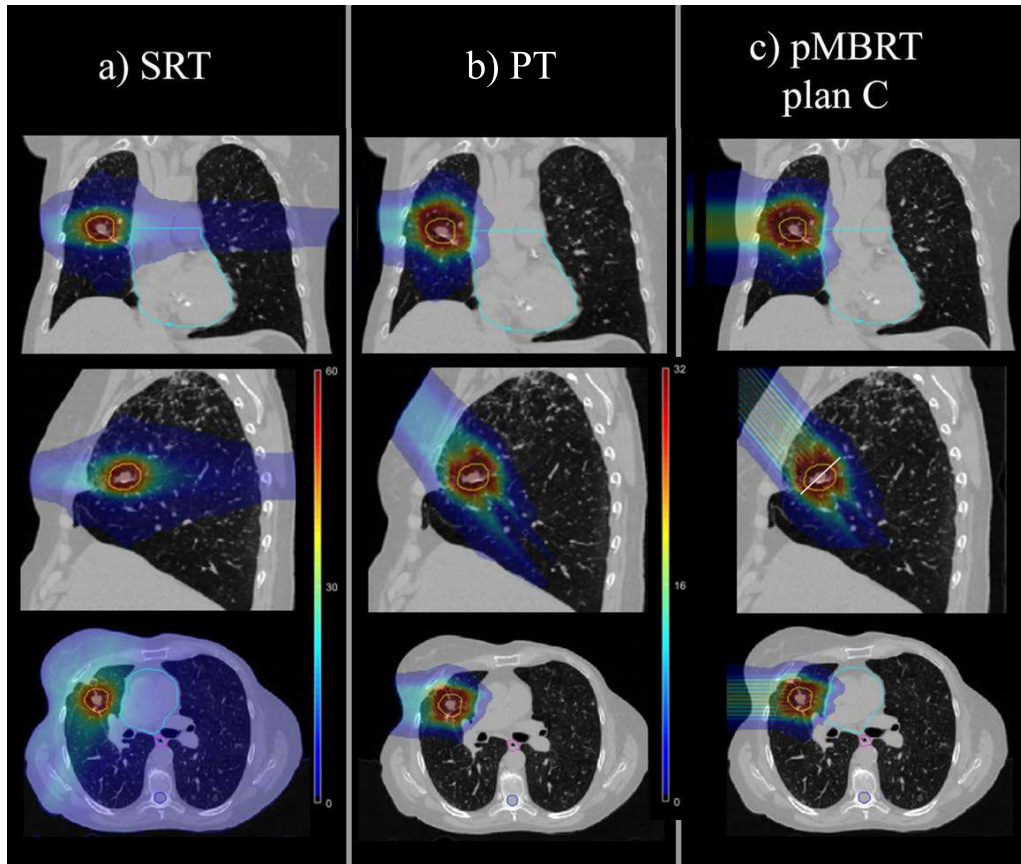


**Figure 4.7:** Examples of dose distributions of the (a) SRT, (b) PT and (c) pMBRT plans in Case 4. The PTV is displayed in yellow, the heart in light blue, and the superior vena cava in pink.

from pMBRT plans when using an optimization methodology tailored to this dose delivery method, as it will be discussed in Section 4.7.

The dose conformity, i.e., the conformation of the dose on the target and volume of surrounding tissue covered by the reference dose [Al-Rawi *et al.* 2022], is not evaluated in pMBRT plans. The main conformity indexes in clinics are based on the ratio of the volume of reference isodose and target volume [Shaw *et al.* 1993], or the target volume covered by the reference isodose and volume of reference isodose [Lomax & Scheib 2003]. In pMBRT, this approach is inappropriate since regions of dose higher than the prescribed one (i.e., peak doses) are distributed along all the irradiated volume, including normal tissues. Therefore, adapted conformity indexes would need to be conceived for pMBRT, which is out of the scope of this thesis. In addition, the dose conformity to the target in this study is not fully optimized since spot configurations are optimized in broad beam conditions, disregarding the specific shaping of the SOBPs by proton minibeam (see Section 2.3.2). Possible strategies to improve the dose conformity of pMBRT treatments will be discussed in Section 4.7.

Case	Plan	D <sub>95%</sub> (%)	V <sub>93%</sub> (%)	D <sub>110%</sub> (%)
1	A (SRT)	89.1	86.8	2.8
	B (pMBRT)	89.0	91.4	2.6
	C (pMBRT)	72.0	68.9	28.2
	D (PT)	94.0	96.1	0.9
2	A (SRT)	89.1	85.1	0
	B (pMBRT)	91.5	85.1	2.0
	C (pMBRT)	79.1	67.0	24.1
	D (PT)	93.9	98.6	0
3	A (SRT)	90.9	91.1	1.4
	B (pMBRT)	92.5	93.9	0.3
	C (pMBRT)	91.0	89.9	4.5
	D (PT)	90.8	97.0	0
4	A (SRT)	90.5	85.1	10.3
	B (pMBRT)	88.0	86.2	4.7
	C (pMBRT)	86.7	80.0	12.4
	D (PT)	93.0	95.2	0.9

**Table 4.3:** Comparison of dosimetric indexes defining the target coverage in the SRT, PT, and pMBRT treatments.

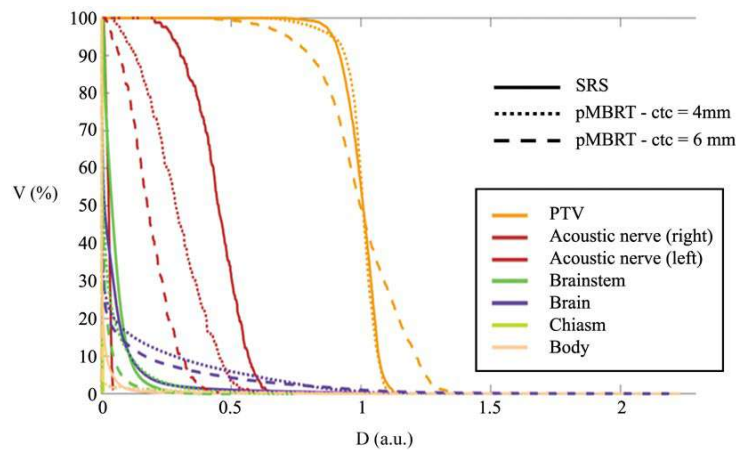


**Figure 4.8:** Comparison of dose-volume histograms in Case 1 for the SRT plans (solid line), pMBRT treatments B (dotted line), and C (dashed line). The dose presented corresponds to the physical dose normalized to the prescribed dose (mean dose to PTV).

In plans B, **homogeneous dose distributions to the target volume are achieved using only one or two pMBRT arrays**. Figure 4.12 shows the lateral dose profiles at the center of the tumor in the four cases studied. Similar results were reported for different clinical indications in other studies. In the work by

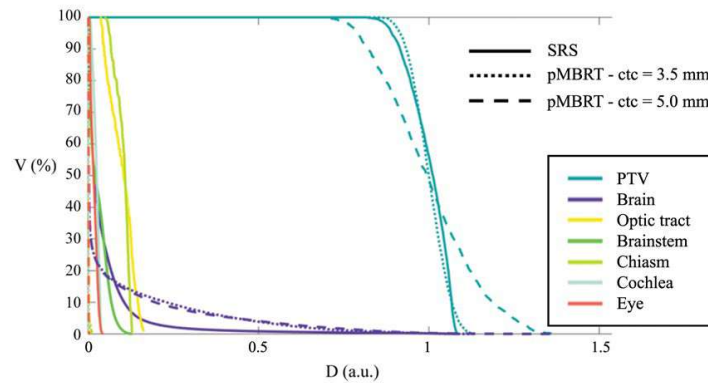


**Figure 4.9:** Comparison of dose-volume histograms in Case 2 for the SRT plans (solid line), pMBRT treatments B (dotted line), and C (dashed line). The dose presented corresponds to the physical dose normalized to the prescribed dose (mean dose to PTV).

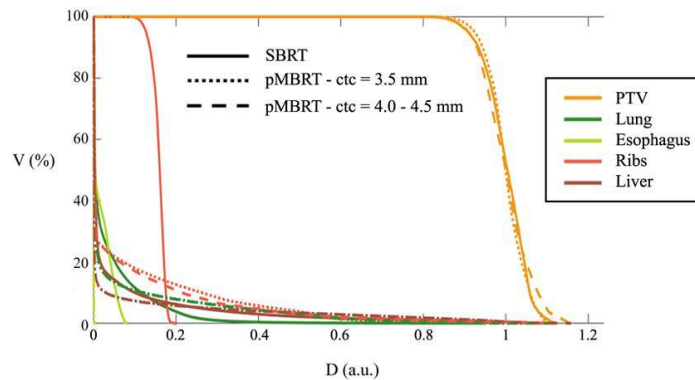


**Figure 4.10:** Comparison of dose-volume histograms in Case 3 for the SRT plans (solid line), pMBRT treatments B (dotted line), and C (dashed line). The dose presented corresponds to the physical dose normalized to the prescribed dose (mean dose to PTV).

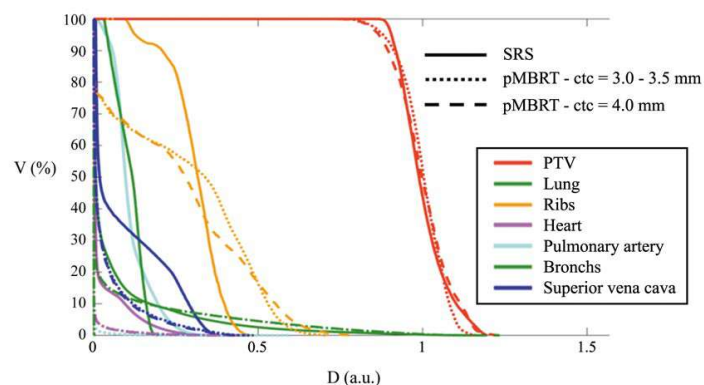


**Figure 4.11:** Comparison of dose-volume histograms in Case 4 for the SRT plans (solid line), pMBRT treatments B (dotted line), and C (dashed line). The dose presented corresponds to the physical dose normalized to the prescribed dose (mean dose to PTV).

Lansonneur *et al.* [Lansonneur *et al.* 2020], a dose homogenization within the target of glioma and meningioma cases was achieved in pMBRT plans consisting of two and three minibeam arrays. As discussed previously (see Section 1.4.4.4), the dose homogenization in-depth using few (one to three) arrays is a consequence of the characteristic lateral scattering and widening of proton minibeams.

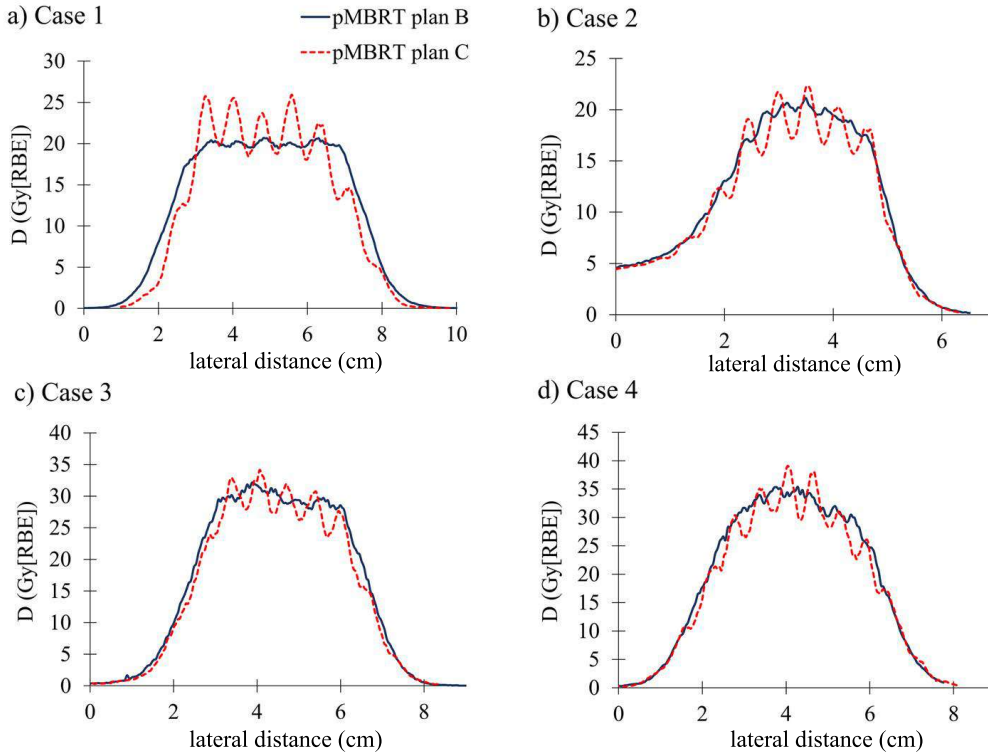


**Figure 4.12:** Lateral dose profiles at the PTV in (a) Case 1, (b) Case 2, (c) Case 3, and (d) Case 4 for pMBRT plans B and C. Profiles considered are represented by a solid white line in Figures 4.4 to 4.7.

The type of plan using a larger *c-t-c* distance (plans C) results in a lower tumor coverage, as observed in Table 4.3 and Figures 4.8 to 4.11, due to the spatial fractionation of the dose in the target volume. These plans deliver a quasi-uniform dose distribution to the target (see Figure 4.12). Mean peak-to-valley dose ratios (PVDR) within the PTV are  $1.29 \pm 0.04$ ,  $1.30 \pm 0.04$ ,  $1.25 \pm 0.04$ , and  $1.31 \pm 0.04$  in Cases 1 to 4, respectively. This level of spatial dose fractionation has been proven effective for achieving equivalent or superior tumor control than seamless irradiations in preclinical trials [Prezado *et al.* 2019]. Indeed, 67 % of long-term survivals free of tumor were obtained in glioma-bearing rats, representing an increment of up to 3 times in comparison to conventional proton beam treatments [Prezado *et al.* 2019]. In addition, the high doses per fraction at peak regions in this type of pMBRT plan (up to 40 Gy[RBE]) may further exploit the benefits of hypo-fractionated treatments in terms of the distinct radiobiological response of the tumor tissue, including additional radiation-induced tumor cell kill due to microvascular damage,

cell apoptosis, the release of tumor-specific antigens and the subsequent immune-mediated response [Alongi *et al.* 2012, Soliman *et al.* 2016].

#### 4.4.2 Mean dose to organs-at-risk

For evaluating the mean dose delivered to OARs, the mean BED to each organ volume was computed. As discussed above, the BED is employed for the sake of comparing treatments using different temporal fractionation regimes (i.e., SRT, PT and pMBRT plans). Its limitations in pMBRT conditions will be discussed in Section 4.7.  $\alpha/\beta$  values reported in the literature [Emami 2013] are used for the BED calculation.

pMBRT significantly reduces the mean dose to critical organs in the cases studied in comparison with SRT plans. In Case 1, pMBRT decreases the mean BED to OARs from 44 % (right acoustic nerve) to 100 % (left acoustic nerve). In Case 2, pMBRT treatments fully spare the OARs considered, including the optic tract, brainstem, and chiasm. In Case 3, the mean BED to the liver and ribs is reduced by 25 % and 75 %, respectively, while avoiding the irradiation of the superior vena cava (SVC). Finally, in Case 4, the mean dose to OARs is reduced from 11 % (ribs) to 100 % (pulmonary artery and bronchi). Figure 4.13 compares the mean BED received by OARs in pMBRT, PT and SRT plans.

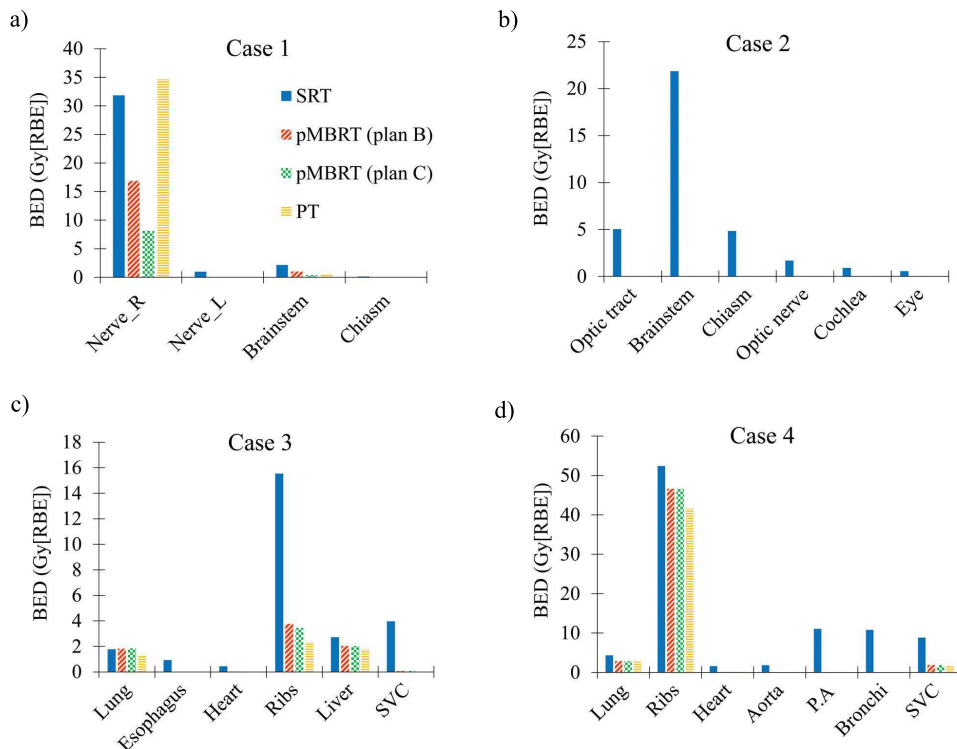


**Figure 4.13:** BED to OARs in Cases 1 to 4 in SRT, PT, and pMBRT plans. SVC stands for superior vena cava and P.A for pulmonary artery.

The mean BED to OARs is similar in PT and pMBRT treatments using the same irradiation schemes, except from the right acoustic nerve in Case 1, which receives up to four times more BED (34.7 Gy) in the PT plan, as compared to pMBRT plan B (16.8 Gy) and plan C (8.15 Gy). The lower dose to this organ in pMBRT treatments arises from placing a valley region close to that OAR. The similar level of dose reduction in PT and pMBRT plans suggests that the reduction in the mean dose delivered to critical structures in pMBRT conditions results from using fewer fields (one or two minibeam arrays), instead of a larger number of arcs as in SRT. This enables the optimization of entrance ports of treatment fields to avoid OAR irradiations. The use of fewer fields is possible due to two main reasons: the reduced radiation toxicity of minibeam arrays, which allows for delivering higher doses per field, and the use of protons, which provide more favorable dose distributions.

The mean BED to the whole body also decreases in pMBRT plans by at least 48 %, 30 %, 33 %, and 65 % in Cases 1 to 4, respectively, as compared to SRT treatments. This reduction is also associated with the fewer number of fields employed [Rana *et al.* 2014]. Overall, the decrease in the integral dose may contribute to diminishing late toxicities since the volume of normal tissue exposed to low doses correlates with the risk of developing long-term secondary malignancies [Hall & Wu 2003].

#### 4.4.3 Assessment of tolerance dose limits

Due to the lack of enough preclinical and clinical data, the exact tolerance dose limits of normal tissues to minibeam arrays are not well-established yet. Therefore, dose constraints for clinical treatments using standard irradiation schemes (treatments delivered in 2 Gy per session) have to be considered instead. To correlate doses in pMBRT plans to equivalent doses in conventional treatments, the normalized total dose at 2 Gy-fractions,  $NTD_{2.0}$  (described in Section 1.2.4.7), is computed. The  $\alpha/\beta$  of brain, liver, and lung tissue considered for the  $NTD_{2.0}$  calculation is 2.1, 1.5, and 3 [Emami 2013], respectively.

Studies on spatially-fractionated microbeams [Dilmanian *et al.* 2002] suggest that the valley dose determines the tissue-sparing effect of such submillimetric beams. It might be assumed that tissues receiving valley doses below tolerance dose limits in seamless conditions would be similarly spared. Therefore, for the brain tissue, valley doses are converted to  $NTD_{2.0}$  and compared against tolerance dose levels in clinics, as also done in previous studies on spatially-fractionated radiotherapy with microbeams [Martínez-Rovira *et al.* 2010]. Valley doses of lateral profiles at the proximity of the PTV (5 mm prior to the target) are considered since this is the point in the brain where valley doses are at the highest. In Case 1, the maximum valley  $NTD_{2.0}$  to the brain is 61 and 46 Gy[RBE] in plans B and C, respectively. In Case 2, 47 and 28 Gy[RBE] are delivered to the normal brain in plans B and C. The maximum  $NTD_{2.0}$  to the normal brain in the SRT treatment was 45 Gy. In both cases, **valley doses to brain tissue in pMBRT treatments remain below the tolerance dose limit** considered for

this organ, i.e., 72 Gy as the dose leading to a 5 % probability of complication within five years [Lawrence *et al.* 2010]. It should be pointed out that, in the type of treatment delivering a quasihomogeneous dose to the target (plan C), valley doses to normal tissues are lower than when a dose homogenization within the PTV was required (plan B). Then, since a uniform dose to the PTV is not required in pMBRT to achieve high rates of tumor control, as it has been previously discussed, a reduced toxicity in normal tissues could be obtained by finding the optimum balance between the degree of spatial fractionation within the target and surrounding tissues. Contrary to pMBRT plans, the maximum  $NTD_{2.0}$  to the healthy brain in PT treatments is 81 Gy[RBE] (Case 1) and 75 Gy[RBE] (Case 2), which are higher than tolerance dose limits set for this organ (i.e., 72 Gy).

The volume of the brain receiving a dose higher than 12 Gy ( $V_{12\text{ Gy}}$ ) was also calculated since this parameter correlates to the risk of radionecrosis [Milano *et al.* 2021]. In PT treatments, the volume of the brain receiving at least 12 Gy is 32 and 20 cm<sup>3</sup> in Cases 1 and 2. These values are above the volume leading to a 20 % probability of necrosis in single-fraction SRT treatments (15 cm<sup>3</sup>). Similarly, pMBRT plans exceed this dose-volume constraint,  $V_{12\text{ Gy}}$  is 65 cm<sup>3</sup> (plan B) and 48 cm<sup>3</sup> (plan C) in Case 1, and 29 cm<sup>3</sup> (plan B) and 32 cm<sup>3</sup> (plan C) in Case 2. However, the applicability of this constraint to pMBRT is limited since volumes receiving doses higher than 12 Gy[RBE] correspond to peak regions distributed within the irradiated volume, i.e., all the cells receiving those doses are not clumped. Also, this dose-volume limit does not consider the more favorable radiobiological response of tissues to minibeam, for instance, the role of surviving stem cells at low-dose regions (valleys), which may assist in repairing and repopulating tissue receiving high doses (peaks) [Hopewell & Trott 2000]. Furthermore, preclinical data showed that glioma-bearing rats treated with similar doses (including peak and valley doses) and configurations showed reduced neurotoxicity compared to standard dose delivery methods [Prezado *et al.* 2019].

Regarding parallel organs, such as the lung and liver, the average dose to the organ was converted to  $NTD_{2.0}$  since the risk of radiation-induced complications is proportional to the mean dose to the whole organ [Aitken & Hawkins 2015]. In pMBRT plans, the maximum  $NTD_{2.0}$  to the lung is 1.1 Gy[RBE] in Cases 3 and 4, which is lower than the dose limit for a 5 % probability of symptomatic pneumonitis (7 Gy). The mean  $NTD_{2.0}$  to the liver in Case 4 (1.7 Gy[RBE]) also remain below 30 Gy, i.e., the dose leading to a 5 % probability of radiation-induced liver disease, as in PT treatments.  $NTD_{2.0}$  in pMBRT plans is equivalent to or lower than in SRT treatments (1.0 Gy and 3.8 Gy to the lung and liver, respectively, in Case 3 and 2.6 Gy to the lung in Case 4).

It is relevant to note that the physical doses converted to quantities derived from the LQ model remained below the upper limit of applicability of this model in *in vivo* studies (i.e., 18 Gy) [Brenner 2008].

Besides the  $NTD_{2.0}$ , other quantities related to OARs' complications were

evaluated. In pMBRT treatments, the critical volume above a threshold dose and the maximum dose points to these organs were computed and compared against dose limit objectives defined in the TG-101 report (the report of AAPM for stereotactic body radiation therapy) [Benedict *et al.* 2010]. The reasons to use the dose-volume constraints published in that report for pMBRT treatments are (i) the comparison with SRT treatments, which met these dose-volume limits, and (ii) the lack of recommendations for pMBRT conditions or other reports for single-fraction treatments.

pMBRT treatments meet the dose limits, i.e., maximum critical volume above a threshold dose and maximum dose point, defined in the TG-101 report, even considering the high-dose peak regions. OARs evaluated include acoustic nerves, brainstem, chiasm, lung, liver, ribs, heart, superior vena cava, esophagus, pulmonary artery, trachea, and medulla. Tables 4.4, 4.5, and 4.6 detail the dose-volume constraints defined in the TG-101 report and values obtained in pMBRT plans for Cases 1, 3, and 4. Dose-volume limits were not evaluated in Case 2 since, as reported below, all OARs were completely spared in pMBRT plans. Contrary to pMBRT, the PT treatment in Case 1 leads to a volume of the right acoustic nerve receiving more than 9 Gy[RBE] (0.1 cm<sup>3</sup>) larger than the dose-volume constraint (0.035 cm<sup>3</sup>).

Case 1							
	TG-101			Plan B c-t-c = 4 mm		Plan C c-t-c = 6 mm	
	Maximum volume above the threshold	Threshold dose (Gy)	Max. dose point (Gy)	V (D <sub>th</sub> ) (cc)	V (D <sub>max</sub> ) (cc)	V (D <sub>th</sub> ) (cc)	V (D <sub>max</sub> ) (cc)
Acoustic nerve (R)	-	-	9	-	0.032	-	0.001
Acoustic nerve (L)				-	0	-	0
Brainstem	< 0.5 cc	10	15	0.1	0	0	0
Chiasm	< 0.2 cc	8	10	0	0	0	0

**Table 4.4:** OAR dose limits defined in the TG-101 report and values obtained in pMBRT treatments in Case 1. The *point* volume is defined as  $\leq 0.035$  cm<sup>3</sup>.

As it will be discussed in Section 4.7, considering dose limits established for seamless dose distributions may overestimate the damage to normal tissues since the distinct biological mechanisms triggered by pMBRT and associated increased tolerance dose are neglected. Therefore, the irradiation of OARs in the pMBRT treatments studied is not expected to lead to additional OAR toxicities.

Finally, doses to the skin were evaluated. Maximum valley doses (and associated PVDRs) in pMBRT plans are  $3.2 \pm 0.1$  Gy[RBE] ( $24.3 \pm 0.5$ ),  $4.1 \pm 0.1$  Gy[RBE] ( $9.5 \pm 0.3$ ),  $4.8 \pm 0.1$  Gy[RBE] ( $6.5 \pm 0.2$ ), and  $6.7 \pm 0.2$  Gy[RBE] ( $7.5 \pm 0.2$ ), in Cases 1 to 4, respectively, which are lower than the doses delivered to the

Case 3							
	TG-101			Plan B c-t-c = 4 mm		Plan C c-t-c = 6 mm	
	Maximum volume above the threshold	Threshold dose (Gy)	Max. dose point (Gy)	V (D <sub>th</sub> ) (cc)	V (D <sub>max</sub> ) (cc)	V (D <sub>th</sub> ) (cc)	V (D <sub>max</sub> ) (cc)
Lung (L)	> 1500 cc	7	-	2904	-	2904	-
	> 1000 cc	7.4		2904		2904	
Lung (R)	> 1500 cc	7		2785		2790	
	> 1000 cc	7.4		2794		2798	
Liver	< 700 cc	9.1	-	1273	-	1274	-
Ribs	< 1 cc	22	30	0.1	0	0.23	0.035
Heart	< 15 cc	16	22	0	0	0	0
SVC*	< 10 cc	31	37	0	0	0	0
Esophagus	< 5 cc	11.9	15.4	0	0	0	0

**Table 4.5:** OAR dose limits defined in the TG-101 report and values obtained in pMBRT treatments in Case 3. The *point* volume is defined as  $\leq 0.035 \text{ cm}^3$ . \*SVC stands for superior vena cava.

Case 3							
	TG-101			Plan B c-t-c = 4 mm		Plan C c-t-c = 6 mm	
	Maximum volume above the threshold	Threshold dose (Gy)	Max. dose point (Gy)	V (D <sub>th</sub> ) (cc)	V (D <sub>max</sub> ) (cc)	V (D <sub>th</sub> ) (cc)	V (D <sub>max</sub> ) (cc)
Lung (L)	> 1500 cc	7	-	2189	-	2189	-
	> 1000 cc	7.4		2189		2189	
Lung (R)	> 1500 cc	7		1697		1696	
	> 1000 cc	7.4		1702		1701	
Ribs	< 1 cc	22	30	0	0	0	0
Pulmonary artery	< 10 cc	31	37	0	0	0	0
Esophagus	< 5 cc	11.9	15.4	0	0	0	0
Trachea	< 4 cc	10.5	20.2	0	0	0	0
Bronchus	< 0.5 cc	12.4	13.3	0	0	0	0
Medulla	< 0.35 cc	10	14	0	0	0	0
	< 1.2 cc	7		0		0	

**Table 4.6:** OAR dose limits defined in the TG-101 report and values obtained in pMBRT treatments in Case 4. The *point* volume is defined as  $\leq 0.035 \text{ cm}^3$ .

skin in PT plans ( $9.1 \pm 0.1$ ,  $5.73 \pm 0.06$ ,  $10.7 \pm 0.1$ , and  $12.0 \pm 0.1 \text{ Gy[RBE]}$  in Cases 1 to 4, respectively). Similar doses and degree of spatial fractionation to the skin did not lead to irreversible skin damage in small-animal preclinical trials [Prezado *et al.* 2017b, Prezado *et al.* 2018]. **These results suggest that**

pMBRT could reduce the radiation-induced skin toxicity of clinical treatments, which remains a side effect in up to 95 % of patients that receive RT [Rosenthal *et al.* 2019].

## 4.5 Evaluation of technical aspects

This study shows that pMBRT can provide satisfactory treatments for the four cases studied by using only one or two fields and one fraction. Besides the dosimetric benefits of pMBRT already discussed in Section 4.4, the use of fewer fields and fractions would be a potential advantage for the clinical implementation of this technique.

The use of fewer fields (one to two arrays), in comparison with SRT treatments (3 to 4 arcs), may result in fewer times the patient needs to be repositioned, reducing the treatment-fraction time and the elapsed time in the treatment room. The use of several fields in SRT may increase the treatment time per fraction. For instance, when using the Cyberknife for treating liver lesions, the treatment time per fraction is of up to 30 to 60 minutes [Aitken & Hawkins 2015]. In contrast, the treatment time of the pMBRT plans of this study (delivered in PBS mode and using mechanical collimators) would range from 5 minutes (Case 1, plan B) to 19 minutes (Case 4, plan C), plus the patient positioning time. These approximate calculations are based on preclinical experiences in our institution. Regarding the management of the target motion, using fewer fields may allow optimizing entry ports to minimize the interplay between dose delivery and the motion of internal structures. For instance, the minibeam field might be delivered in the anterior-posterior direction to minimize the effect of breathing motion on dose distributions. However, the main drawback of using fewer fields is that the robustness of plans may be reduced since, typically, an increased number of fields is assumed to provide more robust treatments. Therefore, special attention should be given to optimizing field arrangements to minimize the effect of potential uncertainties, such as the range uncertainty of proton beams (see Section 1.3.4).

Besides the reduced fraction time, the total treatment time may be considerably reduced in pMBRT plans since treatments are expected to be delivered in only one fraction, contrary to the SRT plans studied, which use three to five fractions. In addition, pMBRT treatments delivered in one fraction may reduce the inter-fraction set-up uncertainties associated with the motion of internal structures. For some indications (e.g., liver metastases), the daily patient set-up and tumor localization are challenging tasks due to the movement of the organ relative to bony anatomy (up to 1 cm [Case *et al.* 2009]), the deformation of the organ between fractions [Aitken & Hawkins 2015], and the similar density of the tumor and the organ tissue.

Regarding the implementation of pMBRT in clinics, the plans evaluated in this work are realizable using the experimental set-up already implemented at ICPO for preclinical trials (see Section 2.1.2). Then, the target and organ motion

during the treatments can be controlled as in current SRT treatments, e.g., using respiration limiting techniques, breath hold, gating, and thermoplastic masks or vacuum cushions [Brandner *et al.* 2017, Atkins *et al.* 2018, Chen *et al.* 2019].

## 4.6 Influence of plan parameters on dose distributions

The distinct dose delivery in pMBRT leads to additional degrees of freedom in the treatment plan optimization process as compared to conventional techniques. For instance, the use of planar minibeam (i.e., multi-slit collimators) requires considering the position, orientation, and separation of minibeam. In this section, how those parameters may influence treatment outcomes is discussed.

### 4.6.1 Orientation and position of the slits

The orientation of the slits, i.e., the direction of the peak-valley pattern, may be optimized to reduce the irradiation of normal tissues and OARs. Planar minibeam should be oriented such that the longitudinal direction of the slits is perpendicular to the direction of the OAR-PTV interface. Thus, valley regions can be placed at the intersection of these two volumes and reduce the scattered dose to the OAR. For instance, adopting this approach in Case 1 plan C (see Sections 4.2 and 4.3.2), the maximum and mean dose to the acoustic nerve is reduced by 6 % and 5 %, respectively, compared to the scenario where the pattern of peak and valleys is oriented along the direction of maximum PTV extension (see Figure 4.14a).

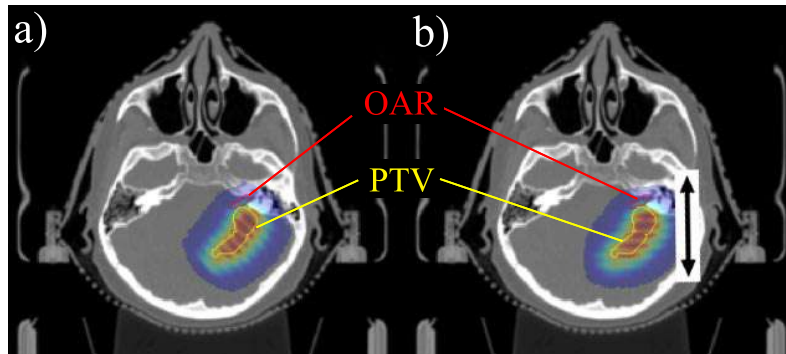


**Figure 4.14:** Illustration of the effect of collimator rotation (i.e., planar minibeam orientation) in dose distributions. In subfigure (a), the direction of the peak-valley pattern follows the direction of maximum PTV extension (i.e., collimator rotation of  $45^\circ$ ), while in subfigure (b), it is parallel to the direction of OAR-PTV intersection (i.e., collimator rotation of  $90^\circ$ ). The arrow in (b) represents the direction of translation of the planar minibeam.

To further illustrate the benefits of this optimization strategy, the position of the collimator (i.e., slits) in the peak-and-valley direction is modified by 3 mm (half of the c-t-c distance in this case) (see Figure 4.14b). As a result, the maximum and

mean dose to the OAR are reduced by 4 % since the peak region is moved away from the OAR-PTV intersection.

It is important to note that the target coverage is not significantly affected by the rotation or translation of the slits in this example (see Figure 4.15).

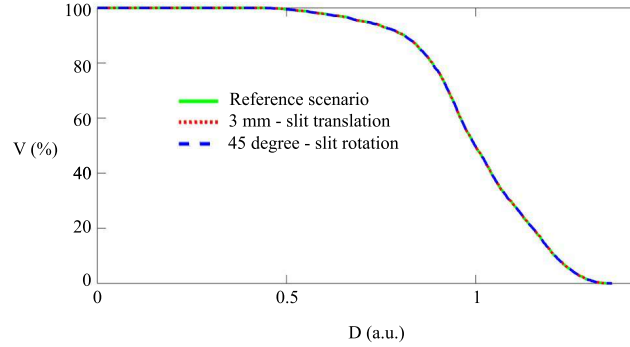


**Figure 4.15:** DVH of the PTV in the reference scenario (collimator rotation of 45° and no slit translation), the 3 mm-slit translation scenario (collimator rotation of 90°), and 90°-slit rotation situation (no slit translation).

#### 4.6.2 Center-to-center distance

The influence of the c-t-c distance on the target coverage has been studied in Section 4.4.1 and other studies [Lansonneur *et al.* 2020]. However, the impact of the separation between minibeam in OAR dose-volume constraints has not been considered yet.

It is assumed that a higher spatial fractionation of the dose (i.e., larger c-t-c distances) promotes the normal tissue sparing of minibeam since valley doses are reduced for a given prescribed dose to the target. However, a higher fractionation leads to higher peak doses. This increase in peak doses may compromise the efficacy of treatment plans where OAR dose-volume constraints are defined by a maximum dose to a point. For instance, in Case 3 plan C (see Sections 4.2 and 4.3.2), the use of a c-t-c distance of 4.5 mm in both arrays leads to 0.06 cm<sup>3</sup> of the rib receiving 30 Gy or more, exceeding the volume set as a constraint in the TG-101 report (0.035 cm<sup>3</sup>). In contrast, by reducing the separation between minibeam to 4 mm in field 2 (see Figure 4.16), the maximum dose point (0.035 cm<sup>3</sup>) meets the dose-volume limit. The variation of the c-t-c distance, in this case, does not significantly affect the degree of spatial dose fractionation in the PTV in the two scenarios, i.e., a PVDR of 1.36 ± 0.04 and 1.25 ± 0.04 are obtained.

These results provide the first insight into the influence of plan parameters specific to pMBRT (e.g., the position and orientation of planar minibeam, and use of different c-t-c distances) on dose distributions. They also highlight the need for guidelines in pMBRT treatment planning, which should be developed for the clinical implementation of this technique. These guidelines, besides the specific

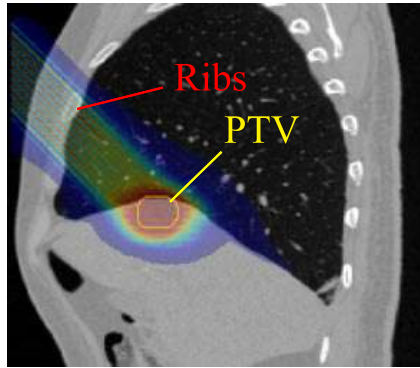


**Figure 4.16:** Dose distributions in Case 3 plan C (see Sections 4.2 and 4.3.2) for field number 2 (see Table 4.1).

dose-volume constraints in pMBRT conditions, must consider the influence of the additional plan parameters presented in this section.

## 4.7 Discussion and conclusions

This chapter presents a theoretical evaluation of the potential benefits of pMBRT for treating different clinical indications. Since it is framed in the context of preparing the potential clinical trials (see Section 1.4.4.4), it considered clinical cases that meet the inclusion criteria proposed for those investigations, i.e., brain metastases of 2 to 4 cm in diameter outside the brainstem. In addition, metastases in other disease sites whose treatment might benefit from pMBRT, i.e., liver and lung, were studied. The figures of merit considered in this work to evaluate the benefits of pMBRT are the target coverage and the reduction in the mean dose to OARs compared to the standard of care for those indications in our institution (ICPO), i.e., SRT, and conventional proton therapy (PT) as well as whether doses to normal tissues in pMBRT treatments remain below tolerance dose limits.

Due to the lack of biological models describing the response of tissues to pMBRT, the methodology employed to evaluate those aspects is based on quantities derived from the LQ model. For instance, to compare pMBRT and PT plans with SRT treatments, the dose prescription relies on delivering the same mean BED to the target. The reduction in the dose to OAR is also computed in terms of the BED. On the other hand, whether pMBRT plans meet dose-volume constraints and tolerance dose limits is evaluated by computing the  $NTD_{2.0}$ .

The applicability of the LQ model in pMBRT conditions is limited. As described in detail in Section 1.2.4.7, this model is uniquely based on the cell death caused by the DNA damage and repair, disregarding any other radiation-induced biological responses. This model is often employed to compare different fractionation schemes in conventional RT since its predictions fit experimental cell survival in most situations (doses per fraction lower than 10 Gy) [Brenner 2008]. However, the model may not accurately predict the responses to pMBRT since it does not consider

the distinct biological mechanism triggered by this specific dose delivery method. Examples of the radiation-induced effects that appear to play a relevant role in the response of tissues to pMBRT are the non-targeted effects, e.g., dose-volume, signaling, inflammatory and immunomodulatory effects, and the migration free radicals and undamaged cells. A detailed description of these biological mechanisms can be found in Section 1.2.4.6. In addition, this model does not consider the differential effect of those mechanisms in tumor and normal tissues, for instance, the positive/cytotoxic bystander-like effects in normal/tumor tissues, respectively.

One of the main conclusions of this work is that, since pMBRT can provide a similar level of target coverage, one may assume that by delivering the same iso-effective dose (i.e., BED) to the target, a similar level of tumor control would be achieved. However, the BED may underestimate the potential of pMBRT in terms of tumor control. In the study by Bertho *et al.* [Bertho *et al.* 2021b] different fractionation schemes in pMBRT conditions were compared using this parameter. For the same BED to the target, differences by up to 3 times were found between the survival rate of groups treated with one and two fractions. These results suggest that the BED may not accurately predict, but probably underestimate, the level of tumor control in pMBRT conditions since it does not consider other biological responses different from DNA damage that contributes to tumor cell death (e.g., vascular effects and cytotoxic signaling effects, ROS diffusion or immune infiltration).

Regarding the assessment of the damage to normal tissues following pMBRT irradiations, also quantities derived from the LQ model, such as the BED and NTD, are employed. In this case, the LQ model is expected to overestimate the toxicity of pMBRT to normal tissues since the increased sparing potential of minibeam is not considered. The biological mechanisms that promote the reduced toxicity of normal tissues in pMBRT, not included in the BED and NTD, are the preferential vascular and positive bystander-like effects, the cell migration, and the reduced inflammation (see Section 1.4.3). In addition, the LQ model is known to overestimate the magnitude of cell killing for doses greater than 10 Gy per fraction [Brenner 2008] as is the case in pMBRT treatments. Moreover, the tolerance dose limits and dose-volume constraints considered in this work were established for conventional seamless irradiation, neglecting the non-targeted effects that favor the normal tissue sparing in pMBRT. Therefore, the radiation-induced toxicity in pMBRT treatments might be even lower than that predicted by the methodology employed in this study.

Overall, the approach adopted in this work to predict treatment outcomes following pMBRT irradiations is conservative since it is expected to (i) underestimate the efficacy of pMBRT in terms of tumor control, and (ii) overestimate the radiation-induced toxicities. Therefore, it may serve as a surrogate of biological models for this dose delivery method.

Nevertheless, radiobiological models and quantities tailored to the distinct dose delivery method in pMBRT are needed, not only to accurately predict treatment outcomes but also to optimize pMBRT irradiation parameters. Those models should include the role of non-targeted effects in pMBRT. Several mathematical

models have been already proposed to describe some of those biological responses, e.g., immunomodulation [Serre *et al.* 2016, Friedrich *et al.* 2022] or vascular effects [Lindblom *et al.* 2019], in seamless conditions or even in GRID and LRT [Asperud *et al.* 2021]. However, they need to be adjusted to include the degree of heterogeneity of pMBRT dose distributions and the potential differential responses in peak and valley areas in their mathematical equations and parameters. In addition, more preclinical and clinical data are required to establish tolerance dose limits in pMBRT, accurately estimate the parameters of the radiobiological models, and define which dosimetric parameters (e.g., dose-volume indexes) correlate to the biological responses to minibeam.

An additional as-of-yet unknown aspect in pMBRT is how the dose should be prescribed. In this work, the mean dose to the target was considered since it is the parameter used for prescribing doses in preclinical investigations. In addition, this approach seems the most natural transition from the current clinical practice, where the mean dose to the PTV is the figure of merit for dose prescription. However, some recent studies have found a strong correlation between the increased lifespan in pMBRT with valley doses [Fernandez-Palomo *et al.* 2022], suggesting that this parameter should be also considered when defining treatment schemes. Moreover, increased tumor control rates have been reported following pMBRT irradiation, compared to conventional PT at the same physical mean dose to the target [Prezado *et al.* 2019, Lamirault *et al.* 2020a, Bertho *et al.* 2021b], which may indicate that the average dose might not be the most appropriate parameter to compare treatment outcomes in pMBRT and conventional seamless techniques. Still, more preclinical data and models are needed for extracting reliable conclusions on how prescribing doses in pMBRT.

Further improvements in this study would imply optimizing pMBRT plans considering the specific Bragg peak of minibeam and to evaluate dose conformity to the PTV. As described in Section 2.3.2, the optimization of treatment plans was performed in seamless conditions since current clinical TPSs do not allow the implementation of pMBRT mechanical collimators, and their dose scoring resolution is not high enough to resolve the size of proton minibeam. Therefore, the dose conformity to the target in pMBRT conditions was not fully optimized. TPSs modules tailored to the distinct dose delivery method in this technique must be developed to address this issue, as discussed in more detail in Chapter 6. The dose conformity to the target was not evaluated in this work due to the lack of conformity indexes adapted to the fact that peak doses outside the target volume are expected to be higher than the prescribed dose (as discussed in Section 4.4.1). The main focus of the present study was to evaluate the radio-induced toxicities of pMBRT treatments rather than optimizing the dose conformity to the target since the endpoint of the Phase I clinical trials would be the study of acute and late neurotoxicity. Therefore, those two issues were out of the primary scope of these investigations. However, forthcoming studies addressing the full optimization of dose distributions to the target employing suitable dosimetric quantities would

be required for Phase II clinical trials, where tumor control would be the figure of merit.

Despite the just mentioned limitations of this study, the obtained results suggest that pMBRT treatments could be successfully delivered in one fraction and using one or two fields. Assuming the approach adopted in this work is valid, pMBRT could provide an equivalent degree of target coverage and, hence, tumor control, as conventional techniques (i.e., SRT) while reducing the dose to OARs and maintaining dose to normal tissues below tolerance dose limits. In addition, more favorable treatment delivery regimes, i.e., reduced number of fractions and fields, may be expected (as discussed in Section 4.5). However, clinical data are warranted to confirm these results.

In conclusion, the results of this study further support the rationale for initiating clinical investigations in pMBRT and aim to guide the discussion on the preparation of the clinical trials.

A research article containing the results of this study has been accepted for publication in the *Medical Physics* journal.

# Proton minibeam arc therapy: a proof-of-concept study

---

## Contents

---

<b>5.1</b>	<b>Rationale</b>	<b>185</b>
<b>5.2</b>	<b>Treatment plans</b>	<b>186</b>
5.2.1	pMBRT plan	187
5.2.2	PAT and pMBAT plans	187
<b>5.3</b>	<b>Evaluation of dose distributions</b>	<b>188</b>
5.3.1	Preservation of the spatial modulation of the dose	188
5.3.2	Dose reduction to normal tissues	190
<b>5.4</b>	<b>Evaluation of LET distributions</b>	<b>192</b>
<b>5.5</b>	<b>Influence of plan parameters on dose distributions</b>	<b>194</b>
5.5.1	Number of minibeam arrays	194
5.5.2	Angular separation between arrays	195
5.5.3	Center-to-center distance	195
5.5.4	Size of the target volume	197
<b>5.6</b>	<b>Discussion and conclusions</b>	<b>197</b>

---

*This chapter presents the proof-of-concept and potential advantages of a new RT technique based on the combination of pMBRT and arc therapy, called proton minibeam arc therapy.*

## 5.1 Rationale

Thus far, only irradiations using one or two arrays of proton minibeam arrays have been considered in pMBRT [Prezado *et al.* 2018, Bertho *et al.* 2021b]. However, using field arrangements that provide dosimetric advantages in other techniques may also benefit pMBRT. An example of these techniques is Proton Arc Therapy (PAT) [Ding *et al.* 2016]. As described in Section 1.2.2.4, PAT enhances the dose conformity at the tumor level and reduces the total dose received by the patient [Seco *et al.* 2013]. In addition, the impact of the proton range uncertainty, one of the main drawbacks of proton therapy, is reduced in PAT since the rotating arc beam diffuses the range uncertainty in distal and proximal regions [Seco *et al.* 2013]. This technique also allows optimizing the linear energy transfer (LET) distribution

[Carabe *et al.* 2020], i.e., PAT concentrates the larger components of LET within the target and reduces the areas of high-LET in normal tissues. The optimization of LET in PAT may increase the effectiveness of proton treatments [Carabe *et al.* 2020]. The potential benefits of this technique have been demonstrated in several disease sites, and indications [Ding *et al.* 2016, Ding *et al.* 2018, Ding *et al.* 2019, Li *et al.* 2018, Chang *et al.* 2020]. However, one of the most appropriate disease sites for PAT appears to be brain tumors since they usually require a short proton range, and the symmetry of the head provides a greater region over which to arc the beam. Thereby, single arcs could replace coplanar arcs, enabling the use of less degraded beams [Carabe-Fernandez *et al.* 2020].

These results encouraged me to evaluate the combination of pMBRT with PAT to improve the treatment of radioresistant brain tumors, as these techniques can be very complementary. Several brain tumors, e.g., bulky brain metastases, have a poor prognosis since the requested dose escalation to increase tumor control rates is jeopardized by the unacceptable toxicity to normal brain tissue [Mitchell *et al.* 2022]. The optimization of LET distributions (i.e., biological optimization) in PAT may enhance the dose escalation while sparing normal tissues due to the reduced neurotoxicity provided by pMBRT. This combined delivery method is termed proton minibeam arc therapy (pMBAT). The combination of both techniques is described in Section 5.2.2.

In this work, I perform a proof-of-concept study to evaluate the potential dosimetric benefits of this approach by comparing pMBAT, pMBRT and PAT (see Sections 5.3 and 5.4). In addition, the influence of the main parameters in the pMBAT treatment planning process on dose distributions are assessed (see Section 5.5).

## 5.2 Treatment plans

In this study, the potential of pMBAT is evaluated in a brain tumor. A virtual 2 cm-diameter planning target volume (PTV) was created in the central region of the patient's brain (see Figure 5.1). Similar target volumes were considered in other theoretical studies on MBRT [Prezado *et al.* 2009a]. The rationale for considering the center of the brain for the target location is that, in this situation, the surrounding normal brain would receive the highest doses for a given dose to the PTV. Therefore, it is the scenario that might benefit the most from the sparing potential of pMBRT. In addition, the target volume size and position meet most of the selection criteria for the potential pMBRT clinical trials (i.e., brain tumors outside the brainstem of at least 2 cm in diameter) (see Section 1.4.4.4).

Three different types of treatment plan were created for the sake of comparing different techniques: (i) single array pMBRT, (ii) pMBAT, and (iii) PAT plans.

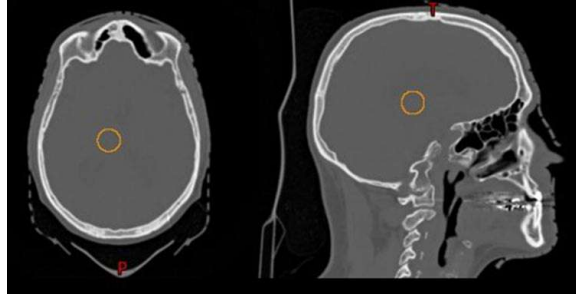


**Figure 5.1:** Representation of the PTV (solid orange line) in the axial and sagittal view of the patient CT.

### 5.2.1 pMBRT plan

The single-array pMBRT plan, referred to as pMBRT hereafter, consists of one array of multiple proton planar minibeam in the caudal direction (see Figure 5.2a). Proton minibeam are shaped by a collimator of fifteen  $400\ \mu\text{m}$ -width slits separated by 4 mm center-to-center (c-t-c) distance (collimator 8 in Table 2.1).

### 5.2.2 PAT and pMBAT plans

The PAT treatment is created by adding a discrete number of fields (13 fields), separated by a constant angle of  $15^\circ$ , forming a  $180^\circ$ -arc around the parietal region of the patient's head (see Figure 5.2b).

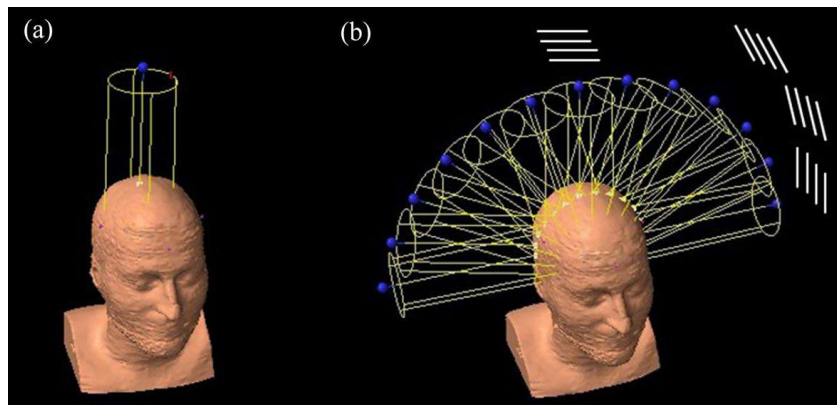


**Figure 5.2:** Beam arrangement in the (a) single-array pMBRT and (b) PAT and pMBAT plans. In (b), a schematic sketch of the rotation of the slits is presented.

In the pMBAT plan, the collimator 8 ( $400\ \mu\text{m}$ -width slits separated by 4 mm c-t-c distance; see Table 2.1) is added to the discrete fields composing the PAT plan. Therefore, the treatment consists of 13 equally-spaced minibeam arrays separated by  $15^\circ$  (see Figure 5.2b). To preserve the spatial fractionation of the dose along the arc, the orientation of the slits (i.e., collimator rotation) is perpendicular to the gantry rotation axis. Figure 5.2b shows a schematic representation of the collimator slits and their rotation around the patient.

As in the work presented in Chapter 4, this study considers the ICPO PBS beamline. Thus, the minimum deliverable proton energy is 100 MeV, i.e., the minimum proton range in nearly water-equivalent materials, such as brain tissue, is around 7 to 8 cm. Since, for some of the field directions, part of the target volume is at a shallower depth than the minimum proton depth, a 30 mm block of PMMA acting as a range shifter is included in all treatment fields. It is placed before the collimator, as could be done in clinical routine, to not reduce the degree of spatial fractionation in the patient. As already discussed in Sections 2.1.4.2 and 4.3.2, placing the range shifter after the collimator would notably increase the width of minibeam and reduce the PVDR in the patient.

It should be noted that pMBAT plans presented above were created such as that they could be implemented using the same technologies as those already used at our institution for pMBRT preclinical trials (see Section 2.1.2). In essence, they consider the ICPO PBS beamline and employ the collimator and range shifter manufactured for clinical trials.

The optimization of treatment plans was performed as described in Section 2.3.2. The ECLIPSE TPS was used to optimize pencil beam spot weight and positions considering seamless conditions. The resulting spot configurations were then imported to TOPAS for the calculation of dose distributions of all treatment plans previously described.

### 5.3 Evaluation of dose distributions

The evaluation of pMBAT dose distributions and comparison with pMBRT and PAT plans consider two main aspects: (i) the maintenance of the spatial modulation of the dose, which is one of the main advantages of pMBRT since it is associated with a tissue-sparing effect, and (ii) the reduction in the dose to normal tissues, which is characteristic of PAT. The evaluation of these two figures of merit is presented in the two following sections.

For the sake of comparing seamless and minibeam dose distributions, the dose is normalized to the mean dose to the PTV. The same approach is typically adopted in preclinical studies to compare pMBRT and conventional PT [Prezado *et al.* 2017b, Prezado *et al.* 2018, Prezado *et al.* 2019, Lamirault *et al.* 2020a, Bertho *et al.* 2021b]

#### 5.3.1 Preservation of the spatial modulation of the dose

**pMBAT preserves the spatial fractionation of the dose in normal tissues**, as Figure 5.3 illustrates. **Neither the characteristic peak-valley pattern nor the peak-to-valley dose ratio (PVDR) are affected by the addition of arrays to form the arc**, as compared to the pMBRT scenario. Figure 5.4 and Table 5.1 show the evolution of the PVDR in normal tissues as a function of depth in pMBAT and pMBRT plans.

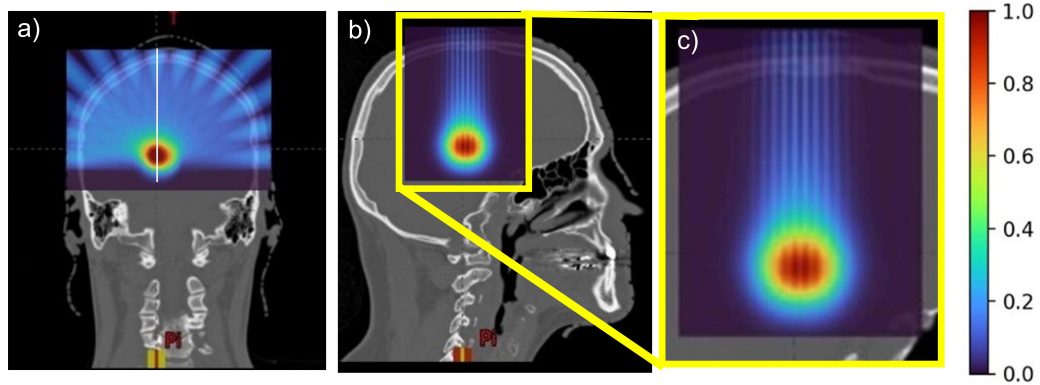


**Figure 5.3:** (a) Coronal, (b) sagittal views of pMBAT dose distributions, and (c) sagittal view zoomed in.

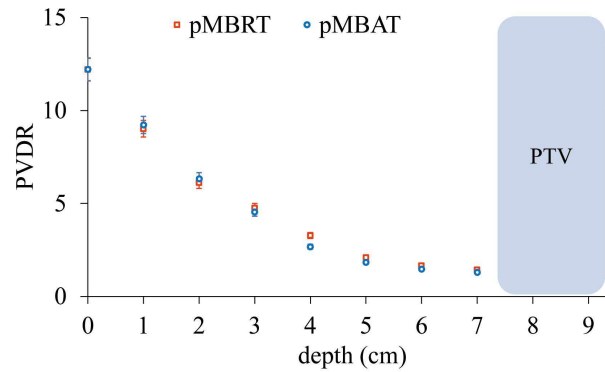


**Figure 5.4:** PVDRs at different depths along the beam path in the pMBRT and pMBAT treatments. The profile considered to evaluate PVDRs is represented by a solid white line in Figure 5.3a.

Depth (cm)	pMBRT	pMBAT
0	$12.6 \pm 0.6$	$12.2 \pm 0.6$
1	$9.0 \pm 0.5$	$9.2 \pm 0.5$
2	$6.1 \pm 0.4$	$6.3 \pm 0.4$
3	$4.8 \pm 0.3$	$4.6 \pm 0.3$
4	$3.3 \pm 0.2$	$2.7 \pm 0.2$
5	$2.1 \pm 0.1$	$1.9 \pm 0.1$
6	$1.65 \pm 0.08$	$1.47 \pm 0.07$
7	$1.43 \pm 0.07$	$1.30 \pm 0.06$

**Table 5.1:** PVDRs in normal tissues as a function of depth in the pMBRT and pMBAT plans. PVDR values were computed along the solid white line in Figure 5.3a.

Regarding the spatial dose fractionation in the target, a quasi-homogeneous dose distribution is created within the PTV in the pMBAT treatment; the PVDR ranges from  $1.06 \pm 0.05$  to  $1.27 \pm 0.06$ . This degree of spatial dose modulation has been proven effective in achieving tumor control rates similar to or even higher than conventional PT [Prezado *et al.* 2018]. For instance, in the work by Prezado *et al.* [Prezado *et al.* 2019], pMBRT treatments characterized by a PVDR around 1.2 at the tumor depth led to a percentage of 67 % glioma-bearing rats surviving long-term free of tumor, a 3-fold increase as compared to homogeneous dose distributions.

As already proven in this thesis (see Section 4.4.1) and other studies [Lansonneur *et al.* 2020], pMBRT could provide a higher level of dose homogenization within the target, if required, by optimizing the c-t-c distance between minibeam. However, several preclinical data demonstrated that a homogeneous dose distribution is not requested in pMBRT for effective tumor control or even tumor ablation [Prezado *et al.* 2018, Prezado *et al.* 2019, Lamirault *et al.* 2020a]. Thus, the possibility of optimizing irradiation parameters to obtain uniform dose distributions within the target is not evaluated in this study.

### 5.3.2 Dose reduction to normal tissues

To evaluate the potential dose reduction in pMBAT, as compared to pMBRT and PAT, depth dose curves in peak and valley regions were analyzed.

**pMBAT treatments result in a significant reduction in peak and valley doses to normal tissues compared to pMBRT.** Both peak and valley doses decrease by 90 % (at shallow depths) to 5 % (at a few millimeters from the PTV) in the cases studied. Figure 5.5 shows the evolution of the dose reduction as a function of depth at peak and valley regions. These values were found for a PDD profile in the caudal direction; however, similar results were found for all the arrays composing the arc in the pMBAT scenario, as illustrated in Figure 5.6.

As compared to PAT, peak doses to normal tissues in the pMBAT case are larger at shallow depths but lower within a few centimeters close to the PTV (see Figure 5.7a). Valley doses in pMBAT are significantly lower than the PAT dose along the proton range (see Figure 5.7b).

The reduction in valley doses in pMBAT, compared to pMBRT and PAT, constitutes a potential advantage since, in minibeam conditions, lower valley doses are meant to correlate, in a directly-proportional relation, with increased normal tissue tolerances (see Section 1.4.3) [Dilmanian *et al.* 2002]. Moreover, the normal tissue preservation in MRT and MBRT does not seem to have a low dose threshold [Dilmanian *et al.* 2012, Eling *et al.* 2021]. The biological mechanism that may be associated with the decreased toxicity at low valley doses is the survival of stem cells in the valley regions, which may migrate to peak areas to repair tissues exposed to high doses [Dilmanian *et al.* 2002].

In addition, the significant dose reduction at shallow depths (up to 90 %) may contribute to the reduction of skin toxicities, a side effect observed in up to 95 % of patients that receive RT [Rosenthal *et al.* 2019].

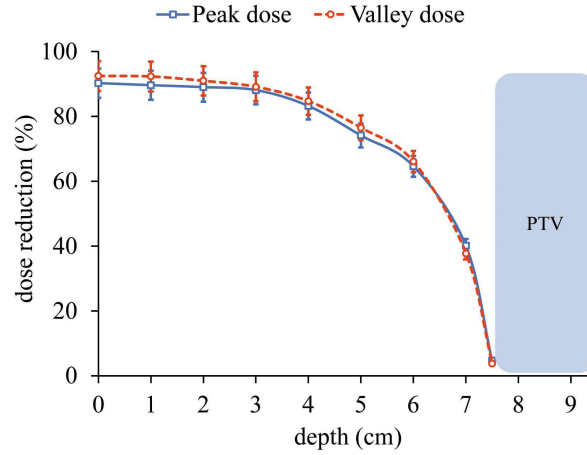


**Figure 5.5:** Dose reduction to normal tissue at peak and valley regions as a function of depth in pMBAT with respect to the pMBRT scenario. The profile considered to evaluate the dose reduction is represented by a solid white line in Figure 5.3a.

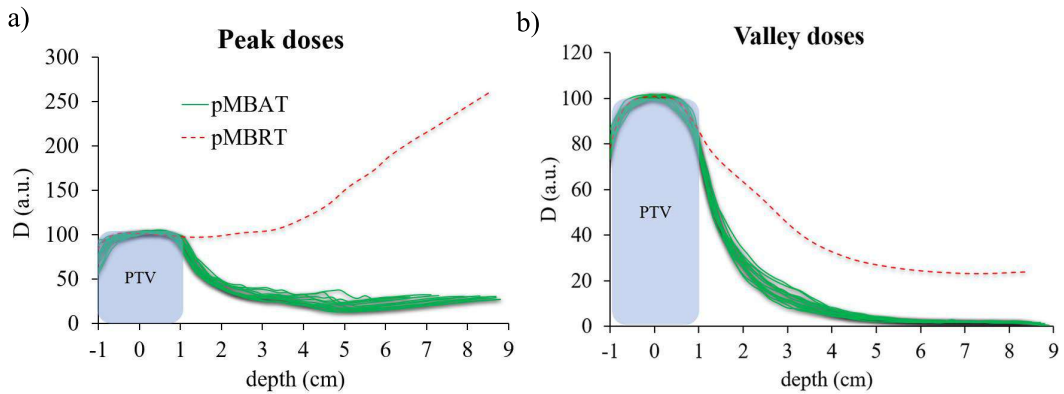


**Figure 5.6:** Depth dose profiles at (a) peak and (b) valleys positions in pMBRT and pMBAT treatments. The 13 arrays composing the pMBAT plan are presented by solid green lines. The origin of the axis of abscissas (depth) is at the PTV position. Doses are normalized to the maximum dose at peaks and valleys, respectively.

Dose-volume histograms (DVH) were also computed in the three scenarios (see Figure 5.8) to evaluate how the reduction in peak and valley doses affects the distribution of high- and low-dose regions within the normal tissue volume. Two volumes are considered in this study: the PTV is considered the target volume, and the whole brain, excluding the PTV, the normal tissue. The DVHs of pMBAT and pMBRT treatments exhibit a less steep curve for the PTV than PAT (i.e., a decreased target coverage) due to the spatial modulation of the dose in the target (described in Section 5.3.1). However, pMBAT provides a higher level of target coverage (i.e., steeper curve) than pMBRT for the same c-t-c distance. This increase in the dose uniformity within the target volume is a characteristic of delivering treatment fields through arcs [Seco *et al.* 2013]. Therefore, pMBAT is expected to maintain an equivalent degree of spatial dose fractionation in normal tissues,

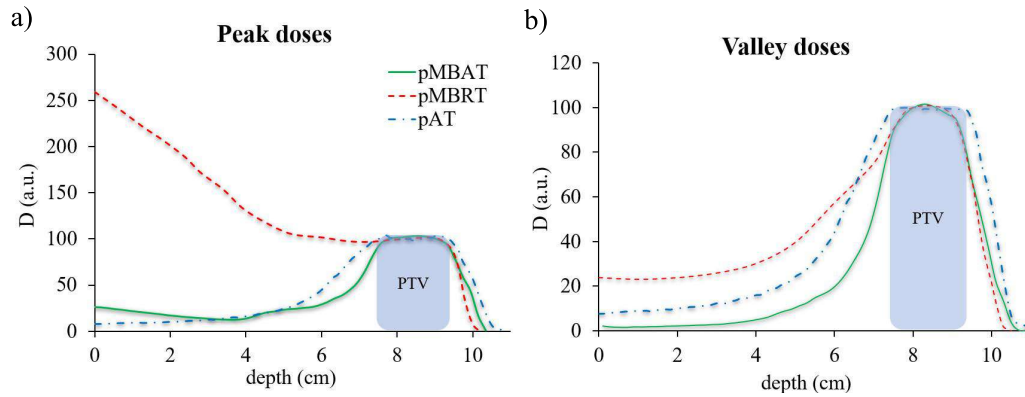


**Figure 5.7:** Depth dose profiles at (a) peak and (b) valleys positions in the pMBAT, PAT, and pMBRT scenarios. The profile considered is represented by a white dotted line in Figure 5.3a. Doses are normalized to the maximum dose at peaks and valleys, respectively.

as compared to pMBRT, while increasing the homogenization of the dose in the target. The dose homogenization in depth while preserving the pattern of peaks and valleys at shallow depths is a characteristic of pMBRT. It is caused by the widening of proton minibeam arrays due to multiple Coulomb scattering (as described in Section 2.1.3).

Regarding the normal tissue volume, the DVH in the pMBAT scenario shows a decrease in the volume receiving high doses and a larger volume covered by low doses, as compared to pMBRT. However, for the same mean dose to the target, the integral dose to normal tissue does not increase in pMBAT compared to pMBRT and PAT. Integral doses to the brain volume, excluding the PTV, were  $0.30 \pm 0.2$ ,  $0.32 \pm 0.3$ , and  $0.33 \pm 0.3$  in PAT, pMBRT, and pMBAT treatments, respectively. These results suggest that the decrease in peak and valley doses in pMBAT is achieved at the expense of the irradiation of a larger volume with lower doses. The potential benefits and drawbacks of that redistribution of the dose within the patient in PAT will be discussed in Section 5.6.

## 5.4 Evaluation of LET distributions

LET distributions were also evaluated to provide an overview of the potential biological optimization in pMBAT. As previously mentioned, PAT provides an optimization of LET distributions in terms of reduction of high-LET areas outside the target volume and concentration of high-LET values within the tumor. Thus, the biological effectiveness in the tumor can be enhanced while reducing the toxicities in normal tissues. For the sake of evaluating whether delivering proton minibeam arrays through arcs also results in a LET escalation, dose-averaged LET ( $LET_d$ ) distributions in pMBAT and pMBRT were qualitatively compared (see Figure 5.9).

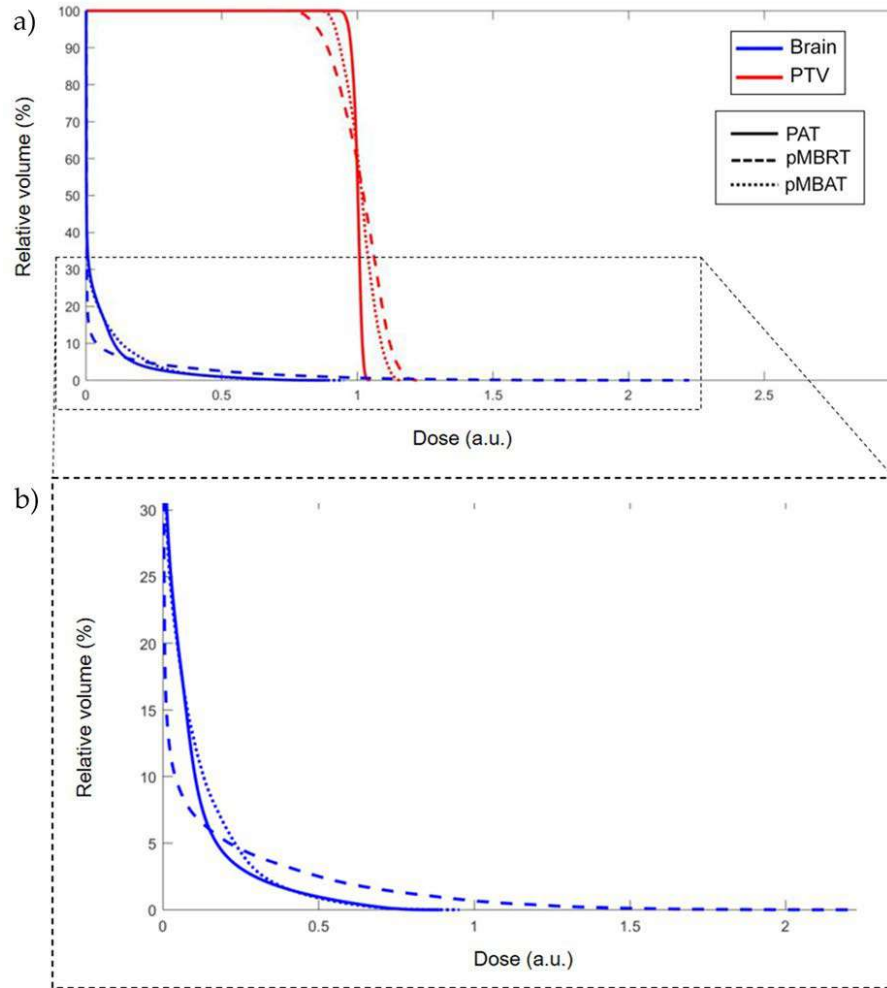


**Figure 5.8:** DVH in pMBRT, PAT, and pMBAT treatments for the PTV and normal brain tissue. (b) Zoomed in view of (a). Doses are normalized to the same average dose to the PTV.

The **pMBAT** treatment reduces the high-LET spots in normal tissue volumes as compared to **pMBRT**. Mean  $LET_d$  values in the normal tissue (i.e., normal brain) are similar in both scenarios, i.e., the mean  $LET_d$  was  $2.0 \pm 0.1$  keV/ $\mu$ m in **pMBRT** and **pMBAT** treatments. These results suggest that the volume receiving high LET values is reduced at the expense of a higher volume receiving intermediate-LET values. Therefore, **pMBAT maintains the benefits of PAT in terms of reducing high-LET levels in normal tissues**, which may allow minimizing the normal tissue toxicity, especially at distal depths.

Regarding LET distributions in the target volume, no significant difference was found between mean  $LET_d$  values in **pMBRT** and **pMBAT** treatments ( $3.5 \pm 0.2$  keV/ $\mu$ m and  $3.6 \pm 0.2$  keV/ $\mu$ m, respectively).

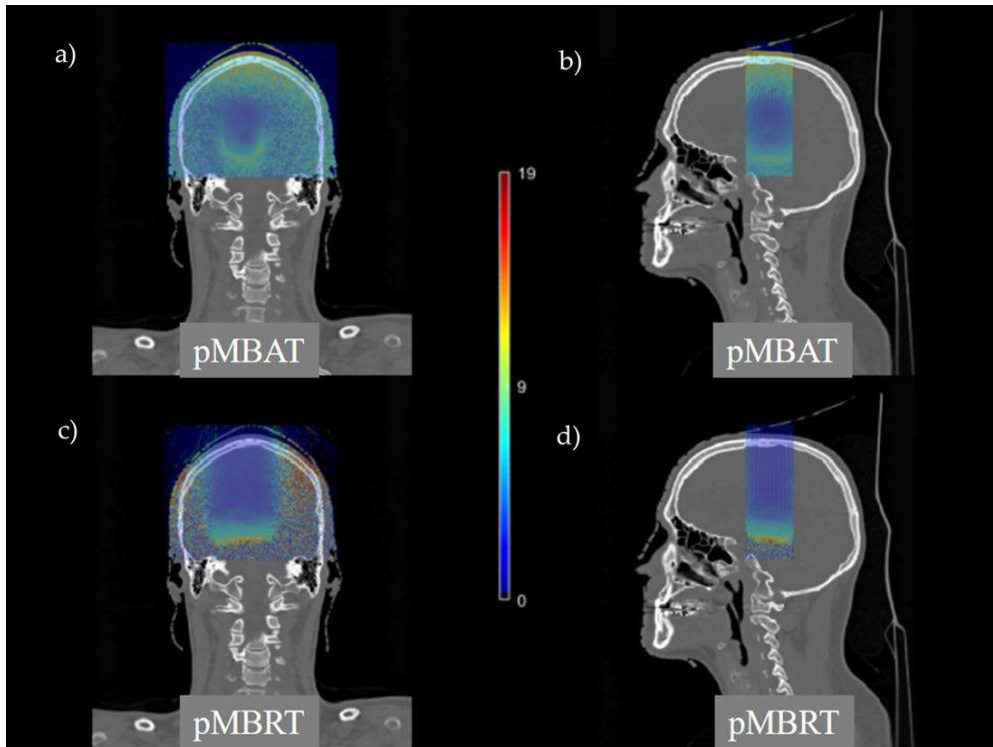


**Figure 5.9:** Coronal and sagittal views of  $LET_d$  distributions in (a,b) pMBAT and (c,d) pMBRT treatments.

## 5.5 Influence of plan parameters on dose distributions

This work also evaluates the influence of different pMBAT plan parameters (angle between consecutive arrays, number of arrays, center-to-center (c-t-c) distances, and PTV size) on dose distributions. The figure of merit to assess the impact on dose distribution is the dose reduction with respect to pMBRT treatments (as also done in Section 5.3.2) The results of this evaluation are presented in the following subsections (Sections 5.5.1 to 5.5.4).

### 5.5.1 Number of minibeam arrays

To study the influence of the number of minibeam arrays on dose distributions, the pMBAT plan presented in Section 5.2.2 (13 arrays) was modified such that the proton arc beam is composed of 11, 9, and 7 proton minibeam arrays (see Figure 5.10). The dose reduction, with respect to the pMBRT case, was evaluated in the pMBAT plans with a different number of fields (i.e., 7, 9, 11 and 13 arrays separated by  $15^\circ$ ).

**An increased number of minibeam arrays composing the pMBAT arc reduces the dose at peak and valley regions in normal tissues** (see Figure 5.11a). For instance, a 15 % difference is observed between plans of 7 and 13 arrays in terms of dose reduction compared to pMBRT.

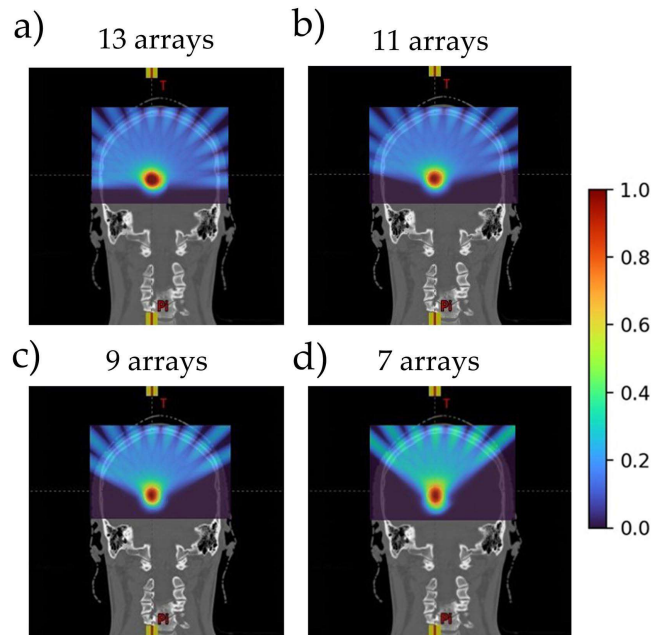


**Figure 5.10:** Coronal view of the pMBAT dose distributions considering a different number of arrays forming the arc, i.e., (a) 13, (b) 11, (c) 9, and 7 arrays.

### 5.5.2 Angular separation between arrays

The angular separation between the fields forming the arc was modified in the pMBAT plan (see Section 5.2.2) to evaluate its effect on dose distributions. Treatment plans composed of 9 minibeam arrays separated by  $10^\circ$ ,  $15^\circ$ , and  $20^\circ$  were compared in terms of dose reduction with respect to the pMBRT scenario (see Figure 5.12).

It was observed that **the larger the angle between the arrays, the lower the peak and valley doses to normal tissues, especially at the proximity to the target** (see Figure 5.11b). For instance, peak and valley doses are reduced by 7 %, on average along the proton range, for each  $5^\circ$  increase in the array spacing. The increment in peak and valley doses as the minibeam arrays are closer to each other is caused by the overlap of two arrays, i.e., the dose of two arrays adds up. Therefore, the dose increases from the depth at which two different arrays superpose. In the case studied, differences in the dose reduction are observed from shallow depths in the case of  $10^\circ$  array separation, as compared to the two other cases, since the arrays overlap close to the patient surface, contrarily to the  $15^\circ$  and  $20^\circ$  cases. Differences between the  $15^\circ$  and  $20^\circ$  angular separation plans are observed from 3 cm depth, where the arrays separated by  $15^\circ$  degrees intersect.

### 5.5.3 Center-to-center distance

To study the impact of the separation between minibeam arrays on the dose reduction in pMBAT with respect to pMBRT, collimators of different c-t-c distances (i.e.,

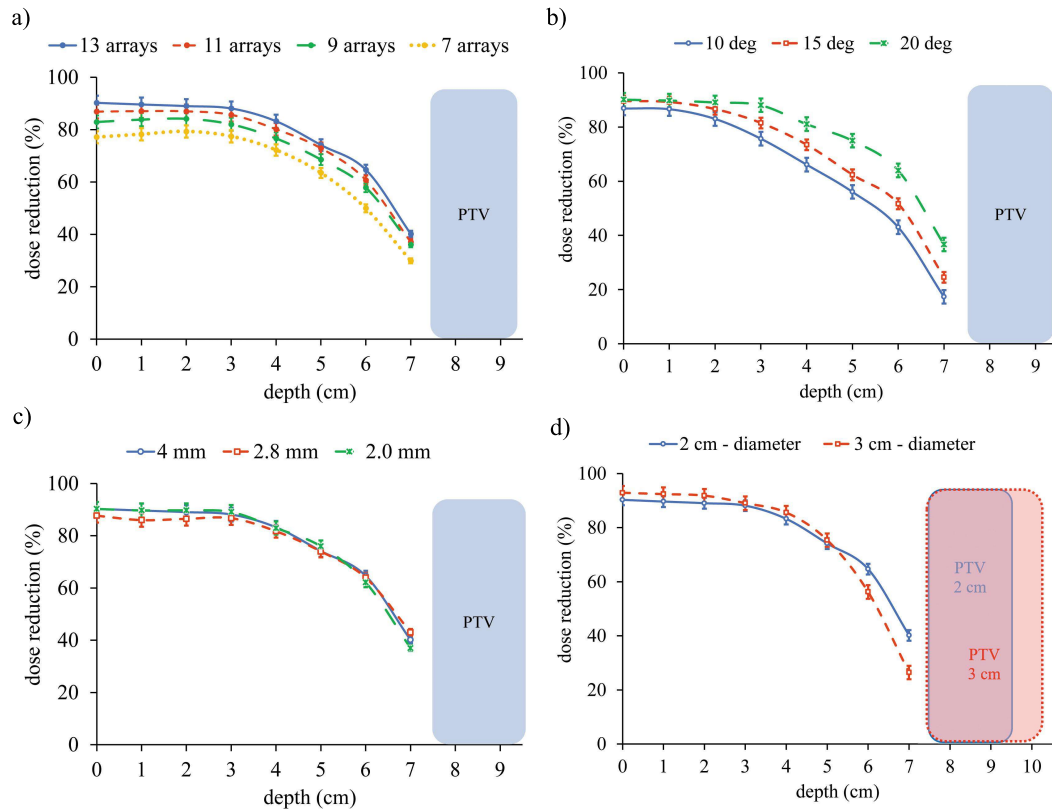


**Figure 5.11:** Dose reduction to normal tissues in pMBAT with respect to pMBRT as a function of depth and (a) number of arrays forming the arc, (b) separation between arrays, (c) c-t-c distance, and (d) PTV diameter.

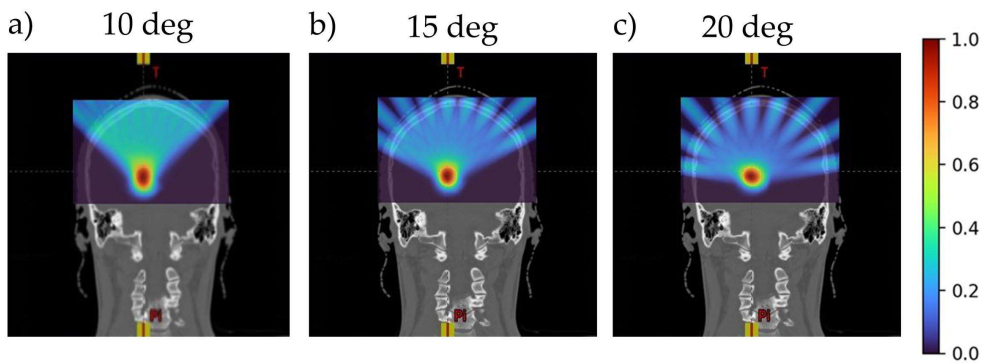


**Figure 5.12:** Coronal view of the pMBAT dose distributions considering a different angular separation between the fields that form the arc, i.e., (a) 10°, (b) 15°, and (c) 20°.

4 mm, 2.8 mm, and 2 mm) were included in the pMBAT and pMBRT plans presented in Section 5.2. Then, peak and valley doses in pMBAT were compared to pMBRT treatments involving the same respective c-t-c distance.

No significant differences in the reduction of peak and valley dose were found

as a function of the *c-t-c* distance (see Figure 5.11c), This result indicates that the choice of the *c-t-c* distance is not expected to influence the dose reduction to normal tissues in *pMBAT*.

#### 5.5.4 Size of the target volume

Finally, the influence of the target size in *pMBAT* dose distributions was evaluated by comparing the *pMBAT* and *pMBRT* plans (presented in Section 5.2) in the treatment of target volumes (i.e., *PTV*) of 2 cm and 3 cm in diameter.

Results of those treatments show that **the dose reduction in *pMBAT* depends on the *PTV* size. The larger the *PTV*, the lower the dose reduction**, as Figure 5.11d illustrates. The increment in peak and valley doses as the target size increases may be explained by the increased longitudinal extension of planar minibeam arrays to cover the larger *PTV* diameter, leading to an overlap of two arrays at shallower depths. As described in Section 5.5.2, the superposition of arrays causes the increase in peak and valley doses by the contribution of two fields to the dose. As observed in Figure 5.11d, this increment in the dose occurs from the point where two arrays overlap.

## 5.6 Discussion and conclusions

This chapter presents the dosimetric evaluation of combining *pMBRT* and *PAT*. This new radiotherapeutic approach is termed proton minibeam arc therapy (*pMBAT*). In this proof-of-concept study, the potential advantages of *pMBAT* are evaluated. The two main figures of merit considered to assess the potential of *pMBAT* for treating brain tumors are: (i) the preservation of the spatial dose modulation of *pMBRT*, which favors the normal tissue sparing [Prezado *et al.* 2017b] and tumor control [Prezado *et al.* 2018], and (ii) the potential reduction of high doses to normal tissues, which results from delivering proton treatment fields through arcs [Seco *et al.* 2013].

The results of this study show that adding up discrete proton minibeam arrays to form an arc in *pMBAT* does not diminish the degree of spatial dose modulation as compared to *pMBRT*. Therefore, the normal tissue-sparing potential of proton minibeam arrays associated with the spatial fractionation of the dose is expected to be maintained in *pMBAT*. For instance, preclinical data showed no significant brain damage [Prezado *et al.* 2017b], nor an impact on the cognitive, motor or emotional functions [Lamirault *et al.* 2020b], and only reversible skin epilation in rats treated with 30 Gy mean dose in a single fraction (i.e., similar fractionation schemes as would be used in clinics, as discussed in Chapter 4).

On the other hand, since *pMBAT* provides a similar degree of spatial dose fractionation within the target as *pMBRT*, the relatively high rates of tumor control in preclinical *pMBRT* treatments (up to 67 % long-term survival rates [Prezado *et al.* 2018]) may be expected in *pMBAT*. In addition, for an equivalent

spatial dose modulation within the tumor and the same mean dose to the target, peak doses to the tumor in pMBAT and pMBRT treatments would be similar. Therefore, pMBAT might preserve the additional radiation-induced tumor cell killing produced in pMBRT treatments when high peak doses per fraction are delivered to the target. The differential response of tumor tissue to high doses of radiation appears to be correlated to microvascular damage, cell apoptosis, the release of tumor-specific antigens, and the subsequent immune-mediated response [Alongi *et al.* 2012, Soliman *et al.* 2016].

pMBAT treatments also lead to a decrease in peak and valley doses to normal brain tissue as compared to pMBRT and PAT. As previously discussed, the reduction of valley doses may enhance the normal tissue preservation in minibeam conditions since the valley dose determines the increment in the tolerance doses to pMBRT (based on preliminary preclinical results). Also, the sparing potential of minibeam does not seem to have a low dose limit [Dilmanian *et al.* 2002, Eling *et al.* 2021]; thus, it can be assumed that the lower the valley dose to normal tissues, the lower the toxicity.

That reduction in peak and valley doses is linked with a larger percentage of normal tissue exposed to low doses. Nevertheless, similar integral doses to the patient are delivered in the pMBAT, pMBRT, and PAT scenarios. The possible development of long-term secondary malignancies following the irradiation of a large volume with low doses is still unknown in pMBRT. However, preclinical data show no late side effects on glioma-bearing rats whose entire brain was irradiated with a pMBRT array [Lamirault *et al.* 2020b]. In addition, the reduction in valley doses within the exposed volume may counterbalance the possible increment in the risk of late side effects, as discussed above.

Besides dose distributions, the potential optimization of LET distributions in pMBAT with respect to pMBRT was evaluated. pMBAT reduces the volumes of normal tissue exposed to high-LET protons at the expense of larger volumes receiving intermediate LET values. The mean LET to the tumor is not affected by the distinct dose delivery method in pMBAT. Therefore, the LET optimization in pMBAT may lead to the enhancement of the biological effectiveness of treatments with respect to pMBRT, i.e., the increased neurotoxicity associated with high-LET values at the distal part of the Bragg peak may be reduced. This LET escalation results from delivering multiple minibeam arrays forming an arc instead of a few discrete fields, as in PAT.

Overall, pMBAT is expected to combine the individual benefits of pMBRT, i.e., the normal tissue sparing effect associated with the spatial fractionation of the dose, and PAT, i.e., dose and LET escalation. This technique is expected to further increase the therapeutic index obtained in pMBRT preclinical investigations. The potential reduction of neurotoxicity in pMBAT may allow using more aggressive irradiation schemes, which could be advantageous in the management of radioresistant tumors.

In addition, this work showed that one of the main benefits of pMBAT, i.e., the

reduction in peak and valley doses, is maintained independently of the pMBAT plan configuration (i.e., the number of arrays to create the arc, the separation between arrays, or the PTV size). Therefore, the proton minibeam arc arrays could be optimized for treating more complex geometries, for instance, by optimizing entry ports.

In conclusion, this study provides the first insight into the possibility of delivering proton minibeam arcs. The favorable results obtained in this work, i.e., optimization of dose and LET distributions, encourage performing treatment plan studies considering clinical cases to further prove the potential of pMBAT.

The results of the study presented in this chapter were published in *Cancers* journal in the form of a research article [Ortiz *et al.* 2021].



# Final discussion and conclusion

---

Since its conception in 1896 [Do Huh & Kim 2020], the treatment of cancer with radiotherapy (RT) has been characterized by a continuous and rapid evolution. In general, the development of new RT techniques has primarily focused on enhancing the dose conformity to the target and reducing the volume of normal tissue exposed to radiation. This progress has been mainly driven by physical and technological advances, e.g., stereotactic dose delivery methods or the MR-linac [Randall *et al.* 2022].

So far, these advances have had a significant impact on the management of cancer; the efficacy of RT treatments has increased significantly for most cancer types in the last decades [American Cancer Society 2022]. However, the treatment outcome of certain types of tumors (e.g., glioblastomas) still remains poor [Mattiuzzi & Lippi 2019]. Generally, those clinical indications may benefit from more aggressive treatments (i.e., higher doses to the tumor), but the needed dose escalation is not achievable since the increased dose to normal tissues would lead to prohibitive toxicities.

One of the main research topics in RT nowadays is the conception of new techniques and strategies to overcome the current limitation in the management of cancer with RT, i.e., the side effects of radiation. From the physics point of view, the development of new strategies to reduce the toxicity to normal tissues without compromising tumor control has likely reached a plateau. In essence, the optimization of physical aspects of RT with the sole objective of enhancing dose conformity and dose escalation is not likely to lead to a major increase in the therapeutic index of treatments. In contrast, the exploitation of the radiobiological effects underlying the tissue response to radiation might improve the efficacy and safety of those difficult-to-treat treatments.

In parallel to the technological advances, progress has been made regarding the knowledge of the radiobiological aspects of radiation, e.g., the role of oxygen, immunomodulation, or the influence of genetic aspects in tissue radiosensitivity. However, the gain in the understanding of those mechanisms has not been fully considered in the development of new RT techniques.

In recent years, several innovative delivery methods have been proposed on the basis of exploiting different radiobiological responses that may favor tumor control and normal tissue sparing. Examples of these approaches are Personalized Ultrafractionated Stereotactic Adaptive Radiotherapy (PULSAR) [Moore *et al.* 2021], FLASH therapy [Favaudon *et al.* 2014], and

Spatially Fractionated Radiotherapy (SFRT) in its different forms (e.g., minibeam radiation therapy [Dilmanian *et al.* 2006]). PULSAR and FLASH reconsider the conventional temporal aspects of RT. In PULSAR, classical fractionation regimes are abandoned by delivering high-dose pulses of radiation separated in time by weeks or months. This approach appears to enhance tumor control by the action of the tumoricidal immune system [Moore *et al.* 2021]. FLASH, on the other hand, employs ultra-high dose rates ( $> 40$  Gy/s), which exploit the so-called FLASH effect, i.e., a reduction of radiation-induced normal tissue toxicities [Favaudon *et al.* 2014]. In contrast, SFRT is based on the spatial fractionation of the dose. This delivery method seems to trigger a distinct tissue response, including immunomodulation, cell signaling, and cohort and dose-volume effects, which leads to a remarkable gain in normal tissue sparing along with relatively high efficacy in tumor control [Prezado 2022].

The promising results already obtained in preclinical studies with these innovative techniques prompted their rapid translation into the clinical domain. For instance, the first treatment with FLASH was performed in 2019 [Bourhis *et al.* 2019], and the first clinical trial (FAST-01) has already been already launched [NLM 2022]. Also, clinical trials on proton minibeam radiation therapy (pMBRT) are being discussed nowadays.

Since most of the biological mechanisms and associated physical parameters in these new approaches are not exploited nor even considered in conventional RT, the development of these new techniques may involve redefining the current assumptions in RT (e.g., optimum dose rates, dose distributions, or fractionation schemes). For instance, SFRT data proved that delivering a lethal dose of radiation to each tumor cell is not necessary anymore to eradicate the tumor, as opposed to the current assumptions. Despite the numerous developments and promising prospects in this field, there are a few unresolved questions that remain to be addressed. These subjects must be tackled from different disciplines.

From the physics point of view, the radically different conditions in these new techniques (e.g., dose rates or spatial dose distributions) require the development and adaptation of current dosimetric protocols (including dosimeters) for the accurate measurement of dose distributions. An example of how protocols may be adapted in the development of a new technique is given in this PhD thesis. In particular, this work focused on the preclinical dosimetry for pMBRT. In this context, I evaluated the suitability of detectors and complementary tools (i.e., Monte Carlo simulations) employed for the dose determination in pMBRT, and assessed the sensitivity of its dose distributions to irradiation and setup parameters. From these results, dosimetric guidelines and protocols were proposed to perform reproducible and reliable dosimetric studies. The type of investigation performed in this thesis is indispensable for advancing the development of a new technique, for instance, proceeding with preclinical and clinical studies.

From the clinical-related perspective, several uncertainties arise regarding how to translate the current radiobiological knowledge from conventional to new techniques.

This includes the way of prescribing treatments, the doses required for tumor control, or the tolerance dose limits of normal tissues. The study performed in this PhD thesis to evaluate the potential benefits of pMBRT for treating clinical indications highlights some of these dilemmas. For instance, it reveals that some of the dosimetric parameters typically used in conventional RT (e.g., dose conformity indexes or dose-volume constraints) are not adequate to evaluate and predict treatment outcomes in these new approaches. It also points out the potential need for specific software for the development of those techniques, for instance, tailored treatment planning systems. This study also provides an example of how to adapt current practices to different dose delivery methods, in this case, pMBRT.

Overall, RT nowadays requires a multi-disciplinary approach for its further development since the boundaries between physics and biology in recent years are becoming less distinct. Although some of the technical advancements in RT are focused on purely physics-related aspects (e.g., the generation of high-dose pulses of radiation), it is becoming more and more evident that an approach combining physics and biology is necessary. For instance, current research focuses on optimizing physical parameters that trigger biological mechanisms to favor tumor eradication and the preservation of normal tissues.

The change of paradigm in the current and future progress in RT also involves adding another dimension in the evaluation of the interaction of radiation with tissues. Whereas conventional RT focuses on the biological responses at the tissue and organ scale, the development of new approaches to RT requires an investigation into the link between physical and biological parameters at much smaller scales (e.g., cellular and DNA scale). For instance, micro- and nano-dosimetry studies have been performed to evaluate the biological effects in minibeam radiation therapy [Dos Santos *et al.* 2020] and optimize carbon-ion treatments [Burigo *et al.* 2019].

In my opinion, the future of pMBRT in particular also lies in advances in its biological and physical facets. The complete characterization of the biological mechanisms that underlie the specific response of tissues to pMBRT is one of the main aspects to be considered in the development of this technique. For that purpose, increasing the amount of biological data in controlled conditions is necessary. The description of the biological responses should be accompanied by the knowledge of the effects of proton minibeam at DNA and cellular scales (e.g., the production and diffusion of free radicals). This combined knowledge would allow the development of radiobiological models considering the correlation between tissue responses (including vascular and immunomodulatory effects) and the physical parameters that describe dose distributions. Adapted dosimetric parameters would also need to be defined to prescribe and evaluate dose distributions in pMBRT since, as discussed in Chapter 4, current parameters used in clinics are not adequate. From the physics perspective, further developments may involve the optimization of the generation of proton minibeam. A current research topic in pMBRT focuses on exploring more efficient and flexible methods to create an array of minibeam different from using mechanical multislit collimators. Although several approaches

have already been proposed, such as magnetic focusing [Schneider *et al.* 2020] and dynamic collimators [Sotiropoulos & Prezado 2021], their implementation in clinical facilities is still a pending task. In addition, an important asset for the thorough implementation of this technique would be the development of a module in treatment planning systems (TPS) for pMBRT treatment optimization. Although some TPS already use dose-scoring resolutions adequate for pMBRT, such as *RayStation* (RaySearch Laboratories AB, Stockholm, Sweden), they do not consider optimization parameters relevant in this technique yet. Besides the current optimization constraints in clinically-available TPSs (i.e., mean, maximum, and minimum dose-volume limits), a TPSs for pMBRT should also include optimization objectives fully describing its dose distributions, such as the transverse and longitudinal optimization of peak-valley dose profiles. Those software should also incorporate radiobiological models specific to this dose delivery method for a plan optimization considering the complete response of tissues to pMBRT.

The future of RT may also involve blurring the lines between different techniques by combining distinct approaches that could be complementary. For instance, fusing SFRT techniques and FLASH therapy has already been proposed to increase the therapeutic index in the treatment of radioresistant tumors [Brahme *et al.* 1980, Schneider *et al.* 2022b]. In this context, this thesis also evaluated the combination of pMBRT with arc therapy for treating brain tumors. The results of this proof-of-concept study highlight the complementary nature and potential benefits of delivering pMBRT through arcs in terms of more favorable dose and LET distributions.

In general, we are witnessing a very exciting era in RT, where the classical dogmas are being questioned. The questioning of these dogmas reveals a potentially promising new landscape of RT in which new approaches to advance in the treatment of cancer will be founded.

*The work performed during this PhD thesis aims to contribute to this period of changes by assisting in the development of a new innovative technique with a promising outlook, i.e., proton minibeam radiation therapy (pMBRT). In this context, this thesis advanced the present, short-, and intermediate-term prospects of this technique by (i) optimizing the current dosimetry practice in its preclinical stage, (ii) evaluating its implementation in the forthcoming clinical trials, and (iii) exploring its future developments in combination with other promising RT approaches.*

# Scientific production

*This chapter presents the publications and scientific communications derived from the work performed in this PhD thesis.*

## Publications in peer-reviewed journals

Bertho A<sup>1</sup>, **Ortiz R**<sup>1</sup>, Juchaux M, Gilbert C, Lamirault C, Pouzoulet F *et al.*. First Evaluation of Temporal and Spatial Fractionation in Proton Minibeam Radiation Therapy of Glioma-Bearing Rats. *Cancers*. 2021; 13(19):4865. <https://doi.org/10.3390/cancers13194865>.

**Ortiz R**, De Marzi L, Prezado Y. Proton Minibeam Radiation Therapy and Arc Therapy: Proof of Concept of a Winning Alliance. *Cancers*. 2022; 14(1):116. <https://doi.org/10.3390/cancers14010116>.

**Ortiz R**, De Marzi L, Prezado Y. Preclinical dosimetry in proton minibeam radiation therapy: Robustness analysis and guidelines. *Med Phys*. 2022;49(8):5551-5561. <https://doi.org/10.1002/mp.15780>.

Bertho A, Iturri L, Brisebard E, Juchaux M, Gilbert C, **Ortiz R** *et al.*. Evaluation of the role of the immune system response following minibeam radiation therapy. *Int J Radiat Oncol Biol Phys*. 2022;S0360-3016(22)03106-6. <https://doi.org/10.1016/j.ijrobp.2022.08.011>.

**Ortiz R**, Belshi R, De Marzi L, Prezado Y. Proton minibeam radiation therapy for treating metastases: A treatment plan study. *Accepted for publication in Med Phys*.

Flynn S, Allport P, De Marzi L, Green S, Homer M, Lee N, **Ortiz R** *et al.*. Development of CMOS dosimetry in proton minibeam for enhanced QA and primary standard absorbed dose calorimetry. *Submitted to JINST, under review*.

## Book chapters

Schneider T, De Marzi L, **Ortiz R**. Chapter 20: Monte Carlo simulation of Proton SFRT. In Zhang H.; Mayr N. (Ed.), Spatially Fractionated, Microbeam and Flash Radiation Therapy: A Physics and Multi-disciplinary Approach. *Submitted to IOP Science, under review*.

---

<sup>1</sup>indicates equal contribution

## Presentations at international conferences

### Oral presentations

**Ortiz R**, De Marzi L, Prezado Y. "First dosimetric assessment of Proton Minibeam Arc Radiation Therapy". *ECMP 2021*, June 2021, Online.

**Ortiz R**, De Marzi L, Prezado Y. "Proton minibeam radiation therapy for treating metastases: a treatment plan evaluation". *ECMP 2022*, August 2022, Dublin, Ireland.

**Ortiz R**, De Marzi L, Prezado Y. "Proton minibeam radiation therapy for treating metastases: a treatment plan evaluation". *FRPT 2022*, November 2022, Barcelona, Spain.

### Poster presentations

**Ortiz R**, De Marzi L, Prezado Y. "First dosimetric assessment of Proton Minibeam Arc Radiation Therapy". *PTCOG 2020*, June 2021, Online.

**Ortiz R**, De Marzi L, Prezado Y. "First dosimetric assessment of Proton Minibeam Arc Radiation Therapy". *ESTRO 2020*, August 2021, Online.

**Ortiz R**, De Marzi L, Prezado Y. "Proton minibeam radiation therapy for treating metastases: a treatment plan evaluation". *PTCOG 2022*, June 2022, Miami, USA.

**Ortiz R**, De Marzi L, Prezado Y. "Preclinical dosimetry in proton minibeam radiation therapy: robustness analysis and guidelines ". *ECMP 2022*, August 2022, Dublin, Ireland.

# Résumé du travail de thèse en français

## Contexte et enjeu

La radiothérapie (RT) est l'utilisation médicale des rayonnements ionisants pour traiter, généralement, des tumeurs malignes à des fins curatives ou palliatives. Elle est basée sur la capacité des rayonnements ionisants à endommager les tissus biologiques. Le principe fondamental des traitements par RT est de délivrer à la tumeur une dose suffisamment élevée pour l'éradiquer tout en limitant les dommages produits aux tissus sains normaux.

À cette fin, plusieurs stratégies ont été proposées, comme l'administration de traitements en plusieurs fractions ou l'amélioration de la conformation de la dose à la tumeur. L'adoption de ces approches a permis d'augmenter le taux de survie des personnes atteintes de cancer au cours des soixante dernières années. Cependant, les taux de survie à 5 ans de certains types de cancer, comme ceux du poumon, du foie, du cerveau ou du pancréas, sont encore inférieurs à 20%. L'une des principales raisons de ce mauvais pronostic est que le traitement de ces tumeurs malignes est compromis par le risque de toxicité pour les tissus normaux, ne permettant pas d'augmenter la dose délivrée à la tumeur pour l'éradiquer. En fait, l'une des principales limites de la RT aujourd'hui est le risque de dommages aux tissus normaux.

Une stratégie permettant de surmonter cette limitation est le fractionnement spatial de la dose. Contrairement aux techniques classiques, où l'on utilise généralement de grands champs de la taille de la tumeur, la SFRT utilise plusieurs champs étroits séparés par une certaine distance. Cette méthode d'administration de la dose entraîne une distribution non uniforme de la dose, caractérisée par une succession de régions à forte dose, appelées pics, et de zones à faible dose, appelées vallées. Le fractionnement de la dose est généralement décrit par le rapport entre les doses de pic et de vallée, appelé rapport de dose de pic à vallée (PVDR). Ce schéma de dose semble activer des mécanismes biologiques différents de ceux impliqués dans la RT standard, ce qui permet une meilleure préservation des tissus.

On suppose que les réponses biologiques distinctes à la SFRT sont dues aux effets vasculaires, de dose-volume et de signalisation, à la diffusion des radicaux libres et aux effets immunomodulateurs. Ces mécanismes biologiques semblent également avoir un effet différentiel sur les tissus normaux et tumoraux. En général, ils favorisent la préservation des tissus normaux tout en augmentant la destruction des cellules tumorales. Bien que ces réponses aient été observées dans plusieurs études sur la SFRT, leur corrélation avec les paramètres physiques de l'irradiation n'est pas encore totalement caractérisée et doit faire l'objet d'études supplémentaires.

Au cours des trois dernières décennies, le concept de fractionnement spatial de

la dose a évolué et, aujourd'hui, la SFRT peut être classée en quatre techniques principales en fonction des caractéristiques physiques des irradiations et, en particulier, de la taille du faisceau. Cette thèse de doctorat s'est concentrée sur une forme de SFRT qui utilise des faisceaux de protons submillimétriques (0,1 - 1 mm) comme forme d'irradiation. Cette technique est appelée radiothérapie par mini-faisceaux de protons (pMBRT).

La pMBRT combine les avantages du fractionnement spatial de la dose en termes d'épargne des tissus normaux avec le schéma de dépôt de la dose plus favorable des faisceaux de protons. Les mini-faisceaux de protons sont généralement créés par des collimateurs mécaniques à fentes multiples. Des études précliniques sur la pMBRT ont déjà montré l'absence de lésions cérébrales significatives et uniquement une épilation cutanée réversible, contrairement aux irradiations conventionnelles par faisceau de protons. Elles ont également signalé une augmentation des taux de survie après une irradiation par pMBRT par rapport à la protonthérapie standard, même lorsque la tumeur était irradiée avec des distributions de dose hétérogènes. Globalement, les données précliniques ont montré jusqu'à présent le potentiel de la pMBRT en termes d'augmentation de la tolérance des tissus normaux et de contrôle supérieur de la tumeur. Ces résultats prometteurs soutiennent l'initiation d'essais cliniques, qui sont actuellement en discussion dans notre institution (Institut Curie - Centre de Protonthérapie d'Orsay).

L'objectif principal de cette thèse de doctorat est de contribuer à la poursuite du développement de la pMBRT sous trois aspects principaux : (i) améliorer la pratique actuelle de la dosimétrie dans les études précliniques, (ii) évaluer les avantages potentiels de cette technique pour traiter différentes indications cliniques dans le contexte de la préparation des essais cliniques à venir, et (iii) explorer de nouvelles formes de pMBRT qui pourraient être bénéfiques en clinique.

## Principaux résultats

### Dosimétrie pour les essais précliniques du pMBRT

La dosimétrie pour la pMBRT est complexe et sujette aux erreurs en raison de la taille très étroite des faisceaux utilisés et des gradients de dose élevés. Ces caractéristiques de champ nécessitent l'utilisation de détecteurs à haute résolution spatiale qui ne sont pas habituellement utilisés dans la pratique clinique et des codes MC adaptés. Avant de procéder aux campagnes dosimétriques, l'utilisation des détecteurs et les simulations MC doivent être validées.

Dans cette thèse, trois détecteurs différents et nos codes MC ont été validés en considérant différentes configurations et profondeurs et en comparant les mesures expérimentales avec les résultats simulés. Dans tous les cas, un bon accord a été trouvé entre les données mesurées et simulées. Les détecteurs validés sont le détecteur microdiamant, la diode RAZOR et deux types de films radiochromiques. Ces dosimètres offrent une haute résolution spatiale ( $< 20$   $\mu\text{m}$ ) permettant de mesurer avec précision les distributions de doses de pMBRT. En ce qui concerne

les simulations MC, j'ai utilisé le logiciel TOPAS avec des paramètres de simulation adaptés à la pMBRT. Cette validation m'a permis d'avoir trois types de détecteurs et un outil complémentaire pour réaliser différentes études dosimétriques et être confiant sur les résultats de ces études.

L'une de ces études consistait en une analyse de robustesse sur la sensibilité des distributions de dose pour la pMBRT à de petites variations des paramètres d'irradiation et de configuration. La grande hétérogénéité des distributions de dose dans le pMBRT conduit à une sensibilité accrue, qui doit être caractérisée afin d'améliorer la reproductibilité des irradiations. Dans cette étude, j'ai considéré les paramètres qui, d'après notre expérience, sont facilement fluctuants et peuvent influencer de manière significative les distributions de dose, comme l'incertitude des spécifications du collimateur (la largeur, la divergence et la séparation des fentes) due au processus de fabrication du collimateur. Les résultats de cette étude ont révélé que la plupart des paramètres pris en compte affectent considérablement les distributions de dose en pMBRT (par exemple, l'espace d'air entre le collimateur et le volume cible ou les caractéristiques du collimateur). Toutefois, le paramètre qui influence le plus les profils de dose latéraux est l'inclinaison du collimateur. Par exemple, une inclinaison du collimateur de  $0,5^\circ$  par rapport à la ligne de faisceau, qui n'est pas facilement détectable dans la routine clinique, entraîne une diminution de 50 % de la PVDR et des doses maximales.

La sensibilité des distributions latérales de dose en pMBRT à une légère variation des paramètres d'installation et d'irradiation affecte non seulement les quantités dosimétriques, mais aussi les réponses biologiques directement corrélées à ces quantités physiques. Pour cette raison, une optimisation de la configuration expérimentale peut être nécessaire lorsque cette technique est mise en œuvre dans une ligne de faisceau clinique. Dans ce travail, j'ai proposé une méthode pour optimiser le dispositif expérimental de notre institution, basée sur l'alignement de la ligne de faisceau par rapport à l'entrée du collimateur, puisque, comme nous venons de le mentionner, l'inclinaison entre le collimateur et la ligne de faisceau est le paramètre qui affecte le plus les distributions de dose en pMBRT. Le résultat de ce processus d'optimisation a été la réduction de l'inclinaison de la ligne de faisceau par rapport au collimateur de  $0,35$  à  $0^\circ$  et une augmentation du fractionnement spatial de la dose allant jusqu'à 65%.

Sur la base des résultats présentés précédemment, j'ai proposé un ensemble de directives et un protocole pour assurer une dosimétrie reproductible dans les investigations précliniques. Il s'agit d'un processus en deux étapes qui comprend l'étalonnage des détecteurs, l'optimisation des conditions d'irradiation et l'assurance de la qualité des traitements en conditions de faisceau large et de pMBRT.

En suivant ce protocole, je réalise la dosimétrie nécessaire pour les essais précliniques menés dans notre institution au cours de cette thèse. Différentes conditions d'irradiation et distributions de doses ont été envisagées pour corrélérer les différents résultats du traitement (tels que le contrôle de la tumeur, la toxicité ou l'infiltration immunitaire) à différentes quantités dosimétriques de pMBRT et

acquérir des connaissances sur le mécanisme biologique derrière la réponse favorable des tissus à la pMBRT.

En général, ce travail sur la dosimétrie préclinique a permis d'évaluer les différents aspects à prendre en compte lors du développement d'une nouvelle technique radiothérapeutique. Il établit également un cadre pour la poursuite des études précliniques permettant d'établir une corrélation fiable entre les quantités dosimétriques pertinentes et les paramètres biologiques, ce qui est important au stade préclinique pour démêler les réponses biologiques à la pMBRT et leur dépendance aux quantités dosimétriques.

### **Évaluation du potentiel du pMBRT pour le traitement des métastases**

Une fois le premier objectif de cette thèse atteint, j'ai évalué la mise en œuvre clinique de la pMBRT pour le traitement des métastases volumineuses du cerveau, du foie et du poumon par une étude du plan de traitement. Ces indications cliniques ont un mauvais pronostic et le pMBRT peut contribuer à augmenter l'efficacité des traitements. Pour évaluer cela, les plans de pMBRT ont été comparés à la norme de soins pour ces tumeurs malignes, la radiothérapie stéréotaxique (SRT) et la protonthérapie conventionnelle (PT). Les chiffres de mérite pour cette comparaison étaient la couverture de la cible, la dose aux organes à risque, et l'évaluation des limites de tolérance de la dose dans les différents traitements.

Cette étude montre que les traitements pMBRT peuvent fournir une couverture de cible similaire ou supérieure à la SRT. On peut donc s'attendre à ce que, en délivrant le même BED à la cible, la pMBRT permette un contrôle de la tumeur similaire, voire supérieur, à celui des techniques conventionnelles.

La pMBRT réduit significativement la dose aux organes critiques (OAR) par rapport aux plans SRT. De même, la dose intégrale reçue par le corps dans le cas de la pMBRT a été réduite de 30 à 65 %. Cette diminution de la dose à l'OAR résulte de l'utilisation de quelques réseaux de mini-faisceaux à protons (un ou deux) au lieu d'un grand nombre d'arcs dans la SRT, ce qui permet d'optimiser les ports d'entrée des champs de traitement pour éviter les irradiations de l'OAR.

Enfin, dans tous les plans de pMBRT, la dose aux tissus normaux était inférieure aux limites de dose de tolérance considérées dans la pratique clinique actuelle, ce qui suggère que ces structures seraient épargnées dans les traitements de pMBRT. Cette analyse a considéré que les doses dans la vallée étaient responsables de l'épargne des tissus normaux. En outre, les doses à la peau étaient similaires aux valeurs délivrées dans les études précliniques, qui n'ont pas conduit à des dommages cutanés irréversibles, ce qui suggère que le pMBRT pourrait réduire la toxicité cutanée radio-induite des traitements cliniques.

Les principales conclusions de cette étude sont que la pMBRT permet d'obtenir un contrôle tumoral similaire ou supérieur à celui de la SRT et que les traitements pMBRT administrés en une seule fraction et utilisant seulement 1 ou 2 champs réduisent la dose aux OAR et respectent les tolérances de dose des tissus normaux.

Ces conclusions sont prudentes car elles sont basées sur des quantités dérivées du modèle LQ, qui devrait sous-estimer le niveau de contrôle de la tumeur et surestimer les dommages causés aux tissus normaux dans des conditions de pMBRT, car il ne tient pas compte des réponses biologiques spécifiques qui contribuent à l'élimination accrue des cellules tumorales et à la préservation des tissus normaux dans cette technique (par exemple, les effets vasculaires, la diffusion des radicaux libres, la migration cellulaire ou l'infiltration immunitaire).

Ces résultats dans la pMBRT ont été obtenus en utilisant un nombre réduit de champs d'irradiation (un ou deux seulement) et une seule fraction, ce qui est rarement possible avec les techniques conventionnelles. Cette réduction des champs et des fractions, par rapport à la RT conventionnelle, conduirait à des régimes de traitement plus favorables puisque le temps de traitement et les incertitudes inter- et intra-fractionnelles seraient considérablement réduits.

En conclusion, les résultats de ce travail soutiennent davantage l'initiation d'essais cliniques.

### **Arcthérapie par mini-faisceaux de protons: une étude de validation du concept**

Jusqu'à présent, seules les irradiations utilisant un ou deux réseaux de mini-faisceaux à protons ont été envisagées dans le cadre de la pMBRT. Cependant, l'utilisation d'arrangements de champs qui offrent des avantages dosimétriques dans d'autres techniques peut également profiter à cette technique, par exemple en délivrant la dose par des arcs dans la thérapie par arc de protons (PAT). Cette méthode d'administration de la dose améliore la conformité de la dose au niveau de la tumeur, réduit l'impact de l'incertitude de la portée des protons et permet d'optimiser la LET. Ces avantages peuvent donc être très complémentaires de la réduction de la toxicité pour les tissus normaux et du contrôle satisfaisant de la tumeur dans la pMBRT. Dans ce travail, j'ai donc évalué les avantages potentiels de la combinaison de ces deux techniques et de la délivrance de réseaux de mini-faisceaux de protons par des arcs. Cette nouvelle technique a été appelée arcthérapie par minibeam de protons (pMBAT). Cette évaluation a porté sur une tumeur cérébrale et trois aspects principaux des distributions de dose ont été considérés : la préservation du fractionnement spatial de la dose, la réduction de la dose aux tissus normaux et l'optimisation du LET.

Les plans pMBAT préservent le fractionnement spatial de la dose dans les tissus normaux. Par rapport au scénario pMBRT, l'ajout de matrices pour former l'arc n'affecte ni le schéma caractéristique pic-vallée ni le PVDR. Dans la tumeur, le PVDR était d'environ 1,2, ce qui a donné des résultats satisfaisants dans les essais précliniques en termes de contrôle de la tumeur. Par conséquent, cette nouvelle approche devrait permettre de préserver les avantages de la pMBRT, à savoir le potentiel d'épargner les tissus normaux et les taux de contrôle de la tumeur.

En ce qui concerne la dose aux tissus normaux, les traitements pMBAT ont entraîné une réduction significative des doses de pic et de vallée aux tissus normaux

par rapport au pMBRT. Les doses de pic et de vallée ont diminué de 90 à 5 %. La réduction des doses de vallée dans le pMBAT constitue un avantage potentiel puisque, dans des conditions de mini-faisceaux, des doses de vallée plus faibles sont censées être corrélées à des tolérances accrues des tissus normaux. La diminution des doses de crête et de vallée est obtenue au prix de l'irradiation d'un plus grand volume avec des doses plus faibles, ce qui ne devrait pas entraîner d'effets secondaires tardifs, selon les données précliniques.

En ce qui concerne les distributions de LET, le traitement pMBAT a réduit les taches de LET élevé dans les volumes de tissu normal par rapport au pMBRT. Comme pour la dose, cette réduction est obtenue au détriment d'un volume plus important recevant des valeurs de LET intermédiaires. Ces résultats suggèrent que l'augmentation de la neurotoxicité associée aux valeurs élevées de LET dans la partie distale du pic de Bragg peut être réduite dans la pMBAT. On s'attend donc à ce que cette approche maintienne également les avantages de la PAT en termes de réduction des niveaux de LET élevé dans les tissus normaux.

Dans l'ensemble, cette étude de preuve de concept a montré que la pMBAT devrait combiner les avantages individuels de la pMBRT, à savoir l'effet de préservation du tissu normal associé au fractionnement spatial de la dose, et de la PAT, c'est-à-dire l'escalade de la dose et du LET. Ensuite, cette nouvelle technique devrait permettre d'augmenter encore l'indice thérapeutique obtenu dans les études précliniques de la pMBRT pour le traitement des tumeurs radiorésistantes en utilisant des schémas de traitement plus agressifs.

## Conclusions

Le travail réalisé au cours de cette thèse vise à contribuer au développement d'une nouvelle technique innovante aux perspectives prometteuses, à savoir la radiothérapie par minibélier à protons (pMBRT). Dans ce contexte, cette thèse a avancé les perspectives actuelles, à court et moyen terme de cette technique en (i) optimisant la pratique actuelle de la dosimétrie dans sa phase préclinique, (ii) évaluant sa mise en œuvre dans les essais cliniques à venir, et (iii) explorant ses développements futurs en combinaison avec d'autres approches de RT prometteuses.

Du point de vue de la physique, cette thèse a adapté les pratiques dosimétriques actuelles aux spécificités de cette technique en validant l'utilisation de différents détecteurs, en révélant la sensibilité des distributions de dose et en développant de nouveaux protocoles dosimétriques. Ces recherches ont fourni la base pour réaliser une dosimétrie reproductible dans les études précliniques, ce qui permettrait d'augmenter la quantité de données biologiques pour caractériser complètement le mécanisme radiobiologique impliqué dans la pMBRT.

D'un point de vue clinique, cette thèse a montré les bénéfiques potentiels de la pMBRT en clinique et a également mis en évidence la nécessité d'adapter les modèles radiobiologiques, les quantités dosimétriques et même les logiciels de planification des traitements aux spécificités de la pMBRT. Enfin, cette thèse ouvre également la

porte aux traitements multimodaux avec la pMBRT en prouvant la synergie de la combinaison de cette technique avec les thérapies d'arc.

En substance, cette thèse a contribué à la période de changements que nous vivons actuellement en RT, où les dogmes et hypothèses classiques sont remises en question pour ouvrir un nouveau paysage dans lequel nous pourrions développer de nouvelles conceptions et approches qui amélioreront le traitement du cancer.



# List of Figures

1.1	Five-year survival estimate for adults diagnosed with different cancer types in England as for 2019. Taken from [Nuffield Trust 2022]. . . .	4
1.2	Main photon interactions with matter. Taken from [Salvat 2015]. . .	6
1.3	Relative importance of the main interactions of photons with matter as a function of the photon energy and the atomic number of the absorber material. Taken from [Pawlicki <i>et al.</i> 2016]. . . . .	7
1.4	Main electron interactions with matter. Taken from [Salvat 2015]. . .	8
1.5	Depth dose profile of a proton beam measured with RCF (dotted blue line), calculated by Monte Carlo (dashed black line), the difference between measured and simulated doses (black squares), and corrected measured dose by using QCF (solid red line). Taken from [Anderson <i>et al.</i> 2019]. . . . .	16
1.6	LINAC operating in (a) electron and (b) X-ray mode. Taken from [Symonds <i>et al.</i> 2012]. . . . .	19
1.7	Representation of a multi-leaf collimator. Taken from [Jeraj & Robar 2004]. . . . .	20
1.8	Depth (a) dose and (b) LET distributions of different radiation beams at clinical energies in water. Taken from [Schneider 2020] and [Delorme <i>et al.</i> 2021], respectively. . . . .	24
1.9	Evolution of the penumbra of photon, proton, and carbon beams in depth. Taken from [Schneider 2020]. . . . .	26
1.10	(a) Schematic representation of a human cell, (b) DNA, and (c) the cell cycle. Taken from [Lodish <i>et al.</i> 2006]. . . . .	28
1.11	Representation of the processes involved in the physical, chemical, and biological stages and their timescale. . . . .	29
1.12	Representation of how two interactions (represented by red stars) can lead to SSBs and DSBs. The DNA double helix is represented in blue. In (a), interaction points are close together but in the same strand. In (b), they are in different strands but far away from each other. Both scenarios only cause the breakage of individual strands (SSBs). Contrarily, in (c), the interaction occurs in the two strands within 10 base pairs, causing the break of the bond between the two strands (DSB). . . . .	30
1.13	(a) Distribution of ionization events (represented by circles) of low- and high-LET radiation and (b) survival fraction for different LET particles. Adapted from [Symonds <i>et al.</i> 2012] and [Joiner & van der Kogel 2018], respectively. . . . .	31
1.14	Examples of DNA damage mis-repair and chromosome aberration formation. Adapted from [Sachs <i>et al.</i> 2004]. . . . .	31

1.15	Cell survival curves for different human tumor cell lines: HX142, HX58, HX156, and RT112 (from more to less radiosensitive) at a dose rate of 1.5 Gy/min. Adapted from [Steel <i>et al.</i> 1989]. . . . .	32
1.16	(a) Survival curves of cells at different phases of the cell cycle, and (b) variation of cell survival (i.e., radiosensitivity) through the cell cycle. Taken from [Joiner & van der Kogel 2018] and [McMahon 2018], respectively. . . . .	33
1.17	(a) Survival curves of tissues exposed to radiation under hypoxic and oxic conditions and (b) experimental determination of the OER dependence with LET. Adapted from [Joiner & van der Kogel 2018] and [Wenzl & Wilkens 2011], respectively. . . . .	34
1.18	Survival fraction curves of a treatment fractionated in N sessions and a single session schedule. $D_1$ and $D_N$ correspond to the dose of the 1- and N-fraction treatments to produce the same effect (2 % cell survival). The shoulders in the survival curve indicate the tissue repair and repopulation after each fraction. Adapted from [Withers 1975]. . . . .	36
1.19	Tolerance dose, defined as the dose that produces a 50 % probability of acute and late skin damage ( $ED_{50}$ ), as a function of the field size (irradiated area). Adapted from [Withers 1975]. . . . .	37
1.20	RBE-LET relationship at different cell surviving fractions (SF). Taken from [Joiner & van der Kogel 2018]. . . . .	39
1.21	(a) Dose-response of early and late responding tissues and (b) representation of the contribution of single-hit and multi-hit events to cell death. Taken from [Symonds <i>et al.</i> 2012] and adapted from [McMahon 2018], respectively . . . . .	40
1.22	Example of TCP (curve A) and NTCP (curve B) in a RT treatment. Taken from [Podgorsak <i>et al.</i> 2005]. . . . .	43
1.23	Schematic representation of the volumes considered for target delineation. . . . .	44
1.24	Relative dose (solid line), fluence (dotted line), and stopping power (dashed line) profiles in-depth in water for a 160 MeV proton beam. Adapted from [Garutti 2013]. . . . .	48
1.25	(a) Generation of the SOBP by adding pristine BP at different depths and weights, and (b) SOBP of different widths as a function of the number of pristine BP. Taken from [Paganetti 2018]. . . . .	49
1.26	Range (in $\text{g}\cdot\text{cm}^{-2}$ ) of a set of proton beams with incident energy from 69 to 231 MeV). Taken from [Paganetti 2018]). . . . .	50
1.27	Evolution of the beam width as a function of depth and beam energy. FWHM states for full-width at half maximum. Adapted from [Pedroni <i>et al.</i> 2005]. . . . .	50
1.28	Dose (dotted line) and total dose-averaged LET (dashed line) and dose-averaged LET for primary protons only (solid line). Taken from [Paganetti 2018]. . . . .	51

---

1.29	Schematic representation of a cyclotron. Taken from [Paganetti 2018].	52
1.30	Schematic representation of (a) a synchrotron and (b) its operating mode. BM: bending magnet, BMPi: bump magnet for injection, QF: quadrupole focusing magnet, QD: quadrupole defocusing magnet, RFC: radiofrequency cavity, ST: steering magnet, SX: sextupole magnet. Taken from [Paganetti 2018].	53
1.31	Schematic representation of a gantry and its dimensions. Taken from [Schippers <i>et al.</i> 2018].	54
1.32	Representation of the depth in the patient of 70-100 MeV proton beams (a) without and (b) with a range shifter (represented by a grey rectangle).	55
1.33	(a) Range modulator wheel composed of three different tracks and (b) a schematic representation of the principle of a range compensator. Taken from [Paganetti 2018]. (c) Range compensator (down) and brass collimator (top).	56
1.34	Schematic representation of a nozzle operating in (a) passive scattering and (b) active scanning mode.	57
1.35	Predicted yield of misrepaired and residual DSBs as a function of LET at doses of (a) 1, (b) 2, and (c) 5 Gy. Taken from [Henthorn <i>et al.</i> 2018].	58
1.36	Physical dose, biological dose considering a variable RBE (RBE-weighted dose), and LET for a 70 MeV proton beam. Adapted from [Wilkens & Oelfke 2004].	59
1.37	Dose distributions in intensity-modulated proton (IMPT) and photon (IMRT) therapy and dose differences between them. Treatments of (A) nasopharyngeal carcinoma and (B) adenoid cystic carcinoma of the hard palate. Taken from [Blanchard <i>et al.</i> 2018].	62
1.38	Schematic representation of beamlets spatially fractionated in (a) two and (b) one dimensions. The center-to-center (c-t-c) distance defines the distance between the center of two beamlets in each of those dimensions.	64
1.39	Representation of (a) lateral dose profiles and (b) dose distributions of different SFRT techniques, i.e., GRID therapy, MBRT, and MRT. The center-to-center (c-t-c) distance refers to the distance between two adjacent peak regions. Taken from [De Marzi <i>et al.</i> 2019b] and [Fernandez-Palomo <i>et al.</i> 2022].	66

1.40	(a) Conceptual representation of a 2D-GRID treatment delivery. Blue cylinders represent the beam collimation and the path of the resulting individual beamlets is displayed in yellow. (b) Representation of the fluence of beamlets arranged in orthogonal and hexagonal patterns. (c) Example of attenuation block attached to a LINAC head acting as a collimator. (d) and (e) shows examples of dose distributions in a GRID therapy treatment in the view orthogonal to the beam direction and in the beam-eye view, respectively. Adapted from (a) [Wu <i>et al.</i> 2010], (b) [Sammer <i>et al.</i> 2017], (c) [Mohiuddin <i>et al.</i> 1996], and (d and e) [Almendral <i>et al.</i> 2013]. . . . .	67
1.41	(a) Conceptual representation of a LRT treatment delivery. Blue lines represent individual fields converging on a small volume within the tumor to create high-dose vertices (displayed in yellow). (b) Example of dose distributions of a LRT treatment. Taken from [Wu <i>et al.</i> 2010].	69
1.42	Lateral and depth dose profiles produced by an array of five (a) X-ray, (b) proton, and (c) carbon minibeam (0.7 mm wide minibeam separated by 3.5 mm c-t-c distance) in a water phantom. Green and red dots illustrate the position of the peak and valley, respectively. Taken from [Schneider 2020]. . . . .	74
1.43	Summary of the effects in normal and tumor tissues caused by the distinct biological responses observed in SFRT. . . . .	76
1.44	Histological analysis of mice brain tissue irradiated with 1-mm and 25- $\mu$ m-wide deuteron beams. A increased tissue preservation is observed following the 25- $\mu$ m-wide beam irradiation as compared to 1-mm-wide beam. Taken from [Zeman <i>et al.</i> 1961]. . . . .	76
1.45	(a) Depth dose profile in water at peak and valley regions, (b) PVDR and (c) peak FWHM as a function of depth in water, and (d) lateral dose profiles at several depths in water of an array of seven 100 MeV minibeam. The slit width of the collimator considered is 400 $\mu$ m, and the c-t-c distance 2.8 mm. . . . .	80
1.46	Contribution of primary and secondary particles to (a) peak and (c) valley doses in-depth, and proportion of different species of secondary particles at (b) peaks and (d) valleys. An array of five minibeam (0.7 mm width; 3.5 mm c-t-c distance) and a monoenergetic 100 MeV field were considered. Taken from [Peucelle 2016]. . . . .	81
1.47	Dose distribution of a pMBRT plan for the treatment of a glioma. Adapted from [De Marzi <i>et al.</i> 2019b]. . . . .	81

1.48	Schematic representation of three methods for producing minibeam. (a) Multislit collimator: A collimator with several submillimetric apertures is placed in front of a seamless field to shape minibeam. (b) Magnetic focusing: A pair of quadrupole magnets, a reduced source-to-target distance, and a shorter drift space in the air allow focusing the proton beam up to submillimeter beamlet sizes. (c) Dynamic scanning collimator: A dynamic collimator creates single slits of the required shape and then moves a given distance (c-t-c distance) to produce other minibeam. In this method, the beam spot follows the shape of each aperture. . . . .	83
1.49	Schematic representation of a (a) planar and (b) pencil-shaped minibeam collimators. Adapted from [De Marzi <i>et al.</i> 2018] and [Charyyev <i>et al.</i> 2020], respectively. . . . .	84
1.50	(a) Survival curves of non-irradiated (controls) rats, and groups treated with standard proton therapy and pMBRT. (b) Example of dose distributions in a pMBRT treatment. The dotted black line represents the tumor depth. Taken from [Prezado <i>et al.</i> 2019]. . . . .	86
1.51	Dose distributions in a pMBRT treatment plan for (a) glioma and (b) meningioma cases. The planning target volume (PTV) is displayed in red color. Taken from [Lansonneur <i>et al.</i> 2020]. . . . .	87
2.1	ICPO PBS beamline: (1) exit window, (2) first ionization chamber, (3)-(4) scanning magnets, (5) second ion chamber, (6) snout holder, (7) snout, and (8) target volume. Taken from [De Marzi <i>et al.</i> 2019a].	90
2.2	Examples of collimators used in this work. (a) Five slit-collimator with 2.8 mm c-t-c distance (collimator 2 in Table 2.1), and (b) 16 x 20 mm <sup>2</sup> broad beam collimator (collimator 7 in Table 2.1), both for small animal irradiations. (c) Collimator with fifteen slits and 4 mm c-t-c distance for clinical purposes (collimator 8 in Table 2.1).	91
2.3	Representation of the collimator attachment into the snout for collimators dedicated to (a) small-animal irradiations (collimator 1 to 7 in Table 2.1) and (b) clinical trials (collimator 8 in Table 2.1).	92
2.4	Illustration of the volume-averaging effect in small-field conditions. The measurement over the sensitive area of the detector (5 mm) misrepresents the small-field dose distribution. Taken from [IAEA 2017]. . . . .	93
2.5	Representation of the microdiamond orientation for measuring pMBRT lateral dose profiles. The detector is placed on-edge (perpendicular to the minibeam direction) to take advantage of the micrometric size of the active area in this orientation. Taken from [Peucelle 2016]. . . . .	97
2.6	Examples of irradiated (a) EBT-XD and (b) OC-1 films. Films are presented in two orientations (facing up and down) to illustrate the transparency and opacity, respectively, of their protective coating. . .	98

2.7	(a) Examples of calibration curves for (a) EBT-XD and (b) OC-1 films in the red channel (with their associated 95 % confidence band). The corresponding functions are also presented at the top of the figure. . . . .	99
2.8	Representation of the vertical and horizontal orientations of pMBRT collimators. . . . .	101
2.9	Illustration of the skull extracted from an adult rat, preparation of the mold and pouring of tissue equivalent material, and rat phantom (from left to right images). Images courtesy of Dr. Dos Santos. . . . .	102
2.10	(a) Rat phantom, (b) CT of the phantom in the sagittal plane, and (c) experimental setup for the irradiations. . . . .	103
2.11	Representation of setups (a) 1, (b) 2, and (c) 3 for preclinical <i>in vivo</i> studies. Setups 1 and 2 consist of a unilateral array of proton minibeam. In setup 1, the tumor was irradiated at the plateau of the proton beam depth dose profile, whereas in setup 2, the Bragg peak was positioned at the tumor position. Setup 3 refers to a crossfire irradiation using two orthogonal arrays. . . . .	103
2.12	Rat treatment in setup 2, i.e., unilateral irradiation of the tumor at the Bragg peak position. . . . .	104
2.13	Organs-at-risk considered in rat treatments in the (a) lateral and (b) craniocaudal irradiations. The proton minibeam are represented in red color. . . . .	105
2.14	Example of the workflow for dose prescription in rat treatments. . . . .	106
2.15	Setup for cell irradiations. . . . .	107
2.16	TOPAS visualization of the ICPO PBS beamline. The components shown in the image are (1) vacuum window, (2) first ion chamber, (3)-(4) scanning (dipole) magnets, (5) second ion chamber, (6) snout holder, (7) snout and (8) target volume. . . . .	112
2.17	Variation of the (a) peak dose, (b) valley dose, and (c) simulation time as a function of the range cut. . . . .	114
2.18	Dose distributions computed by (a) ECLIPSE and (b) TOPAS for the same treatment plan. Taken from [Lansonneur <i>et al.</i> 2020]. . . . .	118
2.19	(a, b) Representation of the standard PTV delineation (in yellow color) and specific PTV definition, $PTV_{\text{optim}}$ , for pMBRT plan optimization (in blue color). (c) Resulting dose distributions of the plan optimization using the standard PTV and specific PTV ( $PTV_{\text{optim}}$ ). . . . .	118
3.1	Relative lateral dose profiles at (a) 0 and (b) 1 cm depth in water computed using MC simulations and measured with the microdiamond (MD) detector and the RAZOR diode. . . . .	123

---

3.2	Depth dose profiles of a 100 MeV proton beam in water calculated by MC and measured with the ppc05 ionization chamber and radiochromic films (EBT-XD and OC-1), and LET depth distribution calculated by MC. Broad beam conditions were considered for those measurements. . . . .	124
3.3	Quenching correction factors (QCF) as a function of (a) LET, and (b) depth for EBT-XD and OC-1 films. A 100 MeV proton beam and broad beam conditions were considered for those measurements. . . .	124
3.4	Lateral dose profiles at 0 cm depth in water measured with the microdiamond detector and EBT-XD and OC-1 films. The dose is expressed as Gy per 1000 MU for the sake of comparing the detectors employed at different dose ranges. The LET along the lateral profile is also displayed. . . . .	125
3.5	Lateral dose profiles at 0 cm depth in water simulated with MC and measured with the microdiamond (MD) detector, RAZOR diode, and OC-1 films. . . . .	125
3.6	Relative lateral dose profiles computed by MC simulations and measured with EBT-XD and OC-1 films at 0, 1, 2, 3, 4, 5, 6, and 7 cm depth in solid water. . . . .	127
3.7	Relative lateral dose profiles computed by means of MC simulations and measured with EBT-XD and OC-1 films at the Bragg peak position.	128
3.8	Relative lateral dose profiles measured with OC-1 and EBT-XD films and calculated by MC at the rat's skin and 1.6 cm depth in the rat phantom. . . . .	128
3.9	Lateral dose distributions in terms of Gy per 1000 MU measured with OC-1 and EBT-XD films at 1 cm depth in water. . . . .	129
3.10	Schematic representation of the parameters studied in the robustness analysis. . . . .	131
3.11	(a) Variation in peak-to-valley dose ratios (PVDRs) and peak and valley doses with respect to the reference scenario ( $0^\circ$ -tilt) as a function of the collimator tilt ( $\theta$ ). (b) Lateral dose profiles at a 1 cm depth in water for different collimator tilts with respect to the beamline. . . . .	133
3.12	Lateral dose profiles at a 1 cm depth in water for (a) different collimator translations with respect to the beamline and (b) different phantom tilt angles with respect to the collimator exit. Profiles were overlapped for the sake of comparing them. . . . .	133
3.13	Variation in peak-to-valley dose ratios (PVDRs) and peak and valley doses with respect to the reference scenario ( $c-t-c = 4$ mm, $\gamma = 0.125^\circ$ , and $w = 400$ $\mu\text{m}$ ; see Table 3.6) as a function of depth and (a) center-to-center ( $c-t-c$ ) distance, (b) slit divergence ( $\gamma$ ), and (c) slit width ( $w$ ). . . . .	135

3.14	Variation in peak-to-valley dose ratio (PVDRs) and peak and valley doses as a function of depth and air gap (a.g.) with respect to the reference scenario (5 cm a.g.). . . . .	135
3.15	Simulated lateral dose profiles at 0 cm depth in water for the vertical and horizontal orientation of the slits and a given pencil beam spot size. . . . .	137
3.16	Lateral dose distributions measured with OC-1 films at 0 cm depth in solid water for the vertical and horizontal orientation of the slits and given incidental beam angle to the collimator entrance. . . . .	139
3.17	Schematic representation of how the ionization chamber offsets influence the beamline angle with respect to the collimator. . . . .	140
3.18	Lateral dose profiles at 0 and 1 cm depths in water (a) before and (b) after the beam alignment. Dose profiles were calculated by Monte Carlo (MC) codes and measured with EBT-XD and OC-1 films, the RAZOR diode, and the microdiamond detector. . . . .	141
3.19	Schematic representation of experimental setups for dose determination prior to preclinical small-animal treatments using (a) a solid water phantom and (b) a heterogeneous phantom composed of solid water and lung equivalent material. . . . .	143
3.20	2D dose distributions in the rat's head from the craniocaudal view considering setup 1 (unilateral irradiation of the rat's brain in the plateau region; see Section 2.1.4.2) and collimators of (a) five slits and 2.8 mm c-t-c distance, (b) five slits and 2 mm c-t-c distance, (c) five slits and 4 mm c-t-c distance, and (d) 16 x 20 mm <sup>2</sup> aperture (collimators 2, 4, 5, and 7 in Table 2.1). The tumor depth is represented by a solid black line. . . . .	147
3.21	Lateral dose profiles at the tumor depth (see solid black line in Figure 3.20) considering setup 1 (unilateral irradiation of the rat's brain in the plateau region; see Section 2.1.4.2) and collimator numbers (a) 2, (b) 4, (c) 5, (d) 7 (see Table 2.1). The prescribed dose, in terms of the mean dose in the profile, was 30 Gy. . . . .	149
3.22	(a) 2D dose distribution in the rat's head from the craniocaudal view and (b) lateral dose profile at the tumor depth considering configuration 2 (see Section 2.1.4.2) and collimator 4 (see Table 2.1). The tumor position is represented by a dotted black line. . . . .	149
3.23	(a) 2D dose distribution in the rat's head from the craniocaudal view and (b) beam arrangement in configuration 3 (crossfire irradiation of the rat's brain in the plateau region; see Section 2.1.4.2) using collimator 2 (five slits separated by 2.8 mm c-t-c distance; see Table 2.1). The tumor implantation depth is represented by a dotted black line. . . . .	150

3.24	Comparison of the survival curves of the non-irradiated control (black line), standard proton therapy (green line), pMBRT delivered in one fraction (red line) or in two fractions using the same physical dose (blue line), and pMBRT delivered in two fractions prescribing an equivalent BED (brown line). . . . .	151
3.25	Representation of three different PVDR definitions, i.e., within the intersection of two valleys (PVDR <sub>1</sub> ), a peak and a valley (PVDR <sub>2</sub> ), or two peaks (PVDR <sub>3</sub> ) of different arrays. . . . .	151
3.26	Lateral dose profiles at the tumor depth for setup 3 (crossfire irradiation of the rat's brain in the plateau region; see Section 2.1.4.2) and collimator 2 (five slits separated by 2.8 mm c-t-c distance; see Table 2.1). The two profiles illustrate the lateral array intersecting (a) a valley and (b) a peak of the craniocaudal array. The prescribed dose, in terms of mean BED in two fractions, was 120 Gy (40 Gy physical dose). . . . .	152
3.27	Lateral dose profiles at the rat's skin measured with OC-1 films during treatments (EXP) and simulated using TOPAS (MC) considering setups 2 and 3. . . . .	153
3.28	(a) Example of a cell plate for <i>in vitro</i> investigations with only the four central wells filled by medium, and (b) experimental setup for pMBRT irradiations. . . . .	154
3.29	Relative dose profile at the cells' position in the pMBRT irradiations. The red square represents the area of the irradiated wells. . . . .	154
4.1	PTV and relevant OARs in (a) Case 1 (brain metastasis at the temporal lobe), (b) Case 2 (brain metastasis at the frontal lobe), Case 3 (liver metastasis), and Case 4 (lung metastasis). . . . .	161
4.2	Field arrangement in (a) Case 1 (brain metastasis at the temporal lobe), (b) Case 2 (brain metastasis at the frontal lobe), Case 3 (liver metastasis), and Case 4 (lung metastasis). . . . .	162
4.3	Schematic representation of a crossfire geometry. The two minibeam arrays are interlaced, forming an angle of 90° between the two peak-valley patterns. . . . .	163
4.4	Examples of dose distributions of the (a) SRT, (b) PT and (c) pMBRT plans in Case 1. The PTV is displayed in yellow, the brainstem in green, and the acoustic nerve in red. . . . .	166
4.5	Examples of dose distributions of the (a) SRT, (b) PT and (c) pMBRT plans in Case 2. The PTV is displayed in yellow, the brainstem in green, and the cochlea in light blue . . . . .	167
4.6	Examples of dose distributions of the (a) SRT, (b) PT and (c) pMBRT plans in Case 3. The PTV is displayed in yellow, the heart in red, and the superior vena cava in blue. . . . .	168

4.7	Examples of dose distributions of the (a) SRT, (b) PT and (c) pMBRT plans in Case 4. The PTV is displayed in yellow, the heart in light blue, and the superior vena cava in pink. . . . .	169
4.8	Comparison of dose-volume histograms in Case 1 for the SRT plans (solid line), pMBRT treatments B (dotted line), and C (dashed line). The dose presented corresponds to the physical dose normalized to the prescribed dose (mean dose to PTV). . . . .	170
4.9	Comparison of dose-volume histograms in Case 2 for the SRT plans (solid line), pMBRT treatments B (dotted line), and C (dashed line). The dose presented corresponds to the physical dose normalized to the prescribed dose (mean dose to PTV). . . . .	171
4.10	Comparison of dose-volume histograms in Case 3 for the SRT plans (solid line), pMBRT treatments B (dotted line), and C (dashed line). The dose presented corresponds to the physical dose normalized to the prescribed dose (mean dose to PTV). . . . .	171
4.11	Comparison of dose-volume histograms in Case 4 for the SRT plans (solid line), pMBRT treatments B (dotted line), and C (dashed line). The dose presented corresponds to the physical dose normalized to the prescribed dose (mean dose to PTV). . . . .	171
4.12	Lateral dose profiles at the PTV in (a) Case 1, (b) Case 2, (c) Case 3, and (d) Case 4 for pMBRT plans B and C. Profiles considered are represented by a solid white line in Figures 4.4 to 4.7. . . . .	172
4.13	BED to OARs in Cases 1 to 4 in SRT, PT, and pMBRT plans. SVC stands for superior vena cava and P.A for pulmonary artery. . . . .	173
4.14	Illustration of the effect of collimator rotation (i.e., planar minibeam orientation) in dose distributions. In subfigure (a), the direction of the peak-valley pattern follows the direction of maximum PTV extension (i.e., collimator rotation of $45^\circ$ ), while in subfigure (b), it is parallel to the direction of OAR-PTV intersection (i.e., collimator rotation of $90^\circ$ ). The arrow in (b) represents the direction of translation of the planar minibeam. . . . .	179
4.15	DVH of the PTV in the reference scenario (collimator rotation of $45^\circ$ and no slit translation), the 3 mm-slit translation scenario (collimator rotation of $90^\circ$ ), and $90^\circ$ -slit rotation situation (no slit translation). . . . .	180
4.16	Dose distributions in Case 3 plan C (see Sections 4.2 and 4.3.2) for field number 2 (see Table 4.1). . . . .	181
5.1	Representation of the PTV (solid orange line) in the axial and sagittal view of the patient CT. . . . .	187
5.2	Beam arrangement in the (a) single-array pMBRT and (b) PAT and pMBAT plans. In (b), a schematic sketch of the rotation of the slits is presented. . . . .	187
5.3	(a) Coronal, (b) sagittal views of pMBAT dose distributions, and (c) sagittal view zoomed in. . . . .	189

---

5.4	PVDRs at different depths along the beam path in the pMBRT and pMBAT treatments. The profile considered to evaluate PVDRs is represented by a solid white line in Figure 5.3a. . . . .	189
5.5	Dose reduction to normal tissue at peak and valley regions as a function of depth in pMBAT with respect to the pMBRT scenario. The profile considered to evaluate the dose reduction is represented by a solid white line in Figure 5.3a. . . . .	191
5.6	Depth dose profiles at (a) peak and (b) valleys positions in pMBRT and pMBAT treatments. The 13 arrays composing the pMBAT plan are presented by solid green lines. The origin of the axis of abscissas (depth) is at the PTV position. Doses are normalized to the maximum dose at peaks and valleys, respectively. . . . .	191
5.7	Depth dose profiles at (a) peak and (b) valleys positions in the pMBRT, PAT, and pMBAT scenarios. The profile considered is represented by a white dotted line in Figure 5.3a. Doses are normalized to the maximum dose at peaks and valleys, respectively. . . . .	192
5.8	DVH in pMBRT, PAT, and pMBAT treatments for the PTV and normal brain tissue. (b) Zoomed in view of (a). Doses are normalized to the same average dose to the PTV. . . . .	193
5.9	Coronal and sagittal views of LET <sub>d</sub> distributions in (a,b) pMBAT and (c,d) pMBRT treatments. . . . .	194
5.10	Coronal view of the pMBAT dose distributions considering a different number of arrays forming the arc, i.e., (a) 13, (b) 11, (c) 9, and 7 arrays. . . . .	195
5.11	Dose reduction to normal tissues in pMBAT with respect to pMBRT as a function of depth and (a) number of arrays forming the arc, (b) separation between arrays, (c) c-t-c distance, and (d) PTV diameter. . . . .	196
5.12	Coronal view of the pMBAT dose distributions considering a different angular separation between the fields that form the arc, i.e., (a) 10, (b) 15, and (c) 20°. . . . .	196



# List of Tables

1.1	Dynamic dose range of EBT-3, EBT-XD, MD-V3 GAFchromic films (Ashland, USA), and OC-1 OrthoChromic films (OrthoChrome, USA), as reported by manufacturers. . . . .	15
1.2	Summary of proton interactions, targets, secondary particles produced, influence on incident particles, and effect on dose distributions. p+, e-, and n stand for proton, electron, and neutron. Adapted from [Newhauser & Zhang 2015]. . . . .	47
1.3	Sources of range uncertainty and magnitudes. Adapted from [Paganetti 2012]. . . . .	61
1.4	Summary of the main characteristics of GRID therapy, LRT, MBRT, and MRT. Adapted from [Prezado 2022]. . . . .	66
2.1	Specifications of collimators employed in the implementation of pMBRT at the ICPO. *c-t-c stands for centre-to-centre. . . . .	92
2.2	Description of the configurations considered in small-animal preclinical studies. Collimators are described in Table 2.1. . . . .	105
3.1	PVDR and peak FWHM of pMBRT lateral dose distributions simulated by MC codes and measured with the RAZOR diode and microdiamond (MD) detector at 0 and 1 cm depth in water. . . . .	123
3.2	PVDR and peak FWHM at 0 cm depth in water calculated by MC and measured with OC-1 films, the RAZOR diode, and the microdiamond (MD) detector. . . . .	125
3.3	PVDR measured with EBT-XD and OC-1 films and simulated by TOPAS (MC) at 0, 1, 2, 3, 4, 5, 6, and 7 cm depth in solid water. . . . .	126
3.4	PVDR and peak FWHM at the rat's skin (0 cm depth) and 1.6 cm depth in the rat phantom calculated by MC and measured with OC-1 and EBT-XD films. . . . .	128
3.5	Dose rates (as Gy per 1000 MU) at peak and valley regions and on average over the whole profile. Dose rates were measured with a ppc05 ionization chamber (IC) and OC-1 and EBT-XD films in pMBRT and broad beam (BB) conditions. . . . .	129
3.6	Values considered for the parameters evaluated. * indicates the reference values. c-t-c and CID stand for center-to-center and collimator-isocenter distance, respectively. . . . .	131
3.7	Variation of peak, valley, and mean doses, PVDR, and peak FWHM in different spot size conditions compared to reference condition 6, where the pencil beam spot is symmetrical. The spot size is expressed as $\sigma_x$ and $\sigma_y$ values. Values in this table correspond to a lateral profile at 0 cm depth. . . . .	136

3.8	Maximum variation of the peak-to-valley dose ratio (PVDR), peak FWHM, and peak, valley, and average doses for a given variation in the evaluated parameters. . . . .	138
3.9	Synopsis of the dosimetry guidelines. . . . .	142
3.10	Mean, peak, and valley doses, PVDRs, and peak FWHM at the skin, 1 cm depth in the rat's head, and the tumor implantation depth for 30 Gy prescribed mean dose. The setup considered was the number 1 (unilateral irradiation of the rat's brain in the plateau region; see Section 2.1.4.2) and collimator numbers 2, 4, 5, and 7 (see Table 2.1) were employed. . . . .	148
3.11	Mean, peak, and valley doses, PVDRs, and peak FWHM at the skin, 1 cm depth in the rat's head, and the tumor implantation depth for 25 Gy prescribed mean dose. The setup considered was the number 2 (see Section 2.1.4.2) and collimator 4 (see Table 2.1) was employed. . . . .	150
3.12	PVDRs and peak and valley doses at the skin, 1 cm depth in the rat's head, and the tumor implantation depth for 120 Gy prescribed mean biological equivalent dose. The setup considered was number 3 (crossfire irradiation of the rat's brain in the plateau region; see Section 2.1.4.2) and collimator 2 (five slits separated by 2.8 mm c-t-c distance; see Table 2.1) was employed. . . . .	152
3.13	PVDR, peak FWHM, and average, peak, and valley doses in the broad beam (BB) and minibeam (MB) irradiations for 2, 5, 10, and 20 Gy mean dose. . . . .	154
4.1	Field specifications in pMBRT treatments. . . . .	163
4.2	Treatment plans evaluated in this study. SRT treatments are denoted by the label A, pMBRT plans considering a uniform dose to the target by the letter B, pMBRT plans delivering a quasi-homogeneous dose distribution to the PTV by the letter C, and PT plans by D. VMAT stands for volumetric modulated arc therapy, DCAT for dynamic conformal arc therapy, and c-t-c for center-to-center. . . . .	164
4.3	Comparison of dosimetric indexes defining the target coverage in the SRT, PT, and pMBRT treatments. . . . .	170
4.4	OAR dose limits defined in the TG-101 report and values obtained in pMBRT treatments in Case 1. The <i>point</i> volume is defined as $\leq 0.035 \text{ cm}^3$ . . . . .	176
4.5	OAR dose limits defined in the TG-101 report and values obtained in pMBRT treatments in Case 3. The <i>point</i> volume is defined as $\leq 0.035 \text{ cm}^3$ . *SVC stands for superior vena cava. . . . .	177
4.6	OAR dose limits defined in the TG-101 report and values obtained in pMBRT treatments in Case 4. The <i>point</i> volume is defined as $\leq 0.035 \text{ cm}^3$ . . . . .	177

---

5.1 PVDRs in normal tissues as a function of depth in the pMBRT and pMBAT plans. PVDR values were computed along the solid white line in Figure 5.3a. . . . . 189



# Bibliography

- [Adam *et al.* 2022] Jean-François Adam, Jacques Balosso, Sam Bayat, Paul Berkvens, Gilles Berruyer, Elke Bräuer-Krisch, Thierry Brochard, Gabriel Chamel, Andréa Desagneaux, Renaud Drevon-Gaudet *et al.* *Toward Neuro-Oncologic Clinical Trials of High-Dose-Rate Synchrotron Microbeam Radiation Therapy: First Treatment of a Spontaneous Canine Brain Tumor.* International Journal of Radiation Oncology\* Biology\* Physics, vol. 113, no. 5, pages 967–973, 2022. (Cited on page 71.)
- [Agostinelli *et al.* 2003] Sea Agostinelli, John Allison, K al Amako, John Apostolakis, H Araujo, Pedro Arce, Makoto Asai, D Axen, Swagato Banerjee, GJNi Barrantet *et al.* *GEANT4—a simulation toolkit.* Nuclear instruments and methods in physics research section A: Accelerators, Spectrometers, Detectors and Associated Equipment, vol. 506, no. 3, pages 250–303, 2003. (Cited on pages 108 and 109.)
- [Aitken & Hawkins 2015] KL Aitken and MA Hawkins. *Stereotactic body radiotherapy for liver metastases.* Clinical oncology, vol. 27, no. 5, pages 307–315, 2015. (Cited on pages 22, 160, 175 and 178.)
- [Akhavanallaf *et al.* 2021] Azadeh Akhavanallaf, Reza Mohammadi, Isaac Shiri, Yazdan Salimi, Hossein Arabi and Habib Zaidi. *Personalized brachytherapy dose reconstruction using deep learning.* Computers in biology and medicine, vol. 136, page 104755, 2021. (Cited on page 17.)
- [Al-Rawi *et al.* 2022] Salam Abdulrazzaq Ibrahim Al-Rawi, Hassan Abouelenein, Magdy Mohammed Khalil, Haidar Hamza Alabdei, Awf Abdulrahman Sulaiman, Dalya Saad Al-Nuaimi and Mohamed El-Sayed EL Nagdy. *Evaluation of Conformity and Homogeneity Indices Consistency Throughout the Course of Head and Neck Cancer Treatment With and Without Using Adaptive Volumetric Modulated Arc Radiation Therapy.* Advances in radiation oncology, vol. 7, no. 5, page 100905, 2022. (Cited on page 169.)
- [Alfieri *et al.* 2001] Sergio Alfieri, Alessio G Morganti, Andrea Di Giorgio, Vincenzo Valentini, Maurizio Bossola, Lucio Trodella, Numa Cellini and Giovanni Battista Doglietto. *Improved survival and local control after intraoperative radiation therapy and postoperative radiotherapy: a multivariate analysis of 46 patients undergoing surgery for pancreatic head cancer.* Archives of Surgery, vol. 136, no. 3, pages 343–347, 2001. (Cited on page 17.)
- [Ali *et al.* 2019] Faisal S Ali, Octavio Arevalo, Soheil Zorofchian, Anthony Patrizz, Roy Riascos, Nitin Tandon, Angel Blanco, Leomar Y Ballester and Yoshua Esquenazi. *Cerebral radiation necrosis: incidence, pathogenesis, diagnostic challenges, and future opportunities.* Current oncology reports, vol. 21, no. 8, pages 1–17, 2019. (Cited on pages 86 and 160.)
- [Allison *et al.* 2016] J Allison, Katsuya Amako, John Apostolakis, Pedro Arce,

- M Asai, T Aso, E Bagli, A Bagulya, S Banerjee, GJNI Barrant *et al.* *Recent developments in Geant4*. Nuclear instruments and methods in physics research section A: Accelerators, Spectrometers, Detectors and Associated Equipment, vol. 835, pages 186–225, 2016. (Cited on page 109.)
- [Almendral *et al.* 2013] Pedro Almendral, Pedro J Mancha and Daniel Roberto. *Feasibility of a simple method of hybrid collimation for megavoltage grid therapy*. Medical Physics, vol. 40, no. 5, page 051712, 2013. (Cited on pages 67 and 218.)
- [Almond *et al.* 1999] Peter R Almond, Peter J Biggs, Bert M Coursey, William F Hanson, M Saiful Huq, Ravinder Nath and David WO Rogers. *AAPM's TG-51 protocol for clinical reference dosimetry of high-energy photon and electron beams*. Medical physics, vol. 26, no. 9, pages 1847–1870, 1999. (Cited on page 11.)
- [Alongi *et al.* 2012] Filippo Alongi, Stefano Arcangeli, Andrea Riccardo Filippi, Umberto Ricardi and Marta Scorsetti. *Review and uses of stereotactic body radiation therapy for oligometastases*. The oncologist, vol. 17, no. 8, pages 1100–1107, 2012. (Cited on pages 173 and 198.)
- [Amendola *et al.* 2010] Beatriz Amendola, Naipy Perez, Marco A Amendola, Xiaodong Wu, Mansoor M Ahmed, Alejandro J Iglesias, Richard Estape, Nicholas Lambrou and Pietro Bortoletto. *Lattice radiotherapy with RapidArc for treatment of gynecological tumors: Dosimetric and early clinical evaluations*. Cureus, vol. 2, no. 9, 2010. (Cited on page 69.)
- [Amendola *et al.* 2018] Beatriz E Amendola, Naipy C Perez, Xiaodong Wu, Jesus Manuel Blanco Suarez, Jiade J Lu and Marco Amendola. *Improved outcome of treating locally advanced lung cancer with the use of Lattice Radiotherapy (LRT): A case report*. Clinical and translational radiation oncology, vol. 9, pages 68–71, 2018. (Cited on page 69.)
- [Amendola *et al.* 2019] Beatriz E Amendola, Naipy C Perez, Xiaodong Wu, Marco A Amendola and Ian Z Qureshi. *Safety and efficacy of lattice radiotherapy in voluminous non-small cell lung cancer*. Cureus, vol. 11, no. 3, 2019. (Cited on page 69.)
- [American Cancer Society 2022] American Cancer Society. *Cancer Facts and Figures 2022*, 2022. (Cited on pages 3 and 201.)
- [Anderson & Simon 2020] Nicole M Anderson and M Celeste Simon. *The tumor microenvironment*. Current Biology, vol. 30, no. 16, pages R921–R925, 2020. (Cited on page 27.)
- [Anderson *et al.* 2019] Sarah E Anderson, Michael P Grams, H Wan Chan Tseung, Keith M Furutani and Chris J Beltran. *A linear relationship for the LET-dependence of Gafchromic EBT3 film in spot-scanning proton therapy*. Physics in Medicine & Biology, vol. 64, no. 5, page 055015, 2019. (Cited on pages 15, 16 and 215.)
- [Apostolakis *et al.* 2007] John Apostolakis, Dennis H Wright and Geant4 Collaboration. *An overview of the GEANT4 toolkit*. AIP Conference

- Proceedings, vol. 896, no. 1, pages 1–10, 2007. (Cited on page 109.)
- [Ares *et al.* 2009] Carmen Ares, Eugen B Hug, Antony J Lomax, Alessandra Bolsi, Beate Timmermann, Hans Peter Rutz, Jan C Schuller, Eros Pedroni and Gudrun Goitein. *Effectiveness and safety of spot scanning proton radiation therapy for chordomas and chondrosarcomas of the skull base: first long-term report*. International Journal of Radiation Oncology\* Biology\* Physics, vol. 75, no. 4, pages 1111–1118, 2009. (Cited on page 61.)
- [Arnold *et al.* 2018] Kimberly M Arnold, Nicole J Flynn, Adam Raben, Lindsay Romak, Yan Yu, Adam P Dicker, Firas Mourrada and Jennifer Sims-Mourrada. *The impact of radiation on the tumor microenvironment: effect of dose and fractionation schedules*. Cancer growth and metastasis, vol. 11, page 1179064418761639, 2018. (Cited on page 36.)
- [Arruebo *et al.* 2011] Manuel Arruebo, Nuria Vilaboa, Berta Sáez-Gutierrez, Julio Lambea, Alejandro Tres, Mónica Valladares and África González-Fernández. *Assessment of the evolution of cancer treatment therapies*. Cancers, vol. 3, no. 3, pages 3279–3330, 2011. (Cited on page 3.)
- [Asperud *et al.* 2021] Jonas Asperud, Delmon Arous, Nina Frederike Jeppesen Edin and Eirik Malinen. *Spatially fractionated radiotherapy: tumor response modelling including immunomodulation*. Phys. Med. Biol., vol. 66, no. 17, page 175012, August 2021. Publisher: IOP Publishing. (Cited on page 183.)
- [ASTRO 2022] ASTRO. *Proton Beam Therapy Model Policy*. ASTRO Model Policies, 2022. (Cited on page 61.)
- [Asur *et al.* 2012] Rajalakshmi S Asur, Sunil Sharma, Ching-Wei Chang, Jose Penagaricano, Indira M Kommuru, Eduardo G Moros, Peter M Corry and Robert J Griffin. *Spatially fractionated radiation induces cytotoxicity and changes in gene expression in bystander and radiation adjacent murine carcinoma cells*. Radiation research, vol. 177, no. 6, pages 751–765, 2012. (Cited on pages 38 and 77.)
- [Atkins *et al.* 2018] Katelyn M Atkins, Itai M Pashtan, Marc R Bussière, Kylie H Kang, Andrzej Niemierko, Jillian E Daly, Thomas M Botticello, Molly C Hurd, Paul H Chapman, Kevin Oh *et al.* *Proton stereotactic radiosurgery for brain metastases: a single-institution analysis of 370 patients*. International Journal of Radiation Oncology\* Biology\* Physics, vol. 101, no. 4, pages 820–829, 2018. (Cited on pages 22, 86 and 179.)
- [Bahreyni & Koshbin 2004] T Bahreyni and Khoshnazar AR Koshbin. *Measurement of stereotactic beam data of 9 MV X-rays using diode detector*. International Journal of radiation research, 2004. (Cited on page 14.)
- [Barkova & Kholin 1971] AM Barkova and VV Kholin. *Theoretical calculation of the spatial distribution of a Co 60 gamma radiation dose field under a grid*. Meditsinskaia radiologiya, vol. 16, no. 11, pages 64–70, 1971. (Cited on page 65.)
- [Bartzsch *et al.* 2020] Stefan Bartzsch, Stéphanie Corde, Jeffrey C Crosbie, Liam Day, Mattia Donzelli, Michael Krisch, Michael Lerch, Paolo Pelliccioli,

- Lloyd ML Smyth and Moeava Tehei. *Technical advances in x-ray microbeam radiation therapy*. Physics in Medicine & Biology, vol. 65, no. 2, page 02TR01, 2020. (Cited on page 70.)
- [Baskar & Itahana 2017] Rajamanickam Baskar and Koji Itahana. *Radiation therapy and cancer control in developing countries: Can we save more lives?* International journal of medical sciences, vol. 14, no. 1, page 13, 2017. (Cited on pages 1 and 3.)
- [Baskar *et al.* 2012] Rajamanickam Baskar, Kuo Ann Lee, Richard Yeo and Kheng-Wei Yeoh. *Cancer and radiation therapy: current advances and future directions*. International journal of medical sciences, vol. 9, no. 3, page 193, 2012. (Cited on page 3.)
- [Bazyar *et al.* 2017] Soha Bazyar, Christina R Inscoc, E Timothy O'Brian, Otto Zhou and Yueh Z Lee. *Minibeam radiotherapy with small animal irradiators; in vitro and in vivo feasibility studies*. Physics in Medicine & Biology, vol. 62, no. 23, page 8924, 2017. (Cited on page 72.)
- [Beddar 2006] AS Beddar. *Plastic scintillation dosimetry and its application to radiotherapy*. Radiation Measurements, vol. 41, pages S124–S133, 2006. (Cited on page 16.)
- [Benedict *et al.* 2010] Stanley H Benedict, Kamil M Yenice, David Followill, James M Galvin, William Hinson, Brian Kavanagh, Paul Keall, Michael Lovelock, Sanford Meeks, Lech Papiez *et al.* *Stereotactic body radiation therapy: the report of AAPM Task Group 101*. Medical physics, vol. 37, no. 8, pages 4078–4101, 2010. (Cited on pages 119 and 176.)
- [Berger *et al.* 1975] MJ Berger, SM Seltzer, SR Domen and PJ Lamperti. *Stopping-power ratios for electron dosimetry with ionization chambers*. In Biomedical dosimetry. National Bureau of Standards, 1975. (Cited on page 108.)
- [Bertho *et al.* 2021a] A. Bertho, E. Brisebard, M. Juchaux, C. Gilbert, C. Lamirault, A. Patriarca, L. De Marzi, F. Pouzoulet and Y. Prezado. *PD-0763 Role of the immune system in anti-tumoral response to proton minibeam radiation therapy*. Radiotherapy and Oncology, vol. 161, page S593, August 2021. (Cited on page 78.)
- [Bertho *et al.* 2021b] Annaïg Bertho, Ramon Ortiz, Marjorie Juchaux, Cristèle Gilbert, Charlotte Lamirault, Frederic Pouzoulet, Laura Polledo, Alethea Liens, Nils Warfving, Catherine Sebriet *et al.* *First evaluation of temporal and spatial fractionation in proton minibeam radiation therapy of glioma-bearing rats*. Cancers, vol. 13, no. 19, page 4865, 2021. (Cited on pages 2, 84, 85, 138, 150, 162, 165, 182, 183, 185 and 188.)
- [Bertho *et al.* 2022] Annaïg Bertho, Lorea Iturri, Elise Brisebard, Marjorie Juchaux, Cristèle Gilbert, Ramon Ortiz, Catherine Sebrie, Laurene Jourdain, Charlotte Lamirault, Gabriel Ramasamy *et al.* *Evaluation of the role of the immune system response following minibeam radiation therapy*. International Journal of Radiation Oncology\* Biology\* Physics, 2022. (Cited on pages 75 and 77.)

- [Bertho 2022] Annaïg Bertho. Early cellular response to pMBRT: a mechanistic study. PTCOG 2022, 2022. (Cited on pages 91 and 153.)
- [Bethe 1930] Hans Bethe. *Zur theorie des durchgangs schneller korpuskularstrahlen durch materie*. Annalen der Physik, vol. 397, no. 3, pages 325–400, 1930. (Cited on page 47.)
- [Bijl *et al.* 2003] Hendrik P Bijl, Peter van Luijk, Rob P Coppes, Jacobus M Schippers, Antonius WT Konings and Albert J van der Kogel. *Unexpected changes of rat cervical spinal cord tolerance caused by inhomogeneous dose distributions*. International Journal of Radiation Oncology\* Biology\* Physics, vol. 57, no. 1, pages 274–281, 2003. (Cited on page 37.)
- [Billena & Khan 2019] Cole Billena and Atif J Khan. *A current review of spatial fractionation: Back to the future?* International Journal of Radiation Oncology\* Biology\* Physics, vol. 104, no. 1, pages 177–187, 2019. (Cited on pages 2, 63, 67, 68 and 69.)
- [Blanchard *et al.* 2018] Pierre Blanchard, Gary Brandon Gunn, Alexander Lin, Robert L Foote, Nancy Y Lee and Steven J Frank. *Proton therapy for head and neck cancers*. Seminars in radiation oncology, vol. 28, no. 1, pages 53–63, 2018. (Cited on pages 62 and 217.)
- [Bloch 1933] Felix Bloch. *Zur bremsung rasch bewegter teilchen beim durchgang durch materie*. Annalen der Physik, vol. 408, no. 3, pages 285–320, 1933. (Cited on page 47.)
- [Böhlen *et al.* 2014] TT Böhlen, Francesco Cerutti, MPW Chin, Alberto Fassò, Alfredo Ferrari, P Garcia Ortega, Andrea Mairani, Paola R Sala, George Smirnov and Vasilis Vlachoudis. *The FLUKA code: developments and challenges for high energy and medical applications*. Nuclear data sheets, vol. 120, pages 211–214, 2014. (Cited on page 108.)
- [Bolst *et al.* 2017] David Bolst, Giuseppe AP Cirrone, Giacomo Cuttone, Gunter Folger, Sebastien Incerti, Vladimir Ivanchenko, Tatsumi Koi, Davide Mancusi, Luciano Pandola, Francesco Romano *et al.* *Validation of Geant4 fragmentation for heavy ion therapy*. Nuclear Instruments and Methods in Physics Research Section A: Accelerators, Spectrometers, Detectors and Associated Equipment, vol. 869, pages 68–75, 2017. (Cited on page 110.)
- [Bouchet *et al.* 2010] Audrey Bouchet, Benjamin Lemasson, Géraldine Le Duc, Cécile Maisin, Elke Bräuer-Krisch, Erik Albert Siegbahn, Luc Renaud, Enam Khalil, Chantal Rémy, Cathy Poillot *et al.* *Preferential effect of synchrotron microbeam radiation therapy on intracerebral 9L gliosarcoma vascular networks*. International Journal of Radiation Oncology\* Biology\* Physics, vol. 78, no. 5, pages 1503–1512, 2010. (Cited on page 75.)
- [Bouchet *et al.* 2013] Audrey Bouchet, Nathalie Sakakini, Michèle El Atifi, Céline Le Clec’h, Elke Brauer, Anaïck Moisan, Pierre Deman, Pascal Rihet, Géraldine Le Duc and Laurent Pelletier. *Early gene expression analysis in 9L orthotopic tumor-bearing rats identifies immune modulation in molecular response to synchrotron microbeam radiation therapy*. PLoS One, vol. 8,

- no. 12, page e81874, 2013. (Cited on pages 75 and 77.)
- [Bouchet *et al.* 2015] Audrey Bouchet, Raphaël Serduc, Jean Albert Laissue and Valentin Djonov. *Effects of microbeam radiation therapy on normal and tumoral blood vessels*. *Physica Medica*, vol. 31, no. 6, pages 634–641, 2015. (Cited on pages 71 and 75.)
- [Bouchet *et al.* 2016] Audrey Bouchet, Elke Bräuer-Krisch, Yolanda Prezado, Michèle El Atifi, Léonid Rogalev, Céline Le Clec’h, Jean Albert Laissue, Laurent Pelletier and Géraldine Le Duc. *Better efficacy of synchrotron spatially microfractionated radiation therapy than uniform radiation therapy on glioma*. *International Journal of Radiation Oncology\* Biology\* Physics*, vol. 95, no. 5, pages 1485–1494, 2016. (Cited on pages 71 and 77.)
- [Bourhis *et al.* 2019] Jean Bourhis, Wendy Jeanneret Sozzi, Patrik Gonçalves Jorge, Olivier Gaide, Claude Bailat, Frédéric Duclos, David Patin, Mahmut Ozsahin, François Bochud, Jean-François Germond *et al.* *Treatment of a first patient with FLASH-radiotherapy*. *Radiotherapy and oncology*, vol. 139, pages 18–22, 2019. (Cited on page 202.)
- [Boustani *et al.* 2019] Jihane Boustani, Mathieu Grapin, Pierre-Antoine Laurent, Lionel Apetoh and Céline Mirjolet. *The 6th R of radiobiology: reactivation of anti-tumor immune response*. *Cancers*, vol. 11, no. 6, page 860, 2019. (Cited on pages 29, 34 and 42.)
- [Brábek *et al.* 2010] Jan Brábek, Claudia T Mierke, Daniel Rösel, Pavel Veselý and Ben Fabry. *The role of the tissue microenvironment in the regulation of cancer cell motility and invasion*. *Cell communication and signaling*, vol. 8, no. 1, pages 1–8, 2010. (Cited on page 27.)
- [Brace *et al.* 2020] Owen J Brace, Sultan F Alhujaili, Jason R Paino, Duncan J Butler, Dean Wilkinson, Brad M Oborn, Anatoly B Rosenfeld, Michael LF Lerch, Marco Petasecca and Jeremy A Davis. *Evaluation of the PTW microDiamond in edge-on orientation for dosimetry in small fields*. *Journal of Applied Clinical Medical Physics*, vol. 21, no. 8, pages 278–288, 2020. (Cited on page 14.)
- [Brahme *et al.* 1980] A Brahme, T Kraepelien and H Svensson. *Electron and photon beams from a 50 MeV racetrack microtron*. *Acta Radiologica: Oncology*, vol. 19, no. 4, pages 305–319, 1980. (Cited on page 204.)
- [Brandner *et al.* 2017] Edward D Brandner, Indrin J Chetty, Tawfik G Giaddui, Ying Xiao and M Saiful Huq. *Motion management strategies and technical issues associated with stereotactic body radiotherapy of thoracic and upper abdominal tumors: a review from NRG oncology*. *Medical physics*, vol. 44, no. 6, pages 2595–2612, 2017. (Cited on page 179.)
- [Bräuer-Krisch *et al.* 2010] Elke Bräuer-Krisch, Raphaël Serduc, EA Siegbahn, Géraldine Le Duc, Yolanda Prezado, Alberto Bravin, Hans Blattmann and JA Laissue. *Effects of pulsed, spatially fractionated, microscopic synchrotron X-ray beams on normal and tumoral brain tissue*. *Mutation Research/Reviews in Mutation Research*, vol. 704, no. 1-3, pages 160–166,

2010. (Cited on page 71.)
- [Brenner 2008] David J. Brenner. *The Linear-Quadratic Model Is an Appropriate Methodology for Determining Isoeffective Doses at Large Doses Per Fraction*. Seminars in Radiation Oncology, vol. 18, no. 4, pages 234–239, October 2008. (Cited on pages 41, 175, 181 and 182.)
- [Burigo *et al.* 2019] Lucas N Burigo, José Ramos-Méndez, Mark Bangert, Reinhard W Schulte and Bruce Faddegon. *Simultaneous optimization of RBE-weighted dose and nanometric ionization distributions in treatment planning with carbon ions*. Physics in Medicine & Biology, vol. 64, no. 1, page 015015, 2019. (Cited on page 203.)
- [Burke *et al.* 2017] Elisa Burke, Daniela Poppinga, Andreas A Schoenfeld, Dietrich Harder, Bjoern Poppe and Hui Khee Looe. *The practical application of scintillation dosimetry in small-field photon-beam radiotherapy*. Zeitschrift für Medizinische Physik, vol. 27, no. 4, pages 324–333, 2017. (Cited on page 16.)
- [Calvo *et al.* 2006] Felipe A Calvo, Rosa M Meirino and Roberto Orecchia. *Intraoperative radiation therapy: First part: Rationale and techniques*. Critical reviews in oncology/hematology, vol. 59, no. 2, pages 106–115, 2006. (Cited on page 17.)
- [Carabe-Fernandez *et al.* 2020] Alejandro Carabe-Fernandez, Alejandro Bertolet-Reina, Ilias Karagounis, Kiet Huynh and Roger G Dale. *Is there a role for arcing techniques in proton therapy?* The British journal of radiology, vol. 93, no. 1107, page 20190469, 2020. (Cited on page 186.)
- [Carabe *et al.* 2013] Alejandro Carabe, Samuel Espana, Clemens Grassberger and Harald Paganetti. *Clinical consequences of relative biological effectiveness variations in proton radiotherapy of the prostate, brain and liver*. Physics in Medicine & Biology, vol. 58, no. 7, page 2103, 2013. (Cited on page 59.)
- [Carabe *et al.* 2020] Alejandro Carabe, Ilias V Karagounis, Kiet Huynh, Alejandro Bertolet, Noelle François, Michele M Kim, Amit Maity, Eric Abel and Roger Dale. *Radiobiological effectiveness difference of proton arc beams versus conventional proton and photon beams*. Physics in Medicine & Biology, vol. 65, no. 16, page 165002, 2020. (Cited on pages 62 and 186.)
- [Carnicer *et al.* 2013] A Carnicer, G Angellier, A Gerard, N Garnier, C Dubois, R Amblard and J Hérault. *Development and validation of radiochromic film dosimetry and Monte Carlo simulation tools for acquisition of absolute, high-spatial resolution longitudinal dose distributions in ocular proton therapy*. Radiation measurements, vol. 59, pages 225–232, 2013. (Cited on pages 15 and 98.)
- [Carrier *et al.* 2004] J-F Carrier, L Archambault, L Beaulieu and R Roy. *Validation of GEANT4, an object-oriented Monte Carlo toolkit, for simulations in medical physics*. Medical physics, vol. 31, no. 3, pages 484–492, 2004. (Cited on page 109.)
- [Case *et al.* 2009] Robert B Case, Jan-Jakob Sonke, Douglas J Moseley, John Kim,

- Kristy K Brock and Laura A Dawson. *Inter-and intrafraction variability in liver position in non-breath-hold stereotactic body radiotherapy*. International Journal of Radiation Oncology\* Biology\* Physics, vol. 75, no. 1, pages 302–308, 2009. (Cited on page 178.)
- [Castro *et al.* 1994] Joseph R Castro, David E Linstadt, Jean-Paul Bahary, Paula L Petti, Inder Daftari, J Michael Collier, Philip H Gutin, Grant Gauger and Theodore L Phillips. *Experience in charged particle irradiation of tumors of the skull base: 1977–1992*. International Journal of Radiation Oncology\* Biology\* Physics, vol. 29, no. 4, pages 647–655, 1994. (Cited on page 23.)
- [Cavallone 2020] Marco Cavallone. *Application of laser-plasma accelerated beams to high dose-rate radiation biology*. phdthesis, Institut Polytechnique de Paris, November 2020. (Cited on page 15.)
- [Cervantes *et al.* 2021] Yunuen Cervantes, Jasmine Duchaine, Ilias Billas, Simon Duane and Hugo Bouchard. *Monte Carlo calculation of detector perturbation and quality correction factors in a 1.5 T magnetic resonance guided radiation therapy small photon beams*. Physics in Medicine & Biology, vol. 66, no. 22, page 225004, 2021. (Cited on page 97.)
- [Chang *et al.* 2014] David S Chang, Foster D Lasley, Indra J Das, Marc S Mendonca, Joseph R Dynlacht *et al.* Basic radiotherapy physics and biology. Springer, 2014. (Cited on pages 5, 7, 9, 42 and 44.)
- [Chang *et al.* 2017] Howard HY Chang, Nicholas R Pannunzio, Noritaka Adachi and Michael R Lieber. *Non-homologous DNA end joining and alternative pathways to double-strand break repair*. Nature reviews Molecular cell biology, vol. 18, no. 8, pages 495–506, 2017. (Cited on page 31.)
- [Chang *et al.* 2020] Sheng Chang, Gang Liu, Lewei Zhao, Joshua T Dilworth, Weili Zheng, Saada Jawad, Di Yan, Peter Chen, Craig Stevens, Peyman Kabolizadeh *et al.* *Feasibility study: spot-scanning proton arc therapy (SPArc) for left-sided whole breast radiotherapy*. Radiation Oncology, vol. 15, no. 1, pages 1–11, 2020. (Cited on pages 63 and 186.)
- [Chaoui 2020] Samia Chaoui. *Effets secondaires de la radiothérapie conventionnelle et de la protonthérapie sur les tissus sains: biomarqueurs sanguins et tissulaires*, 2020. (Cited on page 59.)
- [Chargari *et al.* 2019] Cyrus Chargari, Eric Deutsch, Pierre Blanchard, Sebastien Gouy, Hélène Martelli, Florent Guérin, Isabelle Dumas, Alberto Bossi, Philippe Morice, Akila N Viswanathan *et al.* *Brachytherapy: An overview for clinicians*. CA: a cancer journal for clinicians, vol. 69, no. 5, pages 386–401, 2019. (Cited on pages 16 and 17.)
- [Charyyev *et al.* 2020] Serdar Charyyev, Mark Artz, Gregory Szalkowski, Chih-Wei Chang, Alexander Stanforth, Liyong Lin, Rongxiao Zhang and C-K Chris Wang. *Optimization of hexagonal-pattern minibeams for spatially fractionated radiotherapy using proton beam scanning*. Medical Physics, vol. 47, no. 8, pages 3485–3495, 2020. (Cited on pages 82, 84, 115, 117 and 219.)

- [Chen & Kuo 2017] Helen HW Chen and Macus Tien Kuo. *Improving radiotherapy in cancer treatment: Promises and challenges*. *Oncotarget*, vol. 8, no. 37, page 62742, 2017. (Cited on page 1.)
- [Chen *et al.* 2019] Guofu Chen, Baiqiang Dong, Guoping Shan, Xiuqin Zhang, Huarong Tang, Yuchen Li, Zhenhua Wang, Wei Xu, Gang Xu, Guiming Yan, Feiyan Zhang, Xiao Hu, Jun Yang, Yujin Xu, Ming Chen and Jin Wang. *Choice of immobilization of stereotactic body radiotherapy in lung tumor patient by BMI*. *BMC Cancer*, vol. 19, no. 1, page 583, June 2019. (Cited on pages 110 and 179.)
- [Chetty *et al.* 2006a] Indrin J. Chetty, Mihaela Rosu, Marc L. Kessler, Benedick A. Fraass, Randall K. Ten Haken, Feng-Ming (Spring) Kong and Daniel L. McShan. *Reporting and analyzing statistical uncertainties in Monte Carlo-based treatment planning*. *International Journal of Radiation Oncology, Biology, Physics*, vol. 65, no. 4, pages 1249–1259, July 2006. Publisher: Elsevier. (Cited on page 116.)
- [Chetty *et al.* 2006b] Indrin J Chetty, Mihaela Rosu, Marc L Kessler, Benedick A Fraass, Randall K Ten Haken, Daniel L McShan *et al.* *Reporting and analyzing statistical uncertainties in Monte Carlo-based treatment planning*. *International Journal of Radiation Oncology\* Biology\* Physics*, vol. 65, no. 4, pages 1249–1259, 2006. (Cited on page 108.)
- [Cheung *et al.* 2005] Tsang Cheung, Martin J Butson and KN Peter. *Post-irradiation colouration of Gafchromic EBT radiochromic film*. *Physics in Medicine & Biology*, vol. 50, no. 20, page N281, 2005. (Cited on page 98.)
- [Chicilo *et al.* 2020] Farley Chicilo, AL Hanson, FH Geisler, George Belev, Andy Edgar, KO Ramaswami, D Chapman and SO Kasap. *Dose profiles and x-ray energy optimization for microbeam radiation therapy by high-dose, high resolution dosimetry using Sm-doped fluoroaluminate glass plates and Monte Carlo transport simulation*. *Physics in Medicine & Biology*, vol. 65, no. 7, page 075010, 2020. (Cited on page 70.)
- [Christensen *et al.* 2020] Jeppe Brage Christensen, Grichar Valdes Santurio, Anne Vestergaard, Stine S Korreman and Claus E Andersen. *Designing a graphite calorimeter for scintillator quenching measurements*. *Radiation Measurements*, vol. 132, page 106277, 2020. (Cited on page 94.)
- [Chung & Lee 2020] Hyun-Tai Chung and Dong-Joon Lee. *Stereotactic Radiosurgery*. *Progress in Medical Physics*, vol. 31, no. 3, pages 63–70, 2020. (Cited on page 18.)
- [Cortés-Giraldo & Carabe 2015] MA Cortés-Giraldo and A Carabe. *A critical study of different Monte Carlo scoring methods of dose average linear-energy-transfer maps calculated in voxelized geometries irradiated with clinical proton beams*. *Physics in Medicine & Biology*, vol. 60, no. 7, page 2645, 2015. (Cited on page 114.)
- [Craig *et al.* 2021] Daniel J Craig, Nisha S Nanavaty, Monika Devanaboyina, Laura Stanbery, Danae Hamouda, Gerald Edelman, Lance Dworkin and John J

- Nemunaitis. *The abscopal effect of radiation therapy*. Future Oncology, vol. 17, no. 13, pages 1683–1694, 2021. (Cited on page 38.)
- [Crosbie *et al.* 2010] Jeffrey C Crosbie, Robin L Anderson, Kai Rothkamm, Christina M Restall, Leonie Cann, Saleela Ruwanpura, Sarah Meachem, Naoto Yagi, Imants Svalbe, Robert A Lewis *et al.* *Tumor cell response to synchrotron microbeam radiation therapy differs markedly from cells in normal tissues*. International Journal of Radiation Oncology\* Biology\* Physics, vol. 77, no. 3, pages 886–894, 2010. (Cited on pages 70 and 75.)
- [Curtis 1967] Howard J Curtis. *The use of a deuteron microbeam for simulating the biological effects of heavy cosmic-ray particles*. Radiation Research Supplement, vol. 7, pages 250–257, 1967. (Cited on pages 36 and 137.)
- [Dal Bello *et al.* 2020] Riccardo Dal Bello, Tobias Becher, Martina C Fuss, Michael Krämer and Joao Seco. *Proposal of a chemical mechanism for mini-beam and micro-beam efficacy*. Frontiers in Physics, vol. 8, page 564836, 2020. (Cited on pages 75 and 77.)
- [Dalrymple *et al.* 1966] Glenn V Dalrymple, Ian R Lindsay, John J Ghidoni, James D Hall, John C Mitchell, Harold L Kundel and Ira L Morgan. *Some effects of 138-Mev protons on primates*. Radiation Research, vol. 28, no. 2, pages 471–488, 1966. (Cited on page 59.)
- [Damodar *et al.* 2018] Joshita Damodar, David Odgers, Dane Pope and Robin Hill. *A study on the suitability of the PTW microDiamond detector for kilovoltage x-ray beam dosimetry*. Applied Radiation and Isotopes, vol. 135, pages 104–109, 2018. (Cited on page 14.)
- [Das *et al.* 2008] Indra J Das, George X Ding and Anders Ahnesjö. *Small fields: nonequilibrium radiation dosimetry*. Medical physics, vol. 35, no. 1, pages 206–215, 2008. (Cited on page 93.)
- [Dawson & Sharpe 2006] Laura A Dawson and Michael B Sharpe. *Image-guided radiotherapy: rationale, benefits, and limitations*. The Lancet Oncology, vol. 7, no. 10, pages 848–858, 2006. (Cited on page 21.)
- [de Almeida & Salata 2022] Carlos Eduardo de Almeida and Camila Salata. *Absolute, reference, and relative dosimetry in radiotherapy*. IntechOpen, 2022. (Cited on page 12.)
- [De Marzi *et al.* 2018] Ludovic De Marzi, Annalisa Patriarca, Catherine Nauraye, Eric Hierso, Rémi Dendale, Consuelo Guardiola and Yolanda Prezado. *Implementation of planar proton minibeam radiation therapy using a pencil beam scanning system: A proof of concept study*. Medical Physics, vol. 45, no. 11, pages 5305–5316, 2018. (Cited on pages 82, 83, 84, 90, 96, 113, 122, 123 and 219.)
- [De Marzi *et al.* 2019a] L. De Marzi, A. Da Fonseca, C. Moignier, A. Patriarca, F. Goudjil, A. Mazal, I. Buvat and J. Hérault. *Experimental characterisation of a proton kernel model for pencil beam scanning techniques*. Phys Med, vol. 64, pages 195–203, August 2019. (Cited on pages 90, 111, 112, 113 and 219.)

- [De Marzi *et al.* 2019b] Ludovic De Marzi, Catherine Nauraye, Pierre Lansonneur, Frédéric Pouzoulet, Annalisa Patriarca, Tim Schneider, Consuelo Guardiola, Hamid Mammar, Rémi Dendale and Yolanda Prezado. *Spatial fractionation of the dose in proton therapy: Proton minibeam radiation therapy*. Cancer/Radiothérapie, vol. 23, no. 6-7, pages 677–681, 2019. (Cited on pages 66, 81, 82, 217 and 218.)
- [Debela *et al.* 2021] Dejene Tolossa Debela, Seke GY Muzazu, Kidist Digamo Heraro, Maureen Tayamika Ndalama, Betelhiem Woldemedhin Mesele, Dagimawi Chilot Haile, Sophia Khalayi Kitui and Tsegahun Manyazewal. *New approaches and procedures for cancer treatment: Current perspectives*. SAGE open medicine, vol. 9, page 20503121211034366, 2021. (Cited on page 3.)
- [Delorme *et al.* 2021] Rachel Delorme, Thongchai AM Masilela, Camille Etoh, François Smekens and Yolanda Prezado. *First theoretical determination of relative biological effectiveness of very high energy electrons*. Scientific Reports, vol. 11, no. 1, pages 1–13, 2021. (Cited on pages 24, 25 and 215.)
- [Deman *et al.* 2012] Pierre Deman, Mathias Vautrin, Magali Edouard, Vasile Stupar, Laure Bobyk, Régine Farion, Hélène Elleaume, Chantal Rémy, Emmanuel L Barbier, François Estève *et al.* *Monochromatic minibeam radiotherapy: from healthy tissue-sparing effect studies toward first experimental glioma bearing rats therapy*. International Journal of Radiation Oncology\* Biology\* Physics, vol. 82, no. 4, pages e693–e700, 2012. (Cited on page 73.)
- [Dendale *et al.* 2006] Rémi Dendale, Livia Lumbroso-Le Rouic, Georges Noel, Loïc Feuvret, Christine Levy, Sabine Delacroix, Anne Meyer, Catherine Nauraye, Alejandro Mazal, Hamid Mammar *et al.* *Proton beam radiotherapy for uveal melanoma: results of Curie Institut–Orsay proton therapy center (ICPO)*. International Journal of Radiation Oncology\* Biology\* Physics, vol. 65, no. 3, pages 780–787, 2006. (Cited on page 90.)
- [Desouky *et al.* 2015] Omar Desouky, Nan Ding and Guangming Zhou. *Targeted and non-targeted effects of ionizing radiation*. Journal of Radiation Research and Applied Sciences, vol. 8, no. 2, pages 247–254, 2015. (Cited on pages 37 and 38.)
- [DesRosiers *et al.* 2000] C DesRosiers, V Moskvin, Alex F Bielaiew and L Papiez. *150-250 MeV electron beams in radiation therapy*. Physics in Medicine & Biology, vol. 45, no. 7, page 1781, 2000. (Cited on page 25.)
- [Devic *et al.* 2005] Slobodan Devic, Jan Seuntjens, Edwin Sham, Ervin B Podgorsak, C Ross Schmidlein, Assen S Kirov and Christopher G Soares. *Precise radiochromic film dosimetry using a flat-bed document scanner*. Medical physics, vol. 32, no. 7Part1, pages 2245–2253, 2005. (Cited on page 98.)
- [Devic *et al.* 2016] Slobodan Devic, Nada Tomic and David Lewis. *Reference radiochromic film dosimetry: review of technical aspects*. Physica Medica,

- vol. 32, no. 4, pages 541–556, 2016. (Cited on pages 15 and 99.)
- [Dilmanian *et al.* 2001] FA Dilmanian, GM Morris, G Le Duc, X Huang, B Ren, T Bacarian, JC Allen, J Kalef-Ezra, I Orion, EM Rosen *et al.* *Response of avian embryonic brain to spatially segmented x-ray microbeams*. Cellular and molecular biology (Noisy-le-Grand, France), vol. 47, no. 3, pages 485–493, 2001. (Cited on page 71.)
- [Dilmanian *et al.* 2002] F Avraham Dilmanian, Terry M Button, Géraldine Le Duc, Nan Zhong, Louis A Peña, Jennifer AL Smith, Steve R Martinez, Tigran Bacarian, Jennifer Tammam, Baorui Ren *et al.* *Response of rat intracranial 9L gliosarcoma to microbeam radiation therapy*. Neuro-oncology, vol. 4, no. 1, pages 26–38, 2002. (Cited on pages 64, 75, 137, 138, 148, 152, 174, 190 and 198.)
- [Dilmanian *et al.* 2005] FA Dilmanian, Y Qu, S Liu, CD Cool, J Gilbert, JF Hainfeld, CA Kruse, J Laterra, D Lenihan, MM Nawrocky *et al.* *X-ray microbeams: Tumor therapy and central nervous system research*. Nuclear Instruments and Methods in Physics Research Section A: Accelerators, Spectrometers, Detectors and Associated Equipment, vol. 548, no. 1-2, pages 30–37, 2005. (Cited on page 75.)
- [Dilmanian *et al.* 2006] F Avraham Dilmanian, Zhong Zhong, Tigran Bacarian, Helene Benveniste, Pantaleo Romanelli, Ruiliang Wang, Jeremy Welwart, Tetsuya Yuasa, Eliot M Rosen and David J Ansel. *Interlaced x-ray microplanar beams: a radiosurgery approach with clinical potential*. Proceedings of the National Academy of Sciences, vol. 103, no. 25, pages 9709–9714, 2006. (Cited on pages 65, 72, 73 and 202.)
- [Dilmanian *et al.* 2007] F Avraham Dilmanian, Yun Qu, Ludwig E Feinendegen, Louis A Peña, Tigran Bacarian, Fritz A Henn, John Kalef-Ezra, Su Liu, Zhong Zhong and John W McDonald. *Tissue-sparing effect of x-ray microplanar beams particularly in the CNS: is a bystander effect involved?* Experimental hematology, vol. 35, no. 4, pages 69–77, 2007. (Cited on page 77.)
- [Dilmanian *et al.* 2012] F Avraham Dilmanian, Adam Rusek, Giovanna R Fois, John Olschowka, Nicolle R Desnoyers, Jane Y Park, Istvan Dioszegi, Bari Dane, Ruiliang Wang, Dardo Tomasiet *al.* *Interleaved carbon minibeams: An experimental radiosurgery method with clinical potential*. International Journal of Radiation Oncology\* Biology\* Physics, vol. 84, no. 2, pages 514–519, 2012. (Cited on pages 73, 74 and 190.)
- [Dilmanian *et al.* 2015a] F Avraham Dilmanian, John G Eley and Sunil Krishnan. *Minibeam therapy with protons and light ions: physical feasibility and potential to reduce radiation side effects and to facilitate hypofractionation*. International Journal of Radiation Oncology\* Biology\* Physics, vol. 92, no. 2, pages 469–474, 2015. (Cited on pages 82, 84 and 87.)
- [Dilmanian *et al.* 2015b] F Avraham Dilmanian, John G Eley, Adam Rusek and Sunil Krishnan. *Charged particle therapy with mini-segmented beams*.

- Frontiers in oncology, vol. 5, page 269, 2015. (Cited on page 160.)
- [Ding *et al.* 2016] Xuanfeng Ding, Xiaoqiang Li, J Michele Zhang, Peyman Kabolizadeh, Craig Stevens and Di Yan. *Spot-scanning proton arc (SPArc) therapy: the first robust and delivery-efficient spot-scanning proton arc therapy*. International Journal of Radiation Oncology\* Biology\* Physics, vol. 96, no. 5, pages 1107–1116, 2016. (Cited on pages 62, 185 and 186.)
- [Ding *et al.* 2018] Xuanfeng Ding, Xiaoqiang Li, An Qin, Jun Zhou, Di Yan, Craig Stevens, Daniel Krauss and Peyman Kabolizadeh. *Have we reached proton beam therapy dosimetric limitations?—A novel robust, delivery-efficient and continuous spot-scanning proton arc (SPArc) therapy is to improve the dosimetric outcome in treating prostate cancer*. Acta Oncologica, vol. 57, no. 3, pages 435–437, 2018. (Cited on page 186.)
- [Ding *et al.* 2019] Xuanfeng Ding, Jun Zhou, Xiaoqiang Li, Kevin Blas, Gang Liu, Yinan Wang, An Qin, Prakash Chinnaiyan, Di Yan, Craig Stevens *et al.* *Improving dosimetric outcome for hippocampus and cochlea sparing whole brain radiotherapy using spot-scanning proton arc therapy*. Acta Oncologica, vol. 58, no. 4, pages 483–490, 2019. (Cited on pages 63 and 186.)
- [Do Huh & Kim 2020] Hyun Do Huh and Seonghoon Kim. *History of radiation therapy technology*. Progress in Medical Physics, vol. 31, no. 3, pages 124–134, 2020. (Cited on page 201.)
- [Dos Santos *et al.* 2020] M Dos Santos, R Delorme, R Salmon and Y Prezado. *Minibeam radiation therapy: A micro-and nano-dosimetry Monte Carlo study*. Medical Physics, vol. 47, no. 3, pages 1379–1390, 2020. (Cited on page 203.)
- [Dracham *et al.* 2018] Chinna Babu Dracham, Abhash Shankar and Renu Madan. *Radiation induced secondary malignancies: a review article*. Radiation oncology journal, vol. 36, no. 2, page 85, 2018. (Cited on page 60.)
- [Durante & Flanz 2019a] Marco Durante and Jay Flanz. *Charged particle beams to cure cancer: Strengths and challenges*. Seminars in Oncology, vol. 46, no. 3, pages 219–225, June 2019. Number: 3. (Cited on pages 22 and 23.)
- [Durante & Flanz 2019b] Marco Durante and Jay Flanz. *Charged particle beams to cure cancer: strengths and challenges*. Seminars in Oncology, vol. 46, no. 3, pages 219–225, 2019. (Cited on page 35.)
- [Durante *et al.* 2016] Marco Durante, David J Brenner and Silvia C Formenti. *Does heavy ion therapy work through the immune system?* International Journal of Radiation Oncology, Biology, Physics, vol. 96, no. 5, pages 934–936, 2016. (Cited on page 35.)
- [Edwards *et al.* 2015] JM Edwards, PH Shah, JL Huhn, W St Clair, WF Regine, M Mohiuddin and MR Kudrimoti. *Definitive GRID and fractionated radiation in bulky head and neck cancer associated with low rates of distant metastasis*. International Journal of Radiation Oncology, Biology, Physics, vol. 93, no. 3, page E334, 2015. (Cited on page 68.)
- [Eklund & Ahnesjö 2010] Karin Eklund and Anders Ahnesjö. *Modeling silicon diode*

- dose response factors for small photon fields*. *Physics in Medicine & Biology*, vol. 55, no. 24, page 7411, 2010. (Cited on page 14.)
- [Eley *et al.* 2021] John G Eley, Catherine W Haga, Asaf Keller, Ellis M Lazenby, Charles Raver, Adam Rusek, Farrokh Avraham Dilmanian, Sunil Krishnan and Jaylyn Waddell. *Heavy Ion Minibeam Therapy: Side Effects in Normal Brain*. *Cancers*, vol. 13, no. 24, page 6207, 2021. (Cited on pages 73 and 75.)
- [Eling *et al.* 2021] Laura Eling, Audrey Bouchet, Alexandre Ocadiz, Jean-François Adam, Sarvenaz Kershmiri, Hélène Elleaume, Michael Krisch, Camille Verry, Jean A Laissue, Jacques Balosso *et al.* *Unexpected benefits of multipoint synchrotron microbeam radiation therapy for brain tumors*. *Cancers*, vol. 13, no. 5, page 936, 2021. (Cited on pages 190 and 198.)
- [Elith *et al.* 2011] Craig Elith, Shane E Dempsey, Naomi Findlay and Helen M Warren-Forward. *An introduction to the intensity-modulated radiation therapy (IMRT) techniques, tomotherapy, and VMAT*. *Journal of Medical Imaging and Radiation Sciences*, vol. 42, no. 1, pages 37–43, 2011. (Cited on pages 19 and 20.)
- [Emami 2013] Bahman Emami. *Tolerance of normal tissue to therapeutic radiation*. *Reports of radiotherapy and Oncology*, vol. 1, no. 1, pages 123–7, 2013. (Cited on pages 45, 173 and 174.)
- [Fagundes *et al.* 2015] Marcio Fagundes, Eugen B Hug, Mark Pankuch, Christine Fang, Shawn McNeeley, Ling Mao, Myra Lavilla, Stacey L Schmidt, Clark Ward, Oren Cahlon *et al.* *Proton therapy for local-regionally advanced breast cancer maximizes cardiac sparing*. *International Journal of Particle Therapy*, vol. 1, no. 4, pages 827–844, 2015. (Cited on page 62.)
- [Fardone *et al.* 2018] Erminia Fardone, Benoît Pouyatos, Elke Bräuer-Krisch, Stefan Bartzsch, Hervé Mathieu, Herwig Requardt, Domenico Bucci, Giacomo Barbone, Paola Coan, Giuseppe Battaglia *et al.* *Synchrotron-generated microbeams induce hippocampal transections in rats*. *Scientific reports*, vol. 8, no. 1, pages 1–10, 2018. (Cited on pages 71 and 87.)
- [Favaudon *et al.* 2014] Vincent Favaudon, Laura Caplier, Virginie Monceau, Frédéric Pouzoulet, Mano Sayarath, Charles Fouillade, Marie-France Poupon, Isabel Brito, Philippe Hupé, Jean Bourhis *et al.* *Ultrahigh dose-rate FLASH irradiation increases the differential response between normal and tumor tissue in mice*. *Science translational medicine*, vol. 6, no. 245, pages 245ra93–245ra93, 2014. (Cited on pages 2, 201 and 202.)
- [Fernandez-Palomo *et al.* 2013] Cristian Fernandez-Palomo, Elisabeth Schültke, Richard Smith, Elke Bräuer-Krisch, Jean Laissue, Christian Schroll, Jennifer Fazzari, Colin Seymour and Carmel Mothersill. *Bystander effects in tumor-free and tumor-bearing rat brains following irradiation by synchrotron X-rays*. *International journal of radiation biology*, vol. 89, no. 6, pages 445–453, 2013. (Cited on pages 75 and 77.)
- [Fernandez-Palomo *et al.* 2020] Cristian Fernandez-Palomo, Jennifer Fazzari, Verdiana Trappetti, Lloyd Smyth, Heidrun Janka, Jean Laissue and

- Valentin Djonov. *Animal models in microbeam radiation therapy: a scoping review*. *Cancers*, vol. 12, no. 3, page 527, 2020. (Cited on page 71.)
- [Fernandez-Palomo *et al.* 2022] Cristian Fernandez-Palomo, Sha Chang and Yolanda Prezado. *Should Peak Dose Be Used to Prescribe Spatially Fractionated Radiation Therapy?—A Review of Preclinical Studies*. *Cancers*, vol. 14, no. 15, page 3625, 2022. (Cited on pages 64, 66, 138, 152, 183 and 217.)
- [Flickinger & Kalend 1990] John C Flickinger and Andre Kalend. *Use of normalized total dose to represent the biological effect of fractionated radiotherapy*. *Radiotherapy and Oncology*, vol. 17, no. 4, pages 339–347, 1990. (Cited on page 41.)
- [Fonseca *et al.* 2020] Gabriel P Fonseca, Jacob G Johansen, Ryan L Smith, Luc Beaulieu, Sam Beddar, Gustavo Kertzscher, Frank Verhaegen and Kari Tanderup. *In vivo dosimetry in brachytherapy: Requirements and future directions for research, development, and clinical practice*. *Physics and imaging in radiation oncology*, vol. 16, pages 1–11, 2020. (Cited on page 17.)
- [Fontanella *et al.* 2015] Andrew N Fontanella, Mary-Keara Boss, Michael Hadsell, Jian Zhang, Thies Schroeder, Katherine G Berman, Mark W Dewhirst, Sha Chang and Gregory M Palmer. *Effects of high-dose microbeam irradiation on tumor microvascular function and angiogenesis*. *Radiation research*, vol. 183, no. 2, pages 147–158, 2015. (Cited on page 75.)
- [Fontenot *et al.* 2009] Jonas D Fontenot, Andrew K Lee and Wayne D Newhauser. *Risk of secondary malignant neoplasms from proton therapy and intensity-modulated x-ray therapy for early-stage prostate cancer*. *International Journal of Radiation Oncology\* Biology\* Physics*, vol. 74, no. 2, pages 616–622, 2009. (Cited on page 62.)
- [Forster & Godfrey 1985] R. A. Forster and T. N. K. Godfrey. *MCNP - a general Monte Carlo code for neutron and photon transport*. In Raymond Alcouffe, Robert Dautray, Arthur Forster, Guy Ledanois and B. Mercier, editors, *Monte-Carlo Methods and Applications in Neutronics, Photonics and Statistical Physics, Lecture Notes in Physics*, pages 33–55, Berlin, Heidelberg, 1985. Springer. (Cited on page 108.)
- [Fowler 1989] John F Fowler. *The linear-quadratic formula and progress in fractionated radiotherapy*. *The British journal of radiology*, vol. 62, no. 740, pages 679–694, 1989. (Cited on page 41.)
- [Fracchiolla *et al.* 2015] F Fracchiolla, S Lorentini, L Widesott and M Schwarz. *Characterization and validation of a Monte Carlo code for independent dose calculation in proton therapy treatments with pencil beam scanning*. *Physics in Medicine & Biology*, vol. 60, no. 21, page 8601, 2015. (Cited on page 117.)
- [Friedrich *et al.* 2022] Thomas Friedrich, Michael Scholz and Marco Durante. *A Predictive Biophysical Model of the Combined Action of Radiation Therapy and Immunotherapy of Cancer*. *International Journal of Radiation Oncology\* Biology\* Physics*, 2022. (Cited on page 183.)

- [Fu *et al.* 2008] Shen Fu, Jiade J Lu, Qing Zhang, Zhe Yang, Lihua Peng and Fei Xiong. *Intraoperative radiotherapy combined with adjuvant chemoradiotherapy for locally advanced gastric adenocarcinoma*. International Journal of Radiation Oncology\* Biology\* Physics, vol. 72, no. 5, pages 1488–1494, 2008. (Cited on page 17.)
- [Gafchromic 2022] Gafchromic. *Radiotherapy films.*, 2022. (Cited on pages 15 and 98.)
- [Gao *et al.* 2018] M Gao, MM Mohiuddin, WF Hartsell and M Pankuch. *Spatially fractionated (GRID) radiation therapy using proton pencil beam scanning (PBS): Feasibility study and clinical implementation*. Medical physics, vol. 45, no. 4, pages 1645–1653, 2018. (Cited on pages 16 and 68.)
- [Garnier *et al.* 2018] Nicolas Garnier, Régis Amblard, Rémy Villeneuve, Rodolphe Haykal, Cécile Ortholan, Philippe Colin, Anaïs Gérard, Sarah Belhomme, Franck Mady, Mourad Benabdesselamet *et al.* *Detectors assessment for stereotactic radiosurgery with cones*. Journal of applied clinical medical physics, vol. 19, no. 6, pages 88–98, 2018. (Cited on page 14.)
- [Garutti 2013] E Garutti. *Therapy with protons and ion beams Biomedical Physics Lecture WiSe 2012/13*, 2013. (Cited on pages 48 and 216.)
- [Geant4 Collaboration 2021] Geant4 Collaboration. *Guide For Physics Lists*, 2021. (Cited on page 109.)
- [Geant4 Collaboration 2022] Geant4 Collaboration. *Geant4 validation portal*, 2022. (Cited on page 109.)
- [Gerber & Chan 2008] David E Gerber and Timothy A Chan. *Recent advances in radiation therapy*. American family physician, vol. 78, no. 11, pages 1254–1262, 2008. (Cited on pages 1, 4, 18 and 19.)
- [Gholami *et al.* 2016] Somayeh Gholami, Hassan Ali Nedaie, Francesco Longo, Mohammad Reza Ay, Stacey Wright and Ali S Meigooni. *Is grid therapy useful for all tumors and every grid block design?* Journal of applied clinical medical physics, vol. 17, no. 2, pages 206–219, 2016. (Cited on pages 65 and 68.)
- [Gieschen *et al.* 2001] Holger L Gieschen, Ira J Spiro, Herman D Suit, Mark J Ott, David W Rattner, Marek Ancukiewicz and Christopher G Willett. *Long-term results of intraoperative electron beam radiotherapy for primary and recurrent retroperitoneal soft tissue sarcoma*. International Journal of Radiation Oncology\* Biology\* Physics, vol. 50, no. 1, pages 127–131, 2001. (Cited on page 17.)
- [Girdhani *et al.* 2013] Swati Girdhani, Rainer Sachs and Lynn Hlatky. *Biological effects of proton radiation: what we know and don't know*. Radiation research, vol. 179, no. 3, pages 257–272, 2013. (Cited on pages 30, 58 and 59.)
- [Girst *et al.* 2016] Stefanie Girst, Christoph Greubel, Judith Reindl, Christian Siebenwirth, Olga Zlobinskaya, Dietrich WM Walsh, Katarina Ilicic, Michaela Aichler, Axel Walch, Jan J Wilkens *et al.* *Proton minibeam radiation therapy reduces side effects in an in vivo mouse ear model*. International

- Journal of Radiation Oncology\* Biology\* Physics, vol. 95, no. 1, pages 234–241, 2016. (Cited on pages 82 and 85.)
- [Gomà *et al.* 2016] Carles Gomà, Marco Marinelli, Sairos Safai, Gianluca Veron-Rinati and Jan Würfel. *The role of a microDiamond detector in the dosimetry of proton pencil beams*. *Zeitschrift für Medizinische Physik*, vol. 26, no. 1, pages 88–94, 2016. (Cited on page 14.)
- [Goodenberger & Jenkins 2012] McKinsey L Goodenberger and Robert B Jenkins. *Genetics of adult glioma*. *Cancer genetics*, vol. 205, no. 12, pages 613–621, 2012. (Cited on page 86.)
- [Goodhead *et al.* 1993] DT Goodhead, J Thacker and Roger Cox. *Effects of radiations of different qualities on cells: molecular mechanisms of damage and repair*. *International journal of radiation biology*, vol. 63, no. 5, pages 543–556, 1993. (Cited on pages 30 and 58.)
- [Grams *et al.* 2021] Michael P Grams, Dawn Owen, Sean S Park, Ivy A Petersen, Michael G Haddock, Elizabeth B Jeans, Randi R Finley and Daniel J Ma. *VMAT GRID therapy: a widely applicable planning approach*. *Practical Radiation Oncology*, vol. 11, no. 3, pages e339–e347, 2021. (Cited on page 67.)
- [Granville & Sawakuchi 2015] Dal A Granville and Gabriel O Sawakuchi. *Comparison of linear energy transfer scoring techniques in Monte Carlo simulations of proton beams*. *Physics in Medicine & Biology*, vol. 60, no. 14, page N283, 2015. (Cited on pages 10 and 114.)
- [Grassberger *et al.* 2011] Clemens Grassberger, Alexei Trofimov, Anthony Lomax and Harald Paganetti. *Variations in linear energy transfer within clinical proton therapy fields and the potential for biological treatment planning*. *International Journal of Radiation Oncology\* Biology\* Physics*, vol. 80, no. 5, pages 1559–1566, 2011. (Cited on page 51.)
- [Grevillot *et al.* 2010] Loïc Grevillot, Thibault Frisson, Nabil Zahra, Damien Bertrand, Frédéric Stichelbaut, Nicolas Freud and David Sarrut. *Optimization of GEANT4 settings for proton pencil beam scanning simulations using GATE*. *Nuclear Instruments and Methods in Physics Research Section B: Beam interactions with materials and atoms*, vol. 268, no. 20, pages 3295–3305, 2010. (Cited on pages 113 and 114.)
- [Grimes *et al.* 2017] David Robert Grimes, Daniel R Warren and Mike Partridge. *An approximate analytical solution of the Bethe equation for charged particles in the radiotherapeutic energy range*. *Scientific reports*, vol. 7, no. 1, pages 1–12, 2017. (Cited on pages 12 and 49.)
- [Grotzer *et al.* 2015] MA Grotzer, E Schültke, Elke Bräuer-Krisch and JA Laissue. *Microbeam radiation therapy: Clinical perspectives*. *Physica Medica*, vol. 31, no. 6, pages 564–567, 2015. (Cited on page 70.)
- [Guan 2015] Xiangming Guan. *Cancer metastases: challenges and opportunities*. *Acta pharmaceutica sinica B*, vol. 5, no. 5, pages 402–418, 2015. (Cited on page 160.)

- [Guardiola & Prezado 2020] Consuelo Guardiola and Yolanda Prezado. *High-Energy Charged Particles for Spatially Fractionated Radiation Therapy*. *Frontiers in Physics*, vol. 8, page 299, 2020. (Cited on pages 96, 122 and 123.)
- [Guardiola *et al.* 2017] Consuelo Guardiola, Cécile Peucelle and Yolanda Prezado. *Optimization of the mechanical collimation for minibeam generation in proton minibeam radiation therapy*. *Medical physics*, vol. 44, no. 4, pages 1470–1478, 2017. (Cited on pages 82 and 83.)
- [Gudkov *et al.* 2015] Sergey V Gudkov, Natalya Yu Shilyagina, Vladimir A Vodeneev and Andrei V Zvyagin. *Targeted radionuclide therapy of human tumors*. *International journal of molecular sciences*, vol. 17, no. 1, page 33, 2015. (Cited on page 18.)
- [Gueulette *et al.* 2001] John Gueulette, Jacobus P Slabbert, Lothar Böhm, Blanche M De Coster, Jean-François Rosier, Michelle Octave-Prignot, Arnout Ruifrok, A Nicolaas Schreuder, André Wambersie, Pierre Scalliet *et al.* *Proton RBE for early intestinal tolerance in mice after fractionated irradiation*. *Radiotherapy and oncology*, vol. 61, no. 2, pages 177–184, 2001. (Cited on page 40.)
- [Gul *et al.* 2020] Attia Gul, Shigekazu Fukuda, Hideyuki Mizuno, Nakaji Taku, M. Basim Kakakhel and Sikander M. Mirza. *Feasibility study of using Stereotactic Field Diode for field output factors measurement and evaluating three new detectors for small field relative dosimetry of 6 and 10 MV photon beams*. *Journal of Applied Clinical Medical Physics*, vol. 21, no. 11, pages 23–36, 2020. (Cited on page 14.)
- [Hadsell *et al.* 2013] M. Hadsell, J. Zhang, P. Laganis, F. Sprenger, J. Shan, L. Zhang, L. Burk, H. Yuan, S. Chang, J. Lu and O. Zhou. *A first generation compact microbeam radiation therapy system based on carbon nanotube X-ray technology*. *Applied Physics Letters*, vol. 103, no. 18, page 183505, 2013. (Cited on page 70.)
- [Hall & Wu 2003] Eric J Hall and Cheng-Shie Wu. *Radiation-induced second cancers: the impact of 3D-CRT and IMRT*. *International Journal of Radiation Oncology\*Biophysics\*Physics*, vol. 56, no. 1, pages 83–88, 2003. (Cited on page 174.)
- [Hang *et al.* 2010] Shu Hang, Fang Shou-Xian, Guan Xia-Ling, Tang Jing-Yu, Liu De-Kang, Fu Shi-Nian, Li Gang, Liu Li, Chen Yuan, Jiao Yi and Qiu Jing. *Irradiation methods and nozzle design for the advanced proton therapy facility*. *Chinese Physics C*, vol. 34, no. 4, pages 516–520, apr 2010. (Cited on page 55.)
- [Henry *et al.* 2017] Thomas Henry, Ana Ureba, Alexander Valdman and Albert Siegbahn. *Proton Grid Therapy: A Proof-of-Concept Study*. *Technology in Cancer Research & Treatment*, vol. 16, no. 6, pages 749–757, 2017. (Cited on page 68.)
- [Henthorn *et al.* 2018] NT Henthorn, JW Warmenhoven, Marios Sotiropoulos, Ranald I Mackay, NF Kirkby, Karen J Kirkby and Michael J Merchant. *In*

- silico non-homologous end joining following ion induced DNA double strand breaks predicts that repair fidelity depends on break density*. Scientific reports, vol. 8, no. 1, pages 1–11, 2018. (Cited on pages 58 and 217.)
- [Hesketh 2013] Robin Hesketh. Introduction to cancer biology. Cambridge University Press, 2013. (Cited on page 3.)
- [Hessel *et al.* 2003] F Hessel, C Petersen, D Zips, M Krause, D Pfitzmann, HD Thames and M Baumann. *Impact of increased cell loss on the repopulation rate during fractionated irradiation in human FaDu squamous cell carcinoma growing in nude mice*. International journal of radiation biology, vol. 79, no. 7, pages 479–486, 2003. (Cited on page 34.)
- [Ho & Newman 2003] KH Ho and ST Newman. *State of the art electrical discharge machining (EDM)*. International Journal of Machine Tools and Manufacture, vol. 43, no. 13, pages 1287–1300, 2003. (Cited on page 91.)
- [Holliday *et al.* 2015] Emma B Holliday, Adam S Garden, David I Rosenthal, C David Fuller, William H Morrison, G Brandon Gunn, Jack Phan, Beth M Beadle, Xiarong R Zhu, Xiaodong Zhanget *al.* *Proton therapy reduces treatment-related toxicities for patients with nasopharyngeal cancer: a case-match control study of intensity-modulated proton therapy and intensity-modulated photon therapy*. International Journal of Particle Therapy, vol. 2, no. 1, pages 19–28, 2015. (Cited on page 61.)
- [Hopewell & Trott 2000] John William Hopewell and Klaus-Rüdiger Trott. *Volume effects in radiobiology as applied to radiotherapy*. Radiotherapy and Oncology, vol. 56, no. 3, pages 283–288, 2000. (Cited on pages 2, 36, 37, 76, 137 and 175.)
- [Hopewell *et al.* 1986] JW Hopewell, R Hamlet, JE Coggle, JP Williams, J Wells and MW Charles. *The acute effects of different energy beta-emitters on pig and mouse skin*. In Radiation damage to skin: fundamental and practical aspects. 1986. (Cited on page 36.)
- [Hopewell *et al.* 1987] JW Hopewell, AD Morris and A1 Dixon-Brown. *The influence of field size on the late tolerance of the rat spinal cord to single doses of X rays*. The British Journal of Radiology, vol. 60, no. 719, pages 1099–1108, 1987. (Cited on page 36.)
- [Hoshida *et al.* 2019] Kento Hoshida, Fujio Araki, Takeshi Ohno, Hirofumi Tominaga, Kazuki Komatsu and Kentaro Tamura. *Monte Carlo dose verification for a single-isocenter VMAT plan in multiple brain metastases*. Medical Dosimetry, vol. 44, no. 4, pages e51–e58, December 2019. Number: 4. (Cited on page 108.)
- [Hu *et al.* 2018] Man Hu, Liyang Jiang, Xiangli Cui, Jianguang Zhang and Jinming Yu. *Proton beam therapy for cancer in the era of precision medicine*. Journal of hematology & oncology, vol. 11, no. 1, pages 1–16, 2018. (Cited on page 61.)
- [Huang *et al.* 2018] Sheng Huang, Minglei Kang, Kevin Souris, Christopher Ainsley, Timothy D Solberg, James E McDonough, Charles B Simone and Liyong Lin.

- Validation and clinical implementation of an accurate Monte Carlo code for pencil beam scanning proton therapy.* Journal of applied clinical medical physics, vol. 19, no. 5, pages 558–572, 2018. (Cited on page 110.)
- [Huhn *et al.* 2006] Jeniffer L Huhn, William F Regine, Joseph P Valentino, Ali S Meigooni, Mahesh Kudrimoti and Mohammed Mohiuddin. *Spatially fractionated GRID radiation treatment of advanced neck disease associated with head and neck cancer.* Technology in cancer research & treatment, vol. 5, no. 6, pages 607–612, 2006. (Cited on page 68.)
- [IAEA 2001] IAEA. Absorbed Dose Determination in External Beam Radiotherapy. Number 398 de Technical Reports Series. INTERNATIONAL ATOMIC ENERGY AGENCY, Vienna, 2001. (Cited on pages 11, 12, 13, 95, 101 and 143.)
- [IAEA 2009] IAEA. Calibration of reference dosimeters for external beam radiotherapy. Number 469 de Technical reports series. International Atomic Energy Agency, Vienna, 2009. (Cited on page 12.)
- [IAEA 2017] IAEA. Dosimetry of Small Static Fields Used in External Beam Radiotherapy. Number 483 de Technical Reports Series. INTERNATIONAL ATOMIC ENERGY AGENCY, Vienna, 2017. (Cited on pages 11, 14, 93, 94, 95, 96, 122, 143, 144, 155 and 219.)
- [IBA Dosimetry 2022a] IBA Dosimetry. *Blue Phantom 2*, 2022. (Cited on page 100.)
- [IBA Dosimetry 2022b] IBA Dosimetry. *Lynx PT*, 2022. (Cited on page 100.)
- [IBA Dosimetry 2022c] IBA Dosimetry. *PPC05 Plane Parallel Chamber*, 2022. (Cited on pages 96 and 124.)
- [IBA Dosimetry 2022d] IBA Dosimetry. *RAZOR detector*, 2022. (Cited on pages 97 and 98.)
- [ICRU 1999] ICRU. *ICRU Report 62: Prescribing, Recording and Reporting Photon Beam Therapy (Supplement to ICRU Report 50)*. J ICRU, vol. 32, no. 1, pages 1–52, November 1999. (Cited on page 44.)
- [ICRU 2004] ICRU. *ICRU Report 71: Prescribing, Recording, and Reporting Electron Beam Therapy*. J ICRU, vol. 4, no. 1, pages 1–100, June 2004. (Cited on page 45.)
- [ICRU 2007] ICRU. *ICRU Report 78: Prescribing, Recording, and Reporting Proton-Beam Therapy*. J ICRU, vol. 7, no. 2, pages 1–210, December 2007. (Cited on pages 25, 39 and 45.)
- [ICRU 2010] ICRU. *ICRU Report 83: Prescribing, Recording, and Reporting Photon-Beam Intensity-Modulated Radiation Therapy (IMRT)*. J ICRU, vol. 10, no. 1, pages 1–106, April 2010. (Cited on page 45.)
- [ICRU 2011] ICRU. *ICRU Report 85: Fundamental quantities and units for ionizing radiation*. J ICRU, vol. 11, no. 1, pages 1–31, April 2011. (Cited on pages 9 and 10.)
- [ICRU 2019] ICRU. *ICRU report 91 on prescribing, recording, and reporting of stereotactic treatments with small photon beams : Statement from the DEGRO/DGMP working group stereotactic radiotherapy and radiosurgery*.

- Strahlenther Onkol, vol. 195, no. 3, pages 193–198, March 2019. (Cited on page 45.)
- [Indelicato *et al.* 2019] Daniel J Indelicato, Ronny L Rotondo, Haruka Uezono, Eric S Sandler, Philipp R Aldana, Nathan J Ranalli, Alexandra D Beier, Christopher G Morris and Julie A Bradley. *Outcomes following proton therapy for pediatric low-grade glioma*. International Journal of Radiation Oncology\* Biology\* Physics, vol. 104, no. 1, pages 149–156, 2019. (Cited on page 61.)
- [Jan *et al.* 2011] Sébastien Jan, Didier Benoit, E Becheva, Thomas Carlier, Franca Cassol, Patrice Descourt, T Frisson, L Grevillot, L Guigues, L Maigne *et al.* *GATE V6: a major enhancement of the GATE simulation platform enabling modelling of CT and radiotherapy*. Physics in Medicine & Biology, vol. 56, no. 4, page 881, 2011. (Cited on page 108.)
- [Jeraj & Robar 2004] Matjaž Jeraj and Vlado Robar. *Multileaf collimator in radiotherapy*. Radiology and Oncology, vol. 38, no. 3, 2004. (Cited on pages 20 and 215.)
- [Jiang *et al.* 2021] Liuqing Jiang, Xiaobo Li, Jianping Zhang, Wenyao Li, Fangfen Dong, Cheng Chen, Qingliang Lin, Chonglin Zhang, Fen Zheng, Weisi Yan, Yi Zheng, Xiaodong Wu and Benhua Xu. *Combined High-Dose LATTICE Radiation Therapy and Immune Checkpoint Blockade for Advanced Bulky Tumors: The Concept and a Case Report*. Frontiers in Oncology, vol. 10, 2021. (Cited on page 78.)
- [Joiner & van der Kogel 2018] Michael C Joiner and Albert J van der Kogel. Basic clinical radiobiology. CRC press, 2018. (Cited on pages 26, 27, 28, 29, 30, 31, 32, 33, 34, 38, 39, 215 and 216.)
- [Jursinic 2009] Paul A Jursinic. *Angular dependence of dose sensitivity of surface diodes*. Medical physics, vol. 36, no. 6Part1, pages 2165–2171, 2009. (Cited on page 14.)
- [Kadhim *et al.* 2013] Munira Kadhim, Sisko Salomaa, Eric Wright, Guido Hildebrandt, Oleg V Belyakov, Kevin M Prise and Mark P Little. *Non-targeted effects of ionising radiation—implications for low dose risk*. Mutation Research/Reviews in Mutation Research, vol. 752, no. 2, pages 84–98, 2013. (Cited on page 38.)
- [Kahalley *et al.* 2020] Lisa S Kahalley, Rachel Peterson, M Douglas Ris, Laura Janzen, M Fatih Okcu, David R Grosshans, Vijay Ramaswamy, Arnold C Paulino, David Hodgson, Anita Mahajan *et al.* *Superior intellectual outcomes after proton radiotherapy compared with photon radiotherapy for pediatric medulloblastoma*. Journal of Clinical Oncology, vol. 38, no. 5, page 454, 2020. (Cited on page 61.)
- [Kalholm *et al.* 2021] Fredrik Kalholm, Leszek Grzanka, Erik Traneus and Niels Bassler. *A systematic review on the usage of averaged LET in radiation biology for particle therapy*. Radiotherapy and Oncology, vol. 161, pages 211–221, 2021. (Cited on page 10.)

- [Kalos & Whitlock 2009] Malvin H Kalos and Paula A Whitlock. Monte carlo methods. John Wiley & Sons, 2009. (Cited on page 108.)
- [Kanagavelu *et al.* 2014] Saravana Kanagavelu, Seema Gupta, Xiaodong Wu, Sakhi Philip, Max M Wattenberg, James W Hodge, Mariluz D Couto, Kristina D Chung and Mansoor M Ahmed. *In vivo effects of lattice radiation therapy on local and distant lung cancer: potential role of immunomodulation*. Radiation research, vol. 182, no. 2, pages 149–162, 2014. (Cited on page 77.)
- [Kantemiris *et al.* 2011] I Kantemiris, P Karaiskos, P Papagiannis and A Angelopoulos. *Dose and dose averaged LET comparison of  $^1\text{H}$ ,  $^4\text{He}$ ,  $^6\text{Li}$ ,  $^8\text{Be}$ ,  $^{10}\text{B}$ ,  $^{12}\text{C}$ ,  $^{14}\text{N}$ , and  $^{16}\text{O}$  ion beams forming a spread-out Bragg peak*. Medical Physics, vol. 38, no. 12, pages 6585–6591, 2011. (Cited on page 25.)
- [Karger *et al.* 2021] Christian P Karger, Christin Glowa, Peter Peschke and Wilma Kraft-Weyrather. *The RBE in ion beam radiotherapy: In vivo studies and clinical application*. Zeitschrift für Medizinische Physik, vol. 31, no. 2, pages 105–121, 2021. (Cited on page 23.)
- [Kawrakow & Rogers 2000] I Kawrakow and DWO Rogers. *The EGSnrc code system*. NRC Report PIRS-701, NRC, Ottawa, vol. 17, 2000. (Cited on page 108.)
- [Khachonkham *et al.* 2018] Suphalak Khachonkham, Ralf Dreindl, Gerd Heilemann, Wolfgang Lechner, Hermann Fuchs, Hugo Palmans, Dietmar Georg and Peter Kuess. *Characteristic of EBT-XD and EBT3 radiochromic film dosimetry for photon and proton beams*. Physics in Medicine & Biology, vol. 63, no. 6, page 065007, 2018. (Cited on page 15.)
- [Khan & Gibbons 2014] Faiz M Khan and John P Gibbons. Khan's the physics of radiation therapy. Lippincott Williams & Wilkins, 2014. (Cited on pages 13, 14, 22 and 24.)
- [Kłodowska *et al.* 2015] M Kłodowska, Paweł Olko and MPR Waligórski. *Proton microbeam radiotherapy with scanned pencil-beams—Monte Carlo simulations*. Physica Medica, vol. 31, no. 6, pages 621–626, 2015. (Cited on page 72.)
- [Knopf *et al.* 2011] Antje-Christin Knopf, Katia Parodi, Harald Paganetti, Thomas Bortfeld, Juliane Daartz, Martijn Engelsman, Norbert Liebsch and Helen Shih. *Accuracy of proton beam range verification using post-treatment positron emission tomography/computed tomography as function of treatment site*. International Journal of Radiation Oncology\* Biology\* Physics, vol. 79, no. 1, pages 297–304, 2011. (Cited on page 60.)
- [Kudrimoti *et al.* 2002] M Kudrimoti, WF Regine, JL Huhn, AS Meigooni, M Ahmed and M Mohiuddin. *Spatially fractionated radiation therapy (SFR) in the palliation of large bulky (> 8 cm) melanomas*. International Journal of Radiation Oncology, Biology, Physics, vol. 54, no. 2, pages 342–343, 2002. (Cited on page 68.)
- [Kudulaiti *et al.* 2021] Nijiati Kudulaiti, Zhirui Zhou, Chen Luo, Jie Zhang, Fengping Zhu and Jinsong Wu. *A nomogram for individualized prediction of*

- overall survival in patients with newly diagnosed glioblastoma: a real-world retrospective cohort study.* BMC surgery, vol. 21, no. 1, pages 1–11, 2021. (Cited on page 86.)
- [Kundapur *et al.* 2022] V Kundapur, M Mayer, RN Auer, A Alexander, S Weibe, MJ Pushie and G Cranmer-Sargison. *Is Mini Beam Ready for Human Trials? Results of Randomized Study of Treating De-Novo Brain Tumors in Canines Using Linear Accelerator Generated Mini Beams.* Radiation Research, 2022. (Cited on page 73.)
- [Köhler 1909] A. Köhler. *Theorie einer Methode, bisher unmöglich unanwendbar hohe Dosen Röntgenstrahlen in der Tiefe des Gewebes zur therapeutischen Wirksamkeit zu bringen ohne schwere Schäden des Patienten, zugleich eine Methode des Schutzes gegen Röntgenverbrennungen überhaupt.* Fortschritte auf dem Gebiete der Röntgenstrahlen und der Nuklearmedizin, vol. 14, pages 27–29, 1909. (Cited on pages 64 and 65.)
- [Laissue *et al.* 1999] Jean A Laissue, Nadia Lyubimova, Hans-Peter Wagner, David W Archer, Daniel N Slatkin, Marco Di Michiel, Christian Nemoz, Michel Renier, Elke Brauer, Per O Spanneet *al.* *Microbeam radiation therapy.* Medical Applications of Penetrating Radiation, vol. 3770, pages 38–45, 1999. (Cited on page 70.)
- [Laissue *et al.* 2001] Jean A Laissue, Hans Blattmann, Marco Di Michiel, Daniel N Slatkin, Nadia Lyubimova, Raphael Guzman, Werner Zimmermann, Stephan Birrer, Tim Bley, Patrick Kircheret *al.* *Weanling piglet cerebellum: a surrogate for tolerance to MRT (microbeam radiation therapy) in pediatric neuro-oncology.* Penetrating Radiation Systems and Applications III, vol. 4508, pages 65–73, 2001. (Cited on page 71.)
- [Laissue *et al.* 2007] JA Laissue, H Blattmann, HP Wagner, MA Grotzer and DN Slatkin. *Prospects for microbeam radiation therapy of brain tumours in children to reduce neurological sequelae.* Developmental Medicine & Child Neurology, vol. 49, no. 8, pages 577–581, 2007. (Cited on page 71.)
- [Laissue *et al.* 2013] Jean A Laissue, Stefan Bartzsch, Hans Blattmann, Elke Bräuer-Krisch, Alberto Bravin, Dominique Dalléry, Valentin Djonov, Albert L Hanson, John W Hopewell, Barbara Kaser-Hotzet *al.* *Response of the rat spinal cord to X-ray microbeams.* Radiotherapy and oncology, vol. 106, no. 1, pages 106–111, 2013. (Cited on page 71.)
- [Lamirault *et al.* 2020a] Charlotte Lamirault, Elise Brisebard, Annalisa Patriarca, Marjorie Juchaux, Delphine Crepin, Dalila Labiod, Frederic Pouzoulet, Catherine Sebrie, Laurene Jourdain, Marine Le Dudalet *al.* *Spatially modulated proton minibeam results in the same increase of lifespan as a uniform target dose coverage in F98-glioma-bearing rats.* Radiation Research, vol. 194, no. 6, pages 715–723, 2020. (Cited on pages 84, 85, 138, 160, 165, 183, 188 and 190.)
- [Lamirault *et al.* 2020b] Charlotte Lamirault, Valérie Doyère, Marjorie Juchaux, Frederic Pouzoulet, Dalila Labiod, Remi Dendale, Annalisa Patriarca,

- Catherine Nauraye, Marine Le Dudal, Grégory Jouvionet *et al.* *Short and long-term evaluation of the impact of proton minibeam radiation therapy on motor, emotional and cognitive functions.* Scientific reports, vol. 10, no. 1, pages 1–14, 2020. (Cited on pages 84, 85, 138, 160, 197 and 198.)
- [Landry & Hua 2018] Guillaume Landry and Chia-ho Hua. *Current state and future applications of radiological image guidance for particle therapy.* Medical Physics, vol. 45, no. 11, pages e1086–e1095, 2018. (Cited on page 55.)
- [Lansonneur *et al.* 2020] Pierre Lansonneur, Hamid Mammam, Catherine Nauraye, Annalisa Patriarca, Eric Hierso, Rémi Dendale, Yolanda Prezado and Ludovic De Marzi. *First proton minibeam radiation therapy treatment plan evaluation.* Scientific reports, vol. 10, no. 1, pages 1–8, 2020. (Cited on pages 80, 86, 87, 116, 118, 172, 180, 190, 219 and 220.)
- [Larsson 1967] Börje Larsson. *Radiological properties of beams of high-energy protons.* Radiation Research Supplement, vol. 7, pages 304–311, 1967. (Cited on page 79.)
- [Lawrence *et al.* 2010] Yaacov Richard Lawrence, X Allen Li, Issam El Naqa, Carol A Hahn, Lawrence B Marks, Thomas E Merchant and Adam P Dicker. *Radiation dose–volume effects in the brain.* International Journal of Radiation Oncology\* Biology\* Physics, vol. 76, no. 3, pages S20–S27, 2010. (Cited on page 175.)
- [Leduc *et al.* 2021] Alexandre Leduc, Samia Chaouni, Frédéric Pouzoulet, Ludovic De Marzi, Frédérique Megnin-Chanet, Erwan Corre, Dinu Stefan, Jean-Louis Habrand, François Sichel and Carine Laurent. *Differential normal skin transcriptomic response in total body irradiated mice exposed to scattered versus scanned proton beams.* Scientific reports, vol. 11, no. 1, pages 1–12, 2021. (Cited on page 59.)
- [Lee *et al.* 2008] Kheun Byeol Lee, Jong-Soo Lee, Jeen-Woo Park, Tae-Lin Huh and You Mie Lee. *Low energy proton beam induces tumor cell apoptosis through reactive oxygen species and activation of caspases.* Experimental & molecular medicine, vol. 40, no. 1, pages 118–129, 2008. (Cited on page 39.)
- [Lee *et al.* 2016] Eunsin Lee, Juergen Meyer and George Sandison. *Collimator design for spatially-fractionated proton beams for radiobiology research.* Physics in Medicine & Biology, vol. 61, no. 14, page 5378, 2016. (Cited on pages 82 and 83.)
- [Leite *et al.* 2021] AMM Leite, MG Ronga, Maria Giorgi, Yoann Ristic, Yann Perrot, Francois Trompier, Yolanda Prezado, Gilles Crehange and Ludovic De Marzi. *Secondary neutron dose contribution from pencil beam scanning, scattered and spatially fractionated proton therapy.* Physics in Medicine & Biology, vol. 66, no. 22, page 225010, 2021. (Cited on page 87.)
- [Li & Heyer 2008] Xuan Li and Wolf-Dietrich Heyer. *Homologous recombination in DNA repair and DNA damage tolerance.* Cell research, vol. 18, no. 1, pages 99–113, 2008. (Cited on page 31.)
- [Li *et al.* 2018] Xiaoqiang Li, Peyman Kabolizadeh, Di Yan, An Qin, Jun Zhou,

- Ye Hong, Thomas Guerrero, Inga Grills, Craig Stevens and Xuanfeng Ding. *Improve dosimetric outcome in stage III non-small-cell lung cancer treatment using spot-scanning proton arc (SPArc) therapy*. *Radiation Oncology*, vol. 13, no. 1, pages 1–9, 2018. (Cited on pages 63 and 186.)
- [Li *et al.* 2019] Xiaoqiang Li, Gang Liu, Guillaume Janssens, Olivier De Wilde, Vincent Bossier, Xavier Lerot, Antoine Pouppez, Di Yan, Craig Stevens, Peyman Kabolizadehet *al.* *The first prototype of spot-scanning proton arc treatment delivery*. *Radiotherapy and Oncology*, vol. 137, pages 130–136, 2019. (Cited on page 63.)
- [Liberson 1933] F Liberson. *The value of a multi-perforated screen in deep X-ray therapy: A preliminary report on a new method of delivering multiple erythema doses without permanent injury to the skin*. *Radiology*, vol. 20, no. 3, pages 186–195, 1933. (Cited on page 64.)
- [Lin *et al.* 2021] Haibo Lin, Chengyu Shi, Sheng Huang, Jiajian Shen, Minglei Kang, Qing Chen, Huifang Zhai, James McDonough, Zelig Tochner, Curtiland Deville *et al.* *Applications of various range shifters for proton pencil beam scanning radiotherapy*. *Radiation Oncology*, vol. 16, no. 1, pages 1–10, 2021. (Cited on page 55.)
- [Lindblom *et al.* 2019] Emely Kjellsson Lindblom, Susanta Hui, Jamison Brooks, Alexandru Dasu, Maciej Kujawski and Iuliana Toma-Dasu. *Radiation-induced vascular damage and the impact on the treatment outcome of stereotactic body radiotherapy*. *Anticancer research*, vol. 39, no. 6, pages 2721–2727, 2019. (Cited on page 183.)
- [Lindström *et al.* 1999] G Lindström, Michael Moll and E Fretwurst. *Radiation hardness of silicon detectors—a challenge from high-energy physics*. *Nuclear Instruments and Methods in Physics Research Section A: Accelerators, Spectrometers, Detectors and Associated Equipment*, vol. 426, no. 1, pages 1–15, 1999. (Cited on page 14.)
- [Liu *et al.* 2012] Wei Liu, Xiaodong Zhang, Yupeng Li and Radhe Mohan. *Robust optimization of intensity modulated proton therapy*. *Medical physics*, vol. 39, no. 2, pages 1079–1091, 2012. (Cited on page 60.)
- [Livingstone *et al.* 2016] Jayde Livingstone, Andrew W Stevenson, Duncan J Butler, Daniel Häusermann and Jean-François Adam. *Characterization of a synthetic single crystal diamond detector for dosimetry in spatially fractionated synchrotron x-ray fields*. *Medical physics*, vol. 43, no. 7, pages 4283–4293, 2016. (Cited on page 96.)
- [Lobachevsky *et al.* 2015] Pavel Lobachevsky, Alesia Ivashkevich, Helen B Forrester, Andrew W Stevenson, Chris J Hall, Carl N Sprung and Olga A Martin. *Assessment and implications of scattered microbeam and broadbeam synchrotron radiation for bystander effect studies*. *Radiation Research*, vol. 184, no. 6, pages 650–659, 2015. (Cited on page 77.)
- [Lobachevsky *et al.* 2021] Pavel Lobachevsky, Helen B Forrester, Alesia Ivashkevich, Joel Mason, Andrew W Stevenson, Chris J Hall, Carl N

- Sprung, Valentin G Djonov and Olga A Martin. *Synchrotron X-ray radiation-induced bystander effect: an impact of the scattered radiation, distance from the irradiated site and p53 cell status*. *Frontiers in oncology*, page 1812, 2021. (Cited on page 77.)
- [Lobrich & B. Rydberg 1996] PK Cooper Lobrich and M B. Rydberg. *Non-random distribution of DNA double-strand breaks induced by particle irradiation*. *International journal of radiation biology*, vol. 70, no. 5, pages 493–503, 1996. (Cited on page 59.)
- [Lodish *et al.* 2006] Harvey F Lodish, Arnold Berk, S Lawrence Zipursky, Paul Matsudaira, David Baltimore and James Darnell. *Molecular cell biology*, volume 4. Citeseer, 2006. (Cited on pages 27, 28 and 215.)
- [Lomax & Scheib 2003] Nicoletta J Lomax and Stefan G Scheib. *Quantifying the degree of conformity in radiosurgery treatment planning*. *International Journal of Radiation Oncology\* Biology\* Physics*, vol. 55, no. 5, pages 1409–1419, 2003. (Cited on page 169.)
- [Ma & Jiang 1999] Chang-Ming Ma and Steve B Jiang. *Monte Carlo modelling of electron beams from medical accelerators*. *Physics in Medicine & Biology*, vol. 44, no. 12, page R157, 1999. (Cited on page 108.)
- [Ma & Lomax 2012] CM Charlie Ma and Tony Lomax. *Proton and carbon ion therapy*. CRC press, 2012. (Cited on page 55.)
- [Macchia *et al.* 2017] Gabriella Macchia, Francesco Deodato, Savino Cilla, Silvia Cammelli, Alessandra Guido, Martina Ferioli, Giambattista Siepe, Vincenzo Valentini, Alessio Giuseppe Morganti and Gabriella Ferrandina. *Volumetric modulated arc therapy for treatment of solid tumors: current insights*. *OncoTargets and therapy*, vol. 10, page 3755, 2017. (Cited on page 20.)
- [Macdonald *et al.* 2004] Fiona Macdonald, Chris HJ Ford and Alan G Casson. *Molecular biology of cancer*. Taylor & Francis, 2004. (Cited on page 2.)
- [Malouff *et al.* 2020] Timothy D Malouff, Anita Mahajan, Sunil Krishnan, Chris Beltran, Danushka S Seneviratne and Daniel Michael Trifiletti. *Carbon ion therapy: a modern review of an emerging technology*. *Frontiers in oncology*, vol. 10, page 82, 2020. (Cited on page 23.)
- [Manchado de Sola *et al.* 2018] Francisco Manchado de Sola, Manuel Vilches, Yolanda Prezado and Antonio M Lallena. *Impact of cardiosynchronous brain pulsations on Monte Carlo calculated doses for synchrotron micro-and minibeam radiation therapy*. *Medical Physics*, vol. 45, no. 7, pages 3379–3390, 2018. (Cited on pages 70 and 72.)
- [Marks 1952] Hirsch Marks. *Clinical experience with irradiation through a grid*. *Radiology*, vol. 58, no. 3, pages 338–342, 1952. (Cited on page 64.)
- [Marsolat *et al.* 2016] F Marsolat, L De Marzi, A Patriarca, C Nauraye, C Moignier, M Pomorski, F Moignau, S Heinrich, D Tromson and A Mazal. *Dosimetric characteristics of four PTW microDiamond detectors in high-energy proton beams*. *Physics in Medicine & Biology*, vol. 61, no. 17, page 6413, 2016. (Cited on page 14.)

- [Martínez-Rovira *et al.* 2010] Imma Martínez-Rovira, J Sempau, Jose Maria Fernández-Varea, A Bravin and Y Prezado. *Monte Carlo dosimetry for forthcoming clinical trials in x-ray microbeam radiation therapy*. Physics in Medicine & Biology, vol. 55, no. 15, page 4375, 2010. (Cited on page 174.)
- [Martínez-Rovira *et al.* 2015] I Martínez-Rovira, G Fois and Y Prezado. *Dosimetric evaluation of new approaches in GRID therapy using nonconventional radiation sources*. Medical Physics, vol. 42, no. 2, pages 685–693, 2015. (Cited on page 72.)
- [Martínez-Rovira *et al.* 2017a] Immaculada Martínez-Rovira, Wilfredo González, Stephan Brons and Yolanda Prezado. *Carbon and oxygen minibeam radiation therapy: An experimental dosimetric evaluation*. Medical Physics, vol. 44, no. 8, pages 4223–4229, 2017. (Cited on page 73.)
- [Martínez-Rovira *et al.* 2017b] Immaculada Martínez-Rovira, Josep Puxeu-Vaqué and Yolanda Prezado. *Dose evaluation of Grid Therapy using a 6 MV flattening filter-free (FFF) photon beam: A Monte Carlo study*. Medical Physics, vol. 44, no. 10, pages 5378–5383, 2017. (Cited on page 67.)
- [Mattiuzzi & Lippi 2019] Camilla Mattiuzzi and Giuseppe Lippi. *Current cancer epidemiology*. Journal of epidemiology and global health, vol. 9, no. 4, page 217, 2019. (Cited on pages 1, 3 and 201.)
- [McDonald *et al.* 2016] Mark W McDonald, Yuan Liu, Michael G Moore and Peter AS Johnstone. *Acute toxicity in comprehensive head and neck radiation for nasopharynx and paranasal sinus cancers: cohort comparison of 3D conformal proton therapy and intensity modulated radiation therapy*. Radiation oncology, vol. 11, no. 1, pages 1–10, 2016. (Cited on page 61.)
- [McMahon 2018] Stephen Joseph McMahon. *The linear quadratic model: usage, interpretation and challenges*. Physics in Medicine & Biology, vol. 64, no. 1, page 01TR01, 2018. (Cited on pages 33, 40, 41 and 216.)
- [McNamara *et al.* 2015] Aimee L McNamara, Jan Schuemann and Harald Paganetti. *A phenomenological relative biological effectiveness (RBE) model for proton therapy based on all published in vitro cell survival data*. Physics in Medicine & Biology, vol. 60, no. 21, page 8399, 2015. (Cited on page 80.)
- [Mein *et al.* 2022] Stewart Mein, Benedikt Kopp, Thomas Tessonnier, Jakob Liermann, Amir Abdollahi, Jürgen Debus, Thomas Haberer and Andrea Mairani. *Spot-scanning hadron arc (SHArc) therapy: A proof of concept using single-and multi-ion strategies with helium, carbon, oxygen, and neon ions*. Medical Physics, vol. 49, no. 9, pages 6082–6097, 2022. (Cited on page 23.)
- [Metropolis & Ulam 1949] Nicholas Metropolis and Stanislaw Ulam. *The monte carlo method*. Journal of the American statistical association, vol. 44, no. 247, pages 335–341, 1949. (Cited on page 108.)
- [Meyer *et al.* 2019] Juergen Meyer, John Eley, Thomas E Schmid, Stephanie E Combs, Remi Dendale and Yolanda Prezado. *Spatially fractionated proton minibeam*s. The British journal of radiology, vol. 92, no. 1095, page 20180466,

2019. (Cited on pages 82, 83, 86 and 87.)
- [Milano *et al.* 2021] Michael T Milano, Jimm Grimm, Andrzej Niemierko, Scott G Soltys, Vitali Moiseenko, Kristin J Redmond, Ellen Yorke, Arjun Sahgal, Jinyu Xue, Anand Mahadevan *et al.* *Single-and multifraction stereotactic radiosurgery dose/volume tolerances of the brain*. International Journal of Radiation Oncology\* Biology\* Physics, vol. 110, no. 1, pages 68–86, 2021. (Cited on page 175.)
- [Minniti *et al.* 2011] Giuseppe Minniti, Enrico Clarke, Gaetano Lanzetta, Mattia Falchetto Osti, Guido Trasimeni, Alessandro Bozzao, Andrea Romano and Riccardo Maurizi Enrici. *Stereotactic radiosurgery for brain metastases: analysis of outcome and risk of brain radionecrosis*. Radiation oncology, vol. 6, no. 1, pages 1–9, 2011. (Cited on page 160.)
- [Minniti *et al.* 2016] Giuseppe Minniti, Claudia Scaringi, Sergio Paolini, Gaetano Lanzetta, Andrea Romano, Francesco Cicone, Mattia Osti, Riccardo Maurizi Enrici and Vincenzo Esposito. *Single-fraction versus multifraction (3×9 Gy) stereotactic radiosurgery for large (> 2 cm) brain metastases: a comparative analysis of local control and risk of radiation-induced brain necrosis*. International Journal of Radiation Oncology\* Biology\* Physics, vol. 95, no. 4, pages 1142–1148, 2016. (Cited on page 159.)
- [Miszczyk 2021] Justyna Miszczyk. *Investigation of dna damage and cell-cycle distribution in human peripheral blood lymphocytes under exposure to high doses of proton radiotherapy*. Biology, vol. 10, no. 2, page 111, 2021. (Cited on page 58.)
- [Mitchell *et al.* 2022] DK Mitchell, HJ Kwon, PA Kubica, WX Huff, R O'Regan and M Dey. *Brain metastases: An update on the multi-disciplinary approach of clinical management*. Neurochirurgie, vol. 68, no. 1, pages 69–85, 2022. (Cited on pages 86, 159 and 186.)
- [Miura *et al.* 2006] M Miura, H Blattmann, E Brauer-Krisch, A Bravin, AL Hanson, MM Nawrocky, PL Micca, DN Slatkin and JA Laissue. *Radiosurgical palliation of aggressive murine SCCVII squamous cell carcinomas using synchrotron-generated X-ray microbeams*. The British Journal of Radiology, vol. 79, no. 937, pages 71–75, 2006. (Cited on page 71.)
- [Mizoe *et al.* 2007] Jun-Etsu Mizoe, Hirohiko Tsujii, Azusa Hasegawa, Tsuyoshi Yanagi, Ryo Takagi, Tadashi Kamada, Hiroshi Tsuji, Kintomo Takakura, Organizing Committee of the Central Nervous System Tumor Working Group *et al.* *Phase I/II clinical trial of carbon ion radiotherapy for malignant gliomas: combined X-ray radiotherapy, chemotherapy, and carbon ion radiotherapy*. International Journal of Radiation Oncology\* Biology\* Physics, vol. 69, no. 2, pages 390–396, 2007. (Cited on page 23.)
- [Mohiuddin *et al.* 1990] Mohammed Mohiuddin, Danny Lee Curtis, William T Grizos and Lydia Komarnicky. *Palliative treatment of advanced cancer using multiple nonconfluent pencil beam radiation: a pilot study*. Cancer, vol. 66, no. 1, pages 114–118, 1990. (Cited on pages 64, 65, 67 and 68.)

- [Mohiuddin *et al.* 1996] Mohammed Mohiuddin, James H Stevens, Jay E Reiff, M Saiful Huq and Nagalingam Suntharalingam. *Spatially fractionated (GRID) radiation for palliative treatment of advanced cancer*. Radiation Oncology Investigations: Clinical and Basic Research, vol. 4, no. 1, pages 41–47, 1996. (Cited on pages 67, 68 and 218.)
- [Mohiuddin *et al.* 1999] Mohammed Mohiuddin, Mihoko Fujita, William F Regine, Ali S Megooni, Goeffrey S Ibbott and Mansoor M Ahmed. *High-dose spatially-fractionated radiation (GRID): a new paradigm in the management of advanced cancers*. International Journal of Radiation Oncology\* Biology\* Physics, vol. 45, no. 3, pages 721–727, 1999. (Cited on page 68.)
- [Mohiuddin *et al.* 2009] M Mohiuddin, T Miller, P Ronjon and U Malik. *Spatially fractionated grid radiation (SFGRT): A novel approach in the management of recurrent and unresectable soft tissue sarcoma*. International Journal of Radiation Oncology, Biology, Physics, vol. 75, no. 3, page S526, 2009. (Cited on page 68.)
- [Mohiuddin *et al.* 2014] Mohammed Mohiuddin, Muhammad Memon, Ahmed Nobah, Medhat Elsebaie, Abdullah AL Suhaibani, Rajive Pant, Mahmoud Shaheen, Majid Alyamani and Fouad Al Dayal. *Locally advanced high-grade extremity soft tissue sarcoma: Response with novel approach to neoadjuvant chemoradiation using induction spatially fractionated GRID radiotherapy (SFGRT)*. American Society of Clinical Oncology, 2014. (Cited on page 68.)
- [Mohiuddin *et al.* 2020] Majid Mohiuddin, Connor Lynch, Mingcheng Gao and William Hartsell. *Early clinical results of proton spatially fractionated GRID radiation therapy (SFGRT)*. The British Journal of Radiology, vol. 93, no. 1107, page 20190572, 2020. (Cited on page 68.)
- [Moon *et al.* 2020] Young Min Moon, Wan Jeon, Tosol Yu, Sang Il Bae, Jin Young Kim, Jin-Kyu Kang and Chul Won Choi. *Which is better for liver SBRT: Dosimetric comparison between DCAT and VMAT for liver tumors*. Frontiers in oncology, vol. 10, page 1170, 2020. (Cited on page 21.)
- [Moore *et al.* 2021] Casey Moore, Ching-Cheng Hsu, Wei-Min Chen, Benjamin PC Chen, Chuanhui Han, Michael Story, Todd Aguilera, Laurentiu M Pop, Raquibul Hannan, Yang-Xin Fuet *al.* *Personalized ultrafractionated stereotactic adaptive radiotherapy (PULSAR) in preclinical models enhances single-agent immune checkpoint blockade*. International Journal of Radiation Oncology\* Biology\* Physics, vol. 110, no. 5, pages 1306–1316, 2021. (Cited on pages 201 and 202.)
- [Moorrees & Bezak 2012] J Moorrees and E Bezak. *Four dimensional radiotherapy: a review of current technologies and modalities*. Australasian physical & engineering sciences in medicine, vol. 35, no. 4, pages 399–406, 2012. (Cited on page 22.)
- [Morales-Paliza *et al.* 2011] Manuel A Morales-Paliza, Charles W Coffey and George X Ding. *Evaluation of the dynamic conformal arc therapy in comparison to intensity-modulated radiation therapy in prostate, brain, head-*

- and-neck and spine tumors*. Journal of applied clinical medical physics, vol. 12, no. 2, pages 5–19, 2011. (Cited on page 21.)
- [Morimoto *et al.* 2014] Koichi Morimoto, Yusuke Demizu, Naoki Hashimoto, Masayuki Mima, Kazuki Terashima, Osamu Fujii, Naoki Otsuki, Masao Murakami, Nobukazu Fuwa and Ken-Ichi Nibu. *Particle radiotherapy using protons or carbon ions for unresectable locally advanced head and neck cancers with skull base invasion*. Japanese journal of clinical oncology, vol. 44, no. 5, pages 428–434, 2014. (Cited on page 61.)
- [Mothersill & Seymour 2022] Carmel Mothersill and Colin Seymour. *Low dose radiation mechanisms: The certainty of uncertainty*. Mutation Research/Genetic Toxicology and Environmental Mutagenesis, page 503451, 2022. (Cited on page 37.)
- [Mothersill *et al.* 2018] Carmel Mothersill, Andrej Rusin, Cristian Fernandez-Palomo and Colin Seymour. *History of bystander effects research 1905-present; what is in a name?* International journal of radiation biology, vol. 94, no. 8, pages 696–707, 2018. (Cited on page 38.)
- [Muth *et al.* 1977] CP Muth, D Salewski, FH Glaser and KM Heider. *Grid method in telecobalt therapy*. Radiobiologia, Radiotherapia, vol. 18, no. 6, pages 691–699, 1977. (Cited on page 65.)
- [Neuner *et al.* 2012] Geoffrey Neuner, Majid M Mohiuddin, Noam Vander Walde, Olga Goloubeva, Jonathan Ha, X Yu Cedric and William F Regine. *High-dose spatially fractionated GRID radiation therapy (SFGRT): a comparison of treatment outcomes with Cerrobend vs. MLC SFGRT*. International Journal of Radiation Oncology\* Biology\* Physics, vol. 82, no. 5, pages 1642–1649, 2012. (Cited on page 68.)
- [Newhauser & Zhang 2015] Wayne D Newhauser and Rui Zhang. *The physics of proton therapy*. Physics in Medicine & Biology, vol. 60, no. 8, page R155, 2015. (Cited on pages 47, 49 and 227.)
- [Niemierko 1997] Andrzej Niemierko. *Reporting and analyzing dose distributions: a concept of equivalent uniform dose*. Medical physics, vol. 24, no. 1, pages 103–110, 1997. (Cited on page 42.)
- [Niroomand-Rad *et al.* 2020] Azam Niroomand-Rad, Sou-Tung Chiu-Tsao, Michael P Grams, David F Lewis, Christopher G Soares, Leo J Van Battum, Indra J Das, Samuel Trichter, Michael W Kissick, Guerda Massillon-JL *et al.* *Report of AAPM task group 235 radiochromic film dosimetry: an update to TG-55*. Medical physics, vol. 47, no. 12, pages 5986–6025, 2020. (Cited on page 15.)
- [NLM 2022] NLM. *Feasibility Study of FLASH Radiotherapy for the Treatment of Symptomatic Bone Metastases (FAST-01)*., 2022. (Cited on page 202.)
- [Noel *et al.* 2003] Georges Noel, Jean-Louis Habrand, Sylvie Helfre, Hamid Mammam, Chantal Kalifa, Régis Ferrand, Anne Beaudre, Geneviève Gaboriaud and Jean-Jacques Mazon. *Proton beam therapy in the management of central nervous system tumors in childhood: the preliminary*

- experience of the Centre de Protontherapie d'Orsay*. Medical and pediatric oncology, vol. 40, no. 5, pages 309–315, 2003. (Cited on page 90.)
- [Ntentas *et al.* 2019] Georgios Ntentas, Katerina Dedeckova, Michal Andrlík, Marianne C Aznar, Ben George, Jiří Kubeš, Sarah C Darby and David J Cutter. *Clinical intensity modulated proton therapy for Hodgkin lymphoma: which patients benefit the most?* Practical radiation oncology, vol. 9, no. 3, pages 179–187, 2019. (Cited on page 62.)
- [Nuffield Trust 2022] Nuffield Trust. *Cancer survival rates*, June 2022. (Cited on pages 4 and 215.)
- [Okunieff *et al.* 2006] Paul Okunieff, Anncatrine L Petersen, Abraham Philip, Michael T Milano, Alan W Katz, Laszlo Boros and Michael C Schell. *Stereotactic body radiation therapy (SBRT) for lung metastases*. Acta oncologica, vol. 45, no. 7, pages 808–817, 2006. (Cited on page 22.)
- [OrthoChrome 2022] OrthoChrome. *OrthoChromic film OC-1.*, 2022. (Cited on pages 15 and 98.)
- [Ortiz *et al.* 2021] Ramon Ortiz, Ludovic De Marzi and Yolanda Prezado. *Proton Minibeam Radiation Therapy and Arc Therapy: Proof of Concept of a Winning Alliance*. Cancers, vol. 14, no. 1, page 116, 2021. (Cited on page 199.)
- [Ortiz *et al.* 2022] Ramon Ortiz, Ludovic De Marzi and Yolanda Prezado. *Preclinical dosimetry in proton minibeam radiation therapy: robustness analysis and guidelines*. Medical Physics, 2022. (Cited on pages 143 and 156.)
- [Paganetti *et al.* 2000] H Paganetti, LE Gerweck and M Goitein. *The general relation between tissue response to x-radiation ( $\alpha/\beta$ -values) and the relative biological effectiveness (RBE) of protons: prediction by the Katz track-structure model*. International journal of radiation biology, vol. 76, no. 7, pages 985–998, 2000. (Cited on page 40.)
- [Paganetti *et al.* 2002] Harald Paganetti, Andrzej Niemierko, Marek Ancukiewicz, Leo E Gerweck, Michael Goitein, Jay S Loeffler and Herman D Suit. *Relative biological effectiveness (RBE) values for proton beam therapy*. International Journal of Radiation Oncology\* Biology\* Physics, vol. 53, no. 2, pages 407–421, 2002. (Cited on page 59.)
- [Paganetti 2012] Harald Paganetti. *Range uncertainties in proton therapy and the role of Monte Carlo simulations*. Physics in Medicine & Biology, vol. 57, no. 11, page R99, 2012. (Cited on pages 60, 61 and 227.)
- [Paganetti 2014] Harald Paganetti. *Relative biological effectiveness (RBE) values for proton beam therapy. Variations as a function of biological endpoint, dose, and linear energy transfer*. Physics in Medicine & Biology, vol. 59, no. 22, page R419, 2014. (Cited on page 59.)
- [Paganetti 2015] Harald Paganetti. *Relating proton treatments to photon treatments via the relative biological effectiveness—should we revise current clinical practice?* International Journal of Radiation Oncology, Biology, Physics, vol. 91, no. 5, pages 892–894, 2015. (Cited on page 59.)

- [Paganetti 2018] Harald Paganetti. Proton therapy physics. CRC press, 2018. (Cited on pages 8, 45, 48, 49, 50, 51, 52, 53, 55, 56, 57, 59, 60, 216 and 217.)
- [Pappas *et al.* 2008] E Pappas, TG Maris, F Zacharopoulou, A Papadakis, S Manolopoulos, S Green and C Wojnecki. *Small SRS photon field profile dosimetry performed using a PinPoint air ion chamber, a diamond detector, a novel silicon-diode array (DOSI), and polymer gel dosimetry. Analysis and intercomparison.* Medical physics, vol. 35, no. 10, pages 4640–4648, 2008. (Cited on page 14.)
- [Park *et al.* 2012] Peter C Park, X Ronald Zhu, Andrew K Lee, Narayan Sahoo, Adam D Melancon, Lifei Zhang and Lei Dong. *A beam-specific planning target volume (PTV) design for proton therapy to account for setup and range uncertainties.* International Journal of Radiation Oncology\* Biology\* Physics, vol. 82, no. 2, pages e329–e336, 2012. (Cited on page 60.)
- [Parwaie *et al.* 2018] Wrya Parwaie, Soheila Refahi, Mahdiah Afkhami Ardekani and Bagher Farhood. *Different dosimeters/detectors used in small-field dosimetry: Pros and cons.* Journal of medical signals and sensors, vol. 8, no. 3, page 195, 2018. (Cited on page 14.)
- [Pawlicki *et al.* 2016] Todd Pawlicki, Daniel J Scanderbeg and George Starkschall. *Hendee’s radiation therapy physics.* John Wiley & Sons, 2016. (Cited on pages 4, 5, 6, 7, 15, 45 and 215.)
- [Pedroni *et al.* 2005] E Pedroni, S Scheib, T Böhringer, A Coray, M Grossmann, S Lin and A Lomax. *Experimental characterization and physical modelling of the dose distribution of scanned proton pencil beams.* Physics in Medicine & Biology, vol. 50, no. 3, page 541, 2005. (Cited on pages 50 and 216.)
- [Peeler *et al.* 2016] Christopher R Peeler, Dragan Mirkovic, Uwe Titt, Pierre Blanchard, Jillian R Gunther, Anita Mahajan, Radhe Mohan and David R Grosshans. *Clinical evidence of variable proton biological effectiveness in pediatric patients treated for ependymoma.* Radiotherapy and Oncology, vol. 121, no. 3, pages 395–401, 2016. (Cited on page 59.)
- [Peñagaricano *et al.* 2010] José A Peñagaricano, Eduardo G Moros, Vaneerat Ratanatharathorn, Yulong Yan and Peter Corry. *Evaluation of spatially fractionated radiotherapy (GRID) and definitive chemoradiotherapy with curative intent for locally advanced squamous cell carcinoma of the head and neck: initial response rates and toxicity.* International Journal of Radiation Oncology\* Biology\* Physics, vol. 76, no. 5, pages 1369–1375, 2010. (Cited on page 68.)
- [Perl *et al.* 2012] Joseph Perl, Jungwook Shin, Jan Schümann, Bruce Faddegon and Harald Paganetti. *TOPAS: an innovative proton Monte Carlo platform for research and clinical applications.* Medical physics, vol. 39, no. 11, pages 6818–6837, 2012. (Cited on pages 108, 109 and 110.)
- [Perl 2014] J Perl. *Formal quality control for a proton Monte Carlo system in radiation therapy.* Journal of Physics: Conference Series, vol. 489, no. 1, page 012021, 2014. (Cited on page 110.)

- [Peucelle *et al.* 2015a] C Peucelle, I Martínez-Rovira and Y Prezado. *Spatial fractionation of the dose using neon and heavier ions: A Monte Carlo study*. Medical Physics, vol. 42, no. 10, pages 5928–5936, 2015. (Cited on page 73.)
- [Peucelle *et al.* 2015b] C Peucelle, C Nauraye, A Patriarca, E Hierso, N Fournier-Bidoz, I Martínez-Rovira and Y Prezado. *Proton minibeam radiation therapy: Experimental dosimetry evaluation*. Medical physics, vol. 42, no. 12, pages 7108–7113, 2015. (Cited on pages 79, 82, 83, 96 and 122.)
- [Peucelle 2016] Cecile Peucelle. *Spatial fractionation of the dose in charged particle therapy*. PhD thesis, Université Paris-Saclay (ComUE), 2016. (Cited on pages 79, 81, 84, 97, 99, 101, 116, 218 and 219.)
- [Pilar *et al.* 2017] Avinash Pilar, Meetakshi Gupta, Sarbani Ghosh Laskar and Siddhartha Laskar. *Intraoperative radiotherapy: review of techniques and results*. Ecancermedicallscience, vol. 11, 2017. (Cited on page 17.)
- [Pinto *et al.* 2016] Marco Pinto, Denis Dauvergne, Nicolas Freud, Jochen Krimmer, Jean M Létang and Etienne Testa. *Assessment of Geant4 prompt-gamma emission yields in the context of proton therapy monitoring*. Frontiers in oncology, vol. 6, page 10, 2016. (Cited on page 109.)
- [Podgorsak *et al.* 2005] Ervin B Podgorsak *et al.* Radiation oncology physics. IAEA Vienna, 2005. (Cited on pages 22, 31, 32, 39, 43 and 216.)
- [Podgoršak *et al.* 2006] Ervin B Podgoršak *et al.* Radiation physics for medical physicists, volume 1. Springer, 2006. (Cited on pages 20 and 35.)
- [Poleszczuk & Enderling 2018] Jan Poleszczuk and Heiko Enderling. *The optimal radiation dose to induce robust systemic anti-tumor immunity*. International journal of molecular sciences, vol. 19, no. 11, page 3377, 2018. (Cited on page 36.)
- [Pollack *et al.* 2020] Alan Pollack, Felix M Chinae, Elizabeth Bossart, Deukwoo Kwon, Matthew C Abramowitz, Charles Lynne, Merce Jorda, Brian Marples, Vivek N Patel, Xiaodong Wu *et al.* *Phase I trial of MRI-guided prostate cancer lattice extreme ablative dose (LEAD) boost radiation therapy*. International Journal of Radiation Oncology\* Biology\* Physics, vol. 107, no. 2, pages 305–315, 2020. (Cited on pages 69 and 70.)
- [Poon & Verhaegen 2005] Emily Poon and Frank Verhaegen. *Accuracy of the photon and electron physics in GEANT4 for radiotherapy applications*. Medical physics, vol. 32, no. 6Part1, pages 1696–1711, 2005. (Cited on page 110.)
- [Portella & Scala 2019] Luigi Portella and Stefania Scala. *Ionizing radiation effects on the tumor microenvironment*. Seminars in Oncology, vol. 46, no. 3, pages 254–260, 2019. (Cited on pages 34 and 35.)
- [Potez *et al.* 2019] Marine Potez, Cristian Fernandez-Palomo, Audrey Bouchet, Verdiana Trappetti, Mattia Donzelli, Michael Krisch, Jean Laissue, Vladislav Volarevic and Valentin Djonov. *Synchrotron microbeam radiation therapy as a new approach for the treatment of radioresistant melanoma: potential underlying mechanisms*. International Journal of Radiation Oncology\* Biology\* Physics, vol. 105, no. 5, pages 1126–1136, 2019. (Cited on page 71.)

- [Pouyatos *et al.* 2016] B Pouyatos, C Nemoz, T Chabrol, M Potez, E Bräuer, Luc Renaud, K Pernet-Gallay, F Estève, O David, P Kahane *et al.* *Synchrotron X-ray microtransections: a non invasive approach for epileptic seizures arising from eloquent cortical areas*. Scientific Reports, vol. 6, no. 1, pages 1–7, 2016. (Cited on page 71.)
- [Prezado & Fois 2013] Y Prezado and Giovanna Rosa Fois. *Proton-minibeam radiation therapy: A proof of concept*. Medical physics, vol. 40, no. 3, page 031712, 2013. (Cited on pages 2, 73, 78, 79 and 80.)
- [Prezado *et al.* 2009a] Y Prezado, S Thengumpallil, M Renier and A Bravin. *X-ray energy optimization in minibeam radiation therapy*. Medical physics, vol. 36, no. 11, pages 4897–4902, 2009. (Cited on pages 72 and 186.)
- [Prezado *et al.* 2009b] Yolanda Prezado, Michel Renier and Alberto Bravin. *A new method of creating minibeam patterns for synchrotron radiation therapy: a feasibility study*. Journal of Synchrotron Radiation, vol. 16, no. 4, pages 582–586, 2009. (Cited on pages 70 and 72.)
- [Prezado *et al.* 2011] Y Prezado, I Martínez-Rovira, S Thengumpallil and P Deman. *Dosimetry protocol for the preclinical trials in white-beam minibeam radiation therapy*. Medical physics, vol. 38, no. 9, pages 5012–5020, 2011. (Cited on pages 95 and 143.)
- [Prezado *et al.* 2012a] Y Prezado, I Martínez-Rovira and M Sánchez. *Scatter factors assessment in microbeam radiation therapy*. Medical physics, vol. 39, no. 3, pages 1234–1238, 2012. (Cited on page 95.)
- [Prezado *et al.* 2012b] Yolanda Prezado, Sukhena Sarun, Silvia Gil, Pierre Deman, Audrey Bouchet and Geraldine Le Duc. *Increase of lifespan for glioma-bearing rats by using minibeam radiation therapy*. Journal of synchrotron radiation, vol. 19, no. 1, pages 60–65, 2012. (Cited on page 73.)
- [Prezado *et al.* 2015] Yolanda Prezado, Pierre Deman, Pascale Varlet, Gregory Jouvion, Silvia Gil, Céline Le Clec’H, Hélène Bernard, Géraldine Le Duc and Sukhena Sarun. *Tolerance to dose escalation in minibeam radiation therapy applied to normal rat brain: long-term clinical, radiological and histopathological analysis*. Radiation research, vol. 184, no. 3, pages 314–321, 2015. (Cited on page 72.)
- [Prezado *et al.* 2017a] Y Prezado, M Dos Santos, W Gonzalez, G Jouvion, C Guardiola, S Heinrich, D Labiod, M Juchaux, L Jourdain, C Sebriet *et al.* *Transfer of Minibeam Radiation Therapy into a cost-effective equipment for radiobiological studies: a proof of concept*. Scientific reports, vol. 7, no. 1, pages 1–10, 2017. (Cited on page 72.)
- [Prezado *et al.* 2017b] Yolanda Prezado, Gregory Jouvion, David Hardy, Annalisa Patriarca, Catherine Nauraye, Judith Bergs, Wilfredo González, Consuelo Guardiola, Marjorie Juchaux, Dalila Labiod *et al.* *Proton minibeam radiation therapy spares normal rat brain: Long-Term Clinical, Radiological and Histopathological Analysis*. Scientific reports, vol. 7, no. 1, pages 1–7, 2017. (Cited on pages 2, 72, 84, 85, 150, 160, 165, 177, 188 and 197.)

- [Prezado *et al.* 2018] Yolanda Prezado, Gregory Jouvion, Annalisa Patriarca, Catherine Nauraye, Consuelo Guardiola, Marjorie Juchaux, Charlotte Lamirault, Dalila Labiod, Laurene Jourdain, Catherine Sebriee *et al.* *Proton minibeam radiation therapy widens the therapeutic index for high-grade gliomas*. *Scientific reports*, vol. 8, no. 1, pages 1–10, 2018. (Cited on pages 84, 85, 138, 162, 165, 177, 185, 188, 190 and 197.)
- [Prezado *et al.* 2019] Yolanda Prezado, Gregory Jouvion, Consuelo Guardiola, Wilfredo Gonzalez, Marjorie Juchaux, Judith Bergs, Catherine Nauraye, Dalila Labiod, Ludovic De Marzi, Frederic Pouzoulet *et al.* *Tumor control in RG2 glioma-bearing rats: a comparison between proton minibeam therapy and standard proton therapy*. *International Journal of Radiation Oncology\* Biology\* Physics*, vol. 104, no. 2, pages 266–271, 2019. (Cited on pages 84, 85, 86, 138, 160, 162, 165, 172, 175, 183, 188, 190 and 219.)
- [Prezado *et al.* 2021] Yolanda Prezado, Ryochi Hirayama, Naruhiro Matsufuji, Taku Inaniwa, Immaculada Martínez-Rovira, Olivier Seksek, Annaïg Bertho, Sachiko Koike, Dalila Labiod, Frederic Pouzoulet *et al.* *A potential renewed use of very heavy ions for therapy: neon minibeam radiation therapy*. *Cancers*, vol. 13, no. 6, page 1356, 2021. (Cited on pages 73 and 75.)
- [Prezado 2022] Yolanda Prezado. *Divide and conquer: Spatially fractionated radiation therapy*. *Expert Reviews in Molecular Medicine*, vol. 24, 2022. (Cited on pages 2, 63, 66, 68, 69, 70, 71, 72, 73, 74, 77, 78, 85, 86, 159, 202 and 227.)
- [PTCOG 2022a] PTCOG. *Particle therapy facilities in a planning stage*, 2022. (Cited on page 46.)
- [PTCOG 2022b] PTCOG. *Particle therapy facilities in clinical operation*, March 2022. (Cited on pages 22 and 46.)
- [PTCOG 2022c] PTCOG. *Particle therapy facilities under construction*, February 2022. (Cited on page 46.)
- [PTW 2022a] PTW. *microDiamond*, 2022. (Cited on pages 96 and 97.)
- [PTW 2022b] PTW. *RW3 Slab Phantom*, 2022. (Cited on pages 100 and 111.)
- [Pucci *et al.* 2019] Carlotta Pucci, Chiara Martinelli and Gianni Ciofani. *Innovative approaches for cancer treatment: Current perspectives and new challenges*. *Ecancermedicalsecience*, vol. 13, 2019. (Cited on page 3.)
- [Qi *et al.* 2006] X Sharon Qi, Christopher J Schultz and X Allen Li. *An estimation of radiobiologic parameters from clinical outcomes for radiation treatment planning of brain tumor*. *International Journal of Radiation Oncology\* Biology\* Physics*, vol. 64, no. 5, pages 1570–1580, 2006. (Cited on page 165.)
- [Qin *et al.* 2021] Bin Qin, Xu Liu, Qu-Shan Chen, Dong Li, Wen-Jie Han, Ping Tan, Zhong-Qi Zhang, Chong Zhou, Ao-Te Chen, Yi-Cheng Liao *et al.* *Design and development of the beamline for a proton therapy system*. *Nuclear Science and Techniques*, vol. 32, no. 12, pages 1–11, 2021. (Cited on page 54.)
- [Rackwitz & Debus 2019] Tilmann Rackwitz and Jürgen Debus. *Clinical applications of proton and carbon ion therapy*. *Seminars in oncology*, vol. 46,

- no. 3, pages 226–232, 2019. (Cited on page 25.)
- [Raina *et al.* 2020] Payal Raina, Sudha Singh, Rajanigandha Tudu, Rashmi Singh and Anup Kumar. *Volumetric modulated arc therapy: a dosimetric comparison with dynamic IMRT and step-and-shoot IMRT*. *Journal of Radiotherapy in Practice*, vol. 19, no. 4, pages 393–398, 2020. (Cited on page 20.)
- [Ramos-Méndez 2022] José Ramos-Méndez. *Standard deviation in ProtonLET Scorer*, 2022. (Cited on page 116.)
- [Rana *et al.* 2014] Suresh Rana, Hilarie Simpson, Gary Larson and Yuanshui Zheng. *Dosimetric impact of number of treatment fields in uniform scanning proton therapy planning of lung cancer*. *Journal of Medical Physics/Association of Medical Physicists of India*, vol. 39, no. 4, page 212, 2014. (Cited on page 174.)
- [Randall *et al.* 2022] James W Randall, Nikhil Rammohan, Indra J Das and Poonam Yadav. *Towards Accurate and Precise Image-Guided Radiotherapy: Clinical Applications of the MR-Linac*. *Journal of Clinical Medicine*, vol. 11, no. 14, page 4044, 2022. (Cited on page 201.)
- [RaySearch Laboratories 2021] RaySearch Laboratories. *Heidelberg Ion Beam Therapy Center treats first patient using helium ion therapy with RayStation*, October 2021. (Cited on page 22.)
- [Reggiori *et al.* 2017] Giacomo Reggiori, Antonella Stravato, Maria Pimpinella, Francesca Lobefalo, Vanessa De Coste, Antonella Fogliata, Pietro Mancosu, Fiorenza De Rose, Valentina Palumbo, Marta Scorsetti *et al.* *Use of PTW-microDiamond for relative dosimetry of unflattened photon beams*. *Physica Medica*, vol. 38, pages 45–53, 2017. (Cited on page 14.)
- [Reiser 2008] Martin Reiser. *Theory and design of charged particle beams*. John Wiley & Sons, 2008. (Cited on page 112.)
- [Renaud *et al.* 2013] James Renaud, David Marchington, Jan Seuntjens and Arman Sarfehnia. *Development of a graphite probe calorimeter for absolute clinical dosimetry*. *Medical Physics*, vol. 40, no. 2, page 020701, 2013. (Cited on page 94.)
- [Renaud *et al.* 2018] James Renaud, Arman Sarfehnia, Julien Bancheri and Jan Seuntjens. *Aerrow: A probe-format graphite calorimeter for absolute dosimetry of high-energy photon beams in the clinical environment*. *Medical physics*, vol. 45, no. 1, pages 414–428, 2018. (Cited on page 94.)
- [Ricardi *et al.* 2012] Umberto Ricardi, Andrea Riccardo Filippi, Alessia Guarneri, Riccardo Ragona, Cristina Mantovani, Francesca Giglioli, Angela Botticella, Patrizia Ciammella, Cristina Iftode, Lucio Buffoni *et al.* *Stereotactic body radiation therapy for lung metastases*. *Lung cancer*, vol. 75, no. 1, pages 77–81, 2012. (Cited on page 160.)
- [Rivera *et al.* 2020] Judith N Rivera, Thomas M Kierski, Sandeep K Kasoji, Anthony S Abrantes, Paul A Dayton and Sha X Chang. *Conventional dose rate spatially-fractionated radiation therapy (SFRT) treatment response and*

- its association with dosimetric parameters—A preclinical study in a Fischer 344 rat model.* PloS one, vol. 15, no. 6, page e0229053, 2020. (Cited on page 138.)
- [Romanelli *et al.* 2013] Pantaleo Romanelli, Erminia Fardone, Giuseppe Battaglia, Elke Bräuer-Krisch, Yolanda Prezado, Herwig Requardt, Geraldine Le Duc, Christian Nemoz, David J Ansel, Jenny Spiga *et al.* *Synchrotron-generated microbeam sensorimotor cortex transections induce seizure control without disruption of neurological functions.* PloS one, vol. 8, no. 1, page e53549, 2013. (Cited on page 71.)
- [Romesser *et al.* 2016] Paul B Romesser, Oren Cahlon, Eli Scher, Ying Zhou, Sean L Berry, Alisa Rybkin, Kevin M Sine, Shikui Tang, Eric J Sherman, Richard Wong *et al.* *Proton beam radiation therapy results in significantly reduced toxicity compared with intensity-modulated radiation therapy for head and neck tumors that require ipsilateral radiation.* Radiotherapy and Oncology, vol. 118, no. 2, pages 286–292, 2016. (Cited on page 61.)
- [Ronga *et al.* 2021] Maria Grazia Ronga, Marco Cavallone, Annalisa Patriarca, Amelia Maia Leite, Pierre Loap, Vincent Favaudon, Gilles Créhange and Ludovic De Marzi. *Back to the Future: Very High-Energy Electrons (VHEEs) and Their Potential Application in Radiation Therapy.* Cancers, vol. 13, no. 19, page 4942, 2021. (Cited on page 25.)
- [Rosenthal *et al.* 2019] Amanda Rosenthal, Rachel Israilevich and Ronald Moy. *Management of acute radiation dermatitis: a review of the literature and proposal for treatment algorithm.* Journal of the American Academy of Dermatology, vol. 81, no. 2, pages 558–567, 2019. (Cited on pages 87, 178 and 190.)
- [Rossomme *et al.* 2016] Séverine Rossomme, Jean-Marc Denis, Kevin Souris, Antoine Delor, Florence Bartier, Damien Dumont, Stefaan Vynckier and Hugo Palmans. *LET dependence of the response of a PTW-60019 microDiamond detector in a 62 MeV proton beam.* Physica Medica, vol. 32, no. 9, pages 1135–1138, 2016. (Cited on page 14.)
- [Russo *et al.* 2017] S Russo, A Mirandola, S Molinelli, E Mastella, A Vai, G Magro, A Mairani, D Boi, M Donetti and M Ciocca. *Characterization of a commercial scintillation detector for 2-D dosimetry in scanned proton and carbon ion beams.* Physica Medica, vol. 34, pages 48–54, 2017. (Cited on page 100.)
- [Sabatasso *et al.* 2011] Sara Sabatasso, Jean Albert Laissue, Ruslan Hlushchuk, Werner Graber, Alberto Bravin, Elke Bräuer-Krisch, Stéphanie Corde, Hans Blattmann, Guenther Gruber and Valentin Djonov. *Microbeam radiation-induced tissue damage depends on the stage of vascular maturation.* International Journal of Radiation Oncology\* Biology\* Physics, vol. 80, no. 5, pages 1522–1532, 2011. (Cited on pages 71 and 75.)
- [Sachs *et al.* 1997] R Sachs, K Chen and DJ Brenner. *Proximity effects in the production of chromosome aberrations by ionizing radiation.* International

- Journal of Radiation Biology, vol. 71, no. 1, pages 1–19, 1997. (Cited on page 58.)
- [Sachs *et al.* 2004] RK Sachs, D Levy, P Hahnfeldt and L Hlatky. *Quantitative analysis of radiation-induced chromosome aberrations*. Cytogenetic and Genome Research, vol. 104, no. 1-4, pages 142–148, 2004. (Cited on pages 31 and 215.)
- [Safai *et al.* 2008] Sairos Safai, Thomas Bortfeld and Martijn Engelsman. *Comparison between the lateral penumbra of a collimated double-scattered beam and uncollimated scanning beam in proton radiotherapy*. Physics in Medicine & Biology, vol. 53, no. 6, page 1729, 2008. (Cited on page 57.)
- [Salvat 2015] Francesc Salvat. PENELOPE-2014: A Code System for Monte Carlo Simulation of Electron and Photon Transport. OECD, 2015. (Cited on pages 6, 8, 108 and 215.)
- [Sammer *et al.* 2017] Matthias Sammer, Christoph Greubel, Stefanie Girst and Günther Dollinger. *Optimization of beam arrangements in proton minibeam radiotherapy by cell survival simulations*. Medical physics, vol. 44, no. 11, pages 6096–6104, 2017. (Cited on pages 67 and 218.)
- [Sammer *et al.* 2019] Matthias Sammer, Esther Zahnbrecher, Sophie Dobiasch, Stefanie Girst, Christoph Greubel, Katarina Ilicic, Judith Reindl, Benjamin Schwarz, Christian Siebenwirth, Dietrich WM Walsh *et al.* *Proton pencil minibeam irradiation of an in-vivo mouse ear model spares healthy tissue dependent on beam size*. PloS one, vol. 14, no. 11, page e0224873, 2019. (Cited on page 98.)
- [Schippers *et al.* 2018] Jacobus Maarten Schippers, Anthony Lomax, Adriano Garonna and Katia Parodi. *Can technological improvements reduce the cost of proton radiation therapy?* Seminars in radiation oncology, vol. 28, no. 2, pages 150–159, 2018. (Cited on pages 51, 54 and 217.)
- [Schlegel 2006] Wolfgang Schlegel. *New technologies in 3D conformal radiation therapy: Introduction and overview*. In New Technologies in Radiation Oncology, pages 1–6. Springer, 2006. (Cited on page 19.)
- [Schneider *et al.* 2000] Wilfried Schneider, Thomas Bortfeld and Wolfgang Schlegel. *Correlation between CT numbers and tissue parameters needed for Monte Carlo simulations of clinical dose distributions*. Physics in Medicine & Biology, vol. 45, no. 2, page 459, 2000. (Cited on page 111.)
- [Schneider *et al.* 2020] Tim Schneider, Ludovic De Marzi, Annalisa Patriarca and Yolanda Prezado. *Advancing proton minibeam radiation therapy: magnetically focussed proton minibeam at a clinical centre*. Scientific reports, vol. 10, no. 1, pages 1–10, 2020. (Cited on pages 84 and 204.)
- [Schneider *et al.* 2022a] Tim Schneider, Ludovic De Marzi and Ramon Ortiz. *Chapter 20: Monte Carlo simulation of Proton SFRT*. In H Zhang and Nina A. Mayr, editors, Spatially Fractionated, Microbeam and Flash Radiation Therapy: A Physics and Multi-disciplinary Approach. Submitted to IOP Science, 2022. (Cited on page 115.)

- [Schneider *et al.* 2022b] Tim Schneider, Cristian Fernandez-Palomo, Annaïg Bertho, Jennifer Fazzari, Lorea Iturri, Olga A Martin, Verdiana Trappetti, Valentin Djonov and Yolanda Prezado. *Combining FLASH and spatially fractionated radiation therapy: the best of both worlds*. Radiotherapy and oncology, 2022. (Cited on page 204.)
- [Schneider 2020] Tim Schneider. *Advancing the generation of proton minibeam for radiation therapy*. PhD thesis, Université Paris-Saclay, 2020. (Cited on pages 24, 26, 74, 82, 84, 112, 215 and 218.)
- [Schouten *et al.* 2002] Leo J Schouten, Joost Rutten, Hans AM Huveneers and Albert Twijnstra. *Incidence of brain metastases in a cohort of patients with carcinoma of the breast, colon, kidney, and lung and melanoma*. Cancer, vol. 94, no. 10, pages 2698–2705, 2002. (Cited on page 86.)
- [Schulte & Penfold 2012] Reinhard W Schulte and Scott N Penfold. *Proton CT for improved stopping power determination in proton therapy*. Transactions of the American Nuclear Society, vol. 106, page 55, 2012. (Cited on page 60.)
- [Schültke *et al.* 2008] Elisabeth Schültke, Bernhard HJ Juurlink, Khalid Ataelmannan, Jean Laissue, Hans Blattmann, Elke Bräuer-Krisch, Alberto Bravin, Joanna Minczewska, Jeffrey Crosbie, Hadi Taherian *et al.* *Memory and survival after microbeam radiation therapy*. European journal of radiology, vol. 68, no. 3, pages S142–S146, 2008. (Cited on page 71.)
- [Schültke *et al.* 2017] Elisabeth Schültke, Jacques Balosso, Thomas Breslin, Guido Cavaletti, Valentin Djonov, Francois Esteve, Michael Grotzer, Guido Hildebrandt, Alexander Valdman and Jean Laissue. *Microbeam radiation therapy—grid therapy and beyond: a clinical perspective*. The British journal of radiology, vol. 90, no. 1078, page 20170073, 2017. (Cited on pages 70 and 71.)
- [Schweizer *et al.* 2000] P Schweizer, M Spanne, M Di Michiel, U Jauch and JA Blattmann H Laissue. *Tissue lesions caused by microplanar beams of synchrotron-generated X-rays in Drosophila melanogaster*. International journal of radiation biology, vol. 76, no. 4, pages 567–574, 2000. (Cited on page 71.)
- [Seco *et al.* 2013] Joao Seco, Guan Gu, Tiago Marcelos, Hanne Kooy and Henning Willers. *Proton arc reduces range uncertainty effects and improves conformality compared with photon volumetric modulated arc therapy in stereotactic body radiation therapy for non-small cell lung cancer*. International Journal of Radiation Oncology\* Biology\* Physics, vol. 87, no. 1, pages 188–194, 2013. (Cited on pages 62, 185, 191 and 197.)
- [Serduc *et al.* 2006] Raphaël Serduc, Pascale Vérant, Jean-Claude Vial, Régine Farion, Linda Rocas, Chantal Rémy, Taoufik Fadlallah, Elke Brauer, Alberto Bravin, Jean Laissue *et al.* *In vivo two-photon microscopy study of short-term effects of microbeam irradiation on normal mouse brain microvasculature*. International Journal of Radiation Oncology\* Biology\* Physics, vol. 64, no. 5, pages 1519–1527, 2006. (Cited on pages 71 and 75.)

- [Serduc *et al.* 2008a] Raphaël Serduc, Thomas Christen, Jean Laissue, Régine Farion, Audrey Bouchet, Boudewijn van der Sanden, Christoph Segebarth, Elke Bräuer-Krisch, Géraldine Le Duc, Alberto Bravin *et al.* *Brain tumor vessel response to synchrotron microbeam radiation therapy: a short-term in vivo study*. *Physics in Medicine & Biology*, vol. 53, no. 13, page 3609, 2008. (Cited on page 71.)
- [Serduc *et al.* 2008b] Raphaël Serduc, Yohan Van De Looij, Gilles Francony, Olivier Verdonck, Boudewijn Van Der Sanden, Jean Laissue, Régine Farion, Elke Bräuer-Krisch, Erik Albert Siegbahn, Alberto Bravin *et al.* *Characterization and quantification of cerebral edema induced by synchrotron x-ray microbeam radiation therapy*. *Physics in Medicine & Biology*, vol. 53, no. 5, page 1153, 2008. (Cited on page 71.)
- [Serduc *et al.* 2009] Raphaël Serduc, Elke Bräuer-Krisch, Audrey Bouchet, Luc Renaud, Thierry Brochard, Alberto Bravin, Jean Albert Laissue and Géraldine Le Duc. *First trial of spatial and temporal fractionations of the delivered dose using synchrotron microbeam radiation therapy*. *Journal of synchrotron radiation*, vol. 16, no. 4, pages 587–590, 2009. (Cited on page 162.)
- [Serre *et al.* 2016] Raphael Serre, Sebastien Benzekry, Laetitia Padovani, Christophe Meille, Nicolas André, Joseph Ciccolini, Fabrice Barlesi, Xavier Muracciole and Dominique Barbolosi. *Mathematical Modeling of Cancer Immunotherapy and Its Synergy with Radiotherapy Modeling of Radioimmunotherapy*. *Cancer research*, vol. 76, no. 17, pages 4931–4940, 2016. (Cited on page 183.)
- [Serre *et al.* 2018] Raphaël Serre, Fabrice Barlesi, Xavier Muracciole and Dominique Barbolosi. *Immunologically effective dose: a practical model for immuno-radiotherapy*. *Oncotarget*, vol. 9, no. 61, page 31812, 2018. (Cited on page 42.)
- [Shaffer *et al.* 2010] Richard Shaffer, Alan M Nichol, Emily Vollans, Ming Fong, Sandy Nakano, Vitali Moiseenko, Moira Schmuland, Roy Ma, Michael McKenzie and Karl Otto. *A comparison of volumetric modulated arc therapy and conventional intensity-modulated radiotherapy for frontal and temporal high-grade gliomas*. *International Journal of Radiation Oncology\* Biology\* Physics*, vol. 76, no. 4, pages 1177–1184, 2010. (Cited on page 20.)
- [Shaw *et al.* 1993] Edward Shaw, Robert Kline, Michael Gillin, Luis Souhami, Alan Hirschfeld, Robert Dinapoli and Linda Martin. *Radiation Therapy Oncology Group: radiosurgery quality assurance guidelines*. *International Journal of Radiation Oncology\* Biology\* Physics*, vol. 27, no. 5, pages 1231–1239, 1993. (Cited on page 169.)
- [Shima *et al.* 2012] Katsumi Shima, Kunihiro Tateoka, Yuichi Saitoh, Junji Suzuki, Yuji Yaegashi, Kazunori Fujimoto, Takuya Nakazawa, Akihiro Nakata, Tadanori Abe, Sho Imaie *et al.* *Analysis of post-exposure density growth in radiochromic film with respect to the radiation dose*. *Journal of Radiation*

- Research, vol. 53, no. 2, pages 301–305, 2012. (Cited on page 98.)
- [Shin *et al.* 2017] Wook-Geun Shin, Mauro Testa, Hak Soo Kim, Jong Hwi Jeong, Se Byeong Lee, Yeon-Joo Kim and Chul Hee Min. *Independent dose verification system with Monte Carlo simulations using TOPAS for passive scattering proton therapy at the National Cancer Center in Korea*. *Physics in Medicine & Biology*, vol. 62, no. 19, page 7598, 2017. (Cited on page 110.)
- [Slatkin *et al.* 1992] Daniel N Slatkin, Per Spanne, FA Dilmanian and Michael Sandborg. *Microbeam radiation therapy*. *Medical physics*, vol. 19, no. 6, pages 1395–1400, 1992. (Cited on pages 65 and 70.)
- [Slatkin *et al.* 1994] DN Slatkin, FA Dilmanian, MM Nawrocky, P Spanne, JO Gebbers, DW Archer and JA Laissue. *Design of a multislit, variable width collimator for microplanar beam radiotherapy*. 1994. (Cited on pages 70 and 71.)
- [Smilowitz *et al.* 2006] HM Smilowitz, H Blattmann, E Bräuer-Krisch, A Bravin, M Di Michiel, J-O Gebbers, AL Hanson, N Lyubimova, DN Slatkin, J Stepanek *et al.* *Synergy of gene-mediated immunoprophylaxis and microbeam radiation therapy for advanced intracerebral rat 9L gliosarcomas*. *Journal of neuro-oncology*, vol. 78, no. 2, pages 135–143, 2006. (Cited on page 78.)
- [Smith *et al.* 2018] Richard Smith, Jiayi Wang, Colin Seymour, Cristian Fernandez-Palomo, Jennifer Fazzari, Elisabeth Schültke, Elke Bräuer-Krisch, Jean Laissue, Christian Schroll and Carmel Mothersill. *Homogenous and microbeam X-ray radiation induces proteomic changes in the brains of irradiated rats and in the brains of nonirradiated cage mate rats*. *Dose-response*, vol. 16, no. 1, page 1559325817750068, 2018. (Cited on page 77.)
- [Smyth *et al.* 2018] Lloyd ML Smyth, Jacqueline F Donoghue, Jessica A Ventura, Jayde Livingstone, Tracy Bailey, Liam RJ Day, Jeffrey C Crosbie and Peter AW Rogers. *Comparative toxicity of synchrotron and conventional radiation therapy based on total and partial body irradiation in a murine model*. *Scientific reports*, vol. 8, no. 1, pages 1–11, 2018. (Cited on page 64.)
- [Söderberg & Carlsson 2000] Jonas Söderberg and Gudrun Alm Carlsson. *Fast neutron absorbed dose distributions in the energy range 0.5-80 MeV-a Monte Carlo study*. *Physics in Medicine & Biology*, vol. 45, no. 10, page 2987, 2000. (Cited on page 26.)
- [Soliman *et al.* 2016] Hany Soliman, Sunit Das, David A Larson and Arjun Sahgal. *Stereotactic radiosurgery (SRS) in the modern management of patients with brain metastases*. *Oncotarget*, vol. 7, no. 11, page 12318, 2016. (Cited on pages 22, 173 and 198.)
- [Sonke *et al.* 2019] Jan-Jakob Sonke, Marianne Aznar and Coen Rasch. *Adaptive radiotherapy for anatomical changes*. *Seminars in radiation oncology*, vol. 29, no. 3, pages 245–257, 2019. (Cited on page 21.)
- [Sorriaux *et al.* 2013] Jefferson Sorriaux, A Kacperek, Séverine Rossomme, John Aldo Lee, D Bertrand, Stefaan Vynckier and Edmond Sterpin.

- Evaluation of Gafchromic® EBT3 films characteristics in therapy photon, electron and proton beams.* *Physica Medica*, vol. 29, no. 6, pages 599–606, 2013. (Cited on page 99.)
- [Sotiropoulos & Prezado 2021] Marios Sotiropoulos and Yolanda Prezado. *A scanning dynamic collimator for spot-scanning proton minibeam production.* *Scientific reports*, vol. 11, no. 1, pages 1–11, 2021. (Cited on pages 84 and 204.)
- [Sotiropoulos & Prezado 2022] Marios Sotiropoulos and Yolanda Prezado. *Radiation quality correction factors for improved dosimetry in preclinical minibeam radiotherapy.* *Medical Physics*, 2022. (Cited on pages 93 and 97.)
- [Sotiropoulos *et al.* 2021] Marios Sotiropoulos, Elise Brisebard, Marine Le Dudal, Gregory Jouvion, Marjorie Juchaux, Delphine Crépin, Catherine Sebrie, Laurene Jourdain, Dalila Labiod, Charlotte Lamirault *et al.* *X-rays minibeam radiation therapy at a conventional irradiator: Pilot evaluation in F98-glioma bearing rats and dose calculations in a human phantom.* *Clinical and translational radiation oncology*, vol. 27, pages 44–49, 2021. (Cited on page 73.)
- [Sprung *et al.* 2012] Carl N Sprung, Yuqing Yang, Helen B Forrester, Jason Li, Marina Zaitseva, Leonie Cann, Tina Restall, Robin L Anderson, Jeffrey C Crosbie and Peter AW Rogers. *Genome-wide transcription responses to synchrotron microbeam radiotherapy.* *Radiation Research*, vol. 178, no. 4, pages 249–259, 2012. (Cited on pages 70 and 77.)
- [Steel *et al.* 1989] G Gordon Steel, Trevor J McMillan and JH Peacock. *The 5Rs of radiobiology.* *International journal of radiation biology*, vol. 56, no. 6, pages 1045–1048, 1989. (Cited on pages 29, 32 and 216.)
- [Steel 2002] G. Gordon Steel. *Basic clinical radiobiology.* Arnold, London, 2002. (Cited on page 165.)
- [Suarez *et al.* 2015] Jesus Manuel Blanco Suarez, Beatriz E Amendola, Naipy Perez, Marco Amendola and Xiaodong Wu. *The use of lattice radiation therapy (LRT) in the treatment of bulky tumors: a case report of a large metastatic mixed Mullerian ovarian tumor.* *Cureus*, vol. 7, no. 11, 2015. (Cited on page 69.)
- [Suit *et al.* 1975] Herman D Suit, Michael Goitein, Joel Tepper, Andreas M Koehler, Robert A Schmidt and Robert Schneider. *Exploratory study of proton radiation therapy using large field techniques and fractionated dose schedules.* *Cancer*, vol. 35, no. 6, pages 1646–1657, 1975. (Cited on page 46.)
- [Swisher-McClure *et al.* 2016] Samuel Swisher-McClure, Boon-Keng Kevin Teo, Maura Kirk, Chang Chang and Alexander Lin. *Comparison of pencil beam scanning proton-and photon-based techniques for carcinoma of the parotid.* *International Journal of Particle Therapy*, vol. 2, no. 4, pages 525–532, 2016. (Cited on page 61.)
- [Symonds *et al.* 2012] R Paul Symonds, Charles Deehan, Catherine Meredith and John A Mills. *Walter and miller’s textbook of radiotherapy e-book:*

- Radiation physics, therapy and oncology. Elsevier Health Sciences, 2012. (Cited on pages 4, 5, 6, 7, 8, 9, 13, 15, 16, 17, 18, 19, 23, 25, 30, 31, 40, 45, 46, 215 and 216.)
- [Tepper *et al.* 1977] Joel Tepper, Lynn Verhey, Michael Goitein, Herman D Suit, D Phil and Andreas M Koehler. *In vivo determinations of RBE in a high energy modulated proton beam using normal tissue reactions and fractionated dose schedules.* International Journal of Radiation Oncology\* Biology\* Physics, vol. 2, no. 11-12, pages 1115–1122, 1977. (Cited on page 59.)
- [Testa *et al.* 2013] Mauro Testa, J Schümann, H-M Lu, J Shin, B Faddegon, J Perl and H Paganetti. *Experimental validation of the TOPAS Monte Carlo system for passive scattering proton therapy.* Medical physics, vol. 40, no. 12, page 121719, 2013. (Cited on page 110.)
- [Tommasino & Durante 2015] Francesco Tommasino and Marco Durante. *Proton radiobiology.* Cancers, vol. 7, no. 1, pages 353–381, 2015. (Cited on page 58.)
- [TOPAS MC Inc 2021] TOPAS MC Inc. *TOPAS Documentation*, 2021. (Cited on page 110.)
- [TOPAS MC Inc. 2022] TOPAS MC Inc. *TOPAS MC Inc.*, 2022. (Cited on page 109.)
- [Toussaint *et al.* 2019] Laura Toussaint, Daniel J Indelicato, Katrine S Holgersen, Jørgen BB Petersen, Camilla H Stokkevåg, Yasmin Lassen-Ramshad, Oscar Casares-Magaz, Anne Vestergaard and Ludvig P Muren. *Towards proton arc therapy: physical and biologically equivalent doses with increasing number of beams in pediatric brain irradiation.* Acta oncologica, vol. 58, no. 10, pages 1451–1456, 2019. (Cited on pages 62 and 63.)
- [Underwood & Paganetti 2016] Tracy Underwood and Harald Paganetti. *Variable proton relative biological effectiveness: how do we move forward?* International Journal of Radiation Oncology, Biology, Physics, vol. 95, no. 1, pages 56–58, 2016. (Cited on page 59.)
- [Urano *et al.* 1980] Muneyasu Urano, Michael Goitein, Lynn Verhey, Oscar Mendiondo, Herman D Suit and Andreas Koehler. *Relative biological effectiveness of a high energy modulated proton beam using a spontaneous murine tumor in vivo.* International Journal of Radiation Oncology\* Biology\* Physics, vol. 6, no. 9, pages 1187–1193, 1980. (Cited on page 59.)
- [Valentini *et al.* 2009] Vincenzo Valentini, Claudio Coco, Gianluca Rizzo, Alberto Manno, Antonio Crucitti, Claudio Mattana, Carlo Ratto, Alessandro Verbo, Fabio M Vecchio, Brunella Barbaro *et al.* *Outcomes of clinical T4M0 extra-peritoneal rectal cancer treated with preoperative radiochemotherapy and surgery: a prospective evaluation of a single institutional experience.* Surgery, vol. 145, no. 5, pages 486–494, 2009. (Cited on page 17.)
- [Van Dam *et al.* 1990] J Van Dam, G Leunens and A Dutreix. *Correlation between temperature and dose rate dependence of semiconductor response; influence of accumulated dose.* Radiotherapy and Oncology, vol. 19, no. 4, pages 345–351, 1990. (Cited on page 14.)

- [Van den Aardweg *et al.* 1994] GJMJ Van den Aardweg, JW Hopewell, EM Whitehouse and W Calvo. *A new model of radiation-induced myelopathy: A comparison of the response of mature and immature pigs*. International Journal of Radiation Oncology\* Biology\* Physics, vol. 29, no. 4, pages 763–770, 1994. (Cited on page 71.)
- [van der Kogel 1993] Albert J van der Kogel. *Dose-volume effects in the spinal cord*. Radiotherapy and Oncology, vol. 29, no. 2, pages 105–109, 1993. (Cited on page 36.)
- [Van Der Sanden *et al.* 2010] Boudewijn Van Der Sanden, Elke Bräuer-Krisch, Erik Albert Siegbahn, Clément Ricard, Jean-Claude Vial and Jean Laissue. *Tolerance of arteries to microplanar X-ray beams*. International Journal of Radiation Oncology\* Biology\* Physics, vol. 77, no. 5, pages 1545–1552, 2010. (Cited on pages 71 and 75.)
- [Varian 2022] Varian. *Eclipse*, 2022. (Cited on page 117.)
- [Verhaegen & Seuntjens 2003] Frank Verhaegen and Jan Seuntjens. *Monte Carlo modelling of external radiotherapy photon beams*. Physics in medicine & biology, vol. 48, no. 21, page R107, 2003. (Cited on page 108.)
- [Veronesi *et al.* 2013] Umberto Veronesi, Roberto Orecchia, Patrick Maisonneuve, Giuseppe Viale, Nicole Rotmensz, Claudia Sangalli, Alberto Luini, Paolo Veronesi, Viviana Galimberti, Stefano Zurriga *et al.* *Intraoperative radiotherapy versus external radiotherapy for early breast cancer (ELIOT): a randomised controlled equivalence trial*. The lancet oncology, vol. 14, no. 13, pages 1269–1277, 2013. (Cited on page 17.)
- [Wambersie 1999] André Wambersie. *RBE, reference RBE and clinical RBE: applications of these concepts in hadron therapy*. Strahlentherapie und Onkologie, vol. 175, no. 2, pages 39–43, 1999. (Cited on page 40.)
- [Wang *et al.* 2018] Rong Wang, Tingyang Zhou, Wei Liu and Li Zuo. *Molecular mechanism of bystander effects and related abscopal/cohort effects in cancer therapy*. Oncotarget, vol. 9, no. 26, page 18637, 2018. (Cited on page 38.)
- [Wenzl & Wilkens 2011] Tatiana Wenzl and Jan J Wilkens. *Modelling of the oxygen enhancement ratio for ion beam radiation therapy*. Physics in Medicine & Biology, vol. 56, no. 11, page 3251, 2011. (Cited on pages 33, 34 and 216.)
- [WHO 2020] WHO. *Cancer fact sheets 2020*, December 2020. (Cited on page 3.)
- [Wilkens & Oelfke 2004] JJ Wilkens and U Oelfke. *A phenomenological model for the relative biological effectiveness in therapeutic proton beams*. Physics in Medicine & Biology, vol. 49, no. 13, page 2811, 2004. (Cited on pages 59 and 217.)
- [Wilson *et al.* 1946] Robert R Wilson *et al.* *Radiological use of fast protons*. Radiology, vol. 47, no. 5, pages 487–491, 1946. (Cited on page 46.)
- [Winter *et al.* 2020] Johanna Winter, Marek Galek, Christoph Matejcek, Jan J Wilkens, Kurt Aulenbacher, Stephanie E Combs and Stefan Bartzsch. *Clinical microbeam radiation therapy with a compact source: specifications of the line-focus X-ray tube*. Physics and Imaging in Radiation Oncology,

- vol. 14, pages 74–81, 2020. (Cited on page 70.)
- [Withers 1975] H Rodney Withers. *The four R's of radiotherapy*. Advances in radiation biology, vol. 5, pages 241–271, 1975. (Cited on pages 29, 32, 33, 35, 36, 37 and 216.)
- [Wołowicz & Kukołowicz 2016] P Wołowicz and PF Kukołowicz. *The analysis of the measurement uncertainty with application of small detectors made of Gafchromic EBT films for the range of doses typical for in vivo dosimetry in teleradiotherapy*. Radiation Measurements, vol. 92, pages 72–79, 2016. (Cited on page 15.)
- [Wu *et al.* 2010] Xiaodong Wu, Mansoor M Ahmed, Jean Wright, Seema Gupta and Alan Pollack. *On modern technical approaches of three-dimensional high-dose lattice radiotherapy (LRT)*. Cureus, vol. 2, no. 3, 2010. (Cited on pages 65, 67, 68, 69 and 218.)
- [Wu *et al.* 2020] Xiaodong Wu, Naipy C Perez, Yi Zheng, Xiaobo Li, Liuqing Jiang, Beatriz E Amendola, Benhua Xu, Nina A Mayr, Jiade J Lu, Georges F Hatoumet *et al.* *The technical and clinical implementation of LATTICE radiation therapy (LRT)*. Radiation Research, vol. 194, no. 6, pages 737–746, 2020. (Cited on page 69.)
- [Yan *et al.* 2020] Weisi Yan, Mohammad K Khan, Xiaodong Wu, Charles B Simone, Jiajin Fan, Eric Gressen, Xin Zhang, Charles L Limoli, Houda Bahig, Slavisa Tubinet *et al.* *Spatially fractionated radiation therapy: History, present and the future*. Clinical and translational radiation oncology, vol. 20, pages 30–38, 2020. (Cited on pages 68, 71, 72 and 75.)
- [Yang *et al.* 2022] Dong Yang, Weiwei Wang, Jiyi Hu, Weixu Hu, Xiyu Zhang, Xiaodong Wu, Jiade J Lu and Lin Kong. *Feasibility of lattice radiotherapy using proton and carbon-ion pencil beam for sinonasal malignancy*. Annals of Translational Medicine, vol. 10, no. 8, 2022. (Cited on page 70.)
- [Zaidi 1999] Habib Zaidi. *Relevance of accurate Monte Carlo modeling in nuclear medical imaging*. Medical physics, vol. 26, no. 4, pages 574–608, 1999. (Cited on page 108.)
- [Zeman *et al.* 1959] Wolfgang Zeman, HJ Curtis, EL Gebhard and Webb Haymaker. *Tolerance of mouse-brain tissue to high-energy deuterons*. Science, vol. 130, no. 3391, pages 1760–1761, 1959. (Cited on page 36.)
- [Zeman *et al.* 1961] W Zeman, HJ Curtis and CP Baker. *Histopathologic effect of high-energy-particle microbeams on the visual cortex of the mouse brain*. Radiation research, vol. 15, no. 4, pages 496–514, 1961. (Cited on pages 36, 76 and 218.)
- [Zhang *et al.* 2016] Xin Zhang, Jose Penagaricano, Yulong Yan, Xiaoying Liang, Steven Morrill, Robert J Griffin, Peter Corry and Vaneerat Ratanatharathorn. *Spatially fractionated radiotherapy (GRID) using helical tomotherapy*. Journal of applied clinical medical physics, vol. 17, no. 1, pages 396–407, 2016. (Cited on page 67.)
- [Zhong *et al.* 2003] Nan Zhong, Gerard M Morris, Tigran Bacarian, Eliot M Rosen

and F Avraham Dilmanian. *Response of rat skin to high-dose unidirectional x-ray microbeams: a histological study*. Radiation research, vol. 160, no. 2, pages 133–142, 2003. (Cited on page 71.)

[Zlobinskaya *et al.* 2013] Olga Zlobinskaya, Stefanie Girst, Christoph Greubel, Volker Hable, Christian Siebenwirth, Dietrich WM Walsh, Gabriele Multhoff, Jan J Wilkens, Thomas E Schmid and Günther Dollinger. *Reduced side effects by proton microchannel radiotherapy: study in a human skin model*. Radiation and environmental biophysics, vol. 52, no. 1, pages 123–133, 2013. (Cited on pages 72 and 85.)